

UNDERSTANDING THE ELECTRONIC STRUCTURE OF CUPRATES
A LOCAL APPROCH

A Dissertation
Presented to the Faculty of the Graduate School
of Cornell University
In Partial Fulfillment of the Requirements for the Degree of
Doctor of Philosophy

by
Jacob W. Alldredge
June 2008

© 2008 Jacob W. Alldredge

UNDERSTANDING THE ELECTRONIC STRUCTURE OF CUPRATES

A LOCAL APPROCH

Jacob W. Alldredge Ph. D.

Cornell University 2008

The spectrum of high T_c superconductors as studied by local tunneling, presents many unique conceptual challenges. These spectra display a wide range of behavior, often times varying over the sub-nanometer length scale. We have come to the point where we need a method of categorizing the spectra in order to reveal the underlying physical process, shedding light on to. This must be undertaken with caution, for it is easy to parameterize a series of curves arbitrarily. The parameterization process has to be undertaken with a minimalistic attitude. This is what I have endeavored to present here. Here we have an evolution in the understanding and parameterization of the Local Density of States of the High T_c superconductor Bi-2212. We start with the concept of a d-wave BCS model, to which we add a simple extension in the modeling of the lifetimes, in order to deal with our measured spectra. This model proves highly successful across a wide range of dopings, and allows us to track lifetime changes as they evolve with doping.

However our first model has some short coming, especially at low dopings where the “kink” phenomenon manifests itself. It also fails to reproduce Quasiparticle Interference Patterns (QPI) in q-space. It is here we introduce the second more complex model, that capture both real and k-space phenomena, and allows us to

predict the bulk thermodynamic and electronic properties and trends of our samples.

This can be accomplished at first for individual representative data, and has the possibility to be extended from one spectra to N, although we suffer from lack of computational power, as well as the increased complexity of our fits. These I feel will be overcome in the future, as we gain a better understanding of the relationships and the meaning of our fits.

BIOGRAPHICAL SKETCH

{Place biographical sketch here.]

This is dedicated to Seymour, whom we all miss dearly, even if he is brightening
Joan's bookcase.

ACKNOWLEDGMENTS

There are many people whom without this thesis and work would have not been possible. First there is my advisor Seamus Davis, who gave me enough rope to hang myself, or pull myself out of the pit that is grad school as well as his ability to craft my crude results into a polished centerpiece. I would also like to thank Kyle McElroy without him I would be a Marine Biologist by now. Of course maybe I can blame him for the series of events which culminated in this thesis. Regardless, without him none of this would be possible. Kazu Fujita, is also responsible for many of the physical reasoning behind my work, as well as helping me understand what the hell is happening in the cuprates. I wish to also thank Peter Hirschfeld, whose theoretical help has allowed my observations to be codified. Thanks also goes out to Jinho Lee, and all his coding help, as well as providing a sounding board for my crazy ideas. A special thanks to Prof. Rinzler, at UF who taught me most of my useful labs skills. I also need to thank all those who kept me sane enough to finish this work without resorting to various “plan Bs”, Steve Lyon, Joan Hoffman, PJ Rusello and Nick Alba (more for planning “plan B”). I should not forget those whose data I have analysis, which is pretty much all Davis group STM people, after all it is a very important, if not frequently neglected point. Finally I wish to thank my parents who besides providing support for me through the whole process are mainly responsible for the good things I do in life.

TABLE OF CONTENTS

- 1) Introduction
- 2) Evolution of the electronic excitation spectrum with strongly diminishing hole-density in superconducting $\text{Bi}_2\text{Sr}_2\text{CaCu}_2\text{O}_{8+\delta}$
- 3) Overview of Coherent Termination of Quasiparticles.
- 4) Predictive Model of Electronic Structure of High- T_c Superconductors Derived from Tunnelling Spectroscopy
- 5) Bulk Properties
- 6) Conclusion

Appendix A: Fitting code version1.

Appendix B: Fitting code version 2.

Appendix C: Initial spatial variation of $a(k,\omega)$

Appendix D: Science as Art.

LIST OF FIGURES

LIST OF TABLES

LIST OF ABBREVIATIONS

LIST OF SYMBOL

CHAPTER 1

Introduction

“If a man invents a new physics, it is not so much to arrive at a valid explanation of nature as to escape the boredom of the understood, habitual, vulgarly irreducible universe, to which he arbitrarily attributes as many dimensions as we project adjectives upon an inert thing we are tired of seeing and suffering as it was seen and suffered by the stupidity of our ancestors or of our immediate predecessors.” – E.M. Cioran

Intro

High temperature superconductors present quite an enigma. They have a series of properties that vary over hundreds of degrees that present a combined behavior that have provided a plethora's worth of riddles to the scientific community so far¹. The least of these riddles involves their ability to superconduct at temperatures much higher than previously expected². There have been many attempts to formulate a cohesive explanation that successfully saves us³, but so far there has been no consensus on even the basic level of what is a cause and what is an effect. Part of the problem is that the field has been plagued at the beginning by low quality samples, which led to widely differing results. However in the last decade or so more and more high quality data has been collected, driven by the availability of large, pure, single crystal samples. This has lead to a convergence of ideas and data.

Simultaneously physics has seen an explosion of new techniques driven in a large part by the availability of cheap computing power and storage. These techniques not only have the ability to measure the fine electronic structure on scales formally forbidden, but have massively increased the amount and type of data available for analysis as well as the analysis's possible. We have moved from single curves and graphs, to three or four

dimensional data sets consisting of millions of data curves. This poses a challenge to both experimentalists, and theorists, not only is the data set exponentially large, but it consists of sets of data that one used to spend considerable time and effort analyzing. Clearly the need for new visualization, analysis and data extraction techniques is needed.

This is where my PhD. work comes into the picture. I have developed techniques that take advantage of these challenges. Ones that utilize the massive amounts of data and bridge the gap between the theories and the data in order to provide a better picture or the processes at work that define high temperature superconductors and in doing so extract physical information from the data, rather than simply showing consistency with a simulation. I have strived to do this in the simplest form, while still making a connection to proven physical models that allow one to provide an explanation without, hopefully, the invention of radically new physics. In this way I hope to simplify the problem at hand, at minimum providing a simpler set of riddles to answer.

The tool of my trade is spectroscopic imaging scanning tunneling microscopy (SI-STM) which gains us access to the world of electronic structure variations on the angstrom scale. This is a particularly powerful tool to apply to high temperature superconductors due to the high intrinsic disorder and short length scales involved (coherence lengths on the order of 8nm). This technique also produces massive amounts of data that have, up to this point, lain in the vaults, rarely disturbed with only a cursory examination. Recently these old data sets have been revisited, after all if you can extract more information from years of collected data, and provide a tool that is useful for current and future experiments, then you have made a useful contribution that is far better than proposing experiments that might never be, especially considering the backlog of possible experiments we sit upon daily.

In the first part of this thesis I will give an overview of SI-STM as well as a brief background on our sample of choice. I will then give a brief overview of the features

of interest presented in the collected data. The second part will focus on my first basic model, and its application to data sets, as well as results and limitations. This will be followed by the introduction of new observations about the dual nature of our observations that have led me to revise my model. This will be followed by an improved model that will allow me to accurately predict some bulk properties of our samples. I will then conclude with my thoughts on what is exactly happening in high T_c materials, as well as what measurements could help confirm or disprove my suspicions. These of course will take advantage of the general analysis tools I have developed.

An Intro to STM

Spectroscopy imagining scanning tunneling microscopy (SI-STM) is an advanced technique that builds on standard scanning tunneling microscopy (STM)⁴ that has been around for over twenty years. In STM a metallic tip is placed into close proximity with the surface to be studied, a voltage is applied and the tunneling current is measured, this is illustrated in figure 1-1. By rastering the tip over the surface, inside a feedback loop maintaining constant current an image of the surface can be built up. SI-STM is a variation of this technique, instead of merely recording the constant current at every spatial point, we record the current as a function of voltage at every single point after moving from point to point and disengaging the feedback. This gives us not only a topograph figure 1-2(c) but also a series of curves whose derivative is proportional to the local density of states (LDOS), figure 1-2(a). In effect we get a map of a normalized local density of states (LDOS) with high spatial and energy resolution. Since we are only limited by the size of our Dewar these data sets can be quite large approaching, the largest so far has contained 13 million points of data. In the past these data sets have enabled us to measure the structural properties of vortex cores⁵, the granular nature of the high energy gap⁶, quasiparticle interference (QPI) patterns at low energy^{7,8,9}, the resonance and effect

of impurity atoms^{10,11}, local bosonic coupling¹², doping atoms¹³, and a universal high energy ordering state of the electron cluster glass (ECG)¹⁴. However each of these studies has focused on a particular aspect of the spectrum, leaving behind a great deal of information about the electronic states, while capturing their specific objective. It would be a great addition if instead of pointing to a specific kink or feature in the data set, we could quantitatively extract local information in a general way. This could then allow us a universal parameterization of the electronic structure. This is what I have, in effect, accomplished.

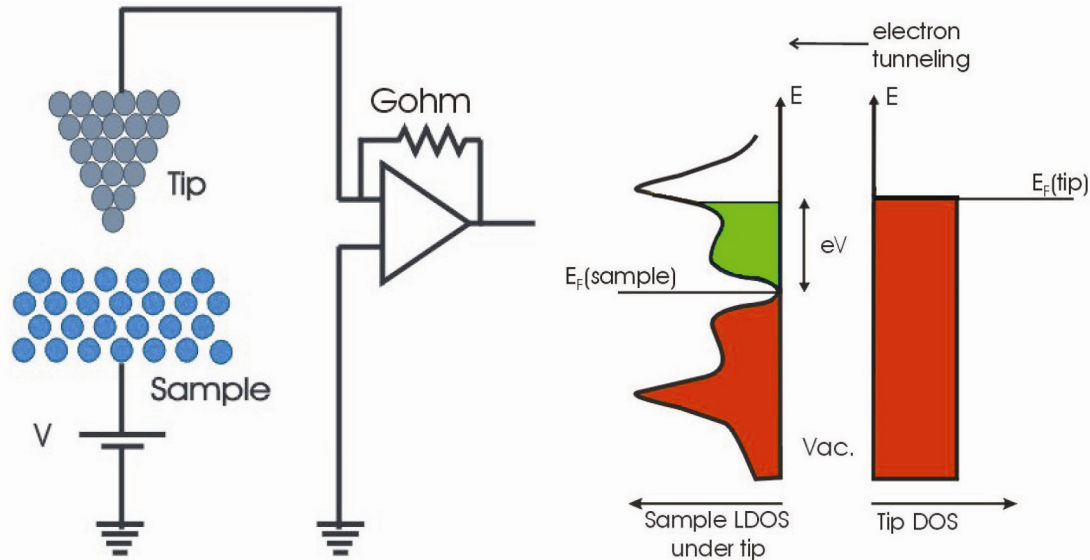


Figure 1- 1: Graphical explanation of the SI-STM process. Showing the potential difference between the tip and the sample driving the tunneling current, while the total current is proportional to the total density of states between the two Fermi levels, while the density of states can be measured from the derivative.

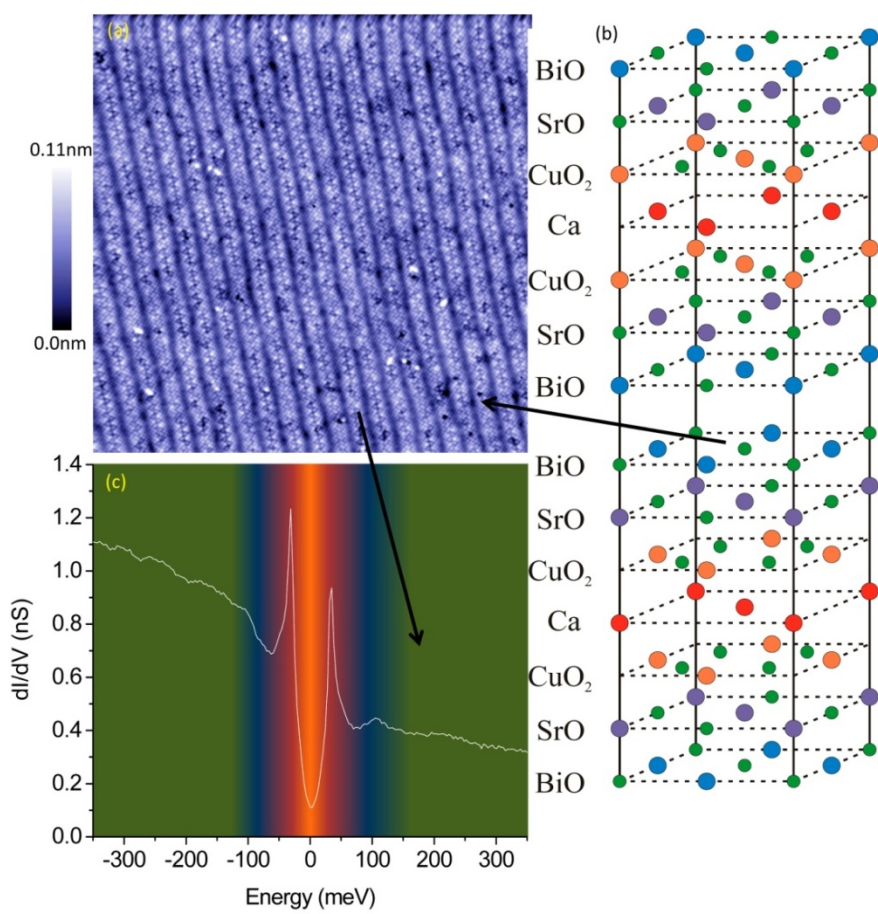


Figure 1-2: a) shows a typical topograph, showing the bi atoms, as well as the supermodulation of the crystal structure, it is roughly a 42nm^2 area. b) shows the crystal structure of Bi₂212, here we cleave between the two BiO planes, these are the planes imaged in (a). c) Shows a typical biscco spectra, out to 350meV. This shows the standard features which we see in spectra, the unit cell measures $5.4 \text{ \AA}^2 \times 30.7 \text{ \AA}$. The green region shows the large background asymmetry that is present in our samples. The blue region the feature ascribed to a phonon mode coupling with the quasiparticles, the red shows the coherence peaks that also tend to show the asymmetry. The orange region is where we see the quasiparticle interference signal, and is bordered on each side by the ‘kink’.

Our particular STM is of a unique design. It is based off a unique take on the slip-stick walker design utilizing peizo stacks pressing polished alumina plates against a sapphire beam. Our STM designs originated with E. W. Hudson, J.C. Davis and S.H. Pan in the late 90’s¹⁵ (utilizing S.H. Pan’s walker design, E. W. Hudson’s work and insight and J.C. Davis Helium-3 expertise), and has been utilized by the Davis group with wildly successful results. In fact many groups have been recently copying the design. A brief schematic overview is shown in figure 1-3(a-c), with pictures of our particular STM in 1-

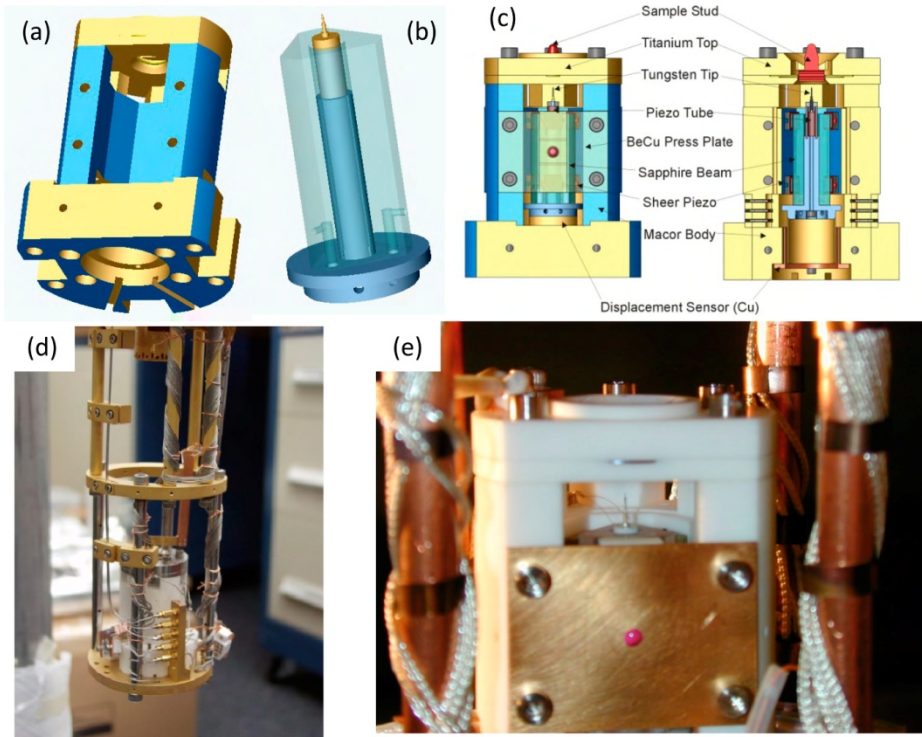


Figure 1-2: (a) View of the STM body (b) sapphire prism, used by the coarse approach walker, showing the scanner assembly topped by the scanner piezo tube, with tip holder. (c) diagram and cut of a STM head. (d) current setup (e) close up of the original setup showing the tip and lines.

3(d-e). My particular STM was originally built in Berkeley by J.E. Hoffmann and Krishna Swami. My first task for the Davis group involved packing it up and moving it across the country. It has then gone through a series of changes to solve noise problems, as well as to allow us to collect data at higher than liquid helium temperatures (up to 55K). These have consisted of replacing all the wiring (three times now), changing the thermal links to the 4k plate, as well as adding a baffle system to reduce the base temperature, and increase the temperature stability. The key replacement that enabled a noise free operation was the replacement of the Dewar that was originally purchased for the system. It turns out that there was a bad weld in the Dewar that would cause loud “pings” when exposed to a temperature gradient. This would cause the STM tip to crash into the surface, destroying it.

This caused a seemingly inexplicable noise issue, and was solved through listening for the noise problems with geophones, as suggested by Kyle McElroy. With this problem corrected we could begin to make successful data maps.

These maps consist of a grid of dI/dV curves, across a field of view, with no tip changes or interruptions and with minimal drift/distortion. In order to extract meaning from our data we use the approximation that our dI/dV is proportional to the LDOS. Now this is not entirely true, the standard approximation is valid only at low energies, and is subject to an ideal tunnel junction. Hence there could be other effects that come into play that act as a filter between the dI/dV and the LDOS. These are usually cast in terms of a tunneling matrix element¹⁶. We assume that the elements of this matrix effect play only a small role, at least at low voltages. We have run into effects which do disrupt our ability to image the underlying LDOS, these take the form of a setup-bias error. At every point we invoke the condition that the total tunneling current is equal to a set uniform value. If we have a phenomena that modulates the LDOS on a large enough scale, then we will see signs of this modulation throughout all our energies, since the setup conditions are being affected by it. However it has been found that by looking at the ratio of positive to negative parts of the spectrum we can remove these subtle effects and clean up the low energy, low amplitude phenomena. It is important to keep in mind these effects in order to ensure that we don't interpret them as actual phenomena.

Once we have our data it can be quite fruitful to look at the spatial dependence of the variations. One tool we use for this is the Fourier transform. Since for the most part the spatial patterns we see are well behaved and coherent, the Fourier transformation allows us to pick out key vectors as well as the coherence/spread of values associated with said vectors. This provides information about what processes are involved by allowing us to very accurately measure the resulting momentum vector involved. As well as providing a crude method of characterizing complex repetitive patterns. We have a lot of room to

expand our techniques these days, with likely sources of improvement coming from the mature field of digital single processing.

Materials overview

The material we study is by choice and by convenience is $\text{Bi}_2\text{Sr}_2\text{Ca}\text{Cu}_2\text{O}_{8+\delta}$. This is often referred to by the shorthand Bi2212 where the numbers refer to the subscripts in the stoichiometric formula. It is a two layer CuO_2 cuprate (crystal structure illustrated in figure 1-2(b)) that has a high max transition temperature (95k) and exists as a broad range of dopings that it can be manufactured in (0.0-0.23). While these are nice properties, the key feature in our studies is the ability to cleave easily. In order to prepare clean surfaces we require the material to cleave easily in situ. In this way we can obtain clean surfaces in a reliable way, and by cleaving while surrounded by a 4k vacuum system, we can keep the samples clean for a surprisingly long time. A typical topograph is shown in figure 1-2(a). Currently the record for our group is 1 year after which the sample was only destroyed by operator error. The downside to working with Bi2212 is its high level of disorder along with the inability to make large high quality crystals, which limits bulk studies and makes the job of comparing our measured local properties to bulk properties that much harder. This could be alleviated by carrying out successful measurements on a material such as LSCO, however such families of cuprates are very hard, and do not provide easily cleavable planes. In fact we have yet found a material that works as well as Bi2212, and for the most part, neither has anyone else.

We have also tried other derivatives of Bi2212, namely single layer (Bi2201) as well as tri-layered (Bi2223) versions. These are interesting in their relationship to the commonly studied bilayer material, in that not only disorder (as measured by the coherence peak height) seems to decrease with increasing # of copper oxide planes but T_c

as well. Bi2201 has a max T_c of around 35k while 2223 has a max T_c of 115k. It would be most enlightening to study the local properties as a function of copper oxide planes, as well as to map out the band structure changes, in order to discover the why the transition temperatures vary and in effect what is driving the increase of T_c with increasing CuO₂ planes. However 2201 is an extremely disordered material, and displays lots of what could possibly be impurity resonances (as well as possibly van Hove singularities), or trapped local states. It is therefore very hard to make heads or tails of the data, and while we have collected a good deal of it, we have refrained from drawing any public conclusions from it. In fact it is very hard to extract any well behaved information. On the 2223 side we are plagued by quite a different problem, and that is one of how do we know its 2223? Since the crystals generally contain a small percentage of 2212, and overall the local properties are not expected to be much different than 2212, except with stronger coherence peaks, differentiating between the two is a tricky task. However with the advent of my analysis tools it should be easy to determine based off the lower scattering rate in 2223¹⁷, this unfortunately has not convinced some and the great bulk of our samples remain unstudied even after early promising data.

Phase diagram

One of the unique properties of cuprate materials is that they give us a unique degree of freedom in which to study superconductivity; that is one of doping. Their properties vary as we add and subtract holes. This changes not only their transition temperature, but also a wide range of bulk properties from super fluid density, to heat capacity jumps, to magnetic susceptibility, to resistance in the normal state. One of the purposes of studying the local states as a function of doping is to discover the connection between the changes in bulk properties and the changes in local phenomena. There are also specific characteristics associated with the under doped state, as opposed to the over doped

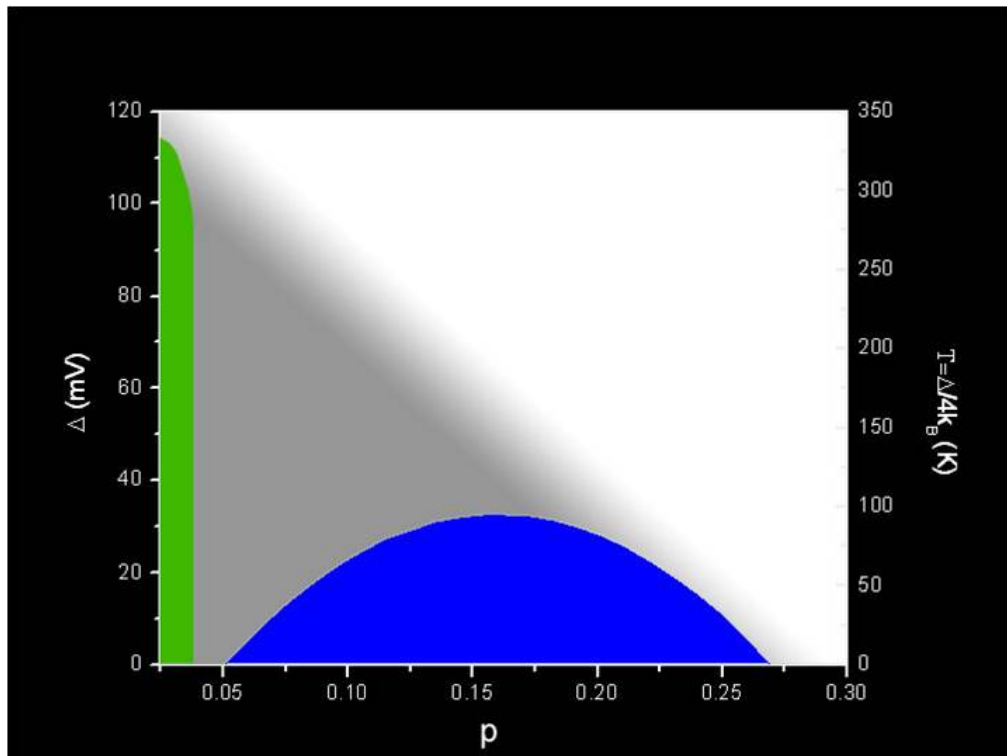


Figure 1-4: Phase diagram, showing the Bi-2212 phase diagram including the AF ordered state (green), the pseudogap state (grey) ,and the superconducting state (blue).

state. The exploration of how these labels apply to local phenomena is of key interest to us and the community as a whole. If we can successfully identify the structure and behavior, we can better understand how its bulk properties are constructed from local ones. It is important to point out here that we are dealing with a highly disordered material. Our fields of views are measured in nanometers, our resolution is sub-angstrom, and we see massive disorder on these length scales. There is only so much bulk probes can do when faced with such a material. The traditional method has been to develop numerical models to simulate local disorder and show that the bulk properties are consistent with said models. These have been very successful, especially when seeded with the types of disorder that we have measured¹⁸, however we would like to make the connection between bulk and local properties directly, or as directly as we can.

This leads us to a general overview of the phase diagram of high T_c superconductors. We have an example of the Bi2212 phase diagram in figure 1-4. There are subtle changes and debates about some of the specifics, but in general this one maps out the major features. Our Phase diagram stretches from $p=0.0$ representing a non-doped Mott-insulator, to 0.30 which is commonly referred to as a ‘strange’ metal. At $p=0.0$ we have a non-conducting, non-superconducting Mott-insulator that has a strong anti-ferromagnetic ordering state. This is represented by green in the phase diagram. As you increase doping, you start to destroy the anti-ferromagnetic ordering and you enter the shaded grey area, this represents the ‘pseudo-gap’ state. There is much debate about what the pseudo-gap state actually represents and how it affects the superconductivity. The pseudogap state is where the Nerst effect lives, as well as the linear resistance with temperature amongst others. It is important for our purposes to note that there is an associated temperature associated with the destruction of the pseudogap state, and hence an energy scale. This is high at low doping, and decreases somewhat linearly till it seems to merge with the superconducting energy scale somewhere around optimal doping $p=0.16$ (max T_c) or the so called critical doping $p=0.19$. How this energy scale relates and appears in our data is important for identifying local behavior associated with the pseudogap state, and features associated with the superconducting state.

The superconducting energy scale is mapped out in the blue area of our phase diagram. This represents the temperature and energy regime where the superconducting condensate lives. The change in T_c with doping causes a change in the heat capacity jump seen with the onset of the normal state. This jump is not a constant 1.43 for the whole phase diagram like it is in a BCS superconductor, but it changes as a function of doping, and becomes smaller and smaller as one moves under doped and reaches 1.43 near critical doping. This is mirrored by the super fluid density or penetration depth measurements which show a high super fluid density when over doped, that drops off as one progresses

towards the under doped side of things. One can draw similarities between these trends and the trends I measure at the beginning of this thesis. However making a direct link requires some additional work, which is done to great success in chapter 4.

Method

For our measurement, we use our STM at a base temperature of 4K. The samples are cleaved in the ultrahigh vacuum produced by surrounding the instrument with Liquid helium. For our tips we use tungsten hat has been electrochemically etched, and then field emitted *in situ*. This enables us to make and keep both a sharp clean tip, and an atomically flat, clean surface. The samples are then approached and data is collected for anywhere between two days to seven (depending on the system and the data set. The STM is vibrationally isolated in two stages. The first is an inertial 20 ton concrete block that floats on 6 air springs, and the second is a second table floated on 3 or 4 air springs. The system is then sealed within one or two layers of sound isolation, and controlled form a neighboring room. This combination allows us to take the extremely accurate and low noise data sets that are presented in this thesis.

Encountered Phenomena

We have hinted in the previous sections as to the name, if not the nature of the phenomena that are present in our data. However we have yet to provide a detailed description of the many facets of our data. Here I will rectify that, first by going over the general spectral shape. This is presented in a rather large energy scale in figure 1-2(c) for a moderately under doped sample ($T_c=64k$). The data is highlighted to show that distinct phenomena that are present in the data, and what must be taken into account when

describing the data. At low energies, in orange background color range we have the Quasiparticle Interface Pattern (QPI), which appears as a feature both in real space, and in Fourier space. QPI has a cutoff energy associated with it that falls between it and the higher energy peak structure. This boundary between the high energy peak and the QPI evolves as one changes doping, and a detailed discussion will be tackled in the second section of this thesis. Outside the coherence peaks we have the ‘dip-hump’ structure that is associated with a boson mode, as well as the oxygen atoms. This for the most part is not touched upon by my work, and its exact relationship to the superconductivity is still under investigation (although much has been gleaned by other members of the Davis group). It is however associated with the isotope effect, and is correlated with the energy position of the large gap structure. This is ripe for a more complex Eliashberg type analysis scheme.

Encountered Phenomena: Gap Disorder

In figure 1-5 we show an example gap map (Δ_1), as well as gap averaged spectra, that shows not only the spatial structure of the high energy disorder, but also the evolution of spectra with increased gap, here defined as the peak-to-peak distance. These spectra are universal as a function of doping as they do not change in shape but merely in their % of each type of curve in a given distribution. This forms a continuum of spectra whose selection window shifts as doping changes. At low energies and high gaps, the ‘kink’ structure becomes visible. This I crudely measure in the first part of the thesis, and define, and understand its origins in chapter 4. Also visible in figure 1-5(b), is the rise of the asymmetry and the preferential suppression of the negative bias peak. The origin of this difference is unknown, although postulated to be due to low doping/local doping effects. However this has not been proven to any degree and therefore still remains an active area of research.

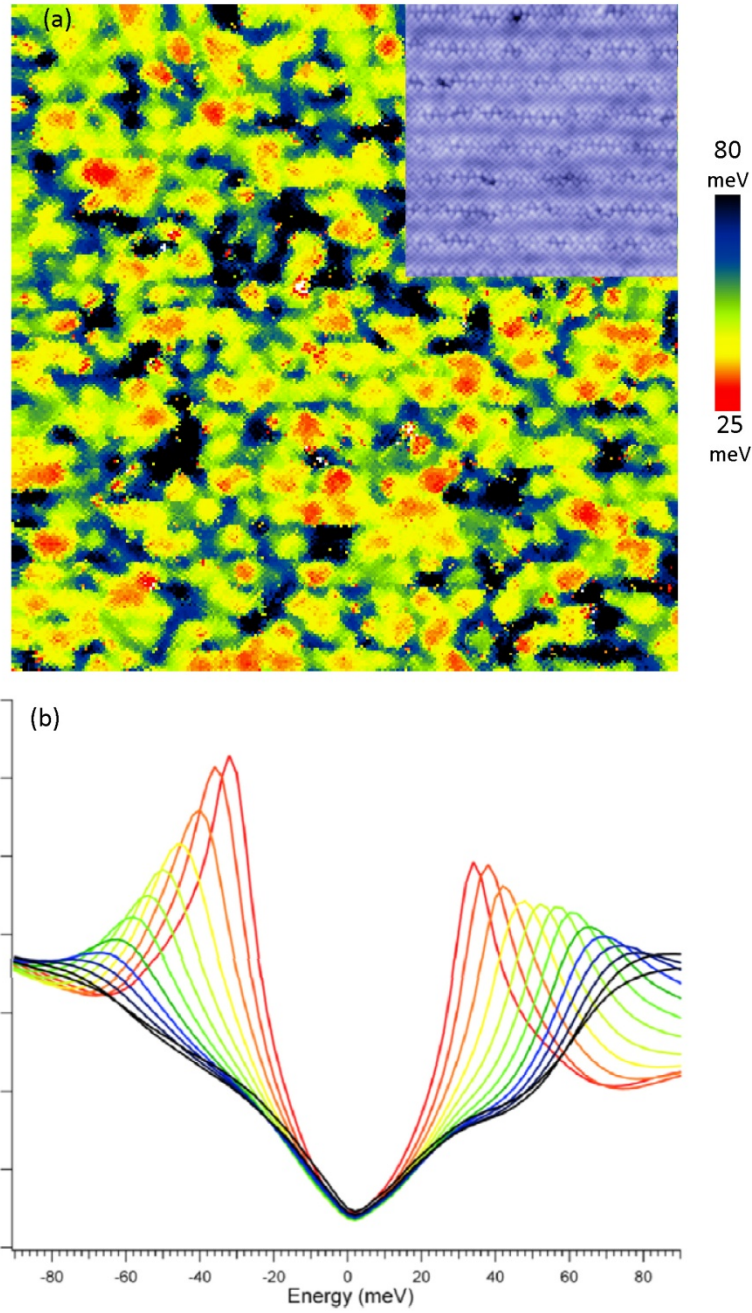


Figure 1-5: a) Is a spatial map of the Δ value taken from a 50nm² UD74k data set. For our data sets there is quite a large disorder in Δ spatially. B) is the gap average curves corresponding to the color scale in (a). Here the presence of lifetime effects as Δ is increased is clearly evident. There is also the ‘kink’ feature which is evident in the large gap curves (blue-black). Inset shows topograph.

Encountered Phenomena: QPI

The QPI presents itself as both a Fourier resolved pattern as well as a real space modulation; these are highlighted in figure 1-6. The QPI is the result of impurity scattering of the coherent superconducting ground state. These show up in both dI/dV 1-6(b),(d) and in the Fourier transform (c). The prospect of extracting information from the real space directly (b) is daunting at best, and therefore the Fourier patterns are analyzed in q-space. Enhanced q-space patterns can be obtained by looking at the ratio of the negative to positive bias layers, which also allows the canceling out of certain setup condition issues that are prevalent at low dopings. Here in 1-6(c) we can resolve many of the individual QPI peaks, and by measuring them we can extract momentum space information about both the band structure and the gap structure. This is accomplish this by using the ‘octet model’ which is a phenomenological model that describes the relationship between the superconducting $a(k,\omega)$ /spectral density of states and the position of the QPI peaks in q-space. The QPI pattern agrees closely with measurements from angle resolved photoemission spectroscopy (ARPES)¹⁹ showing that we are actually measuring the underlying band structure. It should be noted that this pattern fades out at higher energies and is replaced by a set of non-dispersing peaks that depending on the doping, may fade out at higher energies and be replaced with yet another set of q-vectors. These higher energy features will be covered in the second half of this thesis and represent distinct ordering of the electronic states.

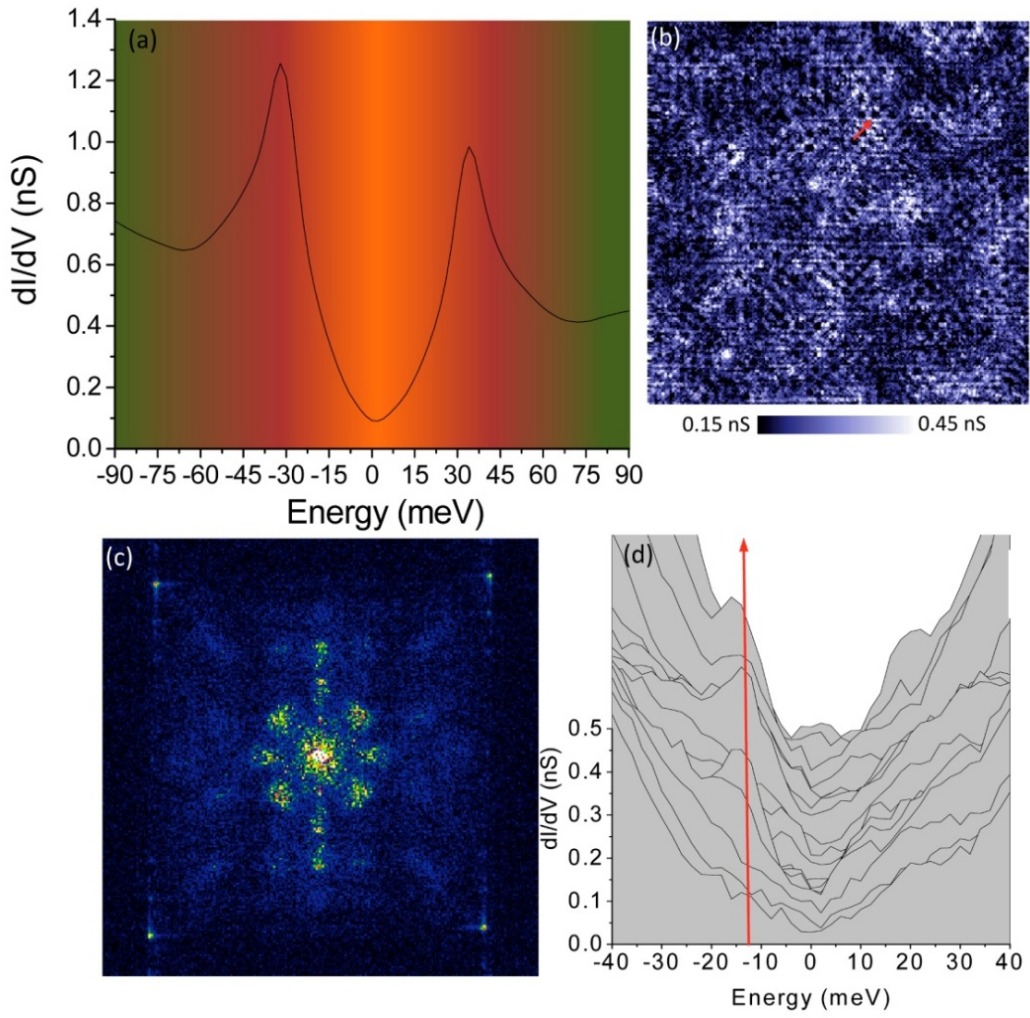


Figure 1-6: a) shows our typical spectra, highlighting the area where the quasiparticle interference lies. The QPI shows up as a departure from the overall background V/U shape of the spectra. This can be seen clearly spatially (b) in the 1-2meV slice of our data set. In (c) the full structure becomes apparent in the FFT of (b). If we take a line cut along the red line in (b) we see (d) which shows the typical amplitude of the QPI signal, as well as the background noise at these energies.

Encountered Phenomena: Kinks

The kink at low energies sits at the boundary between the low energy, coherent phenomena (QPI) and the higher energy gap disorder. This feature presents itself as ‘kink’ in an otherwise nicely structured d-wave type background. This feature becomes more and more apparent as Δ_1 grows in size, increasing the separation between Δ_1 and the QPI termination point. This allows this feature to be accurately detected. The crude original method for detecting it is presented in figure 1-7. Here we look for a dip in the derivate in the spectra, which represents the midpoint of the kink structure. This gives us an idea of the separation between high and low energy regions. As we reduce doping, we encounter a widening of this expanse and an increase in the size of the kink structure. In figure 1-7(c,d) we show that in space our detected kink corresponds to regions where the gap is large, this is the limitation of the first detection scheme. It should be noted for reference that this lower energy feature has a distribution and is in no way homogeneous. The presence of the kink initially presented a stopping point in the effectiveness of our fits. At low dopings the kinks become very large and represented a large error in our fits. However, seizing a hold of this challenge, we have developed a much more comprehensive model that provides an excellent fit to the data and with the QPI story provides a description for what is happening at low energies as well as high energies.

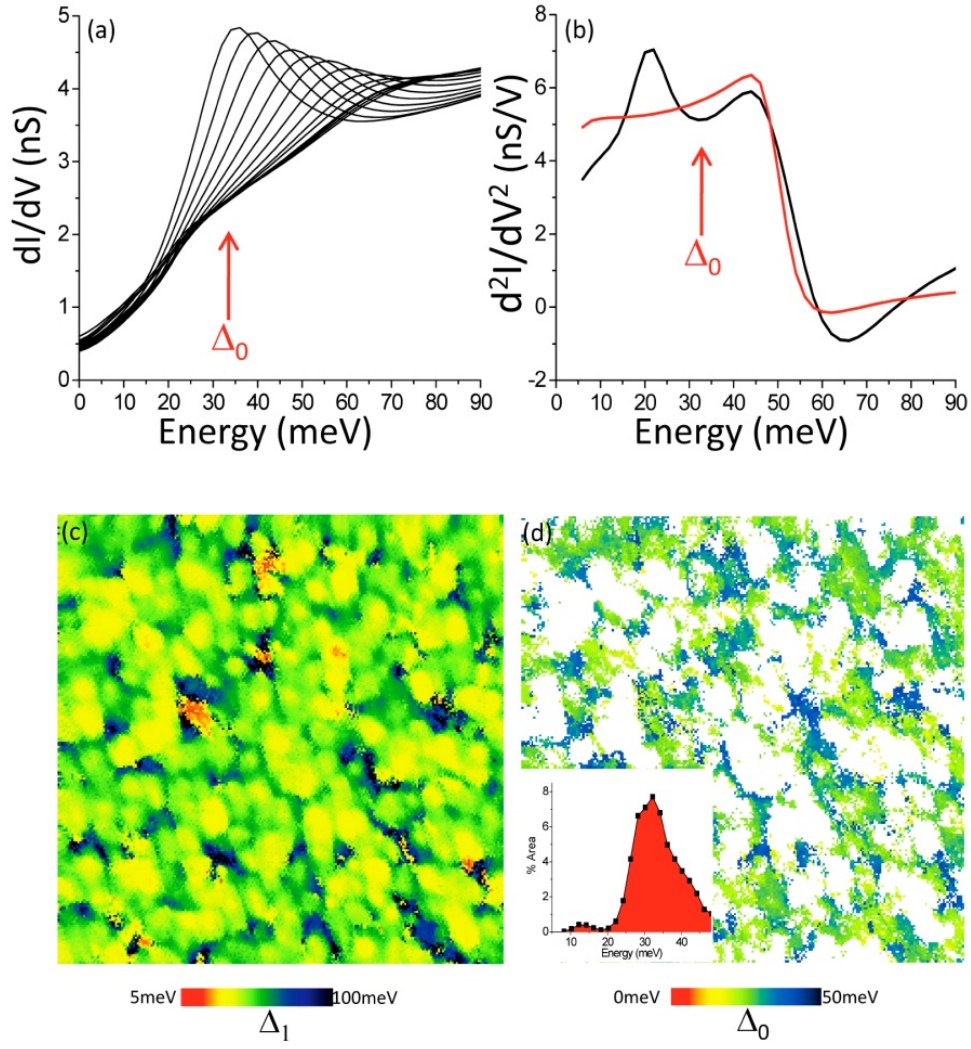


Figure 1-7: a) Is the Δ average spectra showing clearly the kinks presence in this sample around 34meV. The red arrow points it out and marks it as Δ_0 . b) Shows the average derivative of the spectra with the black line, while the red line shows the average derivative of the fits. This shows that the kink is defined and detected in the sample, and also shows it as a clear departure from the fits. c) Shows the Δ_1 map for this sample. (d) Shows the kink map in the same field of view as the Δ_1 map, the white areas are places where the kink is not detected, while the colored areas show the kink energy. The kinks are only detected in regions where Δ_1 is large. The inset is the histogram of the kink energies.

Encountered Phenomena: Boson Mode

Figure 1-8 illustrates the bosonic mode that sits outside the gap. They don't play a large role in any of the studies presented here, due mainly to them lying outside the gap, but they are included here for completeness, and they are a puzzle piece that needs to eventually fit into the puzzle somewhere. Figure 1-8(a) shows the measured signal for their detection. It is taken by looking at the 2nd derivative of the spectra outside the gap, in practice this is done numerically by fitting a high order polynomial to the dip hump structure calculating its derivative. Since the feature represents an inelastic tunneling mode, it is referenced to the gap energy, since it is accessed by exciting an excitation in of the bosonic states on top of an existing quasiparticle excitation. In figure 1-8(b) we show the referenced gap state, and figure 1-8(c) is the resulting map of the bosonic mode. This does have a dependence on Δ_1 referenced energy and is only weakly correlated with Δ_1 , and the appropriate histogram is shown in figure 1-8(d). To show the evolution of this feature in respect to the overall spectra, figure 1-8(e) shows the average spectra with respect to the bosonic energy. It should be noted here that there is considerable smoothing caused by the setup conditions. Hence the kink is smoothed into the peak. The boson feature is rapidly suppressed in strength as one strays away from optimal doping, making it difficult if not impossible to detect in much of the low doping regime in which we carry out studies.

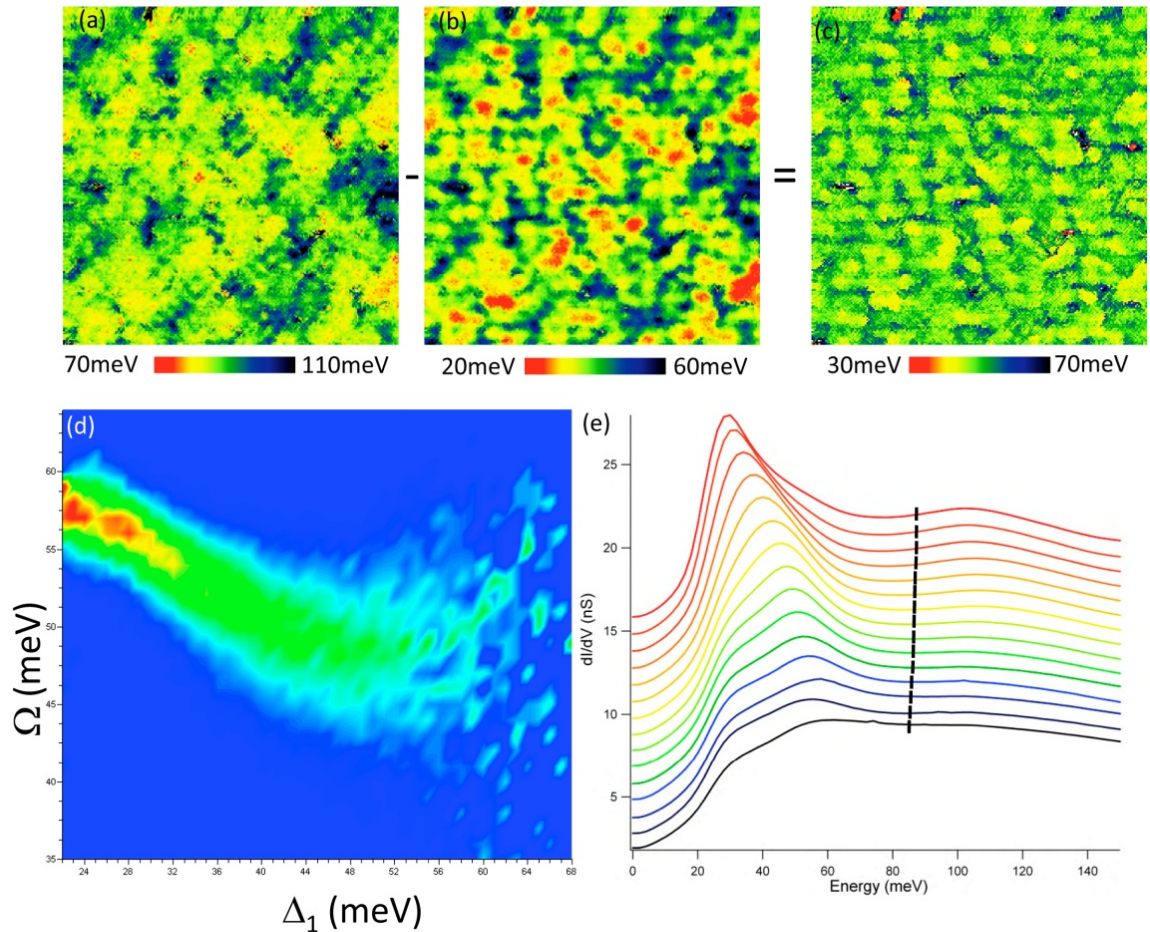


Figure 1-8: a) shows a typical raw dI^2/dV spatial map. From this we subtract the Δ map (b) in order to reveal the actual map of the boson energies (c). d) shows the 2D histogram showing the correlation with boson energy and Δ_1 energy. e) is the spectra sorted by phonon energy (c) showing the position of the boson feature (black dash) as well as how the spectrum changes with decreasing boson energy (increase Δ energy).

Encountered Phenomena: Background Slope

The final feature I wish to touch briefly upon is the asymmetric background. We measure this with a linear background term added onto our fits. Or fitting a line a every data point gives one similar results. Figure 1-9(a) shows the inhomegenity in this measured slope. The slope averaged data is shown in 1-9(b) whose color scale corresponds to (a). It should be noted that here the data setup was set on the negative side causing the area on the negative half to be normalized at each individual point. These curves clearly show that at large gap values we see a large background slope. One can also see lifetime effects coming into play and in fact in different strengths on the positive and negative sides at high gap values. An important point, and something overlooked quite frequently when discussing the slope, is that it does in fact depend on the setup conditions. In figure 1-9(c) we show a series of spectra taken at a single point for a variety of setup conditions. It can be seen that as the tunneling current gets smaller and smaller, the slope gets bigger and bigger. In fact at extremely small currents we get the negative bias peak being faded into the background. This mimics the behavior we see at lower dopings, and the entire effect may be related to this.

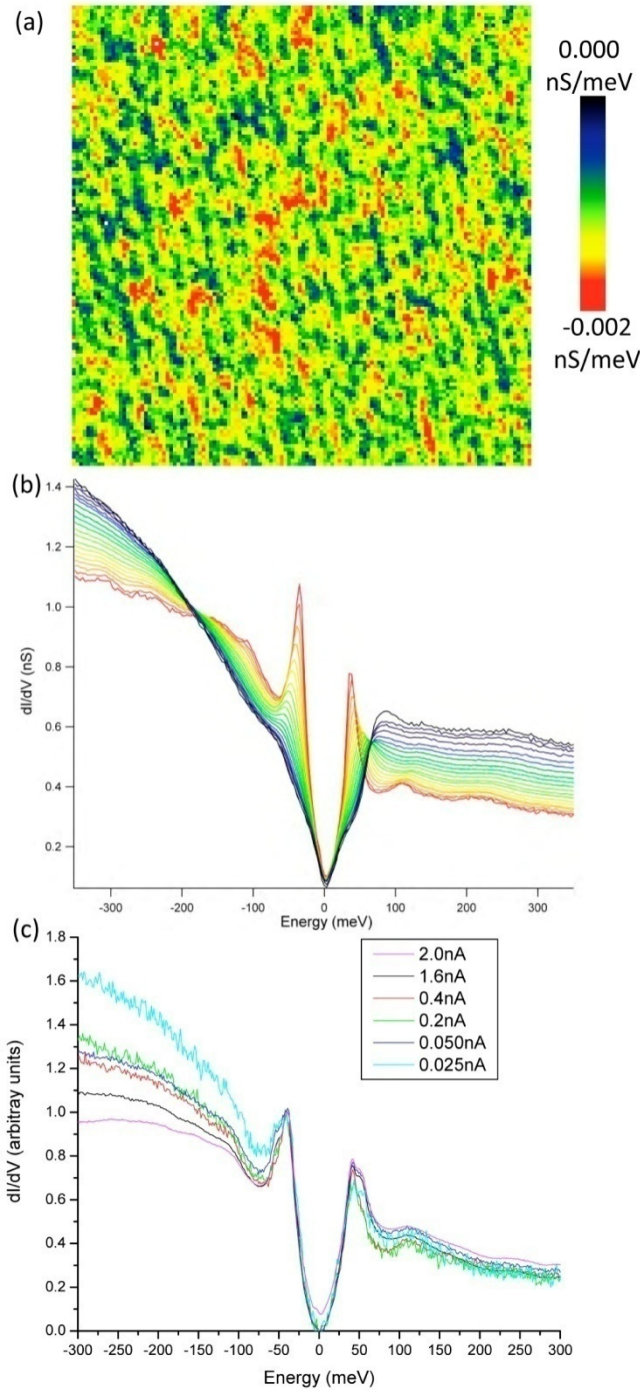


Figure 1-9: a) example map of the background slope between -100meV and 100meV, a crude measure of the overall asymmetry in the data. b) Slope averaged curves extracted using (a). The color scale corresponds roughly to the color scale used in (a). It shows a clear correlation between the background asymmetry and the slope. (c) Spectra collected at the same point in space for a variety of tunneling current conditions.

Conclusion

This completes the broad list of features which we must attempt to account for, or at least ensure that they do not cause issues with our fits of the data. In the forth coming chapters we use an incremental procedure, starting with a fairly simple model that describes a large portion of the data across doping and ending up with a more detailed model that accounts for much more. This of course is the way science works, and considering the complexity of the task at hand, starting off simple ensures we do not add unnecessary complexities. In chapter 2 we begin the process.

REFERENCES

-
- ¹ Burns, G. High-temperature superconductivity an introduction, Academic Press (1992)
- ²
- ³
- ⁴ Chen, C. J., Introduction to Scanning Tunneling Microscopy. Oxford University Press, 2007.
- ⁵ Hoffman, J.E., Hudson, E. W., Lang, K. M., Madhavan, V., Eisaki, H., Uchida, S., Davis, J. C. A four unit cell periodic pattern of quasi-particle states surrounding vortex Cores in $\text{Bi}_2\text{Sr}_2\text{Ca}\text{Cu}_2\text{O}_{8+\delta}$. Science **295**, 466 (2002)
- ⁶ Lang, K.M., Madhavan, V., Hoffman, J.E., Hudson, E.W., Eisaki, H., Uchida, S., Davis, J.C. Imaging the granular structure of high-T_c superconductivity in underdoped $\text{Bi}_2\text{Sr}_2\text{Ca}\text{Cu}_2\text{O}_{8+\delta}$ Nature **415**, 412 (2002)
- ⁷ Hoffman, J.E., McElroy, K., Lee, H-H., Lang, K.M., Eisaki, H., Uchida, S., Davis J.C. Imaging quasiparticle interference in $\text{Bi}_2\text{Sr}_2\text{Ca}\text{Cu}_2\text{O}_{8+\delta}$. Science **297**, 1148 (2002)
- ⁸ McElroy, K., Simmonds, R.W., Hoffman, J.E., Lee, D-H., Orenstein, J., Eisaki, H., Uchida, S., Davis, J.C. Relating atomic scale electronic phenomena to wave-like quasiparticle states in superconducting $\text{Bi}_2\text{Sr}_2\text{Ca}\text{Cu}_2\text{O}_{8+\delta}$. Nature **422**, 592 (2003)
- ⁹ McElroy, K., Lee, D.-H., Hoffman, J. E., Lang, K. M., Lee, Jinho, Hudson, E. W., Eisaki, H., Uchida, S., Davis, J. C. Coincidence of Checkerboard Charge Order and Antinodal State Decoherence in Strongly Underdoped Superconducting $\text{Bi}_2\text{Sr}_2\text{Ca}\text{Cu}_2\text{O}_{8+\delta}$. Phys. Rev. Lett. **94**, 197005 (2005)
- ¹⁰ Pan, S.H., Hudson, E.W., Lang, K.M., Eisaki, H., Uchida, S., Davis, J.C. Imaging the Effects of Individual Zinc Impurity Atoms on Superconductivity in $\text{Bi}_2\text{Sr}_2\text{Ca}\text{Cu}_2\text{O}_{8+\delta}$, Nature, **403**, 746 (2000)
- ¹¹ Hudson, E.W., Lang, K.M., Madhavan, V., Pan, S.H., Eisaki, H., Uchida, S., Davis, J.C. Interplay of magnetism and high-T_c superconductivity at individual magnetic impurity atoms in $\text{Bi}_2\text{Sr}_2\text{Ca}\text{Cu}_2\text{O}_{8+\delta}$, Nature **411**, 920 (2001)

-
- ¹² Lee, Jinho, Fujita, K., McElroy, K., Slezak, J. A., Wang, M., Aiura, Y., Bando, H., Ishikado, M., Masui, T., Zhu, J.-X., Balatsky, A. V., Eisaki, H., Uchida, S., Davis, J. C. Interplay of Electron-Lattice Interactions and Superconductivity in $\text{Bi}_2\text{Sr}_2\text{Ca}\text{Cu}_2\text{O}_{8+\delta}$. *Nature* **442**, 546 (2006)
- ¹³ McElroy, K., Lee, Jinho, Slezak, J.A., Lee, D.-H., Eisaki, H., Uchida, S., Davis, J.C. Atomic-Scale Sources and Mechanism of the Nanoscale Electronic Disorder in $\text{Bi}_2\text{Sr}_2\text{Ca}\text{Cu}_2\text{O}_{8+\delta}$. *Science* **309**, 1048 (2005)
- ¹⁴ Kohsaka, Y., Taylor, C., Fujita, K., Schmidt, A., Lupien, C., Hanaguri, T., Azuma, M., Takano, M., Eisaki, H., Takagi, H., Uchida, S., Davis, J. C. An Intrinsic Bond-Centered Electronic Glass with Unidirectional Domains in Underdoped Cuprates *Science* **315**, 1380 (2007)
- ¹⁵ Pan, S.H., Hudson, E.W., Davis, J.C. *Rev. Sci. Instrum.* **70**, 1459 (1990)
- ¹⁶ Guentherodt, H.-J., Wiesendanger, R. *Scanning Tunneling Microscopy I*, Springer-Verlag 1992.
- ¹⁷ Damascelli, A., Hussain, Z., Shen, Z.X. Angle-resolved photoemission studies of the cuprate superconductors *Rev. Mod. Phys.* **75**, 473 (2003).
- ¹⁸ Nunner, T.S., Andersen, B.M., Melikyan, A., Hirschfeld, P.J., Dopant-modulated pair interaction in cuprate superconductors *Phys. Rev. Lett.* **95**, 177003 (2005)
- ¹⁹ McElroy, K., Gweon, G.-H., Zhou, S. Y., Graf, J., Uchida, S., Eisaki, H., Takagi, H., Sasagawa, T., Lee, D.-H. Lanzara, A. Elastic Scattering Susceptibility of the High Temperature Superconductor $\text{Bi}_2\text{Sr}_2\text{Ca}\text{Cu}_2\text{O}_{8+x}$: A Comparison between Real and Momentum Space Photoemission Spectroscopies *Phys. Rev. Lett.* **96**, 067005 (2006)

CHAPTER 2

Evolution of the electronic excitation spectrum with strongly diminishing hole-density in superconducting $\text{Bi}_2\text{Sr}_2\text{CaCu}_2\text{O}_{8+\delta}$

Introduction I

We have set before us the task of sorting the spectra, and extracting meaning from the variety of types and how they cluster in space. Here we present our first simplistic model that we base off BCS inspired modelling of superconducting lead tunnel junctions doped with impurities carried out some 30 years ago. With little modification we are able to apply not only this model, but the style of thinking that inspired it to our data. This gives us a simple explanation for some of the types of behaviour we see, mainly the decreased lifetimes with increasing energy gaps. The model allows us to analysis the data with higher precision then possible before, giving us not only excellent fits, but also giving us a unique insight into the scattering processes that are occurring. These intrinsic scattering processes are predicted by Honerkamp et al¹⁷. to grow as we lower the doping and move towards the Mott insulator state. Indeed that is what we reveal for the first time here, since no other probe has successfully mapped this progression out in detail as we have here. Our results do not end at mapping out the disorder in detail, but the quality of our fits is such that we deviations from a d-wave BCS background are revealed and quantified for the first time. These deviations, in the form of the ‘kinks’ are also our inspiration

for improvement which leads through chapter 3 to 4 where we develop an effective model for all the electronic states.

Introduction II

Hole-doped copper-oxides have their highest superconducting critical temperature T_c at hole-densities per CuO_2 of $p \sim 16\%$, and the superconductive state exhibits d-wave symmetry. By measuring STM tip-sample differential conductance $dI/dV(r,V) \equiv g(r,V)$ at each location r and bias voltage V one can achieve energy resolved images of the local-density-of-exitations $N(E)$ because $g(r,V) \propto N(r,E=eV)$ (when the $N(E)$ integrated to the junction formation bias is homogeneous¹). Near optimal doping, the $g(V)$ spectra appear highly consistent with the theoretical $N(E)$ of a d-wave superconductor; when superconductivity is suppressed by unitary scattering at a Zn atom^{2,3} or at the center of a vortex core^{3,4}, the two particle-hole symmetric peaks in $g(V)$ are also suppressed as expected of the superconducting coherence peaks. Thus there can be little doubt that the measured $N(E)$ near optimal doping is that of the d-wave superconducting state. But as p is reduced, the electronic excitations begin to exhibit^{5,6,7} a ‘pseudo’ gap (PG). This is a momentum-space anisotropic energy gap⁵⁻⁹ in the excitation spectrum whose effects can be detected by numerous spectroscopic and thermodynamic techniques^{6,7} far above the superconducting T_c (which diminishes to zero as $p \rightarrow 0$). The PG energy scale increases linearly with diminishing p .

Possible explanations for the PG include, for example, effects of hole-doping an antiferromagnetic Mott insulator¹⁰⁻¹⁴. Different models for this situation yield an anisotropic energy-gap whose maximum diminishes linearly with increasing p (heuristically, one can view this as a dilution of the antiferromagnetic exchange energy by the holes). But an alternative type of proposal has been that the PG is due to some distinct electronic phase^{15,16,17,18} whose anisotropic energy gap represents the breaking of a different symmetry. Measurements solely of the PG energy scale versus p have not resulted in discrimination between these two types of proposals and no consensus exists for the cause of the PG in the electronic excitations of copper-oxides^{5,6,7}.

A fully detailed knowledge of the $T \rightarrow 0$ intrinsic spectrum of electronic excitations as a function of doping could help break this impasse. The lifetimes of ‘nodal’ excitations – those with $\mathbf{k} \parallel (\pi, \pi)$ - have actually been widely studied¹⁹⁻²²; these states are not the focus of study here. Instead we focus primarily on higher energy excited states which reach all the way to the antinodes $\mathbf{k} \sim (\pi, 0) : (0, \pi)$. Scattering rates for these states have been studied in the superconducting²³ and non-superconducting²⁴ state at or above optimal doping, revealing strong momentum-space anisotropy of the scattering rate at the Fermi surface. And, using optical techniques Gedik *et al* stimulated these non-nodal excited states and discovered that a dramatic change in their recombination rate occurs near optimal doping²⁵. Despite these recent advances, knowledge of the $T \rightarrow 0$ spectrum of electronic excitations sufficient to constrain the models, does not yet exist.

We have here a technique that will allow us to understand the spatial and doping dependence of the electronic excitation spectrum $N(E)$ of superconducting cuprates. We use single crystals of $\text{Bi}_2\text{Sr}_2\text{CaCu}_2\text{O}_{8+\delta}$ (Bi-2212) grown by the floating zone method. Atomically clean and flat surfaces of BiO are achieved and maintained by cleaving the samples in cryogenic ultrahigh vacuum before insertion into the STM at $T=4.2\text{K}$. We report on samples with six different hole-densities $0.08 \leq p \leq 0.22$ (± 0.01), each within a 40 nm square field of view and, in total, comprising more than 10^6 individual $g(\mathbf{r},V)$ spectra. Our objective is to use this comprehensive data set to explore the evolution with doping of the electronic excitation spectra.

In s-wave superconductors, an increasing quasiparticle inelastic scattering rate reduces their lifetimes and eventually destroys the superconductivity²⁶. The signature of this process is manifest in $g(V)$; at zero temperature and with no scattering, two ‘coherence’ peaks in $g(V)$ occur as singularities on either side of an empty gap and, as scattering rates increase, these peaks decrease in height and increase in width with a rapid increase of the density of excitations near $E=0$. Such $g(V)$ spectra can be very successfully parameterized by adding an imaginary term Γ_1 to the quasiparticle energy E so that $N(E)$ takes the form²⁷

$$N(E, \Gamma) = A \times \text{Re} \left(\frac{E + i\Gamma_1}{\sqrt{(E + i\Gamma_1)^2 - \Delta^2}} \right) \quad (1)$$

Here Γ_1 represents a constant scattering rate for quasiparticles. As Γ_1 is increased keeping Δ constant, the coherence peaks diminish, the peak-peak measure of the energy-gap becomes less well defined, and there is a rapid increase of $N(0)$ – all in excellent agreement with the experimentally observed effects in $g(V)$.

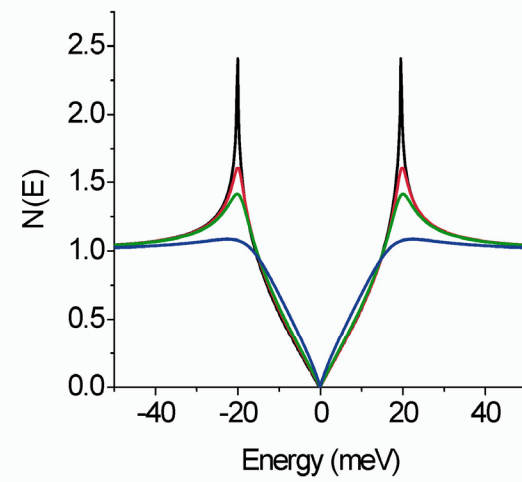
Model

Our goal is to extend this approach to the cuprate excitation spectra. The $N(E)$ we propose is (at least formally) a natural extension of Eqn. 1

$$N(E, \Gamma_2) = A \times \text{Re} \left\langle \frac{E + i\Gamma_2(E)}{\sqrt{(E + i\Gamma_2(E))^2 - \Delta(k)^2}} \right\rangle_{fs} + B \times E \quad (2)$$

Here $\Delta(\vec{k}) = \Delta_1(Cos(k_x) - Cos(k_y))/2$ is a particle-hole symmetric anisotropic energy-gap. We could also introduce a term $i\Gamma_1$ representing a constant scattering rate from near-unitary scatterers (analogous to Eqn. 1) but we find it plays a subsidiary role in the results herein. By contrast the $\Gamma_2(E) = \alpha E$ term which represents an effective scattering rate that is linear in energy, plays a key role. In Eqn. 2, A is a normalization factor and B a linear asymmetry term to deal with the ubiquitous background slope of $g(V)$ of Bi-2212. Eqn. 2 then represents the $N(E)$ function which we fit to each measured $g(V)$ (its exact form is determined over the appropriate Fermi surface at

each doping²⁸ - see methods). Figure 2-1 shows examples of the $N(E)$ calculated from Eqn. 2 as α increases (Δ_1 remaining constant). We see that the peaks are rapidly suppressed but, because $\Gamma_2(0)=0$, an approximately V-shaped gap centered on the chemical potential is retained for all scattering rates. This is crucial for the successful parameterization of all $g(E)$ since, throughout the Bi-2212 phase diagram, such characteristics are ubiquitous.



Results

We use data sets consisting of atomically resolved and registered $g(\mathbf{r}, V)$ maps spanning the range of doping $0.08 \leq p \leq 0.22$ (as determined from $T_c=95K \times (1-82.6(p-0.16))^2$ along with other techniques). Their spectra change continuously from quite

Figure 2-1: Theoretical effect of $\Gamma_2=\alpha E$ inelastic scattering on the density of states $N(E)$. Representative $N(E)$ from Eqn. 2 demonstrating the effect of increasing α for $\Delta_1=20\text{meV}$. The black line represents $\alpha=0.00$, the red line for $\alpha=0.05$, the green line for $\alpha=0.10$ and the blue line for $\alpha=0.40$.

small gaps ($\Delta_1 \sim 10\text{ meV}$) with sharp particle-hole symmetric peaks, to large ($\Delta_1 \sim 65\text{ meV}$) gaps where the vestigial peaks can just be resolved²⁹, to the V-shaped gaps with no apparent peaks which predominate below $p \sim 10\%$ [Ref.'s 1, 30]. To complicate matters further, at each doping there is a distribution in excitation spectra associated with the distribution of non-stoichiometric oxygen dopant atoms³¹, with the probability of these different spectral types varying with doping^{4,29,30,31}. Fitting Eqn. 2 to all these spectra is designed to yield quantitative values for both $\Gamma_2(E)$ and Δ_1 - even when there are no peaks visible and despite both the electronic disorder and the rapid changes in spectral types with doping.

Figure 2-2 shows the distribution of spectral types^{29,30} from within a single field of view, each curve being offset vertically for clarity. The open circles represent the average $g(V)$ spectrum associated with each energy-gap magnitude - the error bars

showing the one- σ variations of each distribution (see supplementary materials). This averaging process is designed to yield the characteristic excitation spectrum associated with each energy-gap maximum while minimizing complications from the spatial variations in $g(r,V)$. Our fits of $N(E)$ are to each individual local $g(r,V)$ spectrum (see supplementary materials). The solid lines in Fig. 2 show the average of the fits of Eqn. 2 to the $g(V)$ data – again with all $N(E)$ exhibiting the same Δ_1 averaged together. It is striking how well a very wide variety of $g(V)$ spectral shapes, ranging from those exhibiting sharp particle-hole symmetric peaks to those with V-like spectra having no

apparent peaks, can be fitted using Eqn. 2. The fit-quality parameter is a normalized χ^2

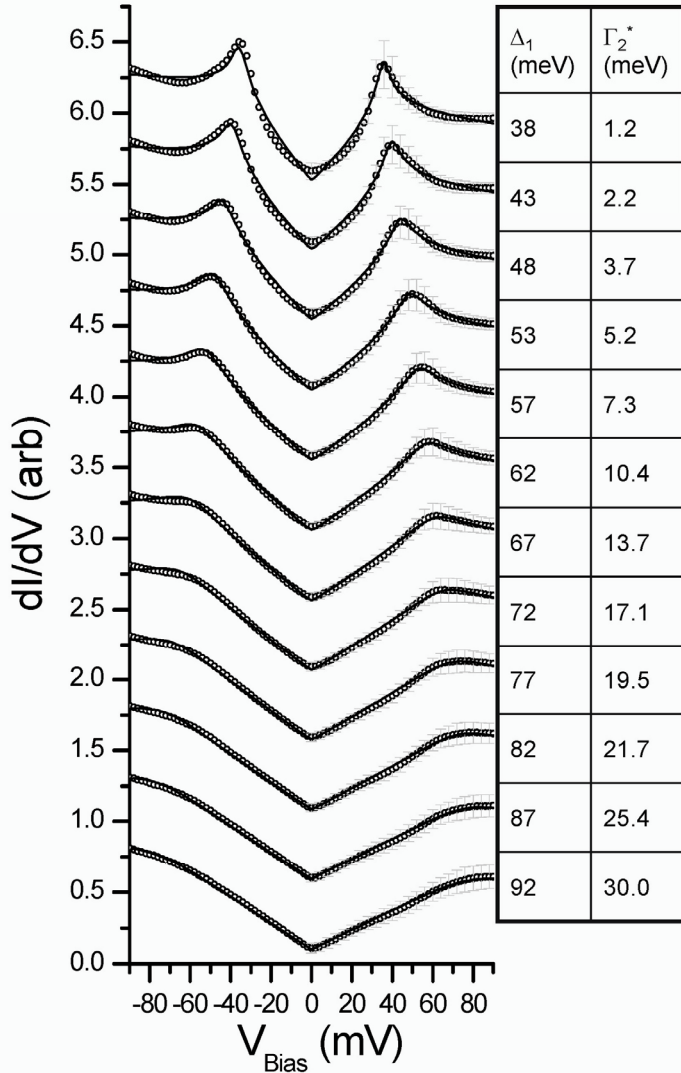
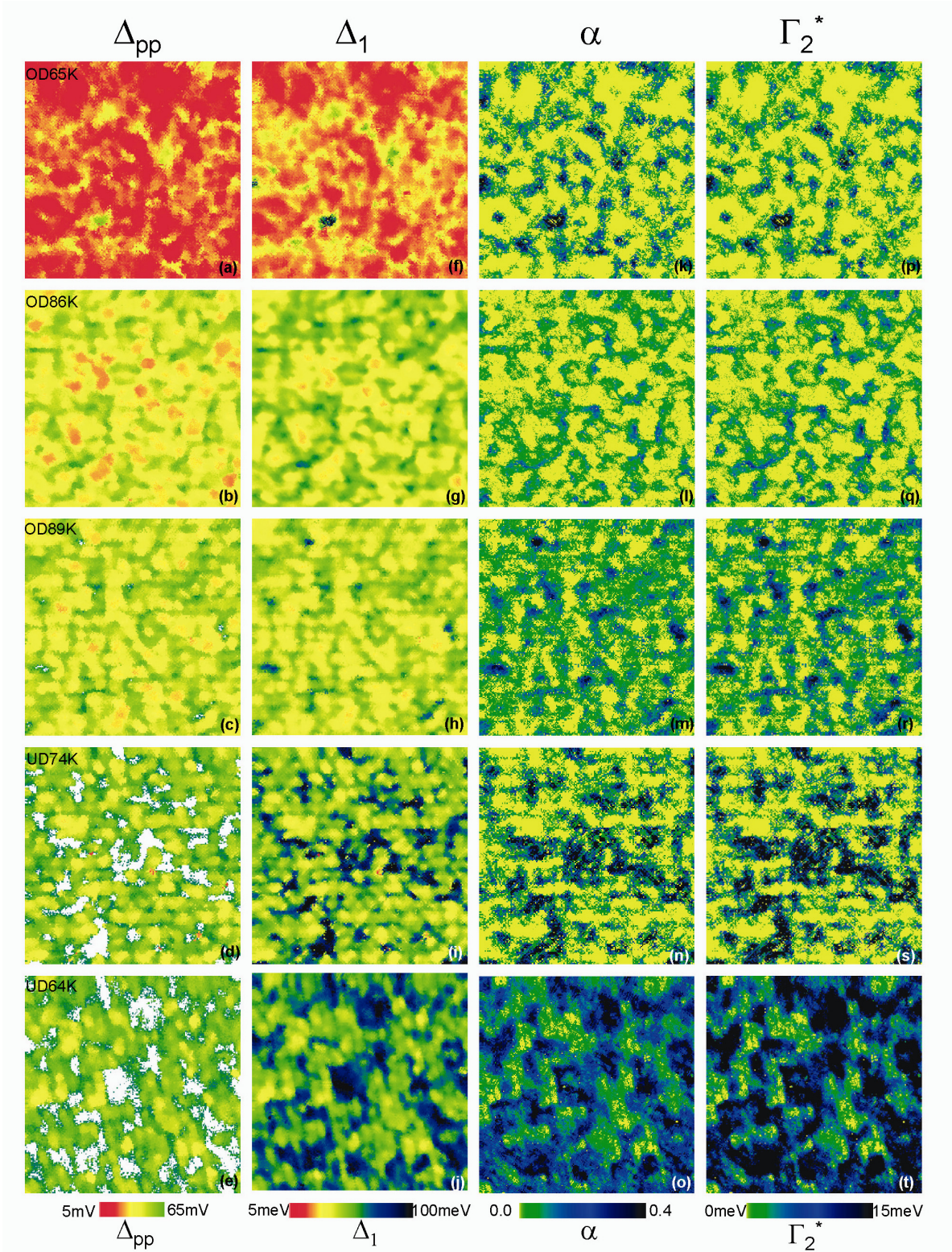


Figure 2-2: Fits of Eqn. 2 $N(E)$ to the average $g(V)$ spectrum for each gap magnitude. Open circles represent the average value of $g(V)$ from all spectra (in one sample with $p=10\%$) that exhibit a given gap magnitude Δ_1 . The error bars give one standard deviation of the distribution in $g(V)$ at each V . The corresponding averages of the fits of all spectra by Eqn. 2 are shown as solid lines. The table shows the fitted values of Δ_1 and $\Gamma_2 = \Gamma_2^*$ ($E = \Delta_1$). The Δ_1 ranges from 38 mV to 93 mV while Γ_2^* spans from below 1 meV to above 25 meV. Each spectrum is offset for clarity. Notice the particle-hole symmetry throughout.

< 0.01 for more than 90% of the spectra $0.1 \leq p \leq 0.22$. For the sixth sample with $p \sim 0.08$, the normalized χ^2 remains higher because the strong tunnelling asymmetry¹ prevents good fits. And for $p > 0.22$ the spectral shape begins to change in a fashion not yet understood. Nevertheless the vast majority of measured $g(r,V)$ spectra for $8\% < p < 22\%$ can be fitted very well (a normalized $\chi^2 < 0.01$) using Eqn. 2 . We show in the methods section typical examples of the fit for each value of Δ_1 .

In previous studies of nanoscale electronic disorder in Bi-2212 a local energy-gap maximum Δ_{pp} was defined as half the energy difference between two particle-hole symmetric peaks in $g(V)$ (wherever such pairs of peaks existed). Figure 2-3, Column 1 shows the spatial and doping dependence of such Δ_{pp} maps (all FOV are 40nm square and all gap scales are the same with white indicating an inability to measure Δ_{pp} because the peaks could not be identified in high gap regions^{29,30}). Figure 2-3, Column 2 shows the spatial and doping dependence of Δ_1 -maps calculated from fits of Eqn. 2 to the identical data sets. We see immediately that the Δ_1 -maps resemble closely the Δ_{pp} -maps. Furthermore, the normalized cross-correlation³¹ between all simultaneous pairs of Δ_1 -maps and Δ_{pp} -maps shown exceeds 0.9 (where identical images would yield 1). These correspondences between Figure 2-3, columns 1 and 2 give strong confidence that the Eqn. 2 fitting scheme is working well since the mathematical procedures to make the two kinds of maps are completely different.

Figure 2-3: Correlations between spatial arrangements of Δ_{pp} , Δ_1 , α and Γ_2^* versus hole-density p . Column 1 (a-e) shows the Δ_{pp} maps as a function of doping - each for a 40nm^2 field of view, the white areas are places where Δ_{pp} cannot be defined. The dopings are calculated from the T_c 's of the samples using the formula $T_c = 95\text{K} \times (1 - 82.6(p-0.16)^2)$ and corroborated by other techniques: (a) 0.22 ± 0.01 , (b) 0.19 ± 0.01 , (c) 0.17 ± 0.01 , (d) 0.14 ± 0.01 and (e) 0.10 ± 0.01 . Tunnelling asymmetry renders fitting the sixth data set at $p \sim 8\%$ very difficult. The Δ_1 maps calculated from the fits to Eqn. 2 using the identical original $g(r,V)$ maps as in Column 1, are presented in Column 2 (f-j). Note that where Δ_{pp} and Δ_1 can both be evaluated they create virtually identical patterns. Column 3 (k-o) shows the calculated concurrently with each Δ_1 from the fits to Eqn. 2. Column 4 (p-t) shows the corresponding maximum effective scattering-rate maps Γ_2^* , calculated from Column 2 and 3. Note that Δ_1 , α , and Γ_2^* create very similar patterns. T_c for each sample is shown as inset to the left hand panels.



New information is immediately available from measurements of the gap maximum Δ_1 . A limitation of previous studies was that, when there were weak or no peaks in $g(V)$ at low doping, it became virtually impossible to determine Δ_{pp} (such areas were represented in black in Ref.'s 29,30,31 and white in Fig. 2-3, Column 1). But Fig. 2-2 shows clearly that with strong effective scattering rates $\Gamma_2(E)$, the particle-hole symmetric peaks should disappear and the density of excited states should appear as a V-shaped spectrum. Therefore Δ_1 can now be extracted in regions where previously it would have been considered unknown. For example, in Fig. 2-3, Column 2 the black regions now represent measured values Δ_1 rising to above 100 meV in small nanoscale patches at our lowest dopings. The extracted values of Δ_1 (Fig. 3,4) follow the doping dependence of PG energy scale^{5,6,7}. Moreover, we find no distinction in terms of the fitted form of $N(E)$ between excitations to the PG energy scale at low dopings, and the familiar excitations of the superconducting state^{2,3,4} at higher dopings and lower energies.

Based on accurate mapping of Δ_1 (e.g. Fig. 2-3, Column 2) we can also examine the doping dependence of electronic disorder for the PG energy scales. In Fig. 2-4a-f we show these Δ_1 -maps, but now each is normalized to the mean value of Δ_1 from that same map and shown using the same colour scale. Remarkably, one cannot distinguish which doping is represented by the images in Fig 2-4a-f. In Fig. 2-4g we show the histograms of $\Delta_1/\bar{\Delta}_1$ from these images; it is immediately obvious

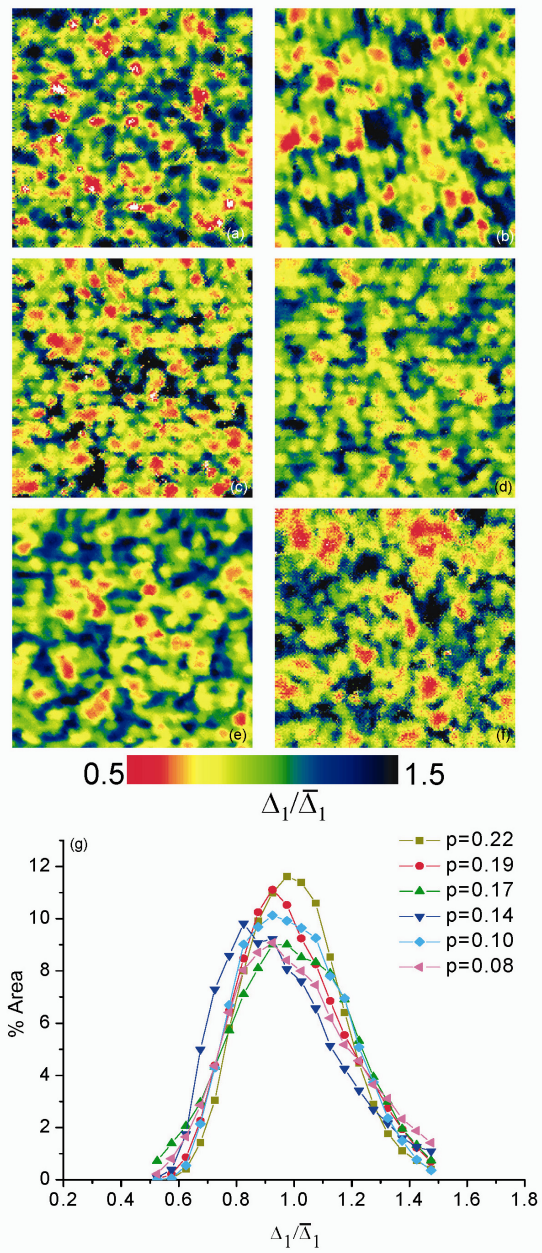


Figure 2-4: Doping dependence of spatial arrangements of $\Delta_1(r)$ normalized by mean value of Δ_1 . (a-f) Normalized Δ_1 maps for six hole-densities $0.8 < p < 0.22$ for $40\text{nm}^2 g(r,V)$ data sets,. The dopings are (a) 0.08, (b) 0.10, (c) 0.14, (d) 0.17, (e) 0.19 and (f) 0.22. The maps were normalized to the average value of Δ_1 value in each $g(r,V)$ maps. For $p=0.08$ we can only estimate the value of Δ_1 from fits to the positive bias part of the spectrum where the steep tunnelling asymmetry is less prominent.
(g) Histograms of the data in Fig 4a-f. Obviously, these distributions are statistically highly similar.

that the distributions are virtually independent of doping. This indicates that the nanoscale trigger for energy-gap disorder is universal (as it should be for disorder from interstitial substitutions and dopant atoms³¹). Furthermore, since the same fractional distribution about the mean gap-energy is observed for PG energy scales at the low dopings (as $T_c \rightarrow 0$), the high energy PG excitations³² appear equally susceptible to nanoscale electronic disorder as those of the superconductor^{4,29,30,31}.

Next we focus on the most significant discrepancies between fits to Eqn. (2) and the related $g(r,V)$ data. These always occur predominantly at the “kinks” which have been reported ubiquitously^{1,29,30,31,32,33} in cuprate STM spectra. In general, these kinks are weak perturbations to $N(E)$ near optimal doping, becoming more clear within nanoscale regions increasing in number as p is strongly diminished^{29,30}. In Figure 2-5a we show representative Δ_1 -sorted spectra. Notice that it is for $\Delta_1 > 50\text{meV}$ (with equivalent data for all dopings shown in the supplementary materials) the kinks become more obvious. Each kink is identified by finding the point of inflection as the minimum in the next derivative d^2I/dV^2 as shown in Fig. 2-5b; its energy is labelled $\Delta_0(r)$. We emphasize that these kinks are weak departures from the fits to $N(E)$ (see 2-10). For the higher energies approaching Δ_1 which are the focus of our study, the kinks neither spoil the excellent fit quality nor the extracted $\Gamma_2(E)$ (see Supplementary Materials Fig. 2). Simultaneous $\Delta_1(r)$ and kink-energy $\Delta_0(r)$ maps can then be derived and are shown in Fig 2-5c,d. By imaging $\Delta_0(r)$ for all dopings, we find that the excitations are always divided into two categories: $E < \Delta_0$ excitations are homogenous

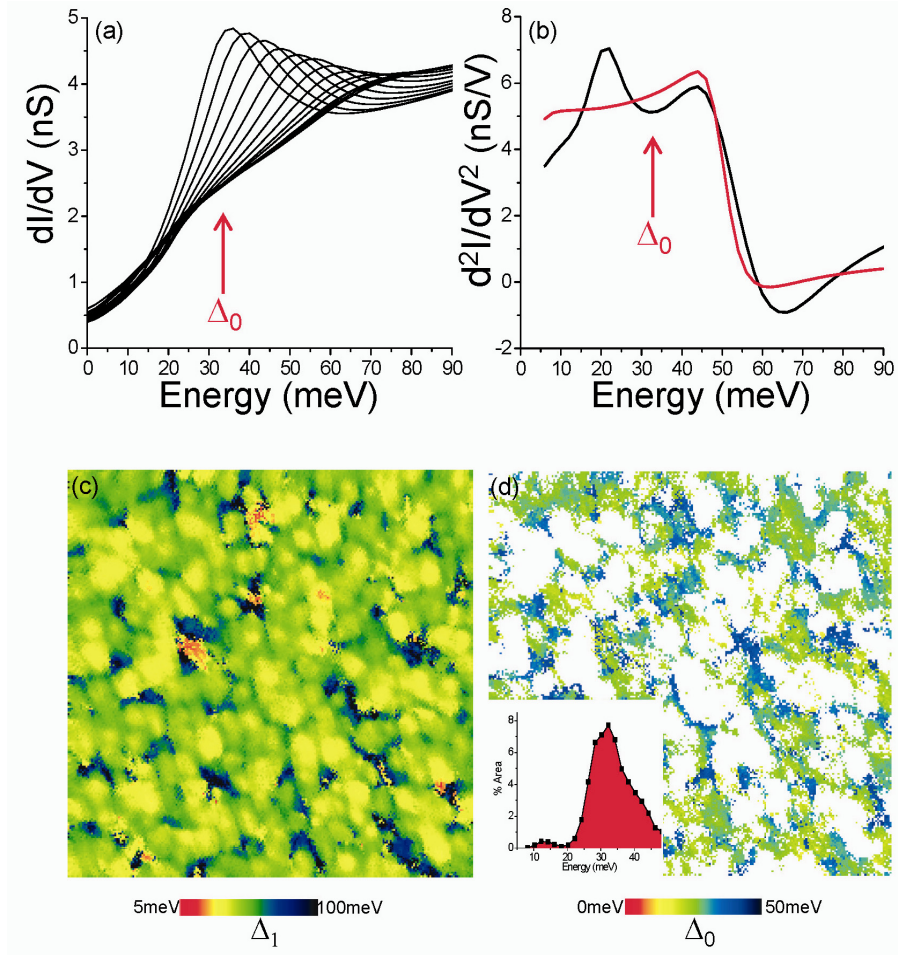


Figure 2-5: Spatial arrangements of kink-energy $\Delta_0(r)$ which separates homogenous from heterogeneous electronic structure.

- (a) A set of Δ_1 -sorted spectra shown with an expanded vertical scale designed to emphasize the representative the kinks occurring ubiquitously in $\Delta_1 > 50$ meV spectra. The red arrow labelled Δ_0 points to average energy at which such kinks are detected in dI/dV .
- (b) Energy of each kink $\Delta_0(r)$ is identified by finding the point of inflection as the minimum in the next derivative d^2I/dV^2 . The black line is the spatially averaged value of d^2I/dV^2 , the red line is the spatially averaged derivative of the fits to Eqn. 2 and the red arrow labelled Δ_0 indicates the kink energy.
- (c) Gap-energy $\Delta_1(r)$ map
- (d) Kink-energy map $\Delta_0(r)$ simultaneous with (c). Clearly the kinks are associated with the higher energy gap spectra, and observation found true at all dopings.

in \mathbf{r} -space and well defined d-wave quasiparticle eigenstates in \mathbf{k} -space^{34,35}, while for $E > \Delta_0$ they are heterogeneous^{29,30,31,32,33} and ill-defined in \mathbf{k} -space. Thus $\langle \Delta_0(\mathbf{r}) \rangle$ represents the average energy scale separating spatially homogenous from heterogeneous excitations.

Another new finding involves the capability to estimate local effective scattering rates. Images of the coefficient $\alpha(\vec{r})$, the linear coefficient of the energy dependence of Γ_2 , are shown in Fig. 2-3 Column 3. These $\alpha(\vec{r})$ range from 0.0 to 0.4 (yellow to black) with the spatially averaged value $\langle \alpha(\vec{r}) \rangle$ growing with falling doping. The scattering rates Γ_2^* at $E = \Delta_1$ are most physically significant. These are determined from $\Gamma_2^*(\vec{r}) = \alpha(\vec{r})\Delta_1(\vec{r})$ and are shown in Fig. 2-3 column 4; they range from yellow (weak scattering) to black (strong scattering) with the maximum effective scattering rates $\Gamma_2^* > 25$ meV for $p \leq 10\%$. One can see the direct correspondence between both the coefficients $\alpha(\vec{r})$ and $\Gamma_2^*(\vec{r})$ with $\Delta_1(\vec{r})$ by comparing Columns 2, 3 and 4. From these, it appears that the relationship between $\Delta_1(\vec{r})$, $\alpha(\vec{r})$ and $\Gamma_2^*(\vec{r})$ is intrinsic and local at the nanoscale.

In Figure 2-6a we show the value of α associated with each value of Δ_1 throughout six samples with different hole-densities. Overlaid on these data as solid black circles are the $\langle \alpha(\vec{r}) \rangle$ versus the spatially average $\langle \Delta_1 \rangle$ for each sample; they are in good agreement with the relationship between local pairs of Δ_1 and α values

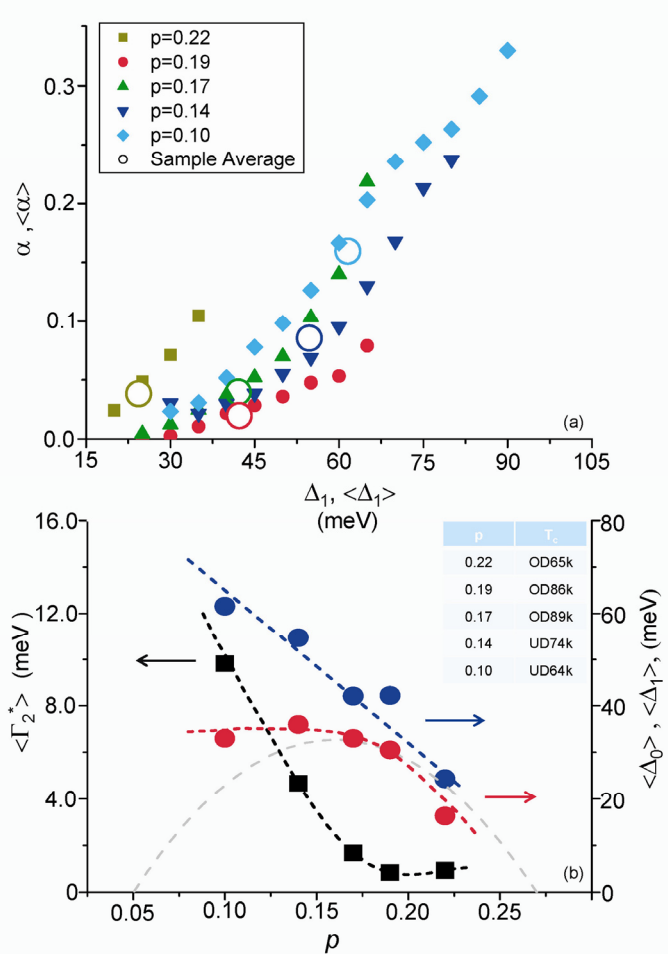


Figure 2-6: Local and global relationships between α and Δ_1 plus ‘phase diagram’ of $\langle \Delta_1 \rangle$, $\langle \Delta_0 \rangle$, and $\langle \Gamma_2^* \rangle$.

(a) The local relationship between $\alpha(\mathbf{r})$ and $\Delta_1(\mathbf{r})$ using all the N(E) fits for the average hole-densities $\langle p \rangle$ shown. The spatial average value of $\langle \Delta_1 \rangle$ and $\langle \alpha \rangle$ for each of the five different samples is plotted as large coloured circles. The global average relationship between $\langle \Delta_1 \rangle$ and $\langle \alpha \rangle$ appears to be indistinguishable from the local relationship between $\alpha(\mathbf{r})$ and $\Delta_1(\mathbf{r})$.

(b) The doping dependence of fitted $\langle \Delta_1 \rangle$ (blue circles), $\langle \Delta_0 \rangle$ (red circles) and $\langle \Gamma_2^* \rangle$ (black squares) each set interconnected by dashed guides to the eye. The higher scale $\langle \Delta_1 \rangle$ evolves along the PG line^{5,6,7} while the lower scale $\langle \Delta_0 \rangle$ represents segregation in energy between homogenous and heterogeneous electronic structure. The separation of $\langle \Delta_1 \rangle$ from $\langle \Delta_0 \rangle$ scales begins to occur at the point where $\langle \Gamma_2^* \rangle$ starts to rise rapidly. T_c and n for each sample is

throughout. These data demonstrate that the relationship between $\Delta_1(\mathbf{r})$: $\alpha(\mathbf{r})$ pairs is local at the nanoscale and apparently intrinsic - since it is the same in all samples at all dopings. Again, we conclude that whatever electronic process perturbs the energy-gap distribution^{29,30,31,32,33,36} perturbs the effective scattering rate $\Gamma_2(E)$ locally in a related fashion.

Significant new insights emerge from these fits when summarized in the form of a phase diagram. In Fig. 2-6b we show $\langle\Delta_1\rangle$ as blue circles; it rises linearly with decreasing p along the well-known^{5,6,7} trajectory for excitations to the PG energy scale. The black circles represent the spatially averaged $E=\Delta_1$ scattering rates $\langle\Gamma_2^*\rangle$; these are very low when $p>16\%$ but undergoes a strong transition to a steeply rising trajectory for $p<16\%$. This dramatic increase of the effective scattering rates for states away from the nodes, culminates in another transition somewhere below $p\sim 10\%$ with the appearance of extreme tunnelling asymmetry^{1,30} (rendering efforts to fit Eqn. 2 impossible). Finally, the red circles represent the spatial average of the second energy scale $\langle\Delta_0\rangle$ where both the ubiquitous ‘kink’ occurs in the $g(r,V)$ spectrum, and above which spatial homogeneity in quasiparticle excitations is lost. Clearly $\langle\Delta_0\rangle$ diverges from $\langle\Delta_1\rangle$, falling slowly as $p\rightarrow 0$.

Discussion/ Conclusions

In this chapter we introduce a new technique for analyzing the tunnelling-derived cuprate electronic excitation spectrum $N(E)$ as $T \rightarrow 0$. The results provide a significantly more quantitative and comprehensive picture of the $T \rightarrow 0$ excitations than was previously available and for a wide range of hole-densities. And, since this fitting technique is demonstrably successful under a very wide variety of circumstances, we can also anticipate its extension to new arenas such as at high temperatures³² or when additional phase fluctuation effects occur near vortex cores⁴. It is important, however, to be aware of the limitations of any interpretation of $\Gamma_2(E)$ simply as a one-particle scattering rate. Equation (2) might be taken as an expression for a classic d-wave superconductor with single-particle scattering rate Γ_2 within BCS theory. Such an interpretation, which may possibly be appropriate in the overdoped materials, would assume weakly interacting quasiparticles. But as the Mott insulator is approached at strong underdoping, this intrinsic effective scattering rate may become so intense that such single-particle k -space excitations are no longer well-defined even in the superconducting state (especially near the Brillouin zone face)^{8,9,21,23,25}. Spin fluctuation theories of d-wave superconductivity suggest relatively weak dependence of the scattering rate on the direction of the quasiparticle momentum^{37,38}. In the underdoped cuprates, pair breaking scattering from vortex-antivortex pairs has been proposed as the origin of large ARPES spectral widths near the antinode^{39,40}. Another caution about the effective scattering rate Γ_2 discussed here is that it is related to the *local* Green's function $G(\mathbf{r},\mathbf{r})$, whose spectral characteristics will be broadened by scattering processes involving the entire Fermi surface. It is then far from clear that a

general fit of the form of Eqn. 2 with a local self-energy should obtain; in an inhomogeneous system, the self-energy is a bilocal quantity $\Sigma(\mathbf{r}, \mathbf{r}')$. Our findings that the vast majority of spectra can be fit, at least for $E > \Delta_0$, by an identical form as Eqn. 2 and that $\Gamma_2(\mathbf{r})$ is spatially correlated with order parameter $\Delta_1(\mathbf{r})$, imply that $\Gamma_2(\mathbf{r})$ does represent the effective ‘local’ self-energy of a quasiparticle sampling a region of size less than or equal to the gap “patch” size, i.e. that the system is self-averaging on this scale. A final caveat is that $\Gamma_2(E) = \alpha E$ represents the first approximation to the true energy dependence of scattering rates consistent with the spectra; it captures very well the low scattering of near nodal quasiparticles and the intense scattering Γ_2^* at $E = \Delta_1$. Eventually, however, a more complex form for $\Gamma_2(E)$ consistent with everything reported herein but capturing finer details of changes in scattering rate throughout \mathbf{k} -space may be required.

A number of important conclusions result from these data and fitting procedures. Local quasiparticle lifetimes $\tau(E) \sim 1/\Gamma_2(E)$ can now be determined from STM data. If we focus on $\langle \Gamma_2 \rangle$ as a function of p , we find a very distinct change near optimal doping characterised by appearance and extremely rapid growth of inelastic scattering rates towards the underdoped regime. This latter effect signifies such intense scattering near the antinodes at lowest dopings, that it must be closely related to the disappearance^{8,9} of well defined \mathbf{k} -states there. Moreover, $\Delta_1(\mathbf{r})$ and the coefficient of energy dependence in the effective scattering rate $\alpha(\mathbf{r})$ appear to be

linked intrinsically and locally - retaining the same relationship throughout all samples. The rapid increase of Γ_2^* scattering rates as the Mott insulator state is approached is likely due to electron-electron interactions but the exact microscopic processes cannot be identified from this study. Significantly, we find no apparent distinction in terms of the form of $N(E)$ in Eqn. 2 between fits to optimally doped $g(V)$ spectra which definitely represent d-wave superconductivity, and the $g(V)$ spectra of strongly underdoped samples down to $p \sim 10\%$ as superconducting T_c diminishes towards 0. This means that a combination of an anisotropic and particle-hole symmetric gap to excitations $\Delta(\vec{k}) = \Delta_1(\cos(k_x) - \cos(k_y))/2$ plus an effective scattering rate $\Gamma_2(E) = \alpha E$ provides a good description of excitation spectra - without recourse to another coexisting electronic ordered state. We emphasize that these conclusions might not hold at $p < 10\%$ because spectra are no longer well fit by Eqn. 2 due to strong tunnelling asymmetry¹. Furthermore, our results for $p > 10\%$, do not imply that there is only one energy scale present: consistent with both the wide variety of long-standing results^{6,7,9,25,29,30,33} and the more recent spectroscopic observations^{41,42,43}, we find that two energy scales always exist on the underdoped side of the phase diagram. The higher scale $\langle \Delta_1 \rangle$ evolves along the PG line. Here we find that the lower scale $\langle \Delta_0 \rangle$, representing segregation in energy between homogenous and manifestly d-wave superconductive³⁴ low energy electronic structure and the heterogeneous high energy electronic structure, diverges from $\langle \Delta_1 \rangle$ when the Γ_2 scattering rates begin to increase rapidly.

An intriguing scenario stimulated by these observations would be that superconducting cuprates exhibit an anisotropic / particle-hole symmetric excitation energy scale $\Delta(\vec{k}) = \Delta_1(\cos(k_x) - \cos(k_y))/2$ but that the electronic excitations experience rapidly increasing inelastic scattering rates as $p \rightarrow 0$. This scenario has recently become the focus of intense theoretical study⁴⁴ yielding a number of far reaching conclusions including (i) realistic calculations of impurity- and spin-fluctuation scattering contributions to local density of states showing that typical quasiparticle scattering rates are indeed quasi-linear in energy and proportional to Δ_1 , (ii) demonstration of how the mean free path falls drastically with increasing quasiparticle energy so that, below a critical bias, all quasiparticles explore so many heterogeneous gap patches that their spectra appear homogeneous, (iii) evidence that that the quasiparticle interference modulations^{34,35} could be weakened primarily by inelastic scattering represented by $\Gamma_2(E)$ and, (iv) reconciliation of photoemission with STM tunnelling and neutron-scattering lifetimes, by inclusion of gap inhomogeneity-induced broadening of ARPES spectral function. Moreover, quasiparticles subject to scattering rates above some critical value of $\Gamma_2(E)$ should not retain sufficient coherence to contribute to the superfluidity in the ground state⁴⁵ thus leading to the ultimate breakdown of superconductivity as Γ_2^* diverges at low doping.

To test these new hypotheses will require (i) determination of whether the superconducting quasiparticles are actually governed by a pairing gap on the scale of

Δ_1 as $p \rightarrow 0$, and (ii) microscopic identification of the Γ_2 scattering process and its relationship to Δ_0 where energy-segregation of homogenous from heterogeneous electronic structure begins. The next step is of course to precisely determine this energy segmentation. For this to work, we need to include the separation intrinsically in our model. This will also require the insight gained from a high precision study of the QPI pattern as it varies as a function of energy and doping. The phenomena seen in k/q -space, explained in the next chapter, will allow us to take our basic model we have proposed here and expand it into a complete description of the low and high energy states in chapter 4. However that is not to disparage the model we have developed here. Indeed we have shown that the Mottness plays a key role in the properties through an intrinsic decrease in lifetime as we approach the insulator state. As well as showing the intrinsic universal disorder structure. Without this model, and its results we would have been unable to make the connections between real space and k -space phenomena that are to come.

Methods

While Eqn. 2 appears to be quite simple, it is numerically intensive. We use the Levenberg-Marquardt algorithm implemented in C¹. The algorithm computes the Jacobian of the function $N(E)$ and looks at the difference between the $g(V)$ and the fit

¹ Lourakis, M.I.A. <http://www.ics.forth.gr/~lourakis/levmar/> (2004)

as a function of the small changes in the parameters. With each step, the Levenberg-Marquardt algorithm computes this change and diminishes the difference with iteration.

For a given doping, the Fermi surface is designated using the tight binding model parameterized by Norman *et al.* An array of points equally spaced in distance along the Fermi surface is then calculated for E=0. Equation 2 is evaluated for each of these points, adding the k_x, k_y coordinate into the d-wave gap equation. These results are then numerically integrated along the Fermi surface to yield N(E).

Because of the Fermi surface evaluation, each five parameter fit requires approximately a minute. For roughly 10^6 curves, approximately two years of processing would then be required. Instead, we use hundreds of processors in parallel – a task made simpler by the fact that each fit is independent from all the rest. A typical field of view (256X256 curves) is broken into 8X8 pieces and distributed to 100-200 processors and allowed to run for 1-3 days. The fitting processes to carry out 5-10 times, with different starting parameters in order to minimize the chances of finding a false local minimum.

The quality of fits of N(E) to each spectrum throughout the data set can be demonstrated in a variety of different ways. We use a normalized χ^2 as a measure of the quality of our fit:

$$\chi^2 = \frac{1}{n-p} \sum_{i=0}^n \frac{(x_i - f_i)^2}{x_i}$$

This is the standard χ^2 normalized by the number of points minus the number of fitting parameters to allow us to compare data sets that have a varying numbers of points per curve. Here n is the number of points per curve, p is the number of fitting parameters, x is the measured data value and f is the fit value.

In Figure 2-7 we demonstrate the fits to $N(E)$ to individual $g(V)$ spectra along with the fit parameters. In Figure 2-8 we show that the histogram of fit quality parameter for a complete data set of $>64,000$ spectra remains low for all Δ_1 . For representative individual spectra, we demonstrate the fit quality represented by these low values of χ^2 and also indicate by a red line the location of the ‘kink’ as identified by a local minimum in d^2I/dV^2 . We see directly that each ‘kink’ is merely a small departure from an overall very successful fit; this is universally true when $\chi^2 < 0.01$. Figure 2-9 we show the Δ_1 -averaged $g(V)$ spectra and their Δ_1 averaged $N(E)$ fits for spectra from samples at five different dopings demonstrating how the fit quality is preserved across much of the phase diagram. Figure 2-10a shows gap-averaged spectra and their corresponding fits (Fig. 2-10b). The derivate of these spectra shows a small dip which is associated with the kink, but the derivative of the fits (Fig. 2-10d) does not. Thus, overall, the effect of kinks is very weak and only detectable globally because of the excellent quality of our fits to Eqn 2.

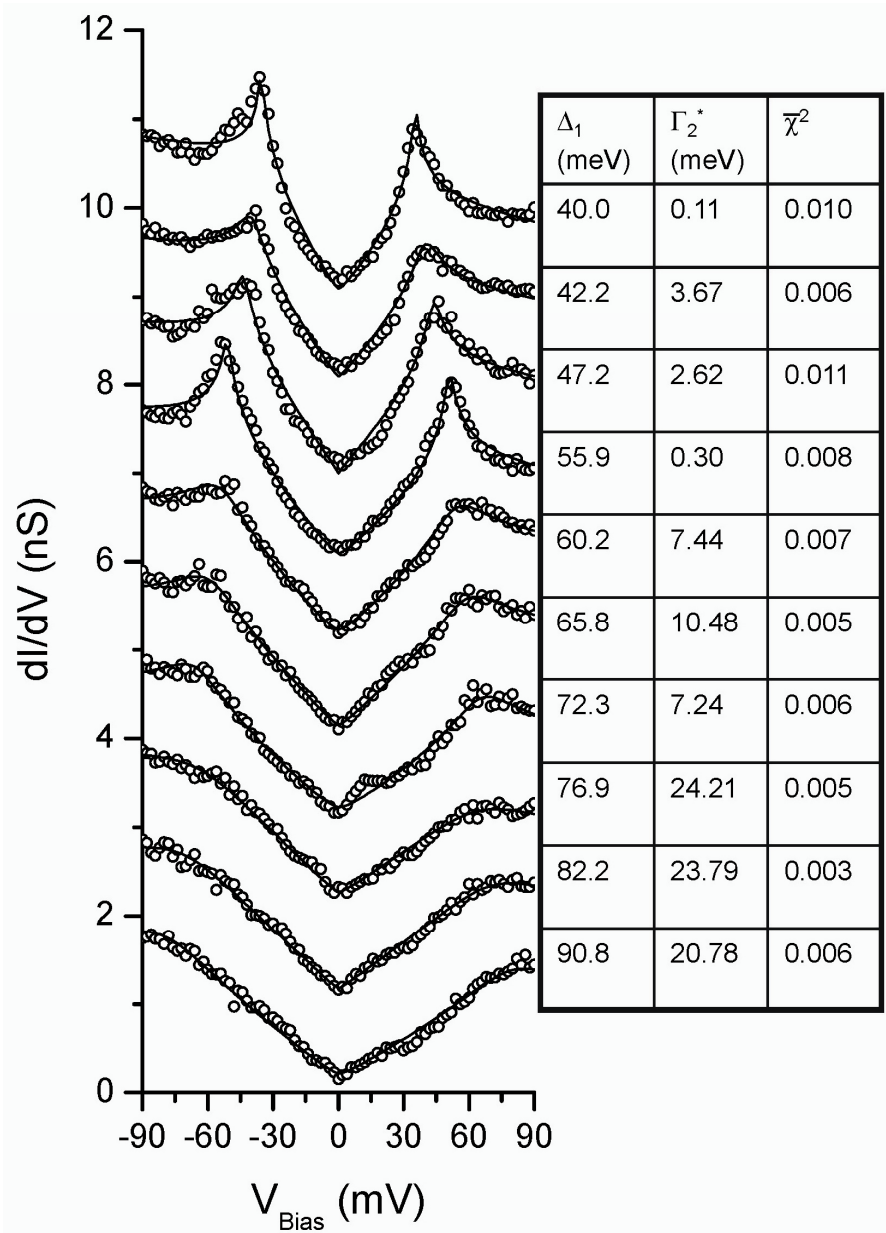


Figure 2-7: Individual spectra and fits taken at ten different points. These data span a 50 meV range in Δ_1 . The open circles are the raw data, and the solid lines are the fits to the data. The table on the right shows the fit parameters for each of the curves. This is for $p=0.10$.

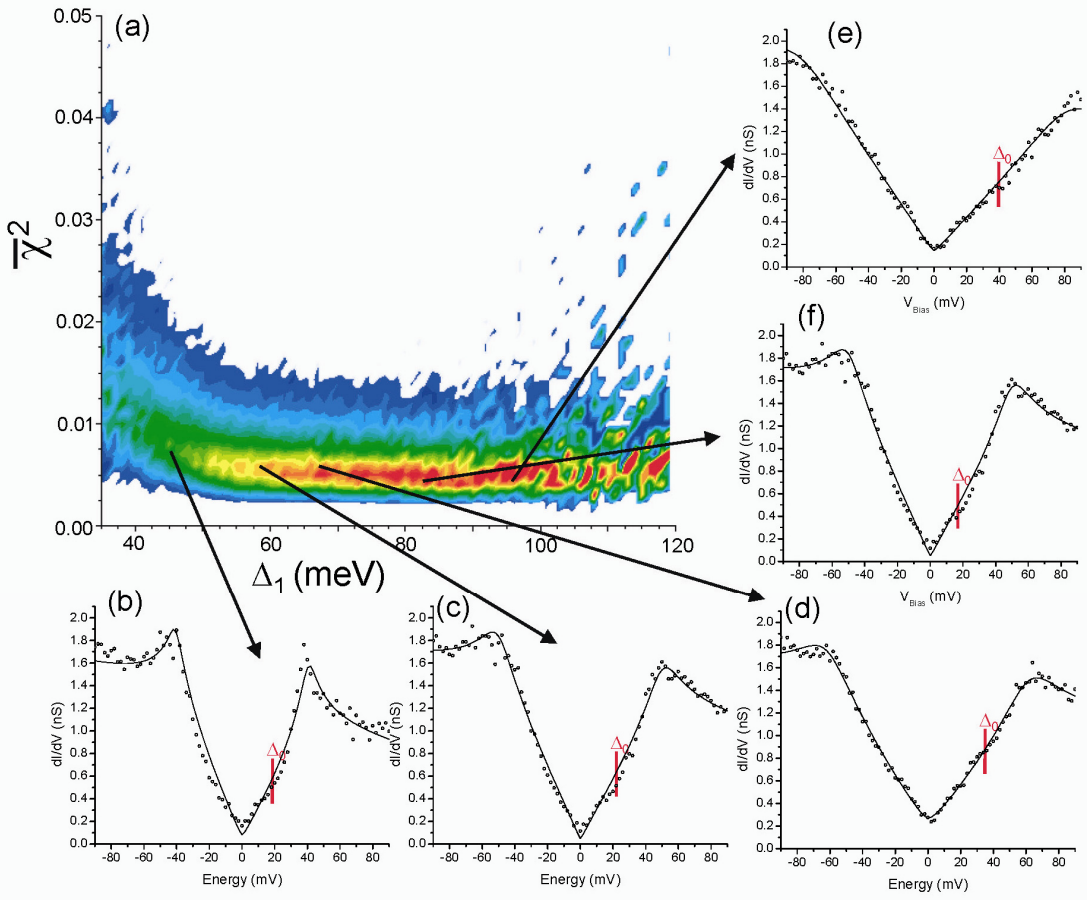


Figure 2-8: Normalized χ^2 histogram with example curves. (a) A 2D histogram showing the grouping of the normalized χ^2 as a function of Δ_1 . The scale stretches from colored (red being the highest number of points) to white (zero points). From this histogram five example curves of quality of fit represented by these $\chi^2 < 0.01$ are shown. The red line marked by Δ_0 shows the kink location for each of the example curves. The normalized χ^2 remains extremely low despite the presence of the kink.

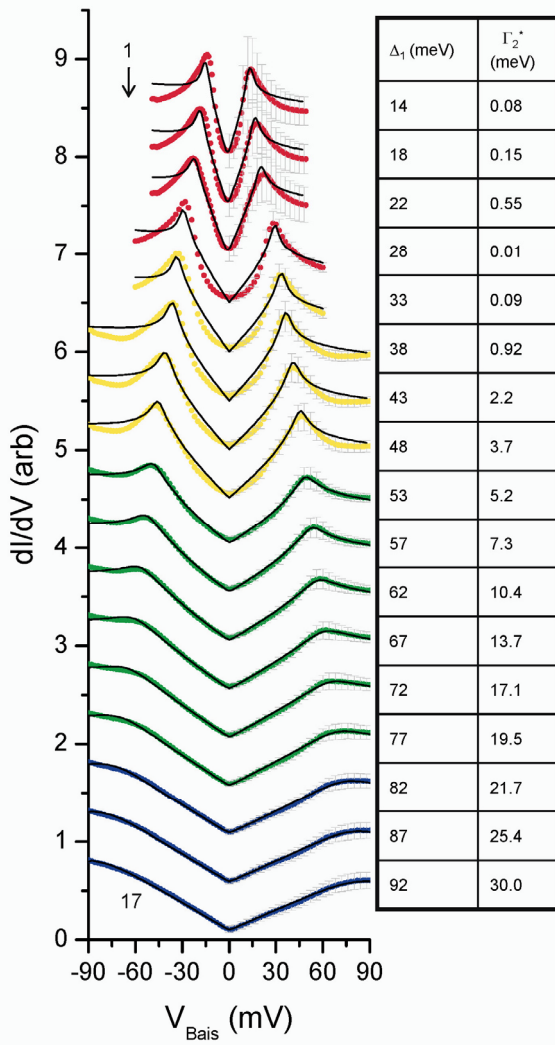


Figure 2-9: Δ_1 averaged spectra and fits taken from 4 different dopings and spanning the range of Δ_1 values. The error bars are the $1-\sigma$ distribution for the Δ_1 averaging of the spectra. Spectra, counting down from the top, are 1-3 from $p=0.22$, spectra 4-5 from 0.19, spectra 6-8 from 0.17, and spectra 9-17 from $p=0.10$. The colors correspond roughly to the Δ_1 map color scale in Figure 3.

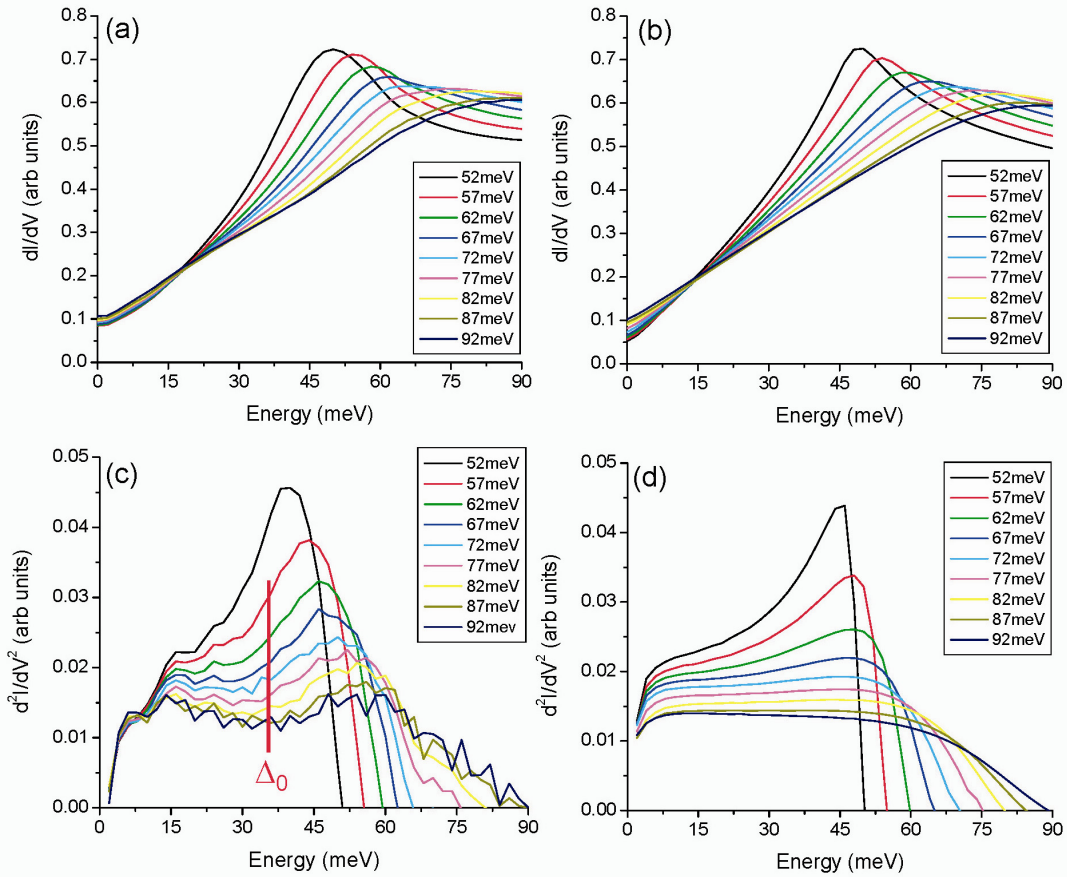


Figure 2-10: Expanded view of gap-averaged spectra for $\Delta > 50$ meV

(a) Gap-averaged spectra from the complete data set whose individual fit quality is demonstrated in Suppl. Fig. 2, (b) the corresponding gap-averaged fits , (c) shows the derivate of the spectra with the approximant kink energy Δ_0 shown by the red line, (d) presents the derivative of these fits. The departure due to kinks of measured spectra from the fits appears as a small dip in $d^2 I/dV^2$ in (c) with no equivalent dip in the fit derivative (d).

REFERENCES

- ¹ Kohsaka, Y., Taylor, C., Fujita, K., Schmidt, A., Lupien, C. et al An intrinsic bond-centered electronic glass with unidirectional domains in underdoped cuprates *Science* **315**, 1380-1385 (2007)
- ² Balatsky, A.V., Vekhter, I., Zhu, J.X. *Rev. Mod. Phys.* Impurity-induced states in conventional and unconventional superconductors **78**, 373-433 (2006).
- ³ Hussey, N.E. Low-energy quasiparticles in high-T-c cuprates *Adv. In Phys.* **51**, 1685-1771 (2002).
- ⁴ Fischer, O., Kugler, M., Maggio-Aprile I., Berthod C., Renner C. Scanning tunneling spectroscopy of high-temperature superconductors *Rev. Mod. Phys.* **79**, 353-419 (2007)
- ⁵ Orenstein, J., Millis, A.J. Advances in the physics of high-temperature superconductivity *Science* **288**, 468-474 (2000)
- ⁶ Timusk T., Statt B. The pseudogap in high-temperature superconductors: an experimental survey *Rep. Prog. Phys.* **62**, 61-122 (1999)
- ⁷ Huefner, S., Hossain, M.A., Damascelli, A., Sawatzky, G.A. Two gaps make a high temperature superconductor *Cond-Mat* 0706.4282 (2007)
- ⁸ Campuzano, J. C., Norman, M. R. , Randeria, M., *The Physics of Superconductors, Vol. II*, 167-273 (Springer, New York, 2004).
- ⁹ Damascelli, A., Hussain, Z., Shen, Z.X. Angle-resolved photoemission studies of the cuprate superconductors *Rev. Mod. Phys.* **75**, 473-541 (2003).
- ¹⁰ Anderson, P.W. The resonating valance bond state in La₂CuO₄ and superconductivity *Science* **235**,1196-1198 (1987).
- ¹¹ Zhang, F.C., Gros, C., Rice, T.M., Shiba H. A renormalized hamiltonian approach to a resonant valence bond wavefunction *Super. Sci. & Tech..* **1**, 36-46 (1988).

-
- ¹² Kotliar, G. *Phys. Rev. B* A resonating valence bonds and d-wave superconductivity **37**, 3664 - 3666 (1988).
- ¹³ Paramekanti, A., Randeria, M., Trivedi, N. Projected wave functions and high temperature superconductivity *Phys. Rev. Lett.* **87**, 217002 (2001).
- ¹⁴ Anderson, P.W., Lee, P.A., Randeria, M., Rice, T.M., Trivedi, N. et al The physics behind high-temperature superconducting cuprates: the 'plain vanilla' version of RVB *J. Phys. Cond. Matt.* **16**, R755-R769 (2004).
- ¹⁵ Chakravarty, S., Laughlin, R.B., Morr, D.K., Nayak, C. Hidden order in the cuprates *Phys. Rev. B* **63**, 094503 (2001).
- ¹⁶ Varma, C.M. Non-Fermi-liquid states and pairing instability of a general model of copper oxide metals *Phys. Rev. B* **55**, 14554-14580 (1997)
- ¹⁷ Honerkamp, C., Fu, H.C., Lee, D.H. Phonons and d-wave pairing in the two-dimensional Hubbard model *Phys. Rev. B* **75**, 014503 (2007)
- ¹⁸ Newns, D.M., Tsuei, C.C. Fluctuating Cu-O-Cu bond model of high-temperature superconductivity *Nature Phys.* **3**, 184-191 (2007)
- ¹⁹ Valla, T., Fedorov, A.V., Johnson, P.D., Wells, B.O., Hulbert, S.L. et al Evidence for quantum critical behavior in the optimally doped cuprate $\text{Bi}_2\text{Sr}_2\text{CaCu}_2\text{O}_{8+\delta}$ *Science* **285**, 2110-2113 (1999).
- ²⁰ Yamasaki, T., Yamazaki, K., Ino, A., Arita, M., Namatame, H. et al Unmasking the nodal quasiparticle dynamics in cuprate superconductors using low-energy photoemission *Phys. Rev. B* **75**, 140513 (2007)
- ²¹ Valla, T., Kidd, T.E., Rameau, J.D., Noh, H.J., Gu, G.D. et al *Physical Review B*, **73**, 184518 (2006).
- ²² Basov, D.N., Timusk, T. Electrodynamics of high-T-c superconductors *Rev. Mod. Phys.* **77**, 721-779 (2005).
- ²³ Valla, T., Fedorov, A.V., Johnson, P.D., Li, Q., Gu, G.D. et al Temperature dependent scattering rates at the Fermi surface of optimally doped $\text{Bi}_2\text{Sr}_2\text{CaCu}_2\text{O}_{8+\delta}$ *Phys. Rev. Lett.* **85**, 828-831 (2000).

-
- ²⁴ Kaminski, A., Fretwell, H.M., Norman, M.R., Randeria, M., Rosenkranz, S. Momentum anisotropy of the scattering rate in cuprate superconductors *Phys. Rev. B* **71**, 014517 (2005)
- ²⁵ Gedik, N., Yang, D.S., Logvenov, G., Bozovic, I., Zewail, A.H. Nonequilibrium phase transitions in cuprates observed by ultrafast electron crystallography *Science* **316**, 425-429 (2007).
- ²⁶ Tinkham, M. *Introduction to Superconductivity* (1996)
- ²⁷ Dynes, R.C., Narayanamurti, V., Gurno, J.P. Direct measurement of quasiparticle-lifetime broadening in a strong-coupled superconductor *Phys. Rev. Lett.* **41**, 1509-1512 (1978)
- ²⁸ Norman, M. R., Randeria, M., Ding, H., Campuzano, J. C. Phenomenological models for the gap anisotropy of $\text{Bi}_2\text{Sr}_2\text{CaCu}_2\text{O}_8$ as measured by angle-resolved photoemission spectroscopy *Phys. Rev. B* **52**, 615-622 (1995)
- ²⁹ Lang, K.M., Madhavan V., Hoffman, J.E., Hudson, E.W., Eisaki, H. et al Imaging the granular structure of high-T-c superconductivity in underdoped $\text{Bi}_2\text{Sr}_2\text{CaCu}_2\text{O}_{8+\delta}$ *Nature* **415**, 412-416 (2002)
- ³⁰ McElroy, K., Lee, D.H., Hoffman, J.E., Lang, K.M., Lee, J., et al Coincidence of checkerboard charge order and antinodal state decoherence in strongly underdoped superconducting $\text{Bi}_2\text{Sr}_2\text{CaCu}_2\text{O}_{8+\delta}$ *Phys. Rev. Lett.* **94**, 197005 (2005)
- ³¹ McElroy, K., Lee, J., Slezak, J.A., Lee, D.H., Eisaki, H. et al Atomic-scale sources and mechanism of nanoscale electronic disorder in $\text{Bi}_2\text{Sr}_2\text{CaCu}_2\text{O}_{8+\delta}$ *Science* **309**, 1048-1052 (2005).
- ³² Gomes, K.K., Pasupathy, A.N., Pushp, A., Ono, S., Ando, Y. et al Visualizing pair formation on the atomic scale in the high-T-c superconductor $\text{Bi}_2\text{Sr}_2\text{CaCu}_2\text{O}_{8+\delta}$ *Nature* **447**, 569-572 (2007)

-
- ³³ Howald, C., Fournier, P., Kapitulnik, A. Phys. Rev. B Inherent inhomogeneities in tunneling spectra of $\text{Bi}_2\text{Sr}_2\text{CaCu}_2\text{O}_{8-x}$ crystals in the superconducting state **64**, 100504 (2001)
- ³⁴ McElroy, K., Simmonds, R.W., Hoffman, J.E., Lee, D.H., Orenstein, J. et al Relating atomic-scale electronic phenomena to wave-like quasiparticle states in superconducting $\text{Bi}_2\text{Sr}_2\text{CaCu}_2\text{O}_{8+\delta}$ *Nature* **422**, 592-596 (2003).
- ³⁵ Hanaguri, T., Kohsaka, Y., Davis, J.C., Lupien, C., Yamada, I. et al Quasiparticle interference and superconducting gap in $\text{Ca}_{2-x}\text{Na}_x\text{CuO}_2\text{Cl}_2$ *Nature Physics* **3**, 865 - 871 (2007).
- ³⁶ Nunner, T.S., Andersen, B.M., Melikyan, A., Hirschfeld, P.J. Dopant-modulated pair interaction in cuprate superconductors *Phys. Rev. Lett.* **95**, 177003 (2005).
- ³⁷ Quinlan, S.M., Hirschfeld, P.J., Scalapino, D.J. Infrared conductivity of a d(x(2)-y(2))-wave superconductor with impurity and spin-fluctuation scattering *Phys. Rev. B* **53**, 8575 (1996).
- ³⁸ Dahm, T. Anisotropy of the quasiparticle damping in the high-T-c superconductors $\text{Bi}_2\text{Sr}_2\text{CaCu}_2\text{O}_8$ and $\text{YBa}_2\text{Cu}_3\text{O}_{6.9}$ as seen from angle-resolved photoemission experiments *Phys. Rev. B* **54**, 10150-10154 (1996).
- ³⁹ Franz, M., Millis, A.J. Phase fluctuations and spectral properties of underdoped cuprates *Phys. Rev. B* **58**, 14572-14580 (1998).
- ⁴⁰ Millis, A.J., Norman, M. Antiphase stripe order as the origin of electron pockets observed in 1/8-hole-doped cuprates *Phys. Rev. B* **76**, 220503(R) (2007)
- ⁴¹ Kanigel, A., Norman, M.R., Randeria, M., Chatterjee, U., Souma, S. et al Evolution of the pseudogap from Fermi arcs to the nodal liquid *Nature Physics* **2**, 447-451 (2006).

-
- ⁴² Tanaka, K., Lee, W.S., Lu, D.H., Fujimori, A., Fujii, T. et al Distinct Fermi-momentum-dependent energy gaps in deeply underdoped Bi2212 *Science* **314**, 1910-1913 (2006).
- ⁴³ Boyer, M. C., Wise, W. D., Chatterjee, Kamlesh, Yi, Ming, Kondo, Takeshi et al Imaging the two gaps of the high-temperature superconductor Bi₂Sr₂CuO_{6+x} *Nature Physics* **3**, 802-806 (2007).
- ⁴⁴ S. Graser, P.J. Hirschfeld and D.J. Scalapino, Local quasiparticle lifetimes in a d-wave superconductor *Cond-Mat* 0801.0101 (2007)
- ⁴⁵ Chubukov, A.V., Norman, M.R., Millis, A.J., Abrahams, E. Gapless pairing and the Fermi arc in the cuprates *Phys. Rev. B* **76**, 180501 (2007)

CHAPTER 3

Quasiparticle Interference shines a light on our fits

Overview

QPI is created by the interference between coherent quasiparticles scattered off impurities. This pattern is the coherent superconducting analogy of Friedel oscillations which were first observed in copper back in 1988 by Neddermeyer¹. Our QPI patterns were first reported back in 2002². Since that time a series of studies has been undertaken mapping the properties of the QPI patterns both as a function of limited doping³, and energy⁴. Since their initial observation, it has been known that the QPI patterns become fainter at lower dopings although this effect has been hard to quantify. It has also been known that the QPI pattern becomes impossible to observe at higher energies, or rather there is a transformation that takes place with the establishment of non-dispersive features and the disappearance of the dispersive ones. The ability to extract information about the gap structure in k-space from the QPI, as well as the ability to extract the underlying band structure has also existed for some time³. However only recently has it become possible to do this across a wide range of dopings with high enough precision to quantify both accurately. This has been the result of both an increase in the number of data sets, and increased complexity of the analyses tools. Recently the important observation that if one takes the ratio of positive to negative biases one vastly improves the signal to noise⁵, has allowed the cataloguing of QPI derived quantities to move forward with leaps and bounds.

The energy range where the QPI phenomenon lives is in the low energy, coherent states. These are separated by the kink from the higher, gap disordered states. By looking at a line cut of our data we can clearly resolve, not only The lower energy states, where

there is little variance, but also the higher energy gap disordered states. This is illustrated in figure 3-1, where we can see a high quality line cut taken showing the homogenous nature of the lower energy states. It is because of this homogenous nature that we can see the excitations in momentum space. In fact to have a well defined k/q -space we require translational invariance, which only exists on a long length scale at low energies. If we look at particular energies extracted from the dI/dV of a large field of view, with high resolution we can see the coherent excitations that are QPI.

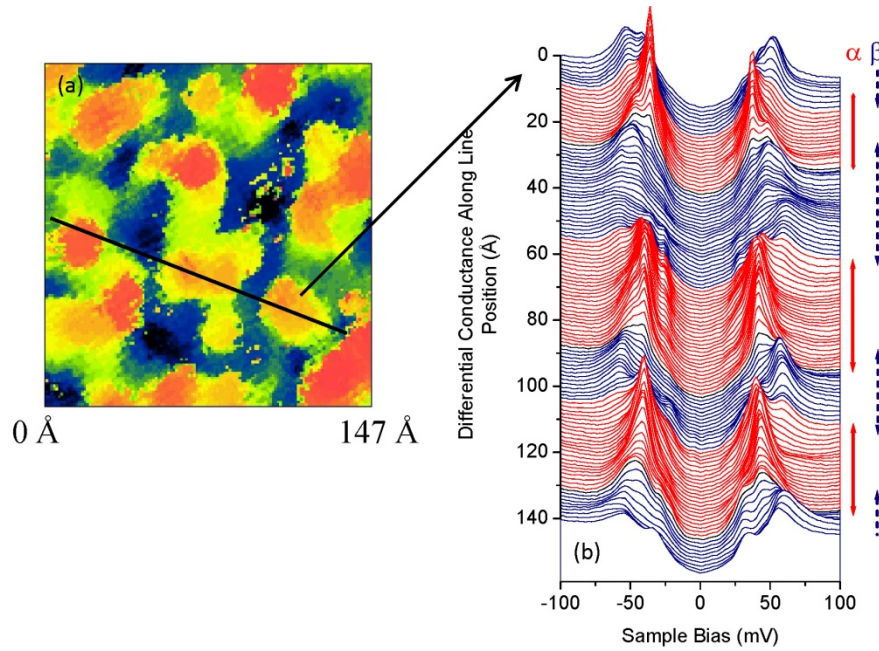


Figure 3-1: (a) peak to peak gap map, with line showing the cut in (b). (b) dI/dV line cut showing the low energy homogeneous states, as well as the higher disorder.

This is what we have done in figures 3-2 and 3-3 as a function of energy. These show first the real space QPI pattern seen in the positive, negative bias layers as well as the improved signal to noise of the ratio map. In the real space data, the pattern starts off faint, and then at the higher energy layers show the local breakdown of the QPI pattern, and the

nucleation of growing ‘white spots’ that represent large increases in the LDOS, that result in a breakdown of the phase coherence between the regions. This is caused by the onset of the higher energy gap disorder, and the white spots begin their nucleation in regions where the overall large scale Δ_1 gap energy is small. Once the QPI pattern starts to be destroyed we are left with only q_1 or the ‘checkerboard’ q-vector in regions where the higher energy disorder has not set in. What is interesting is the negative side seems to advance at a slightly faster clip than the positive side. One can see this by comparing the size of the white spots on the positive and negative side at equal energies, and they appear to be bigger for equivalent energy on the negative side as opposed to the positive. This effect also shows up in the FFT, which I have provided in figure 3-2. Here we can see that the QPI pattern is stronger on the negative side. The ratio column shows a marked improvement in the signal to noise concerning the quasiparticle signal, for both the real space (3-2), and the q-space images (3-3).

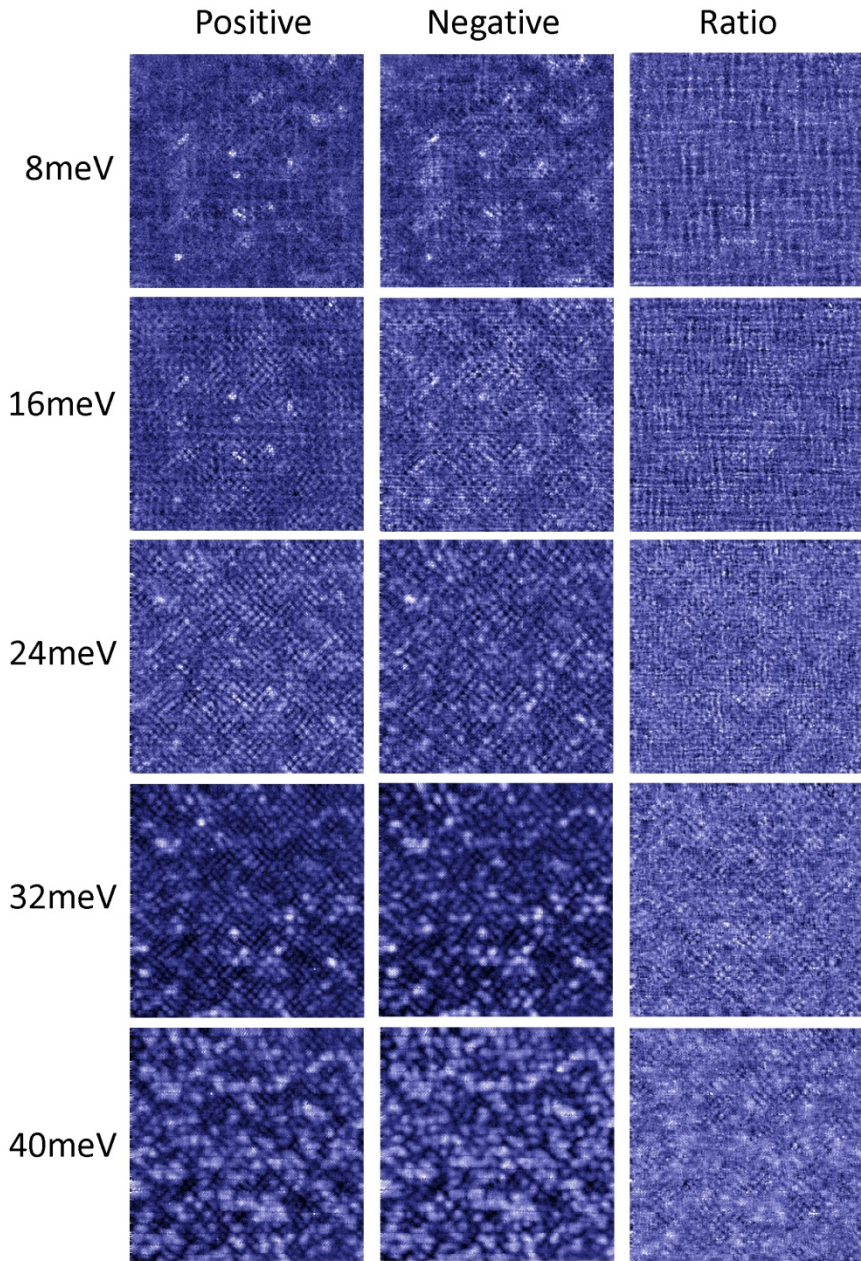


Figure 2-2: Selected layers from a UD74K data set. The left column shows the positive bias layers, the middle layer shows the negative bias layers at the same energy and the right column shows the ratio of the two, highlighting the increased signal to noise in this real space data. The termination energy for this sample is around 36meV, although it is clearly evident at higher energies that the destruction is a localized caused by the onset of higher energy disorder (notice the nucleation of the white checkerboard type regions). These are 50nm^2 fields of view, with 256X256 resolution.

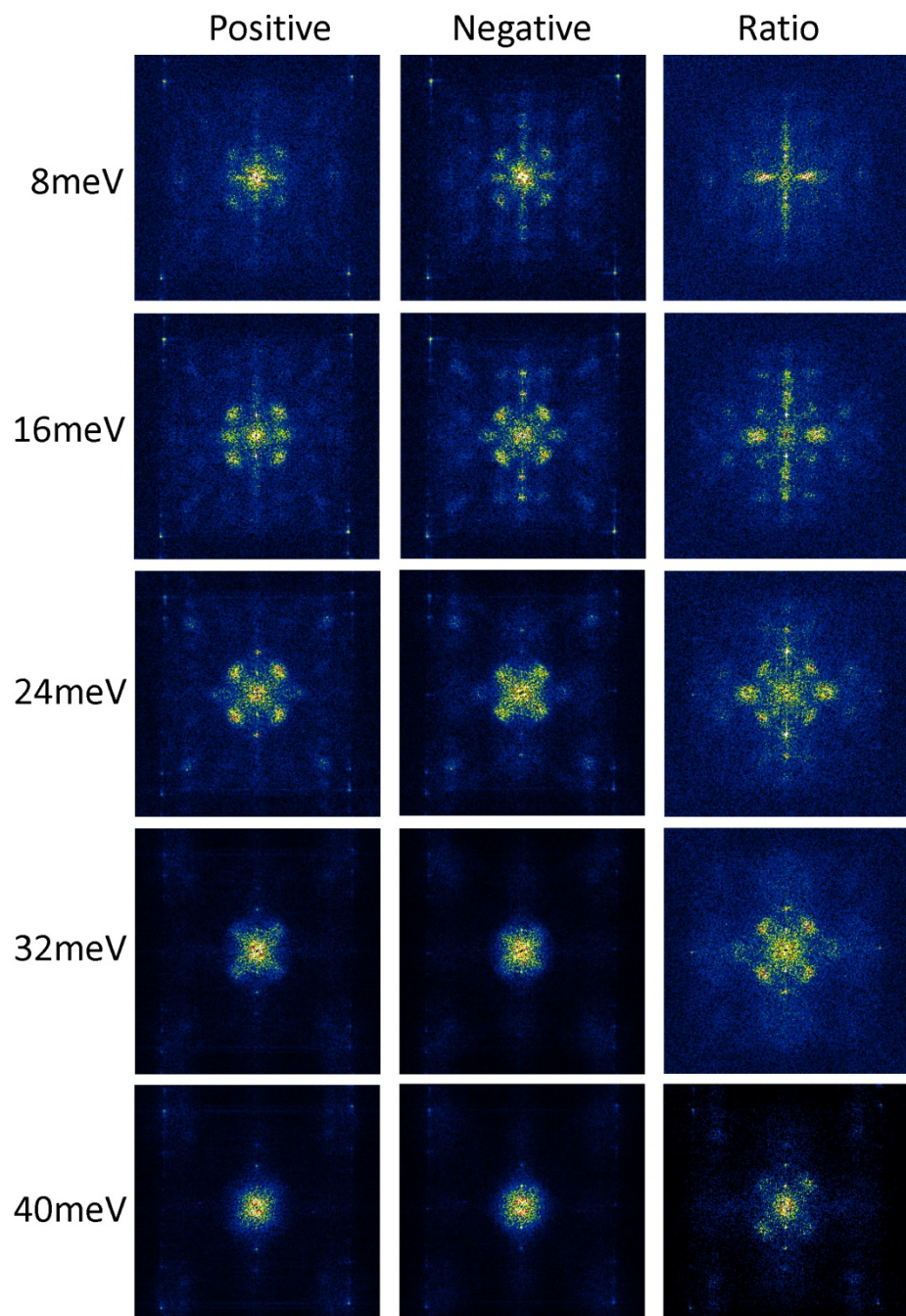


Figure 3-3: Selected layers from a UD74K data set. The left column shows the positive layers, the middle layer shows the negative layers at the same energy and the right column shows the ratio of the two, highlighting the increased signal to noise in q-space. It is also clear that the negative layers seem to fade out first. If you move down the figure in a zig zag between positive and negative it completely makes sense, especially at higher energies.

Theory

Our understanding of the QPI pattern starts with its initial observation in the early 2000's. The original theory was developed by D.-H. Lee⁶ and is referred to as the octet model. In this model of the d-wave bogoliubov bands, you have an octet of 'hot spots', places in k-space with a high density of states. These are the only points which contribute to the QPI pattern. This leads to seven unique vectors which contribute to the QPI pattern. Due to symmetry these vectors can be roatated by 90 degrees, resulting in the highly symmetrized QPI pattern we see. These hot spots sit at the ends of the superconducting 'bananas' that are observed from ARPES, and which can be calculated with a spectral density of states, or $a(k,\omega)$ function. The dispersion of the superconducting state thus moves these spots causing the QPI pattern to disperse. This leads to a very straight forward relationship between the q-vectors we can measure and their k-space points, given by

$$\begin{aligned} \mathbf{q}_1 &= (2k_x, 0) & \mathbf{q}_4 &= (2k_x, 2k_y) & \mathbf{q}_7 &= (k_x - k_y, k_y - k_x) \\ \mathbf{q}_2 &= (k_x + k_y, k_y - k_x) & \mathbf{q}_5 &= (0, 2k_y) \\ \mathbf{q}_3 &= (k_x + k_y, k_y + k_x) & \mathbf{q}_6 &= (k_x - k_y, k_y + k_x) \end{aligned}$$

where the equations are numbered for each of the q-vectors as shown in figure 3-4(a). In this way we can gather k-space information from our scattering observation. Figure 3-4(a) shows not only the labeled scattering vectors, but also the superconducting $a(k,\omega)$ (contour plot) in the first brillion zone. The hot spots are represented by the red circles. In 3-4(b) we show the measured positions for most of the q-vectors as a function of energy, the solid lines represent a fit from the octet model, coupled with a d-wave gap. This demonstrates the ability of the octet model describe the data as well as our ability to extract the position accurately. In figure 3-4(c) the k-space gap function obtained from the data in 3-4(b) is

shown. The gap function includes a higher harmonic term, and in fact it would not be possible to pass through more than a few data points with a pure d-wave gap. Finally in 3-4(d) we show the k-space points along with a fitted Norman band structure. These figures demonstrate that we obtain the underlying band structure as well as the energy dependence of the low energy states from the QPI.

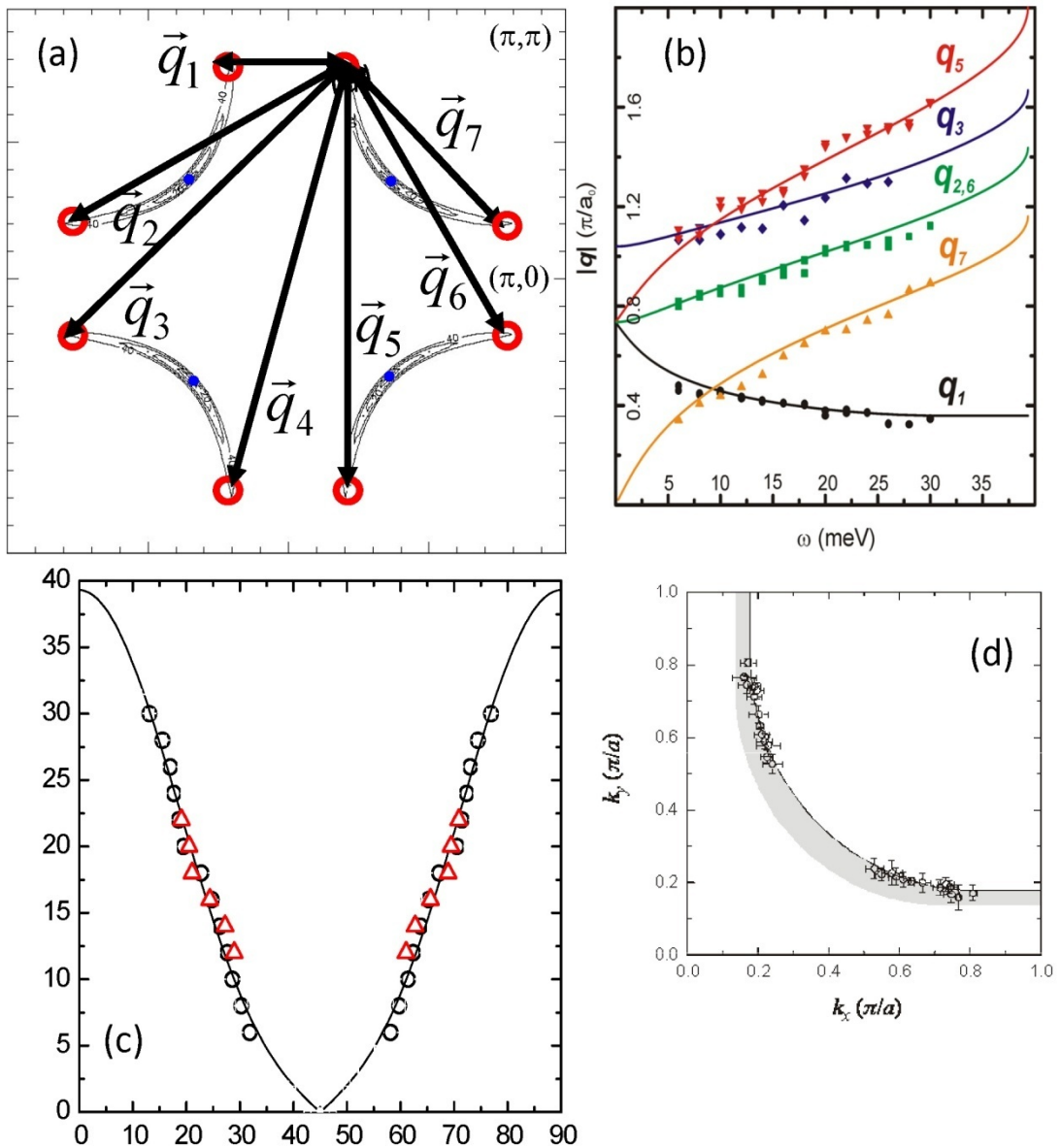


Figure 2-4: (a) The first brillouin zone of the superconducting band structure. The red circles represent the ‘hot spots’ which represent points of large spectral weight. These contribute primarily to the QPI pattern according to the octet model. These represent the vectors which we track as the band structure disperses. (b) Shows the length of these vectors as they disperse as well as the fit from the octet model with a gap with a higher harmonic portion. (c) shows the fitted gap as a function of angle (y-axis) in k-space while (d) shows the k-space location of these points, as well as a fitted norman band structure.

A New Understanding

The vastly improved signal to noise obtained from the ratio map combined with a wide range of data sets spanning the under doped side of the phase diagram, allow us to map out the behavior of these coherent low energy quasiparticles. This has been successfully done for a wide range of dopings, and some of the results are shown in figure 3-5. Here we show the k-space origin points for observed dispersive q-vectors for a wide range of dopings. The k points are the result of the extraction of the individual q-vectors from the QPI pattern, coupled with the equations listed above. The ability to obtain this enables us not only to extract the chemical potential by fitting a ridged Norman band structure, but also it allows us to map the termination point of the QPI in k-space. As we increase energy we can watch as the QPI points fade away. While this would normally make it quite hard to determine a termination point, we see both q_1 and q_5 change from dispersing points to non-dispersing points. This allows us to accurately determine an energy, and a location in k-space where the qpi terminates. It is extremely interesting to note that this happens at the dotted line.⁷ This represents the anti-ferromagnetic zone boundary, where the anti-ferromagnetic alignment dispersion becomes accessible, resulting in a renormalization of the band structure. This is especially pertinent if this anti-ferromagnetic state is highly disordered. If we look at the energy where the band structure crosses this zone we note that this is approximately the same energy as the kink structure we have observed in the past. This is also the energy that represents the onset of the higher energy gap disorder. Now we can associate this energy with the destruction of the coherent states.

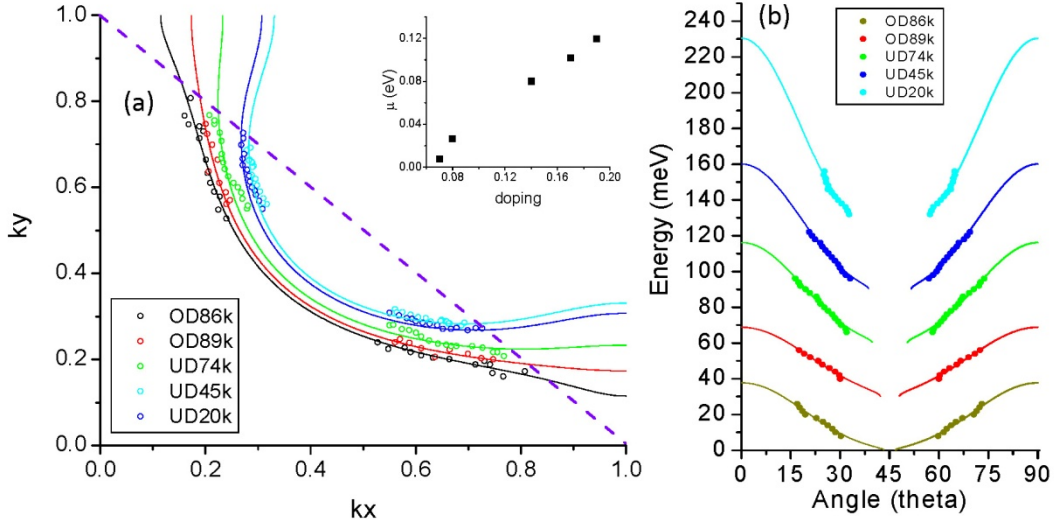


Figure 3-5: (a) The open circles show the k -space origin of the QPI vectors, plotted in a $\frac{1}{4}$ of the brillouin zone. The lines represent a fit to Normans parameterization of the band structure. The dashed line represents the AF-zone boundary. This is where the majority of q-vectors fade out and are replaced by a non-dispersive ‘checkerboard’ q-vector pattern. The insert shows the chemical potential scaling with doping. (b) shows the energy fit to a d-wave gap with a higher harmonic term.

Using this line as a boundary between two distinct regions allows us to make the following ansatz; that the lower energy region acts like a d-wave BCS superconductor, while the higher energy region does not contribute to the bulk superconducting properties and represents some sort of local state. It is important to point out, that we make the fewest possible claims as to the nature of the higher region, and its effect on the superconductivity. It would be very easy to get carried away and use loaded terms to describe what we see, however we attempt to just stick with the facts, without embellishing our claims. However that said, we can use this ansatz to not only fit the QPI data, but also the LDOS data with consistent parameters and we can put these parameterizations to good use by calculating bulk properties of our material, showing that we have indeed captured the critical phenomena involved, at least to first order. This will enable us to map out our electronic structure not just as a function of doping, but as a

function of anything we can vary, giving us a powerful tool in understanding what exactly is happening. In the next section we go into detail of this process for our current data sets.

Addendum: Some notes on band structure effects

Before I continue on I would like to point out some observations that play an important role in our understanding of the ratio map, and the band structure in general. The exact reason for why the signal to noise is increased when studying the ratio map has been ascribed to the canceling out of matrix elements⁵, or a direct measure of the superconducting angle⁸, however I will show that there is an innate difference simply from differences between the negative and positive dispersions as calculated from the spectral density of states for a d-wave superconductor. While this may be a minor effect, it should be kept in mind when one is discussing differences between ratio maps and unprocessed data, and what conclusions are drawn from them.

For my model, I use a spectral density of states $a(k,\omega)$, that is extracted from UD74K data. In this demonstration the $a(k,\omega)$ that I use is that for a d-wave BCS coupled with a Norman type band structure. This is the most basic model which allow me to calculate a realistic $a(k,\omega)$, and for this discussion it is sufficient to show the differences between positive and negative energies due to simply the electronic structure.

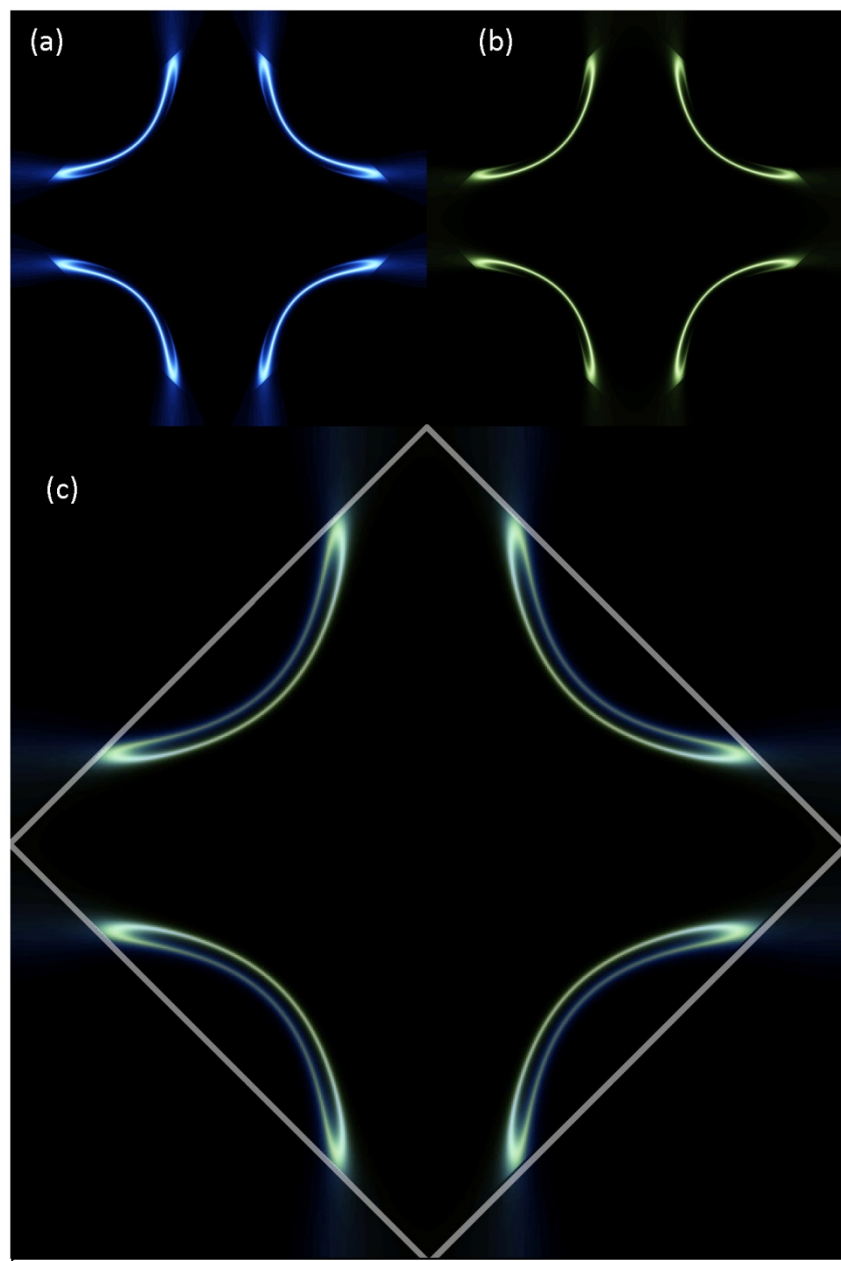


Figure 3-6: Calculated 34meV $a(k,\omega)$ for the UD 74K sample. The blue data in (a) is the positive layer, and the green (b) is the negative layer. The AF-zone cutoff is represented by the loss in intensity along the diagonal line (shown in white in c). This illustrates that the weight in the negative states is shifted from the positive cases.

In figure 6 we show the $a(k,\omega)$ or the spectral density of states for both the positive and negative energies. This represents where the states sit in k -space and energy space. The line where intensity is diminished represents the AF zone boundary and is included simply for illustration. Here we can see while the initial states reaching the AF zone boundary is the banana tip, which is symmetric about zero energy, the states that rest in the arc are clearly asymmetric and result in a higher q -vector connecting the impact points of the negative side, then the one connecting the points of the positive side. In 6c I show the two energies overlaid, showing the green (negative) on the inside track, and the blue (positive) on the outside. There is a clear difference between the two, and this may result in all or some of the differences between the positive and negative layers observed.

We can simulate the QPI pattern by looking at the Joint Density of States (JDOS)⁹ which can be calculated by taking out $a(k,\omega)$ and looking at its autocorrelation. This shows a marked difference between the two QPI patterns 7a and 7b. However the majority of this difference seems to occur in the arced regions of the QPI which we do not observe for the majority of samples. We can attempt highlight this difference by overlaying the two images, and indeed looking at the diagonal direction, one can see a marked difference in q_1 . This should be important not only in the dispersive regime, but also above the QPI termination (since the QPI terminates with two different q vectors). I can clarify the difference by looking at the subtraction of the negative layer by the positive one. This is presented in 7d, where black or grey areas represent where the positive QPI pattern is larger than the negative, and white or light orange represent where the negative is stronger. Here we can see several points where there is a marked difference, most striking q_1 and q_7 both of which we should be able to easily resolve in the data.

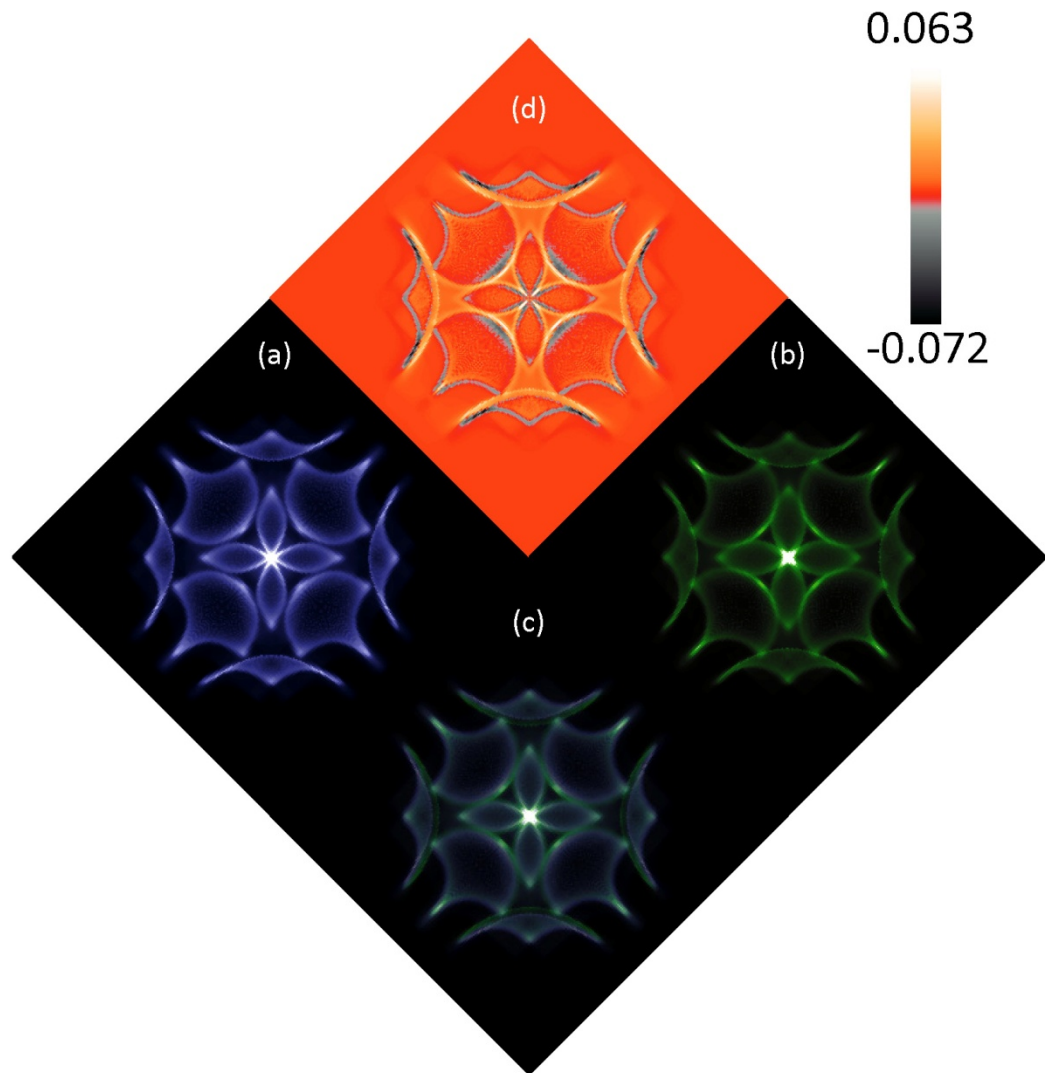


Figure 3-7: (a) autocorrelation of figure 3(a), showing the JDOS for +34meV. Figure 3-3(b) autocorrelation of figure 3(b) showing the JDOS -34meV. Notice the marked difference in the arc, and the long wavelength vectors from their positive counterparts. (c) Shows the overlay of the positive and negative JDOS patterns, highlighting the differences between (a), and (b). (d) Is the subtraction of the negative layer showing in grey regions where the positive pattern is stronger, and in orange-white, where the negative pattern is more intense.

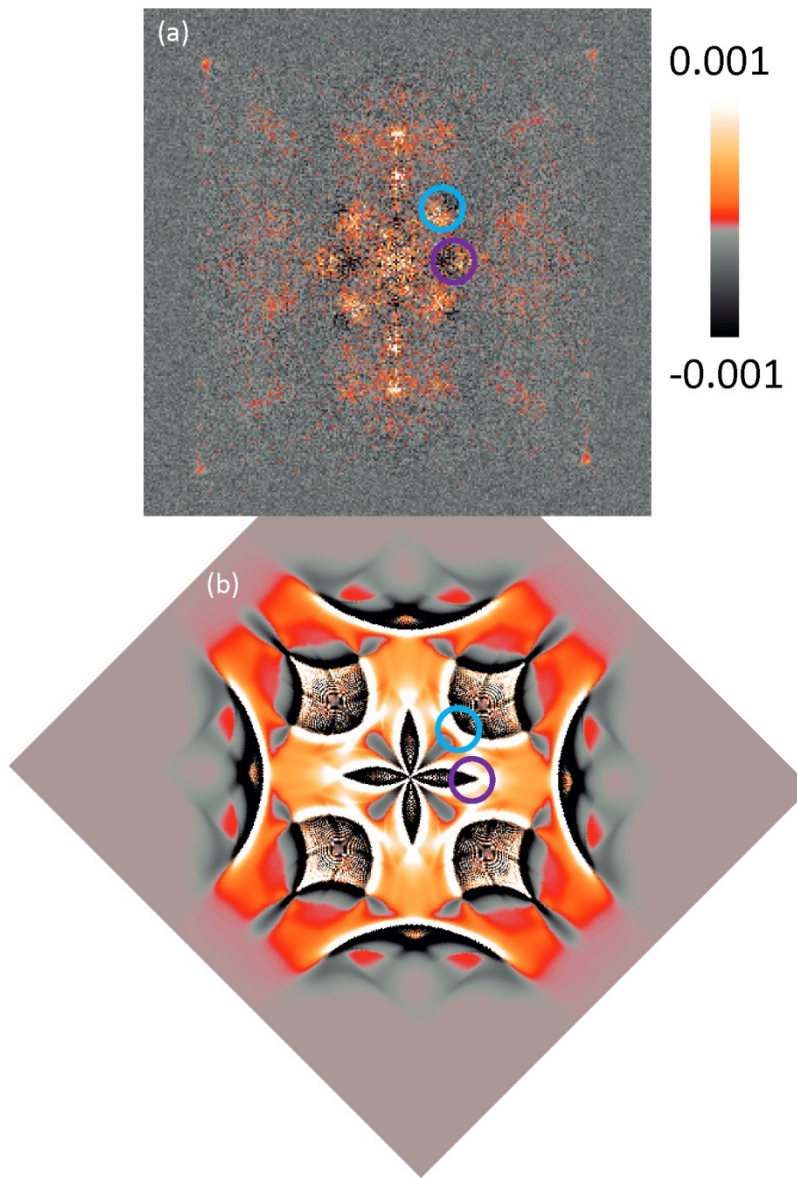


Figure 3-8: (a) The negative FFT of the 14meV layer minus the FFT of the positive 14meV layer. Black regions are places where the positive side is larger, white, orange, negative. (b) JDOS result for the 14meV layer, while showing a more complex pattern, it does mimic, the white then the black for q_1 (45 degrees first bright from center, marked with the blue) does show the alternation from white to dark. As well as q_7 (horizontal closest one to center, marked with the purple circle) alternates from black to white. This illustrates the band structure effects on the differing positions of certain q -vectors.

Indeed in figure 8 I take the difference of the 14meV FFT layer. Here we can see clearly for the high intensity q-vectors (q_1 and q_5) that there is a marked difference between the positive and negative q-vectors. In fact we can use our $a(k,\omega)$ and show that this is exactly what one would expect given a superconducting d-wave band structure. I have highlighted the q_1 and q_5 spots since the pattern is quite complex.

While this may play a minor role in the analysis of the ratio maps and for the most part a model $a(k,\omega)$ can be compared to the QPI pattern quite successfully, there are differences that will arise. These differences have to be kept in mind when making conclusions based off the analysis of these ratio maps, especially since it is far too easy to throw small effects into the “matrix element” bin and ignore them, even if they are actually the result of the underlying physical processes at work.

REFERENCES

-
- ¹ Brodde, A., Tosch, St., Neddermeyer, H., Journal of Microscopy 152, 441 (1998)
- ² Hoffman, J.E., McElroy, K., Lee, D.-H., Lang, K.M., Eisaki, H., Uchida, S., Davis, J.C. Science, 297 1148 (2002)
- ³ McElroy, K., Lee, D.-H., Hoffman, J.E., Lang, K.M., Lee, J. Hudson, E.W., Eisakim H., Uchida, S., Davis, J.C. Phys. Rev. Lett. 94, 197005 (2005)
- ⁴ McElroy, K., Simmonds, R.W., Hoffman, J.E., Lee, D.-H., Orenstein, J., Eisakim, H., Uchida, S., Davis, J.C. Nature, 422, 592, (2003)
- ⁵ Hanaguri, T., Kohsaka, Y., Davis, J.C., Lupien, C., Yamada, I., Azuma, M., Takano, M., Ohishi, K., Ono, M., Takagi, H. Nature Physics 3, 865 (2007)
- ⁶ Wang Q.-H., Lee D.-H. Phys. Rev. B 67, 020511 (2003)
- ⁷ Kohsaka, Y. Taylor, C. Wahl, P. Schmidt, A., Lee, Jihnhwan, Fujita, K., Alldredge, J.W., Lee, Jinho, McElroy, K. Eisaki, H., Uschida, S. Lee, D.-H., Davis, J.C. Nature submitted
- ⁸ Fujita, K., Grigorenko, I., Lee, J., Wang, M., Zhu, Jian Xin, Davis, J.C., Eisaki, H., Uchida, S., Balatsky, A.V. arXiv:0709.0632v1 (2007)
- ⁹ McElroy, K., Gweon, G.-H., Zhou, S. Y., Graf, J., Uchida, S., Eisaki, H., Takagi, H., Sasagawa,T., Lee, D.-H., Lanzara, A. Phys. Rev. Lett. 96, 067005 (2006)

CHAPTER 4

Predictive Model of Electronic Structure of High-Tc Superconductors Derived from Tunneling Spectroscopy

Introduction

While our previous LDOS model has been very successful, we have seen in chapter 3 that it does take into account the termination of the low energy coherent states. This, we hypothesis, shows up as the kink phenomena in real space at lower dopings (bigger D1s). SO what we need is some why to include this energy scale in our LDOS, and to hopefully do so in a simple and intuitive way. We would also like to be able to describe the QPI data within the same model giving us a much more general description that can be applied to more complex problems (nature of scattering). Here we overcome these problems, and starting with a generalized k-space model we develop a cohesive description of the electronic states that describes all of these phenomena. We start out with a very robust, if not computationally intensive model. For the moment this will not be a problem, although certain tradeoffs and ticks will have to be played when we come to the attempt to generalize our routines to allow fitting N spectra, where N is greater than five. This is covered in appendixes B,C.

To start we need to closely examine our average LDOS as a function of doping. These are shown in figure 4-1. Here we see the spectra normalized at high energy for median gap averaged LDOS's spawning the range from $p=0.07-0.019$ (UD20K-OD86K). As we move out in energy, we see both the suppression of the higher energy gap structure (D1), as well as the evolution of the kink structure as the higher energy scale becomes larger and larger. Looking at the heavily underdoped curves (UD45K, UD20K), we see that this effectively divides the spectra into two sections. One contains the high energy peak, and the other consists of a little dip and

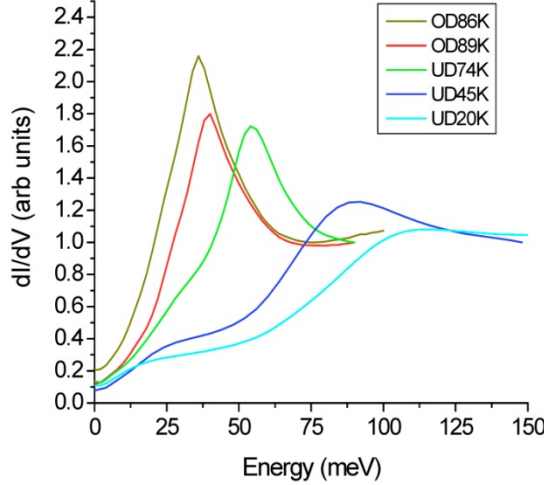


Figure 4-1: Median gap averaged spectra's across several dopings. These are normalized to the spectral value at high energy. The highest is the OD86K (yellow) then OD89K (red), UD74K (green), UD45K (blue), and UD20K teal.

then a plateau. We have seen in the past that there are several unique phenomena associated with the higher energy states, namely ECG and Gap disorder, while the low energy states contain the coherent QPI. The goal of our research is to understand this divide, and to quantitatively understand it in a way that will eventually lead to mapping out its spatial variation. Our model, will also serve as an effective theory if we can make use the electronic states to map out bulk properties of the system. While we may not know the pairing mechanism, we can determine the properties of the system as a parameterized function of doping.

The QPI data ends around 30meV for all of our under doped data. This is roughly the energy scale we have seen from our initial crude kink analysis. We also have seen that the QPI data requires the addition of a higher harmonic term in order to be accurately described, however it is emphatically clear from our initial fitting that the higher energy LDOS states do not. Therefore we must synthesis these two regions. One needs a higher harmonic term, one does not. We have a transition structure in k -space and real space that we need to model. These two observations are what has led us to develop our theory.

These two regions must merge at higher dopings. When we go to the extreme over doped side, we have a system that can be quite nicely described with d-wave BCS, therefore we would expect that at extreme over doping we end up with a d-wave BCS model. We have found in the past that the spectra and in fact the properties of our material vary smoothly with T_c , and in fact the spectra evolve in a continuous fashion. Therefore our model must smoothly evolve from a d-wave BCS consistent model, to one of two separate energy scales, and we expect it to do so smoothly and continuously. Hence starting with a d-wave BCS model and evolving it with doping to match our data is a logical place to begin.

Model

Here we begin with the spectral density function, $a(k,\omega)$ for a d-wave BCS system. It is modified to include our energy dependant lifetime that we have already demonstrated to be necessary and physically relevant to the description of our data. The $a(k,\omega)$ we use is of the standard form

$$A(\vec{k}, \omega) = \frac{\text{Im} \Sigma(\vec{k}, \omega)}{(\omega - \varepsilon(\vec{k}) - \text{Re} \Sigma(\vec{k}, \omega))^2 + \text{Im} \Sigma(\vec{k}, \omega)^2}$$

With the self energy described by

$$\Sigma(\vec{k}, \omega) = -i\Gamma + \frac{\Delta_k^2}{\omega + \varepsilon(\vec{k}) + i\Gamma}$$

Our lifetime term is the familiar term of

$$\Gamma = \Gamma_1 + \Gamma_2(k)$$

$$\Gamma_2(k) = \alpha \Delta(k)$$

Now we need to modify this to include two separate energy scales. Up to an energy, say Δ_0 , there exists a coherent state, with a d-wave BCS like structure with the inclusion of a higher harmonic gap term and above that energy a d-wave like structure with no harmonic contribution lives. The simplest thing we can do is to splice the two together. This leads to a d-wave BCS structure with a higher harmonic term up to Δ_0 and then an energy jump to Δ_{00} with a d-wave like structure up through the gap energy Δ_1 . It is important to note that the overall gap energy Δ_1 is the same in both regions, as well as the lifetime term. It is only the higher harmonic term coupled with a cutoff energy that causes a jump in energy and segments our structure into two separate regions (three really). The gap formulation in this model, Δ_k , is $\Delta_1 * B * \cos(2\theta) + (1 - B) * \Delta_1 * \cos(6\theta)$. Here we apply $B=1.0$ above Δ_0 and B as a fit parameter below. In this way the low energy states, have all the necessary freedoms to be fit, and the higher energy states could be fit using basically the same model as before (chapter 2). Hence this model represents an addition to our previous one, and not a contradiction.

This model is illustrated in figure 4-2. In 4-2(a) we show a rather complicated diagram. The base of it is the Fermi surface in k -space for a typical sample. This is in the k_x, k_y plane. The z axis is the gap magnitude energy. The red line represents a d-wave BCS gap. This is incapable of fitting our QPI data, as it cannot be made to pass through the data points. The lower black curve and its continuation in yellow represent's this higher harmonic gap function. Now in our proposed model we have to combine the two sections. This is represented by the black curve which contains the jump from Δ_0 to Δ_{00} . We also show our proposed two components. The light teal section represents the QPI coherent momentum space range, while the darker teal would be where the ECG or localized states would live. If we take this gap structure and compute the LDOS we get 4-2(b) where the solid black line represents the LDOS,

while he dotted line would be that of a d-wave BCS. We can see here that clearly this allows us to reproduce the kink structure. It also divides the energy range into three regions, not just the two in momentum space. We postulate that the region in between Δ_0 and Δ_{00} is where the checkerboard pattern exists and is a state separate from the ECG. The jump therefore represents a set of points in k-space that do not disperse and contain the transition from states well defined in momentum space to those well defined in real. In 4-2(c) we have an angle projection of our model gap structure.

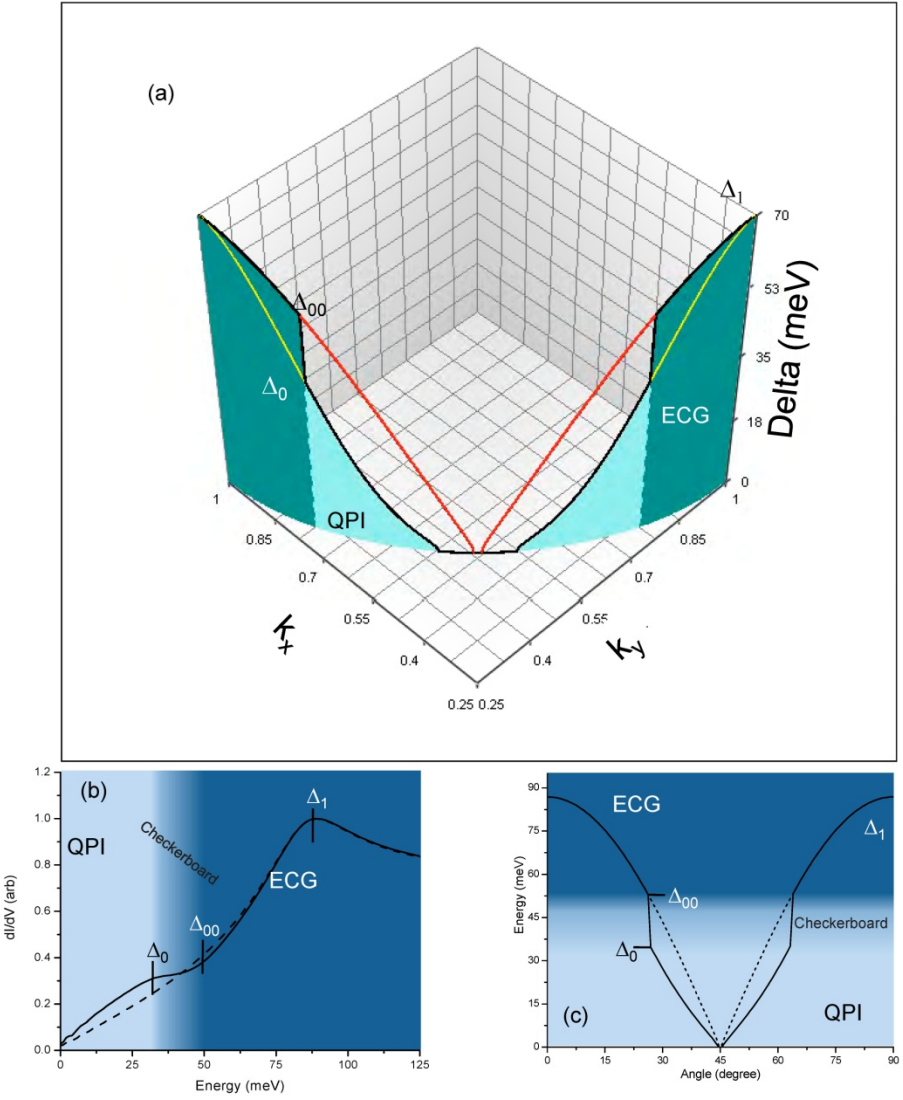


Figure 4-2: (a) schematic figure of our model in k-space, the red line shows a normal d-wave BCS gap along the Fermi surface. This is modified by our inclusion of a higher harmonic gap term at low energies, below Δ_0 , this is shown as the lower black curve, that transitions into the yellow curve if continued to higher energies. The combination of these two curves results in the black curve with a discontinuity in it. This separates k-space into two distinct regions, the lower light teal region where there are coherent excitations of the quasiparticles, and the higher darker teal region where the ECG structure is present. These are separated with a non-dispersive checkerboard pattern that exists in the discontinuity. (b) LDOS generated using the above gap, showing the different regions. (c) gap function as a function of angle in k-space as opposed to along the Fermi surface. Showing the same picture as (a) and (b).

QPI/LDOS Fits

Now that we have a model, the question is “can we fit our QPI data with it?” The answer as shown in figure 4-3 is yes. Here we fit the QPI points, by calculating our model $a(k,\omega)$ in k -space, and extracting the peak locations as a function of energy, since the strongest LDOS states should be the source of the QPI vectors. Since we are only fitting the low energy states, we are in effect just using a d-wave BCS model with a higher harmonic gap term. However our model produces a sharp disjointed dispersion, which can in fact be seen in the QPI data. As termination is reached we have a series of energies that should not have any dispersive q -vectors. These should end when the energy reaches Δ_{00} . This is exactly the case as we will see (see addendum). We use a levenberg-marquardt fitting algorithm to fit the data, similar to our previous fits. However our function is not as well-defined in terms of its partial derivatives as we would like. Therefore we must also use a fine grid of starting points, in order to a large section of phase space in order to get accurate fits which converge. This acts as a time multiplier for our fits, and can lead to a convergence time of several hours.

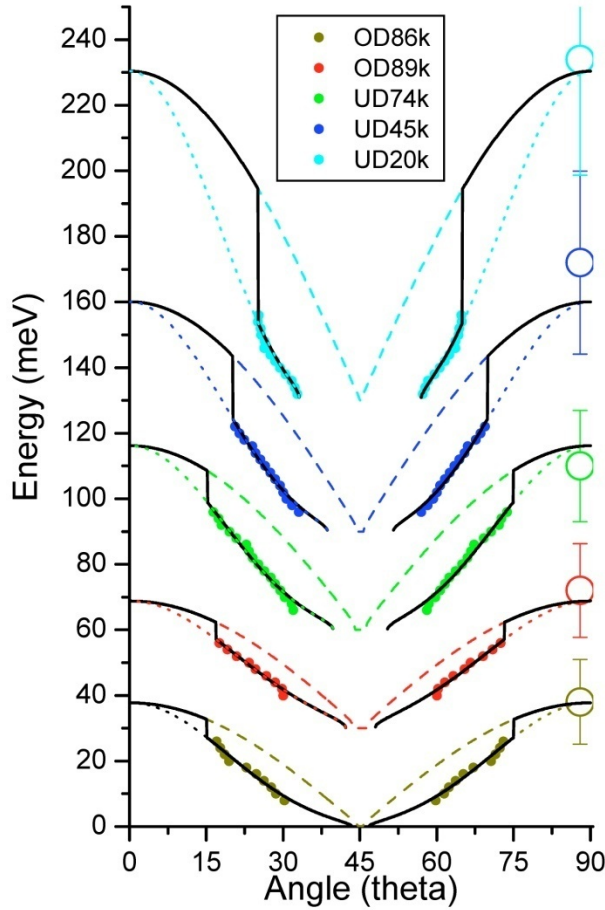


Figure 4-3: QPI extracted gap fits. The filled circles are the data for each particular doping, offset for clarity. The solid black lines are out fits, while the dashed lines are the fits for a d-wave BCS with no higher harmonic term. The dotted lines are the continuation of the fits for the d-wave BCS with a higher harmonic term. The open circles represent the spatial $\Delta_{\text{p-p}}$, with the error bars representing the $1-\sigma$ distribution.

p	T_c	Δ_1	Γ_1	α	μ	Δ_{00}	B	Δ_0
0.19	OD86k	37.8	1.1	0.08	0.119	32.7	0.83	27.2
0.17	OD89k	38.8	2.8	0.11	0.102	32.3	0.87	27.1
0.14	UD74k	56.2	3.2	0.12	0.080	48.5	0.81	38.2
0.08	UD45k	70.1	2.7	0.15	0.026	53.5	0.73	35.5
0.07	UD20k	100.6	1.02	0.14	0.007	64.4	0.73	23.5

Table 4-1: Fitting parameters returned from our QPI fits.

However just fitting the QPI data is not enough, after all we have seen that that is in effect only half of our model. In order to show we really do have this two part function, we must fit the LDOS which contains energy information across all energies. We must do so with parameters similar if not the same as those from the QPI fits. Otherwise, our model would be a failure. The LDOS is generated by summing the $a(k,\omega)$ over all of k-space

$$N(\omega) = \int \frac{1}{2\pi} A(k, \omega) dk$$

and using the result in a levenberg-marquardt fitting algorithm. Once again we must use a fine grid of starting parameters in order to insure and accurate fit. The results are displayed in figure 4-4. If we look at the return values of our QPI and LDOS fits in tables 4-1 and 4-2, we can see very close agreement between the two, and in fact we can take their average, and see how well this compares to the data. These averages are displayed in table three, and the generated QPI dispersion and LDOS curves are shown in figures 4-5 and 4-6. These agree very well with our measured data.

We have in effect completely described the zero temperature electronic states of the system within the window provided by SI-STM. This is in it of itself a remarkable achievement, and one which has many implications. Firstly when searching for a solution to the general problem of high Tc we must confine ourselves to solutions that result in a spectral density of states similar to the one we have now. This is an important constant on theorists and one that they should be able to easily tackle (and have already begun). We also have provided the bases for further calculation, once we have knowledge of the LDOS, and the exact number of states as a function of doping, we can calculate bulk properties of everything from heat capacity,

to superfluid density. This provides not only a check of our model, but also in a sense represents a description of the system.

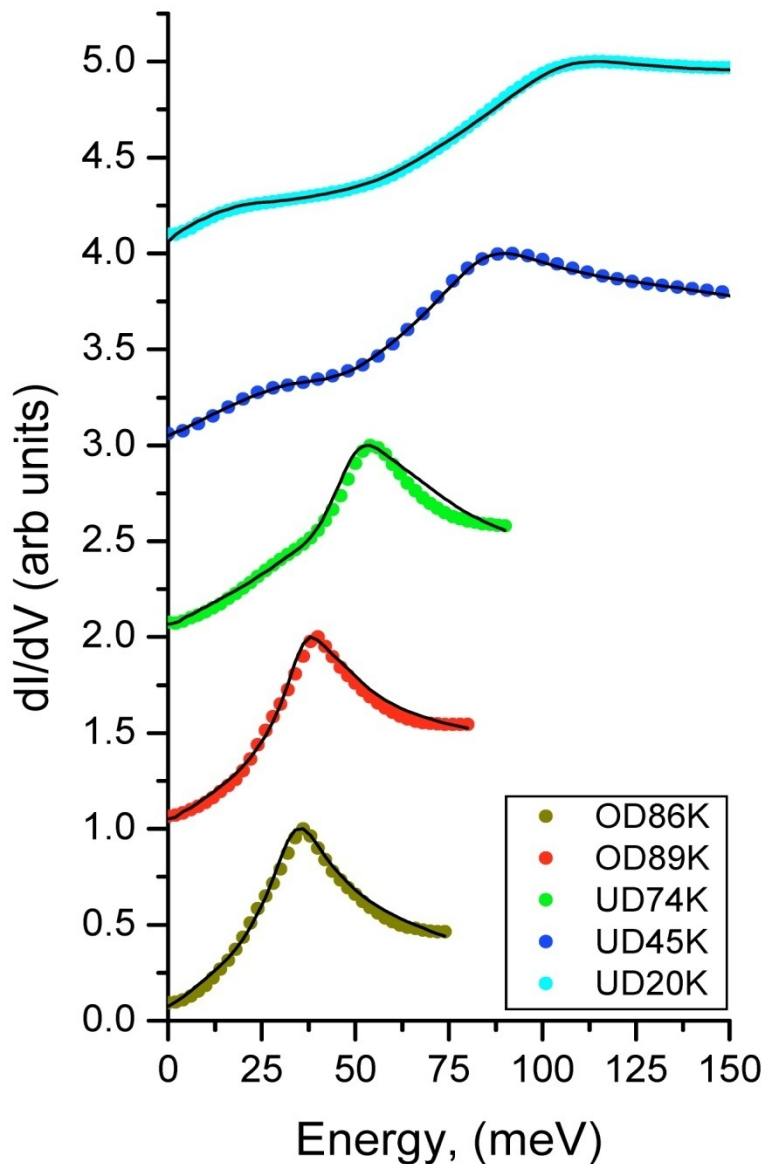


Figure 4-4: Median gap averaged data for our 5 samples as well as their fits. The data are represented by the filled circles, which are offset for clarity. The solid black line represents our fits.

p	T_c	Δ_1	Γ_1	α	slope	μ	Δ_{00}	B	Δ_0
0.19	OD86k	34.0	1.33	0.17	-1.6E-5	0.119	33.3	0.90	32.0
0.17	OD89k	36.7	1.13	0.11	-4.2E-6	0.102	33.4	0.96	32.5
0.14	UD74k	51.3	1.60	0.11	-8.9E-6	0.080	40.5	0.92	35.6
0.08	UD45k	86.7	1.66	0.13	2.6E-6	0.026	52.0	0.88	36.0
0.07	UD20k	108.0	0.77	0.15	1.3E-5	0.007	61.1	0.77	22.9

Table 4-2: LDOS fitting parameters, compare favorably to the QPI fits.

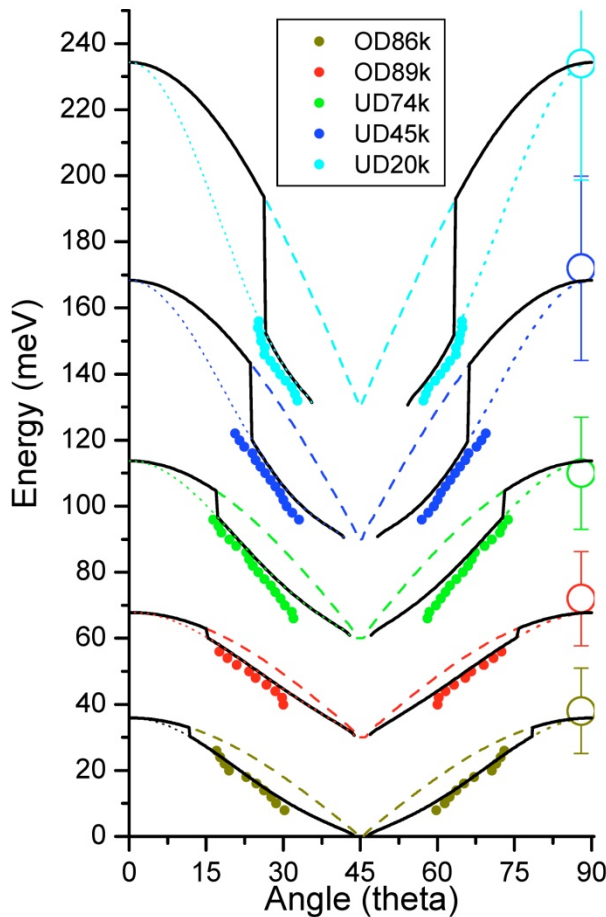


Figure 4-5: QPI data for our data sets, laid on top of our average fit data. Solid black line shows our fits, while the dashed line represents a single d-wave gap and the dotted line a d-wave gap with a higher harmonic term.

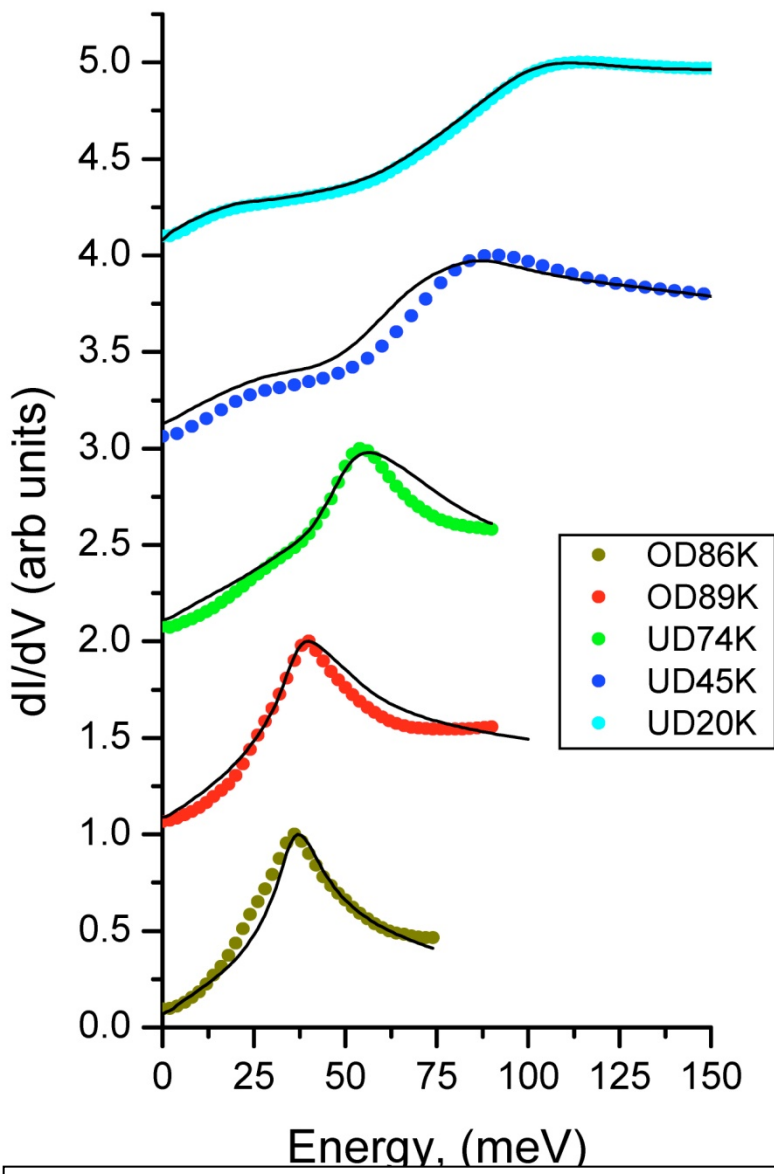


Figure 4-6: Median gap averaged data, with corresponding average fit overlays. Offset for clarity

p	T_c	Δ_1	Γ_1	α	μ	Δ_{00}	B	Δ_0
0.19	OD86k	35.9	1.22	0.125	0.119	33.0	0.87	30.2
0.17	OD89k	37.8	1.97	0.11	0.102	32.9	0.92	30.3
0.14	UD74k	53.75	2.4	0.12	0.080	44.5	0.87	36.9
0.08	UD45k	78.4	2.18	0.14	0.026	52.8	0.81	30.2
0.07	UD20k	104.3	0.90	0.15	0.007	62.8	0.75	22.7

Table 4-3: The average fitting parameters for all our data sets.
Averaged between QPI and LDOS fitting.

Addendum: Physical Checks of Parameters

In order to for our model to make physical sense, we need to make sure that our parameterization is constant and associated with observables besides the QPI and the LDOS. We have already made the connection of Δ_0 with the QPI termination energy, and while this is true, the QPI termination energy is a bit of a nebulous quantity, due to the fading out of the signal that is the nature of the termination. Here in figure 4-7 we look at the variance of the ratio map as a function of percent of the Δ_1 value. This allows us to look at the level of local variation as we span our gap. This we postulate should allow us to extract different phenomena, by looking at the level of disorder or structure at each energy. This can be coupled with an FFT to allow us to readily identify the phases present. Indeed starting at low energies we see a massive spike due to QPI, that fades off and stops. This happens at Δ_0 , there is then a flattish decrease in the variance up until another point, Δ_{00} where the ECG + gap disorder sets in¹. This has a maximum at Δ_1 . We can map the Δ_{00} point or the minima in the variance across doping, and we can plot the values with those returned by our fits and we indeed see a very strong correlation between the two. If we extract the energy layers associated with the three energy values, along with a reprehensive QPI energy, we can see their difference in real and q-space. This shows us that we have intially a very strong varance asscoated with QPI that is replaced with the checkerboard at Δ_0 .

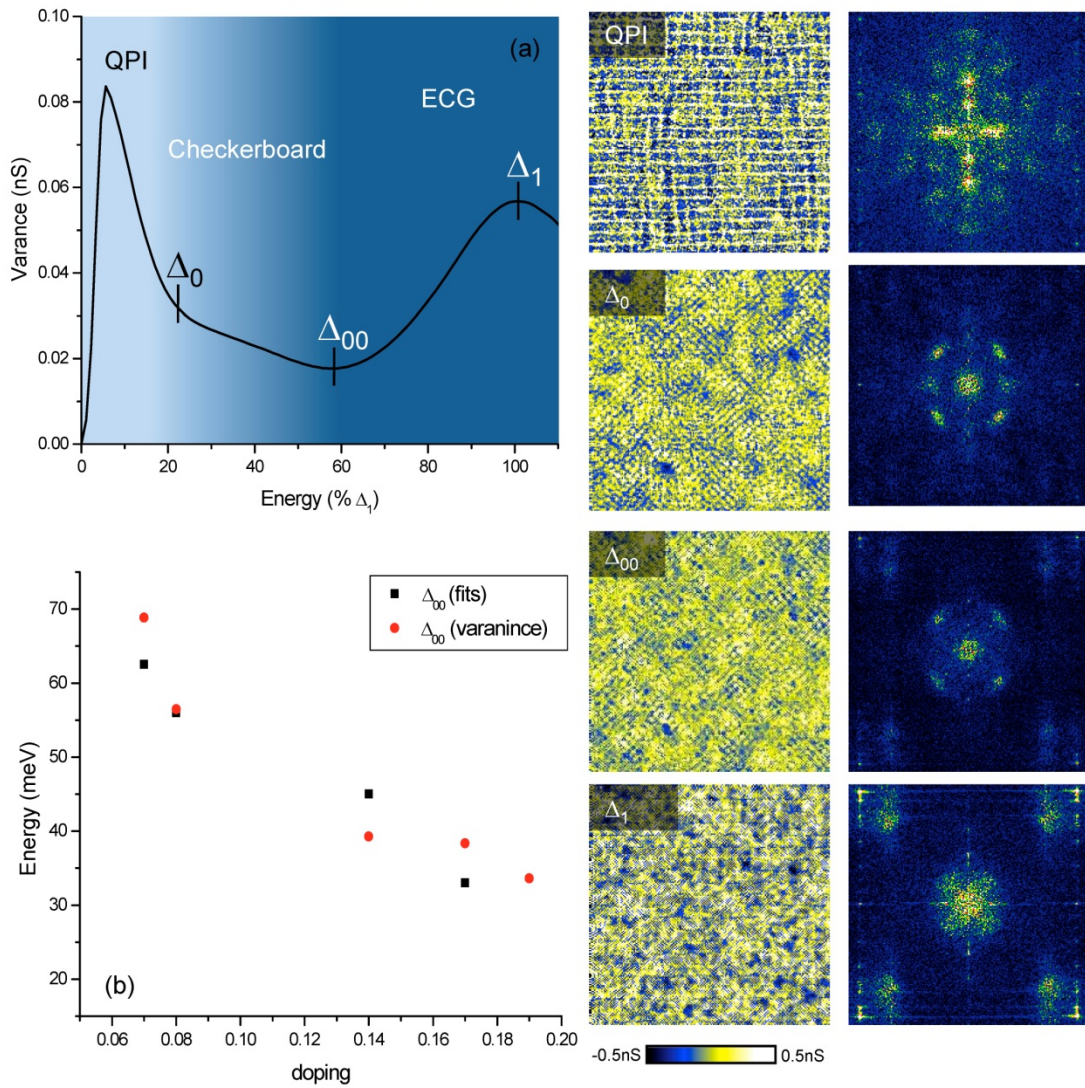


Figure 4-7: (a) a plot showing the variance as a function of energy normalized to Δ_1 . This shows clearly the three separate regions, based off the amount of fluctuations over the field of view. (b) A plot of the detection in the minimum of the variance (defined as Δ_{00}) vs the value for Δ_{00} obtained from our fits. The first column shows the real space patterns in the ratio map. This displays the marked transition between QPI and the checkerboard at Δ_0 then the transition between the checkerboard and the ECG at Δ_{00} . This is backed up by the FFT in the left most column that shows the QPI, then checkerboard and finally the ECG.

This pattern becomes weaker (less variance) till it reaches Δ_{00} where we see the transition to an ECG type pattern. There is no reason to suspect that these transition happen simultaneously across the sample, or even the field of view. This could describe the phenomena smoothly fading into one another.

We can enhance the S/N by integrating over the two regions, from Δ_0 - Δ_{00} and from Δ_{00} - Δ_1 to highlight the different phases in each region. This is done in figure 4-8 for both UD20K data and UD45K data, with two different fields of view. In the UD20K data in the Δ_0 - Δ_{00} regime we see a very large scale pattern that is the checkerboard 4-8(a), and is backed up by the FFT 4-8(b). There is a marked shift from this to the Δ_{00} - Δ_1 regime in (c) and FFT (d). This is marked with a much smaller length scale ordering that is associated with the ECG pattern. We can see this by taking a line cut along the π, π direction for both integrations and comparing. In fact we see the complete disappearance of the $\frac{1}{4}$ peak associated with the checkerboard pattern. This analysis can be repeated for UD45K as well, and we see similar results in the rest of figure 4-8.

Check of our fits is whether we have captured the termination or Δ_0 correctly. If we have we should see that this termination point lies on the AF-zone boundary, as reported². From our fits we can calculate the termination points k-space coordinates. This is done in figure 4-9 for both the QPI results (upper left) and the LDOS results (lower right). We can see that they all occur close to the AF-zone boundary; although particularly in the LDOS there is some scatter. But we expect that light could be shed on this by looking at fitting a vast array of spectra, and not just one, to see if there is a disorder effect on this transition.

Therefore our parameterization captures three phases and their termination points successfully. This represents the first time that they have been identified

concurrently and their energy dependence has been mapped as a function of doping. It is an important test of our model, if we believe that it describes the electronic states completely.

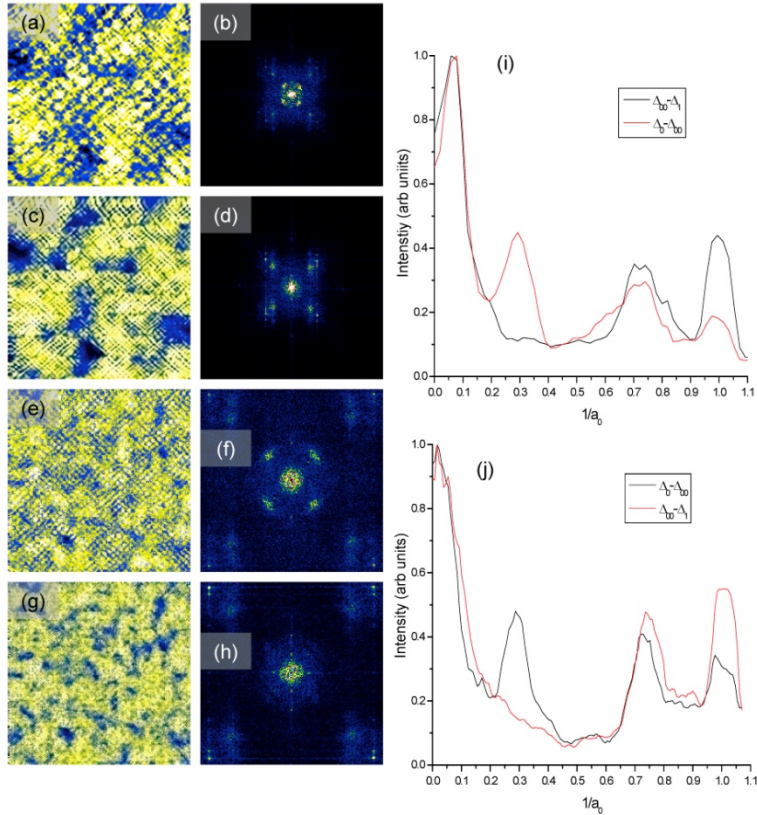


Figure 4-8: Integrated ratio map intensities between $\Delta_0 - \Delta_{00}$ (a) for UD20K 20nm^2 field of view ($26\text{meV}-56\text{meV}$), (e) for UD45K 45nm^2 field of view ($36\text{meV}-52\text{meV}$), showing the checkerboard pattern. This is contrasted with the integrated ratio map from $\Delta_{00} - \Delta_1$ shown in (c) ($60\text{meV}-108\text{meV}$) and (g) ($56\text{meV}-84\text{meV}$) where we clearly see a change in the scale of the ordering. These are also seen in a shift in the FFT weights, from the $\frac{1}{4}$ peaks to the $\frac{3}{4}$'s peak (b to d and f to h). By extracting line cuts along the Pi, Pi direction we see a complete suppression of the $\frac{1}{4}$ " structure seen in the checkerboard pattern between $\Delta_0 - \Delta_{00}$.

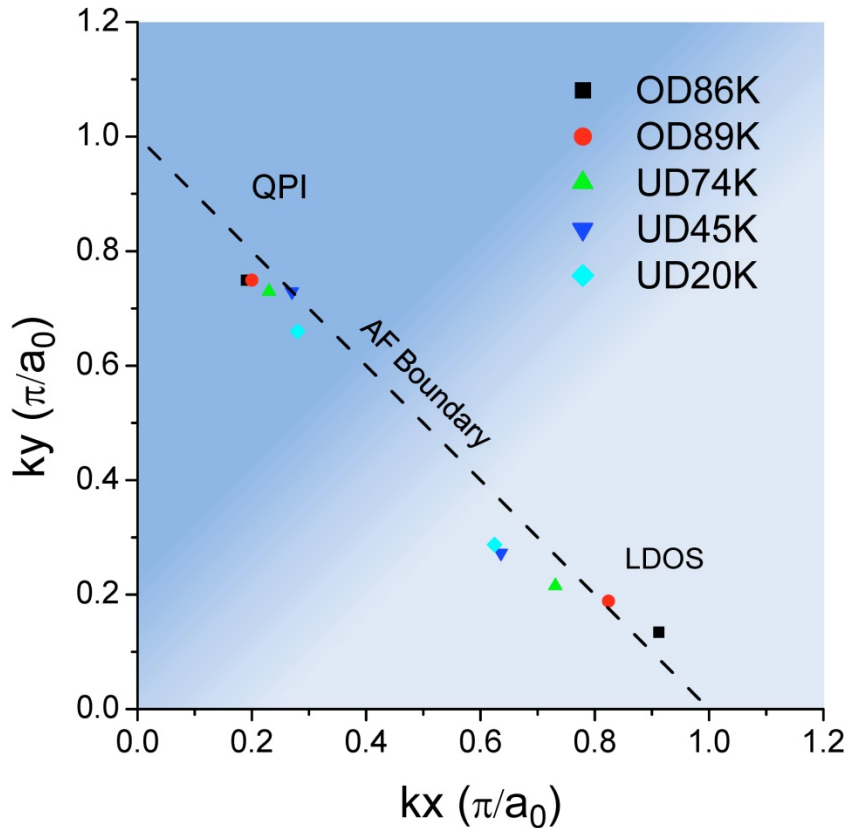


Figure 9: Results from fits, showing where the termination point lies in k -space. This is down in the upper left quadrant for the QPI fits, and in the lower right for the LDOS fits. These show the termination happening at the AF-zone boundary for all our data, although there is scatter.

REFERENCES

¹ Kohsaka, Y., Taylor, C., Fujita, K., Schmidt, A., Lupien, C., Hanaguri, T., Azuma, M., Takano, M., Eisaki, H., Takagi, H., Uchida, S., Davis, J.C. An Intrinsic Bond-Centered Electronic Glass with Unidirectional Domains in Underdoped Cuprates Science 315, 1380 (2007)

² Kohsaka, Y. Taylor, C. Wahl, P. Schmidt, A., Lee, Jihnhwan, Fujita, K., Alldredge, J.W., Lee, Jinho, Mcelroy, K. Eiaski, H., Uschida, S. Lee, D.-H., Davis, J.C. Nature submitted (2008)

CHAPTER 5

Bulk Properties from $a(k,\omega)$

Introduction

We now have an accurate description of the zero temperature electronic structure of Bi-2212 for a wide range of dopings. Based off other measurements (ARPES)¹, we can propose a model for the temperature dependence of our data. Here we propose that the low energy or coherent states close do the closing of the gap in this region as we approach Tc. This follows a d-wave BCS model for the gap closure with increasing temperature. Here for simplicity we assume that this happens at one temperature and is uniform across the sample. Once again we can appeal to the d-wave BCS like states in the over doped state as a starting point. However this is something which should be investigated with high resolution and accuracy in the future. For numerical calculations we have calculated the temperature dependence of the gap for a d-wave BCS and use a 9th order polynomial fit in order to simplify the calculation. We also add in thermal broadening effects, through a convolution with the derivative of the Fermi function. However we should note that the LDOS we simulate will not accurately reflect our data measured at temperature. This is because in the STM setup any temperature increase will also affect the Fermi distribution of the tip, which will cause the STM to measure a much broader distribution in fact $3.3 kT$ instead of just kT , something often times overlooked in the literature. An example of our proposed temperature trend is shown in 5-1(b). We can see slight thermal effects on the large gap structure as well as the filling in of the low energy states that is caused by the d-wave BCS like closing. This is consistent with point tunneling data where this is modeled as a jump in a constant scattering rate².

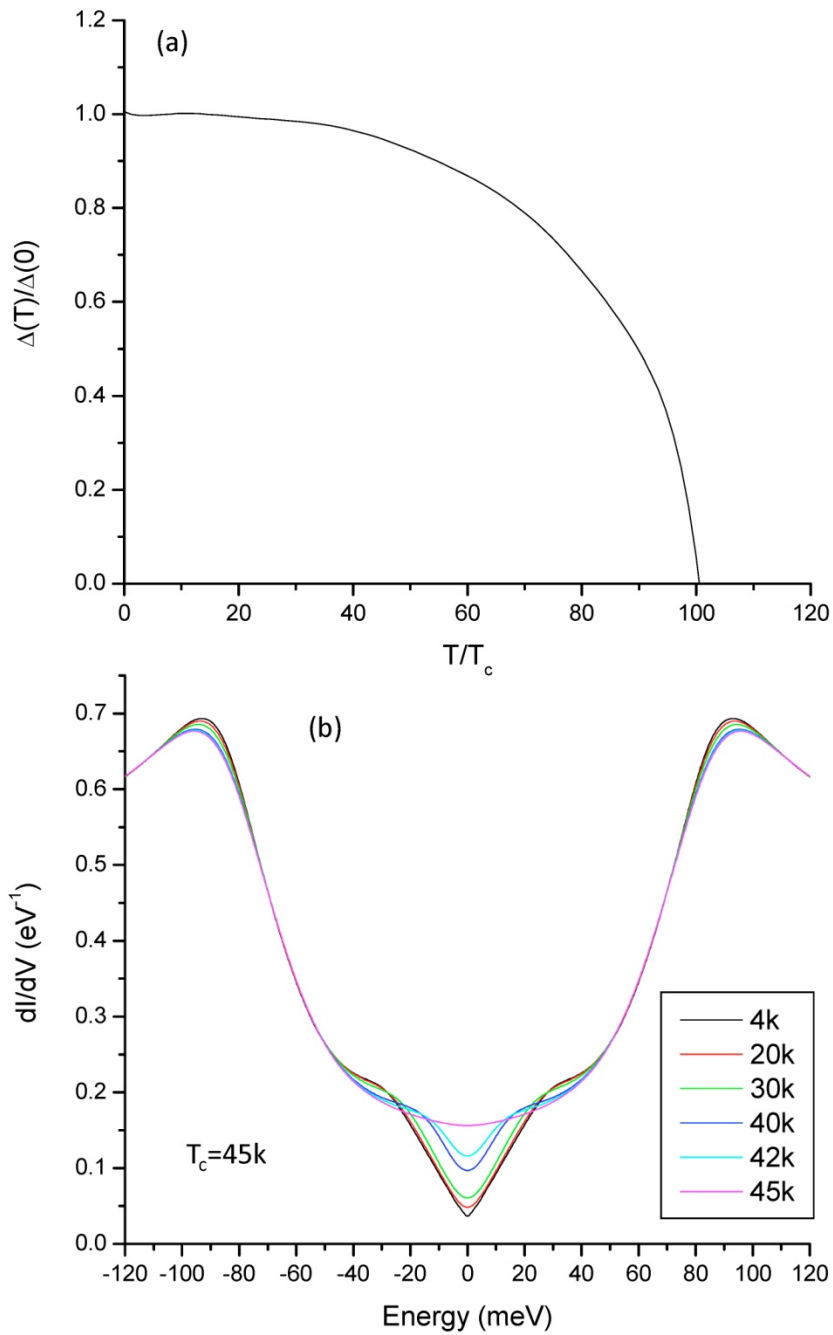


Figure 10: (a) a d-wave BCS gap dependence function used in these calculations. (b) Symmetrized gap for UD45K showing the structure and closure of the low energy states as a function of temperature. This represents LDOS and an actual STM measurement would show much more thermal broadening due to the tip temperature (3.3kT instead of kT).

Thermodynamics

Using this model we can calculate bulk thermodynamic properties, assuming non-interacting, or weakly interacting quasiparticle. This is consistent at least around optimal doped Bi-2212 where the effective mass is only thought to be around $2m_e$. Our formula for the calculation of the energy takes the form³ of

$$S = 2k_B \int_0^{\infty} (f(1-f) + \ln f(1-\ln f)) N(\omega) d\omega$$

We do this integral numerically so we must take into account our entire step sizes, as well as conversion factors to get from the equation to a real world unit.

First we have $dk=4.0*\pi^2/(xsize*ysize)$, $d\omega$ is set by our resolution. We then need to add in the $2k_B$, and then we need to make the leap from a single unit cell to a gram atom. This gives us Na , the number of atoms in a mol with a division by 60 the number of atoms in a unit cell to give us gats, since our $a(k,\omega)$ represents the states of one unit cell. So all together we have

$$\frac{4\pi^2}{xsize \times ysize} d\omega \times 2k_B \times \frac{Na}{60}$$

When calculating heat capacity we need to also divide by the temperature spacing after doing the numerical derivative.

In order to insure that we maintain a closed sample size, we keep the total number of particles constant by integrating $f(\omega)*N(\omega)$ at $4k$ and keeping this value constant as a function of temperature, although in practice this changes our calculation very little.

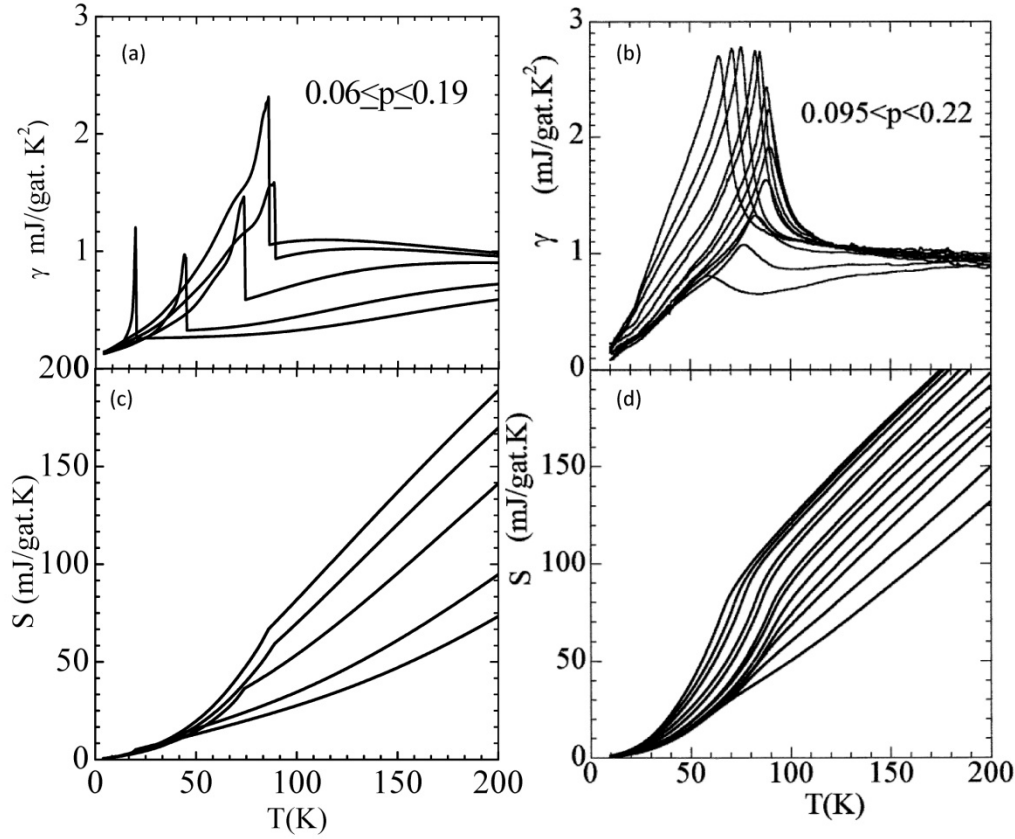


Figure 5-2: (a) heat capacities from our calculations. (b) data reported by Tallon and Loram⁴. (c) entropies from the same calculation, as well as data (d).

The results of this calculation are shown in figure 5-2(c). The derivative showing the heat capacity as a function of temperature is shown in 5-2(a). These can be compared quite favorably to data from Talon and Loram⁴ in 5-2(b)-(d). The biggest discrepancy we have is with the heat capacity jump, which is based on the exact rate of closure of the gap, as well as in our case the assumption of a uniform closing. This might not be true, and in fact closing rate could be easily influenced by localized states at higher energies which may act in some sense as a 0d superconductor⁵, or it is possible that there is a distribution in Transition temperatures⁶. This would not affect the entropy curves until one approached the transition temperature range and would round out the transition to something that could easily resemble the data. As we can see from the

entropy curves, our transitions are very sharp compared with the measured data and out heat capacity jumps at low doping are also too high.

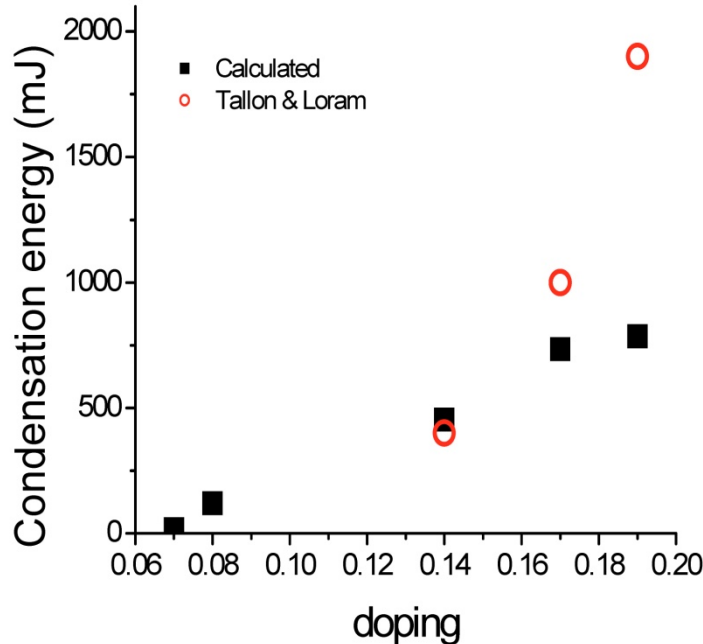


Figure 5-3: Condensation energy from our fits as a function of doping. Also plotted is Tallon and Lorams results. The deviation can be explained due to their lack of a model for the normal state, they admit this could give them an error by a factor of about 2.

We can use our entropy curves and our model to accurately extract the condensation energy. This is accomplished by calculating the electronic entropy for the superconductor as we have done already, and then calculating the entropy assuming the lower energy states were closed at zero temperature. By calculating the difference between the two curves we can calculate the condensation energy. When we do this, figure 5-3, we find that we come in a factor of two below Talon and Lorm's³. However this is most likely due to the fact that we have a complete model for our electronic states, and they have admitted that this could cause their estimation to be off by a factor of 2 or more⁷.

Magnetic Susceptibility

We use a similar non-interacting quasiparticle method to calculate the zero temperature magnetic susceptibility through³

$$\chi_s = -2\mu_B \int_0^\infty \frac{\partial f}{\partial E} N(\omega) d\omega$$

This contains no diamagnetism, and is simply the calculation for the pauli paramagnetism. However this does successfully reproduce the higher temperature features seen in the susceptibility. These features show the steady increase in the susceptibility with increasing temperature until a certain temperature where it levels out. This has been associated with the pseudogap temperature⁸, and indeed in our calculation this is the result of the separation in energy scales. As we go over doped, eventually the two energy scales merge and after that the magnetic susceptibility decreases with increasing temperature. Once again the magnetic susceptibility trends are constant with our model. The results are shown in figure 5-4, which show that we obtain roughly the same magnitude and trends.

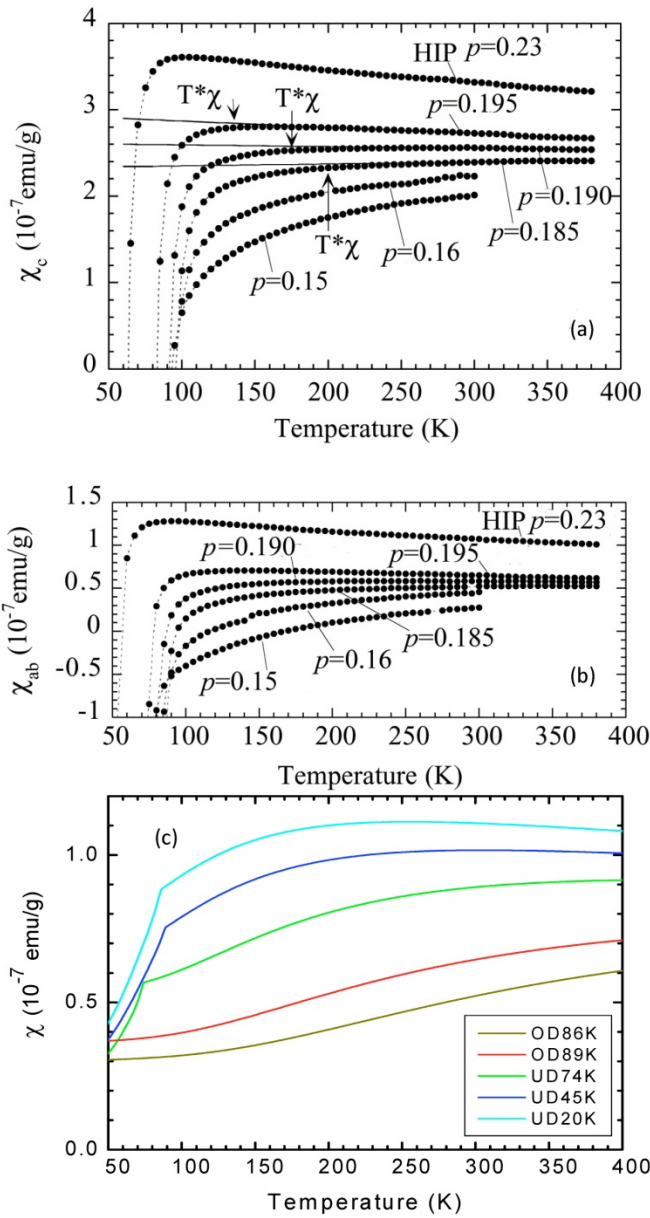


Figure 5-4: (a) the magnetic susceptibility of BI2212 of the c axis (perpendicular to the CuO planes, for a variety of doping. (b) same as (a) except for the direction, here it is the magnetic susceptibility of the planes. This shows the Onset of a superconducting meisner effect . (c) results from our model, showing a favorable comparison, although it is very clear that our superconducting transition is too sharp, and does not have any contribution from the superconducting state. However it does display similar high temperature behavior, although in our case the slope levels off as we approach optimal doping, not critical doping. This could be do to error in our doping data or theirs.

Super fluid Density

In order to calculate the super fluid density we need a more complicated model. This is to take into account subtle changes in interactions with doping, as well as the 2-D nature of our material. In BCS the zero temperature super fluid density was described³ by

$$\lambda_L = \left(\frac{4\pi \cdot ne^2}{mc^2} \right)^{-2}$$

Where n is the density of carriers in 3d. However for our material we must use the following equation⁹

$$\frac{1}{\lambda^2} = \frac{\mu_0 e^2 n}{4\pi\hbar^2} \sum_k \left[\left(\frac{\partial \varepsilon_k}{\partial k_x} \right)^2 \frac{\Delta_k^2}{E_k^2} - \frac{\partial \varepsilon_k}{\partial k_x} \frac{\partial \Delta_k}{\partial k_x} \frac{\Delta_k \varepsilon_k}{E_k^2} \right] \times \left[\frac{1}{E_k} - \frac{\partial}{\partial E_k} \right] \tanh\left(\frac{E_k}{2k_B T}\right)$$

where n is instead defined as the carrier density divided by the number of planes. This takes into account the suppression of the super fluid density as we approach the Mott-insulator state, as well as the incoherent tunneling between the CuO₂ planes and changes in the effective mass. However in order to take advantage of this formula we need to parameterize the important physical parameters for each doping as a function of doping. This enables us to take the derivatives in the equation, as well as provides an accurate description of the electronic states as a function of doping in our samples. These parameterizations are only meant to be taken in a phenomenological way and we don't claim that they have any significance besides providing a smooth parameterization. These fits are shown in figures 5-8, 5-9 and 5-10 as well as the functional form and the data. This allows us to calculate the super fluid density

displayed in figure 5-5. In figure 5-5 we display the measured penetration depths from two different publications (open circles) as well as the BCS limit (dotted blue line). Our calculation is displayed in green. In order for this calculation to work, we apply our ansatz about only the lower energy states condensing, and thus we consider the gap only bellow Δ_0 in this calculation. This stems from our observation that only states below that level are coherent and well defined in momentum space. We believe these are the only states that contribute to the superconducting condensate, and this follows from our calculation of the heat capacity and entropy. It goes without saying that this matches the data very closely.

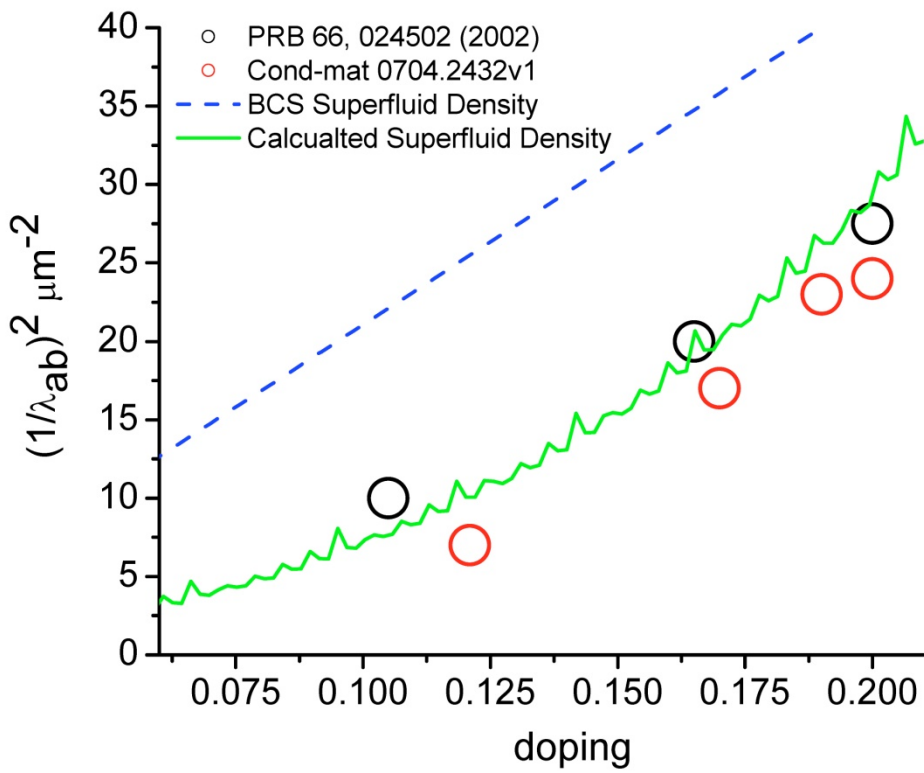


Figure 5-5: Super fluid density from two sources as well as our calculation.

Conclusion

Our model thus is capable of producing a wide range of High Tc's unique properties. This is the first time such a parameterization has been developed for High Tc's and it represents the first step in actually understanding the nature of the superconducting state, and the boundaries in which it lives. Without the ability to accurately describe the electronic structure and its evolution as the doping is changed, we are left with a nebulous problem at best. The features we are trying to describe can be arbitrarily chosen, after all we have no criteria regarding which properties are essential and which are merely distractions. One can cherry pick the features one

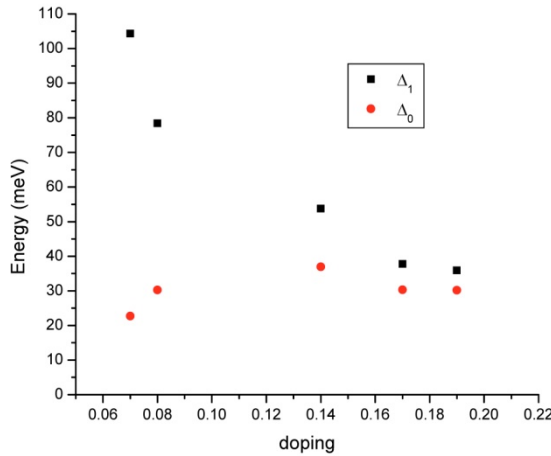


Figure 5-6: Phase diagram showing the limit of the low energy coherence state as well as the higher energy ‘pseudo-gap’ scale.

wishes to describe. The unique features present are so numerous that getting any real handle on the situation is nigh impossible. Of course one could make the same argument here, but I believe that our simple model shall in time be born out, and that the separation we see is both real, and critical to a understanding of high Tc. The measurement of these two scales brings us into line with other probes¹⁰ (figure 5-6). However we have moved beyond this, showing not only the two scales, but also a

underlying structure that enables us to in effect predict properties of the cuprates from basic solid state theory. We are also in the unique position of have a view of the localness of these phenomena, as well as their spatial extent and are posed to map out these energy scales as a function of area and temperature. These local states we measure are also associated with phenomena, checkerboard, ECG, that are pinned to their values, proving that this parameterization is not just a 7 parameter fit, but an actual description of the segmentation and structure of the electronic states. This leads us to a two component solution to superconductivity (figure 5-7), reminiscent of a disordered helium systems. The identification and classification of the exact nature of the higher energy states is still unknown, however we believe a study into their doping, and area dependence will help to further flush out their description. We also expect a study of the exact nature and area dependence of the transition from the superconducting to the pseudogap/normal state should enable us to understand the role these states play in their interactions or lack thereof of superconductivity. In the under doped case we expect the low energy coherent states to be destroyed as we transition above T_c and to be replaced with a ‘checkerboard’ state. This state has already been observed to form within vortex cores, and we expect to see it above T_c . The implementation of our procedure to all three cases, vortex core, above T_c , and below T_c , will provide a crucial test of our ansatz, as well as a common description of the two states, above T_c and vortex cores. In this way our phenomenological theory of high T_c ’s can be tested and validated

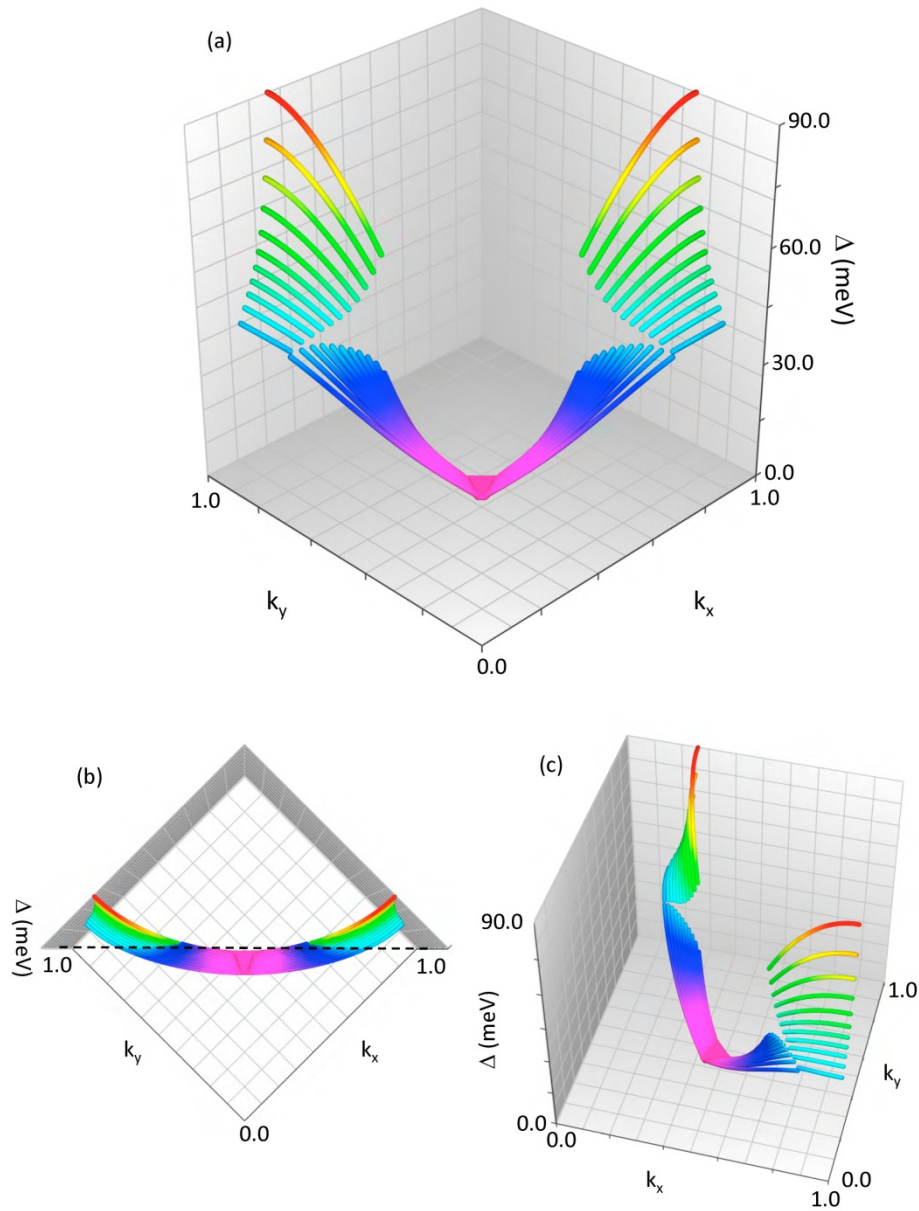


Figure 5-7: (a) Gap function in k-space as a function of doping. Here we go near optimal doped to extremely under doped (UD20K). This shows the separation of the two energy scales as doping is decreased. (b) we show a top down view. The separation happens at the AF-zone boundary, however far on the under doped side this happens slightly inside the AF-ZONE boundary, and could be related with the failure of our small energy scale to close fast enough (could be an error), (c) shows another view.

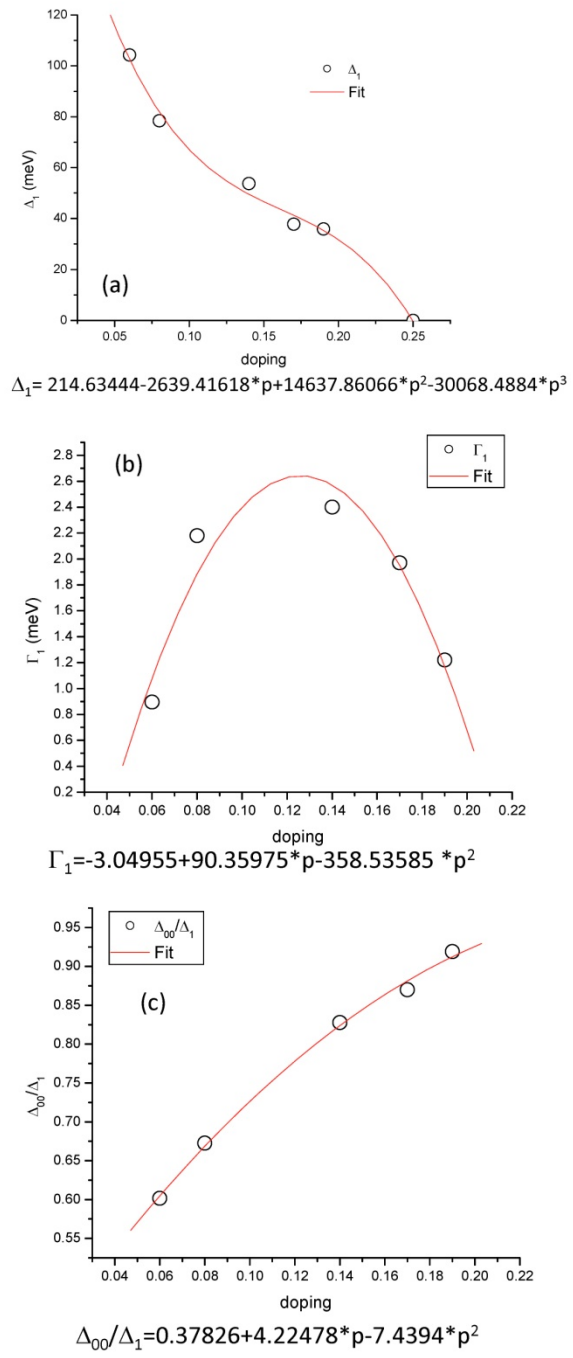


Figure 5-8: The beginning of our continuous model for the parameters which determine our superconductors evolution over the phase diagram as well as the fitting function. (a) Δ_1 , (b) Γ_1 , (c) Δ_{00}/Δ_1 parameterized to avoid Δ_{00} bigger than Δ_1 .

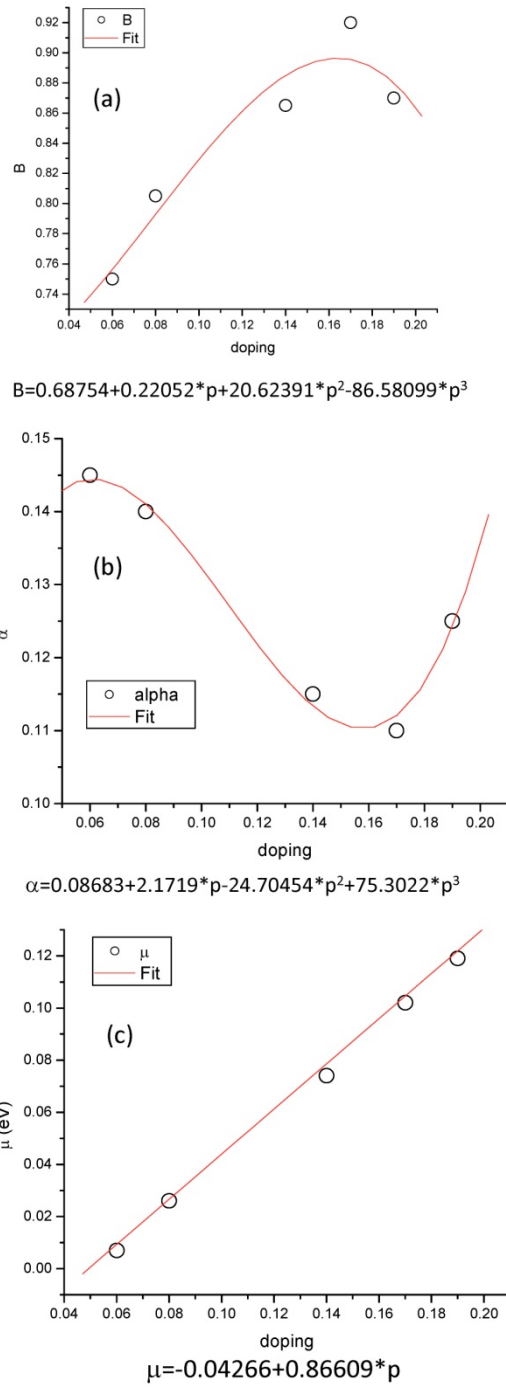


Figure 5-9: The continuation of our continuous model for the parameters which determine our superconductors evolution over the phase diagram as well as the fitting function. (a) B , (b) α , (c) μ .

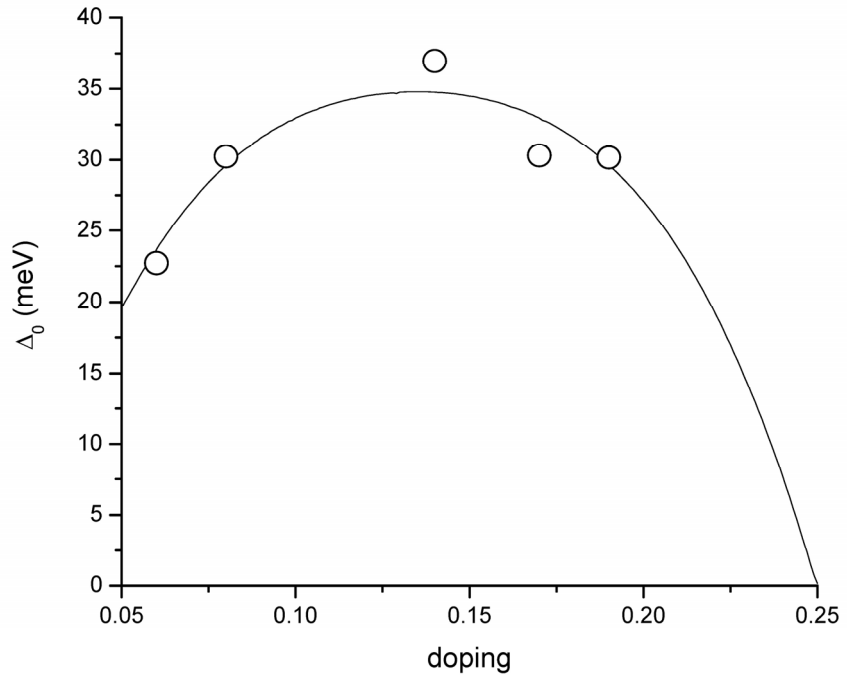


Figure 5-10: The solid line represents the Δ_0 result of our parameterization as a result of our fit for B and Δ_{00}/Δ_1 . The open circles are our data points from our fits. Curiously it does not go to zero at low dopings, however it remains near a tipping point and is highly non-linear here, so the zero remains within our error.

REFERENCES

-
- ¹ Lee, W.S., Vishik, I. M., Tanaka, K., Lu, D. H., Sasagawa, T., Nagaosa, N., Devereaux, T. P., Hussain, Z., Shen, Z. -X. Abrupt Onset of Second Energy Gap at Superconducting Transition of Underdoped Bi2212 Nature 450, 81 (2007)
- ² Franz, M., Millis, A.J. Phys. Rev. B 58, 14572 - 14580 (1998)
- ³ Parks, R.D. Superconductivity, Vol I, Marcel Dekker (1969)
- ⁴ Loram, J.W., Luo, J., Cooper, J.R., Liang, W.Y., Tallon, J.L. J. Phys. Chem Solids. 62, 59 (2001)
- ⁵ Tinkham, M. Introduction to Superconductivity McGraw-Hill (1996)
- ⁶ Andersen, B.M., Melikyan, A., Nunner, T.S., Hirschfeld, P.J. Phys. Rev. B 74, 060501(R) (2006)
- ⁷ Marel, D. van der, Leggett, A.J., Loram, J.W., Kirley, J.R. Phys. Rev. B 66, 140501R (2002)
- ⁸ Watanabe, T., Fujii T., Matsuda, A. Pseudogap in $\text{Bi}_2\text{Sr}_2\text{CaCu}_2\text{O}_{8+\delta}$ Studied by Measuring Anisotropic Susceptibilities and Out-of-Plane Transport Phys. Rev. Lett. 84 5848 (2000)
- ⁹ Sheehy, D.E., Davis, T.P., Franz, M. Phys. Rev. B 70, 054510 (2004)
- ¹⁰ Le Tacon, M., Sacuto, A., Georges, A., Kotliar, G., Gallais, Y., Colson, D., Forget, A. Two energy scales and two distinct quasiparticle dynamics in the superconducting state of underdoped cuprates Nature Physics 2, 537 (2006)

CHAPTER 6

Conclusion

Looking backwards, what I have accomplished is a vast simplification of the STM data for high T_c materials. The ability to take a complicated data set and reduce it to a hand full of parameters in a model that accurately describes the electronic structure in a physically relevant way is an important one. It is hoped that by mapping these parameters and their relationships to each other across space and doping, that we can finally shed light on the underlying important physical processes, and come to a conclusion as to the nature of the processes involved. However, for this to be true, the parameters must be linked with actual physical processes, real divisions in the electronic structures. This is an ongoing process, especially in relation to the new three part separation of energy scales. The exact relationship of this new parameterization to the physical phenomena, can be better understood by looking at the spatial structure of the variables, which increases our statistics and our ability to match them up to existing measured phenomena.

High T_c's may be one of the first materials that SI-STM will play a key role in its understanding. We have a material that is massively disordered compared to traditional systems, and whose features vary rapidly on the nanometer and sub-nanometer scale which are inaccessible by traditional probes. These may be divided into regions with varying superconducting phases, causing bulk probes to be ineffective at revealing the underlying structure. This in turn may hide from these other probes how superconductivity survives this disorder or how it could even be enhanced by it. Unfortunately, how to relate these atomic scale measurements to other bulk probes has kept many of the insights SI-STM has provided from being fully appreciated. Here I have shown that what SI-STM sees is entirely consistent with bulk

probes, validating the atomic scale measurements and making it impossible for the implications of them to be ignored. Not only that but the fact that a very simple d-wave BCS and non-interacting quasiparticle model works extremely well goes a long way to dispelling many overly complicated proposals (hopefully).

However, mapping out the phenomena is all well and good, but it still leaves the mystery as to the nature of the mechanism for high temperature superconductivity. After all, the endgame is an understanding of this mechanism, its limits, and, hence, the ability to engineer or select materials that have the promise of increasing the T_c. In this vain is important to map out what sets the limits and map out what is limiting not only our superfluid density, but the condensation strength and energy. However in order to do so, we must take out simplistic models and compare it to theory, and extract what each parameter actually means and where it may come from. In our ansatz we propose that Δ_0 is in fact the end of the coherent superconducting condensate, and this indeed seems to the case, and is supported not only by our calculations, but by other probes, which see this energy scale as the ‘small gap’. This is the clearest and most straight forward parameter to interpret. It is interesting that this energy value occurs at the intersection of the AF-zone, especially when we consider that this is linked to both the chemical potential and the gap structure. As we approach 0.05 doping we expect this value to go to zero, after all superconductivity ceases at finite temperature here. However if things continue to evolve as we have mapped them then we can predict the doping level where the Fermi surface lies entirely inside the AF zone. This doping is, in fact, a negative doping for our simple extrapolation which is unexpected, but it is not too much of a leap to assume that the chemical potential shifts much more rapidly as the dopant atoms are spread further and further apart. It could also be that we move into a different regime all together, once the coherence length is smaller than the dopant atom spacing. If we use our

parameterization of all the relevant parameters as given in chapter 4, we can calculate that B would have to drop to 0.63 to kill superconductivity completely at a doping level of 0.05. This is not an absurd number, and indeed depending on the exact trend in the span of the ECG regime, this number can be higher still. Hence we can postulate that it is the interplay between this AF ordering and coupling strength that kills off superconductivity at low doping. Indeed if one believes that the coupling is caused by the AF ordering, then increasing the strength with decreasing doping, kills off the superconductivity in it of itself, due to the constraints of the AF-zone boundary.

The Higher harmonic term also has a relatively straight forward theory attached to it. It represents increasing anti-ferromagnetic coupling. This agrees with the trend we see in this term, that is as we go further and further underdoped, we see the B increasing, and this is as we approach the anti-ferromagnetic ordering zone. Also B increases as the Fermi surface moves closer to the AF-zone boundary. One can imagine that as we decrease doping we eventually reach the state where the Fermi surface lies entirely inside the AF-zone boundary, resulting in a complete localization of charge due to this ordering. It would be of great interest to see if this regime can be explored with the STM, and how far we can track the Fermi-surface through tunneling before the concept of a Fermi surface becomes ill defined, and/or tunneling into the sample fails. However we should continue to see an increase in B as we progress further towards the AF-zone and the chemical potential continues to decrease.

On the overdoped side we have the continued decrease in the contestation strength driven by the closing Δ_1 , the large gap which likely sets the overall pairing strength. This is driven by the increased chemical potential which drives us further and further away from the AF-zone boundary increasing the charge carriers and cooper pair densities while decreasing the coupling strength, eventually the repulsion will be stronger than the AF coupling and that will be the end of the superconductor. It is of

some interest to map out this process as well, although obtaining over doped 2212 is harder than underdoped, and the max doping available runs somewhere around 0.23. One would also expect the kink phenomena to disappear once the Fermi surface is entirely inside the AF-zone, however, at our highest measured doping, it is still present, although at much reduced energy (as Δ_1 decreases past critical, 0.19 doping and intersects the Δ_{00} energy scale, the kink energy decreases too). There is also a shift in the QPI pattern towards looking more like the JDOS, with broad arcs rather than individual points. I speculate that this is due to a change in the scattering mechanism, and this might cause a change in the energy dependence of our scattering rate and a change in the overall gap structure. This is somewhat backed up by the poor quality of the fits in the overdoped regime as well as the beginning in a gamma² reversal, that is the beginning of equal lifetimes at node and anti-node (as seen from ARPES). However to draw any conclusions we need a more systematic set of data over the whole overdoped range would help illuminate the truth or fallacy of these suspicions.

It is important to establish the nature of the ECG and the ‘checkerboard’ region, especially in relation to the fitting parameters. It is clear that these represent in some sense the ‘pseudogap’ state. We can also reference the appearance of the checkerboard in the magnetic vortices as well as above Tc. It is clear that this represents a state that is not superconducting, but still behaves ‘strangely’ in the high Tc sense. I would like to draw the link between the arrangement seen in the checkerboard state and properties above Tc in the underdoped regime. One interesting fact is that our Δ_1 overestimates the pseudogap energy scale at extremely low dopings, while the Δ_{00} falls in line with other probes quite nicely. I also believe that the higher energy ECG state represents some sort of localization due to intense anti-ferromagnetic interactions. Thus the ECG would represent an extremely high energy

alignment of spins on a grid that affix the carriers in space and removes them from play. The checkerboard would then be a sort of transitional state between the two regions, the superconducting condensate and a localized background or it could be a sign of semi-localized phase disordered cooper pairs¹. The pairs would be driven by spin interactions to be localized, not having enough energy to make the hop to the next site. There would also be a regimen of the ordering to minimize the energy when a magnetic field is present, or conversely, the magnetic field penetration would be confined to those points where pairs are not present. In this sense the checkerboard observed around a vortex and the checkerboards observed above Tc are one and the same. However the localization is strong enough to destroy the superconductivity, it is not a complete localization, the energy barrier to hop is high but not too high, thus when a voltage is applied there is movement, but at the cost of energy.

So what sets the maximum transition temperature for a material? A good answer to this could be found by doing a detailed study of different layer flavors of biscco. We know that the peak height, or the lifetime increase with increasing layer number. We also know that the crude ‘kink’ energy also increases. Therefore it’s a good bet that it is one of these two things which sets the max Tc. Either we need cleaner systems with less innate disorder, or we need to increase the size of the condensate energy scale, by increasing the AF strength while at the same time increasing the amount of the Fermi-surface that lies within the zone boundary. Both of these are interesting propositions, and if we expand our studies to other materials, and other layered compounds, it is most probable that we can sort out which exact it is. This of course, would be a major step forward; if not a great leap, towards a final solution to the problem of high temperature superconductors.

REFERENCES

¹ Kadin A.M. J. Super. Novel Mat. 20, 4 285 (2007)

APPENDIX A

Fitting Code Fermi surface

In this appendix I present my first fitting code. This requires both the C code for the Levenberg-Marquardt algorithmⁱ as well as Jinho Lee's files for reading in toppometrix style files. The code reads in a parameter text file as well as a gap map file, and uses the information to set limits and starting. The code generates a Fermi surface and uses a numerical integration technique to integrate the gap function over. This can be replaced with in reality any function that is numerically viable. The code also writes a text file updating the status. When it is finished it dumps the output to a series of toppometrix TFR files. It is important to use individual TFR files because unlike the NVL format IDL uses, the 1FL files have a single 16bit scale for all layers, this may be fine for spectra, but it functions very poorly when you have fit parameters and returned chi-square fluctuating over 8 orders of magnitude in cases.

Since the data files are usually cut up and distributed, they are reassembled by some simple IDL code and then post processed by looking for outlier points and re running the fit on them, with boundary conditions set by the points neighbor.

```

C:\Documents and Settings\Aardvark....-Code\Visual Studio 2005\dos-full\fermi.cpp 1
//#include <iostream>
#include <stdio.h>
#include <algorithm>
#include "lm.h"
#include "malloc.h"
#include <stdlib.h>
#include "fermi.h"
using namespace std;
float const pi = 3.14159265359;
/*struct pass2 {
    float * x;
    float & gap;
    complex <float> & energy;
    valarray <float> & gapf;
    int l;
};*/
struct globalthis din;
struct pass2 cheese;

//function to determine energies from band structure. Change this to change your band
//structure.
float __fastcall kenergy(float kx, float ky) {
    float ky1, kx1, out;
    float t1, t2, t3, t4, t5, mu, a;
    ky1=ky*pi;
    kx1=kx*pi;
    t1=-0.5951;
    t2=.1636;
    t3=0;//t3=-0.0519;
    t4=0;//t4=-0.1117;
    t5=0;//t5=0.0510;
    mu=.1305;
    a=1.0;
    out=t1*(cos(kx1*a)+cos(ky1*a))/2+t2*(cos(kx1*a)*cos(ky1*a))+mu+
        t3*(cos(2*kx1*a) + cos(2*ky1*a))/2+t4*(cos(2*kx1*a)*cos(ky1*a)
        + cos(kx1*a)*cos(2*ky1*a))/2+ t5*cos(2*kx1*a)*cos(2*ky1*a);
    return out;
}
//this code finds the fermi surface
int __fastcall gen_energy(float r, float E, valarray<float> * zerokx, valarray<float> * zero
ky) {
    int n,p;
    //safety
    if(E > .9 || E < -.4) return 0;
    n=floor( 0.001/r)+1;
    (*zerokx).resize(1800*n+1,0.0); //makes a guess at the right size
    (*zero
ky).resize(1800*n+1,0.0);
    float kx, ky, kxb, ky, error, bad, q, theta, thetab, arx, ary;
    kx=1.0;
    ky=0.18;
    error=100;
    n=0;
    bad=1.0;
    //finds the first point, for kx=1.0 should be around .18
    while(fabs(error) > 0.000001) {
        ky=kyb;
        error=E-kenergy(kx,ky);
        kyb=ky+error/2.0;
        n++;
        if(n > 500) error=0.0;
    }
    //if this fails in the case of E being negative, looks for the point where ky=0.0
}

```

```

C:\Documents and Settings\aaardvark....-code\Visual Studio 2005\dos-full\fermi.cpp 2
    if (n > 500) {
        n=0;
        ky=0.0;
        kxb=0.0;
        error=100;
        //loop to find point
        while(fabs(error)> 0.000001) {
            kx=kxb;
            error=E-kenergy(kx,ky);
            kxb=kx+error/2;
            n++;
            if(n > 500) error=0.0;
        }
        baq=kx;
    }
    (*zerokx)[0]=kx;
    (*zeroky)[0]=ky;
    q=ky;
    error=100;
    theta=0.0;
    n=0;
    p=0;
    thetab=pi;
    // goes along the line till it reaches the ending condition. Importnat that poitns are ↵
    equal distance, otherwise cause distortions in fermi surface
    //no longer a proper line intergal.
    while(ky < baq) {
        arx=kx;
        ary=ky;
        n=0;
        //starts off with a fixed radius and moves a line until it finds the point on line ↵
        while(fabs(error) > 0.000001) {
            theta=thetab;
            kx=arx+r*cos(theta);
            ky=ary+r*sin(theta);
            error=E-kenergy(kx,ky);
            thetab=theta-error/(50*r);
            if(n > 500) error=0.0;
            n++;
        }
        (*zerokx)[p]=kx;
        (*zeroky)[p]=ky;
        error=100.0;
        p++;
    }
    //makes the size right
    (*zerokx).resize(p);
    (*zeroky).resize(p);

    //returns 0 for no reason.
    return 0;
}

//this is our actual function, that determines dos
DP gapg(const DP a, struct pass2 & ch) {
    float t,p;
    t=(ch.gapf)[(int) a]*(*ch.gap);
    t=t*0.5;//add aug 29 to check the factor of two error
    ch.out=(*ch.energy)/sqrt(t*t-(*ch.energy)*(*ch.energy)); //this is the actual ↵
    function integrated
    p=ch.out.imag();
    return p; //returns imaginary part
}
//here we call a numericla recipes file to do numeric intergration along our line,
// tricking it to use our indicies. ↵

```

```

C:\Documents and Settings\aaardvark....-code\Visual Studio 2005\dos-full\fermi.cpp 3
float __fastcall integrate(complex<float> en, float r, struct globalthis & gvar) {
    int end=(*(&gvar.pass).gapf).size()-1;
    (*gvar.pass).energy=&en;
    return NR::qromb(gapg,0,end,gvar.EPS,(*gvar.pass))*r; //does the actual intergration, ✓
    all stuff needed in cheese.

}

//searches valarrays, needed for finding zero's
int __fastcall searchme(valarray <float> &x, float w) {
    int end=x.size();
    for (int y=0; y<=end; y++) {
        if (w== x[y]) {
            return y;
        }
    }

    for (int y=0; y<=end; y++) {
        if (floor(w)*100== floor(100*x[y])) {
            return y;
        }
    }

    for (int y=0; y<=end; y++) {
        if (abs(w)==abs(x[y])) {
            return y;
        }
    }
    return -1;
}

//reverse valarrays so that our input can be independent of direction
valarray <float> __fastcall reverseval(valarray <float> x) {
    valarray <float> b(x.size());
    int q=x.size();
    for( int i=0; i<q; i++) {
        b[i]=x[q-1-i];
    }
    return b;
}

//this is a container fucntion for our LDOS generation, it sets up all the variables, and ✓
//initializes,
//as symatrizing the integration to cut our computation time in half.
float * __fastcall ldos(valarray<float> &x, float gam, float gaps ,float r, struct
    globalthis & gvar, float gam2) { ✓
    float mina,maxa;
    complex<float> xl;
    int i,p,q,s,si;
    (*gvar.xab)=x.apply(fabs); //makes a temp arrary of the abs of x to figure out where ✓
    zero is

    mina=(*gvar.xab).min();
    maxa=(*gvar.xab).max();
    //finds the center point
    p=searchme(x,mina); //simple search for the min and mx, used for extracting half a x✓
    axis from a full
    q=searchme(x,maxa);
    //resizes the energy axis array to half the size
    (*gvar.xa).resize(abs(p-q)+1);
    (*gvar.pass).gap=&gaps; //throws the gap into the structure
    gvar.half=(float *) realloc(gvar.half,sizeof(float)*(abs(p-q)+1)); //makes sure the ✓
    half arrary is the right size
    if(p<q+1) (*gvar.xa)=x[slice(p,q+1,1)]; //these pull out half the x axis
    else (*gvar.xa)=x[slice(q,p+1,1)];
    if((*gvar.xa)[0] > (*gvar.xa)[abs(p-q)]) {(*gvar.xa)=reverseval((*gvar.xa));} //✓
    reverses the x axis if its backwards, so that the direction is
}

```

```

C:\Documents and Settings\aaardvark....-code\Visual Studio 2005\dos-full\fermi.cpp 4

//remormalizes the gammas by gap
gam=gam*gaps; //constant from this point out
gam2=gam2*gaps;
i=0;
(*gvar.xao).resize(abs(p-q)+1); //makes sure the temp energy arrary is the right size
while(i < abs(p-q)+1) {
    //note gamma2=gammal in the literature, this is just due to the history in
    //encoding this
    complex <float> c((*gvar.xa)[i],gam2+(*gvar.xa)[i]*gam/gaps); //throws in the
    complex energy and gamma gam2+gvar.xa[i]*gam/gaps
    (*gvar.xao)[i]=c;
    i++;
}

i=0;
//does the integration using the correct half of the energy axis
while(i < abs(p-q)+1) {
    gvar.half[i]=integrate((*gvar.xao)[i],r, gvar); //does the work
    i++;
}
s= x.size();
si=(abs(p-q)+1);
if (si==s) { //determines if the original data is only half an axis if so returns it, ✓
if not
    return gvar.half;
}
else {
    gvar.full=(float *) realloc(gvar.full,sizeof(float)*x.size()); //makes sure the ✓
    full data arrary is right size
    i=0;
    //mirrors the ldos to make a full energy +/- one
    while (i < x.size()) {
        if (i < si) gvar.full[i]=gvar.half[si-i-1];
        if (i >= si) gvar.full[i]=gvar.half[i-si+1]; //puts the half and the reverse ✓
        of half into output in right way
        i++;
    }
    return gvar.full;
}
return gvar.half;
}

//this function is used by the fitting routine to fgenreate the dos, since it has to ✓
//accpet passed variables in a certain specific way,
//also adds the slope
void dosfit(float *p, float *x, int m, int n, void *data) {
    float q, *tempout;
    int i=0;
    //gets varriables
    din=(globalthis *) data;
    valarray<float> in((*din.pass).x,(*din.pass).l);
    q=1/( (float) ((*din.pass).gapf).size());
    //makes the ldos
    tempout=ldos(in,p[2],p[1],q, din, p[4]);
    for(int i=0; i<(*din.pass).l;i++) {
        //adds slope
        x[i]=tempout[i]*p[0]+(*din.pass).x[i]*p[3];
    }
}

//the actual called fitme function, uses slevmar_bc_dif, which can be found in the ✓
//apporperate c file
float * fitme(struct globalthis & gvar, float *input, int loops, float *p, float *low, ✓
float *high, float *opts) {
    void *adata;

```

```

C:\Documents and Settings\aaardvark....-code\Visual Studio 2005\dos-full\fermi.cpp      5
    float *data;
    int po,i,n,q1,z1;
    float info[LM_INFO_SZ];
    adata=&gvar; /*throws the passing structure into a void array to pass through the fitting program
    q1=sizeof(p)/sizeof(float);
    data=new float[14];
    /*opts[0]=1E-03; //default 1E-03 LM_INIT_MU
    opts[1]=1E-17; //default 1E-17 LM_STOP_THRESH
    opts[2]=1E-17; //default 1E-17 LM_STOP_THRESH
    opts[3]=1E-17; //default 1E-17 LM_STOP_THRESH
    opts[4]=1E-3;  //default 1E-06 LM_DIFF_DELTA */
    po=slevmar_bc_dif(dosfit, p, input, 5, (*gvar.pass).l, low, high, loops, opts, info, NULL, NULL, adata);
    //returns output, plus fitting information contained in the info file
    for(i=0;i<5;i++) data[i]=p[i];
    for(i=0;i<sizeof(info)/sizeof(float);i++) data[5+i]=info[i]; //puts the data into the idl ptr, and ends
}

return data;
}

```

```

C:\Documents and Settings\aaardvark....C-code\Visual Studio 2005\dos-full\main.cpp 1
#include <cmath>
#include <stdio.h>
#include <algorithm>
#include "lm.h"
#include "malloc.h"
#include "nr.h"
#include "numericalrecipes.h"
#include "stdafx.h"
#include <stdlib.h>
#include "fermi.h"
#include <stddef.h>
#include "TopoMetrix.h"
#include <string>
#include <time.h>
#include <sys/types.h>
#include <sys/timeb.h>

using namespace std;

float const pi = 3.14159265359;

int main(int argc, char *argv[]) {

//read in text file with prefs, input file name, output file name, loops, high, low limits
//EPS, opts, gapmap file
    string filename;
    filename=argv[1];
    char *inputname, *outputname, *gapmapname, *temp, *p;
    float EPS, high[5], low[5], opts[5], opts2[5];
    int loops, i=0,o;
    BOOL t;
    ifstream file (filename.c_str());
    if (! file) {
        // NO, abort program
        cerr << "can't open input file \\" " << filename << "\\"
            << endl;
        exit (EXIT_FAILURE);
    }

//reads in the preferane file, where it gets limits, chemical potential, and path
//information
    inputname=(char *) malloc(sizeof(char)*100);
    file.getline(inputname,100);
    inputname=(char *) realloc(inputname,file.gcount()*sizeof(char));
    outputname=(char *) malloc(sizeof(char)*100);
    file.getline(outputname,100);
    outputname=(char *) realloc(outputname,file.gcount()*sizeof(char));
    gapmapname=(char *) malloc(sizeof(char)*100);
    file.getline(gapmapname,100);
    gapmapname=(char *) realloc(gapmapname,file.gcount()*sizeof(char));

    temp=(char *) malloc(10*sizeof(char));
    for(i=0;i<5;i++) {
        temp=(char *) realloc(temp,10*sizeof(char));
        file.get(temp, 10, ',');
        temp=(char *) realloc(temp,file.gcount()*sizeof(char));
        file.ignore();
        high[i]=atof(temp);
    }
    for(int i=0;i<5;i++) {
        temp=(char *) realloc(temp,10*sizeof(char));
        file.get(temp, 10, ',');
        temp=(char *) realloc(temp,file.gcount()*sizeof(char));
        file.ignore();
        low[i]=atof(temp);
    }
}

```

```

    for(int i=0;i<5;i++) {
        temp=(char *) realloc(temp,10*sizeof(char));
        file.getline(temp, 10,';');
        temp=(char *) realloc(temp,file.gcount()*sizeof(char));
        file.ignore();
        opts[i]=atof(temp);
        opts2[i]=opts[i]*0.1;
    }
    temp=(char *) realloc(temp,100*sizeof(char));
    file.getline(temp, 100);
    file.getline(temp, 100);
    temp=(char *) realloc(temp,file.gcount()*sizeof(char));
    EPS=atof(temp);
    temp=(char *) realloc(temp,100*sizeof(char));
    file.getline(temp,100);
    temp=(char *) realloc(temp,file.gcount()*sizeof(char));
    loops=atof(temp);
    file.close();

//read in gap + ifl file sets up output files, all from jinho
SCANPARAMSSIMPLE inpath;
SCANPARAMSSIMPLE gaph;

bool test;
CFile inp;
CFile gapp;

DOCUMENTINFO inpd;
DOCUMENTINFO gapd;
CTFRfile input;
CTFRfile gapmap;
test=inp.Open((const char *) inputname,CFile::modeRead);
input.ReadDocumentInfo(inpd,inp); //THIS MUST BE IN THIS ORDER!!
input.ReadScanParamsSimple(inpath,inp);
inp.Close();
test=gapp.Open((const char *) gapmapname,CFile::modeRead);
gapmap.ReadDocumentInfo(gapd,gapp);
gapmap.ReadScanParamsSimple(gaph,gapp);
gapp.Close();
test=input.OpenFile(inputname);
test=gapmap.OpenFile(gapmapname);

//sets up for the fits, generates energies
float *data, *tout, *output, *outputt, start[5], startb[5], *t1,*t2,*t3,*t4,*t5,*t6,*
tc, *t7, *xa, maxa[7], mina[7],tfl;
//sets up output files as needed
output=new float[14];
outputt=new float[14];
data=new float[input.nosts];
tout=new float[input.nosts];
xa=new float[input.nosts];
t1=new float[input.noypixels*input.noypixels];
for(int i=0;i<7;i++) {
    //initializes the max and min arrays, important for writing files.
    maxa[i]=-100.0;
    mina[i]=100.0;
}
t2=new float[input.noypixels*input.noypixels];
t3=new float[input.noypixels*input.noypixels];
t4=new float[input.noypixels*input.noypixels];
t5=new float[input.noypixels*input.noypixels];
t6=new float[input.noypixels*input.noypixels];
t7=new float[input.noypixels*input.noypixels];
tc=new float[input.noypixels*input.noypixels*input.nosts];

//sets up the files to store the fermi surface, sets up two,

```

```

C:\Documents and Settings\Aardvark....C-code\Visual Studio 2005\dos-full\main.cpp 3

valarray<float> zeroKx1;
valarray<float> zeroKy1;
valarray<float> zeroKx2;
valarray<float> zeroKy2;
valarray<float> gapf1,gapf2;
valarray<float> x(input.nosts);
xa=new float[input.nosts];
for(int i=0;i<input.nosts;i++) {
    //makes the energy axis file
    x[i]=(input.stsend-input.stsstart)/(input.nosts-1)*i+input.stsstart;
    xa[i]=x[i];
}
//sets up some structures to pass data, these get referenced inside the global gvar
variable passign structure.
struct fitdata1, fitdata2;
int zeroNum=input.nosts/2+1;
//generates the zero axis...
o=gen_energy(0.001,0.0,&zeroKx1,&zeroKy1);
o=gen_energy(0.0005,0.0,&zeroKx2,&zeroKy2);
zeroKx1=zeroKx1*pi; //they all need pi
zeroKy1=zeroKy1*pi;
zeroKx2=zeroKx2*pi;
zeroKy2=zeroKy2*pi;
//resizes the gap storage array
gapf1.resize(zeroKx1.size());
//then stores the gap and transfers it into fitdatas
gapf1=zeroKx1.apply(cos)-zeroKy1.apply(cos); //evaluate the gap so it only has to be done once
fitdata1.gap=&gapf1;
fitdata1.x=xa;
fitdata1.l=input.nosts;
fitdata2.x=fitdata1.x;
fitdata2.l=fitdata1.l;
for(int i=0;i<input.nosts;i++) x[i]=fitdata1.x[i];
gapf2.resize(zeroKx2.size());
gapf2=zeroKx2.apply(cos)-zeroKy2.apply(cos);
fitdata2.gap=&gapf2;
//following makes and initializes global structure
struct globalThis gvara;
//more initialization of varries arrays used latter, as well as the temp half and full
store files, dumps them into the global
valarray<float> xab1;
valarray<complex<float>> xao1(51);
complex<float> out;
float *half, *full;
half=(float *) malloc(51*sizeof(float));
full=(float *) malloc(100*sizeof(float));
gvara.half=half;
gvara.full=full;
gvara.EPS=EPS;
gvara.xab=&xab1;
gvara.xa=&xao1;
gvara.xao=&xao1;

//this sets up a status file to write crap too
char tmpbuf[9];
char dbuffer [9];

string tempfilen;
tempfilen=outputname;
tempfilen = tempfilen + "status.txt";
ofstream filea (tempfilen.c_str());
if (! file) {
    // NO, abort program
}

```

```

C:\Documents and Settings\aaardvark....C-code\Visual Studio 2005\dos-full\main.cpp 4
        cerr << "can't open status file \" " << filename << "\"
                           << endl;
                           exit (EXIT_FAILURE);
}

filea.write("Start ",6);
_strftime( tmpbuf );
_strdate( dbuffer );
filea.write(tmpbuf,9);
filea.write(" ",1);
filea.write(dbuffer,9);
filea.put(10);
filea.flush();
char *pas;
pas=new char[3];
float zerotemp;

//does actual fits, goes through all points, pulls data, fits, then fits, generates
//curves, and ends
for(int xx=0;xx<input.noxpixels;xx++) {
    for(int yy=0;yy<input.noxpixels;yy++) {
        for(int i=0;i<input.nosts;i++) {
            //grabs the data
            data[i]=input.GetConductanceFromRawData(input.GetData(xx,yy,i));
        }
        gvara.pass=&fitdata1;
        gvara.EPS=EPS;
        //does a number of loops with different starting conditions
        for(int ioo=0;ioo<11;ioo++) {
            if(ioo==0) {
                start[0]=fabs(input.GetConductanceFromRawData(input.GetData(xx,yy,0)));
            ; //prefactor
                start[1]=fabs(gapmap.GetConductanceFromRawData((unsigned short) xx+      ↵
gapmap.noxpixels*yy)); //gap
                start[2]=0.005*start[1]+0.0001; //alpha
                start[3]=0.0; //slope
                //gamma starts related to the zero bias conductance
                start[4]=fabs(input.GetConductanceFromRawData(input.GetData(xx,yy,      ↵
zeronum))); //gammal
                for(int u=0;u<5;u++) startb[u]=start[u];
            }
            //if(ioo==1) {
            //    for(int u=0;u<5;u++) start[u]=startb[u];
            //    start[1]=(float) startb[1]*1.5;
            //}
            if(ioo==1) {
                for(int u=0;u<5;u++) start[u]=startb[u];
                start[1]=(float) startb[1]*2.0;
            }
            if(ioo==2) {
                for(int u=0;u<5;u++) start[u]=startb[u];
                start[1]=(float) startb[1]*0.5;
            }
            //if(ioo==4) {
            //    for(int u=0;u<5;u++) start[u]=startb[u];
            //    start[1]=(float) startb[1]*0.666;
            //}
            if(ioo==3) {
                for(int u=0;u<5;u++) start[u]=startb[u];
                start[4]=0.0;
            }
            if(ioo==4) {
                for(int u=0;u<5;u++) start[u]=startb[u];
                start[2]=0.0001;
            }
            if(ioo==5) {
                for(int u=0;u<5;u++) start[u]=startb[u];
            }
        }
    }
}

```

```

C:\Documents and Settings\aaardvark....C-code\Visual Studio 2005\dos-full\main.cpp      5
    start[2]=0.2;
}
//if(ioo==6) {
//  for(int u=0;u<5;u++) start[u]=startb[u];
//  start[1]=(float) start[1]*0.5;
//  start[4]=0.0;
//  start[2]=0.2;
//}
if(ioo==6) {
  for(int u=0;u<5;u++) start[u]=startb[u];
  start[1]=start[1]*0.5;
  start[2]=0.0001;
}
if(ioo==7) {
  for(int u=0;u<5;u++) start[u]=startb[u];
  start[1]=start[1]*0.5;
  start[4]=0.0;
}
if(ioo==8) {
  for(int u=0;u<5;u++) start[u]=startb[u];
  start[1]=start[1]*0.5;
  start[2]=0.0001;
}
if(ioo==9) {
  for(int u=0;u<5;u++) start[u]=startb[u];
  start[1]=start[1]*2.0;
  start[4]=0.0;
}
if(ioo==10) {
  for(int u=0;u<5;u++) start[u]=startb[u];
  start[1]=start[1]*2.0;
  start[2]=0.0001;
}
//if(ioo==12) {
//  for(int u=0;u<5;u++) start[u]=startb[u];
//  start[1]=start[1]*2.0;
//  start[4]=0.0;
//  start[2]=0.2;
//}
if(ioo==11) {
  for(int u=0;u<5;u++) start[u]=startb[u];
  start[1]=start[1]*2.0;
  start[2]=0.2;
}
//if(ioo==16) {
//  for(int u=0;u<5;u++) start[u]=startb[u];
//  start[4]=0.0;
//  start[2]=0.2;
//}
//the fit
for(int u=0;u<5;u++) {
  //makes sure the starting values aren't outside out limits casues code to crash if not done
  if(start[u]>high[u]) start[u]=high[u];
  if(start[u]<low[u]) start[u]=low[u];
}
//calls fitting function
outputt=fitme(gvara,data,loops,start,low,high,opts);
//stores it in our temp output if interation zero, if ntno zero, sees if the chi-square is smaller and if so stores it
if(ioo==0) for(int xae=0;xae<14;xae++) outputt[xae]=outputt[xae];
if(outputt[6]<output[6]) {
  for(int xae=0;xae<14;xae++) outputt[xae]=outputt[xae];
  //stores the iteration that was selected to be the best for optimizartion purposes
  t7[xx+input.noxpixels*yy]=ioo;
}

```

```

C:\Documents and Settings\aaravark....C-code\Visual Studio 2005\dos-full\main.cpp 6
//uses the lowest error from above to run a longer interation fit.

}

for(int a=0;a<5;a++) start[a]=output[a];
//starts a final fit that requires a higher convergance
output=fitme(gvara,data,loops,start,low,high,opts2);
cout <<xx << " " << yy << endl;
//dumps the data
//generates curves based off above fit
t1[xx+input.noxpixels*yy]=output[0];
if(maxa[0]<output[0]) maxa[0]=output[0];
if(mina[0]>output[0]) mina[0]=output[0];
t2[xx+input.noxpixels*yy]=output[1];
if(maxa[1]<output[1]) maxa[1]=output[1];
if(mina[1]>output[1]) mina[1]=output[1];
t3[xx+input.noxpixels*yy]=output[2];
if(maxa[2]<output[2]) maxa[2]=output[2];
if(mina[2]>output[2]) mina[2]=output[2];
t4[xx+input.noxpixels*yy]=output[3];
if(maxa[3]<output[3]) maxa[3]=output[3];
if(mina[3]>output[3]) mina[3]=output[3];
t5[xx+input.noxpixels*yy]=output[4];
if(maxa[4]<output[4]) maxa[4]=output[4];
if(mina[4]>output[4]) mina[4]=output[4];
t6[xx+input.noxpixels*yy]=output[6];
if(maxa[5]<output[5]) maxa[5]=output[6];
if(mina[5]>output[5]) mina[5]=output[6];
float r=1/( float ) (*fitdata2.gapf).size());
gvara.pass=&fitdata2;
gvara.EPS=1E-6;
//generates the fit return at a high precision level
tout=ldos(x, output[2], output[1] ,r , gvara, output[4]);
for(int i=0; i<input.nosts;i++) {
    tfl=tout[i]*output[0]+x[i]*output[3];
    tc[xx+input.noxpixels*yy+input.noxpixels*input.noxpixels*i]=tfl;
    if(tfl>maxa[6]) maxa[6]=tfl;
    if(tfl<mina[6]) mina[6]=tfl;
}
//deletes the output, reformed each time to make sure we don't get mixed up ✕
with old variables
delete[] output;
}
//writes status file
filea.write("Line ",6);
ltoa(xx,pas,10);
if(xx<10) filea.write(pas,1);
if(xx>=10) if(xx<100) filea.write(pas,2); else filea.write(pas,3);
filea.write(" end ",5);
_strtime( tmpbuf );
_strdate( dbuffer );
filea.write(tmpbuf,9);
filea.write(" ",1);
filea.write(dbuffer,9);
filea.put(10);
filea.flush();
}
filea.close();
//saves actual files
unsigned short *outdata, *outdata2;
outdata=new unsigned short[input.noxpixels*input.noypixels];
outdata2=new unsigned short[input.noxpixels*input.noypixels*input.nosts];
CString tempstring, tempfilename;
tempfilename=outputname;

tempstring.Format("1factor");
tempfilename = tempfilename.SpanExcluding(".") + tempstring + ".tfr";

```

```

C:\Documents and Settings\aaardvark....C-code\Visual Studio 2005\dos-full\main.cpp 7
    tempstring.Format("prefactor");
    strcpy(gapd.szDescription,(const char*)tempstring);
    gapd.fDActoWorld=(maxa[0]-mina[0])/pow(2,16);
    gaph.fScanZmax=maxa[0];
    gaph.fScanZmin=mina[0];
    gapd.iDACDisplayZero = mina[0]/gapd.fDActoWorld;
    gapd.fDActoWorldZero = mina[0];
    gapd.iDACDisplayRange = pow(2,16);
    gapd.iDACmax = pow(2,16);
    gapd.iDACmin = 0;
    gapd.iDACDisplayZero=0;           // [333..334] z adjust zero point in DAC units
    gapd.iDACDisplayRange=pow(2,16);
    gapd.iCols=gapmap.noxpixels;
    gapd.iRows=gapmap.noypixels;
    gapd.iWorldUnitType = 1;
    gapd.iLayers = 1;
    gapd.bHasBkStrip = 0;
    gapd.iTilt = 1;
    for(int n=0;n<8;n++) gapd.dTiltC[n] = 0.;//{0,0,0,0,0,0,0,0};
    gaph.iDataTpe = 5; // ?
    gaph.iDataMode = 6; // ?
    gaph.iADC = 0;
    gaph.iLayers = 1;

    for(int i=0;i<input.noxpixels*input.noypixels;i++) outdata[i]=(t1[i]-mina[0])/(maxa[0]-
    -mina[0])*pow(2,16);
    input.SaveTFFFile(tempfilename,gapd,gaph, outdata);

    tempstring.Empty();
    tempfilename=outputname;
    tempstring.Format("2GapValue");
    tempfilename = tempfilename.SpanExcluding(".") + tempstring + ".tfr";
    tempstring.Format("Gap Value");
    strcpy(gapd.szDescription,(const char*)tempstring);
    gapd.fDActoWorld=(maxa[1]-mina[1])/pow(2,16);
    gaph.fScanZmax=maxa[1];
    gaph.fScanZmin=mina[1];
    gapd.iDACDisplayZero = mina[1]/gapd.fDActoWorld;
    gapd.fDActoWorldZero = mina[1];
    for(int i=0;i<input.noxpixels*input.noypixels;i++) outdata[i]=(t2[i]-mina[1])/(maxa[1]-
    -mina[1])*pow(2,16);
    input.SaveTFFFile(tempfilename,gapd,gaph, outdata);

    tempstring.Empty();
    tempfilename=outputname;
    tempstring.Format("3Gamma2");
    tempfilename = tempfilename.SpanExcluding(".") + tempstring + ".tfr";
    tempstring.Format("Gamma 2");
    strcpy(gapd.szDescription,(const char*)tempstring);
    gapd.fDActoWorld=(maxa[2]-mina[2])/pow(2,16);
    gaph.fScanZmax=maxa[2];
    gaph.fScanZmin=mina[2];
    gapd.iDACDisplayZero = mina[2]/gapd.fDActoWorld;
    gapd.fDActoWorldZero = mina[2];
    for(int i=0;i<input.noxpixels*input.noypixels;i++) outdata[i]=(t3[i]-mina[2])/(maxa[2]-
    -mina[2])*pow(2,16);
    input.SaveTFFFile(tempfilename,gapd,gaph, outdata);

    tempstring.Empty();
    tempfilename=outputname;
    tempstring.Format("4Slope");
    tempfilename = tempfilename.SpanExcluding(".") + tempstring + ".tfr";
    tempstring.Format("Slope");
    strcpy(gapd.szDescription,(const char*)tempstring);
    gapd.fDActoWorld=(maxa[3]-mina[3])/pow(2,16);
    gaph.fScanZmax=maxa[3];
    gaph.fScanZmin=mina[3];

```

```

C:\Documents and Settings\aaardvark....C-code\Visual Studio 2005\dos-full\main.cpp 8
    gapd.iDACPDisplayZero = mina[3]/gapd.fDACtoWorld;
    gapd.fDACtoWorldZero = mina[3];
    for(int i=0;i<input.noPixels*input.noPixels;i++) outdata[i]=(t4[i]-mina[3])/ (maxa[3]-
    -mina[3])*pow(2,16);
    input.SaveTFFFile(tempfilename,gapd,gaph,outdata);

    tempstring.Empty();
    tempfilename=outputname;
    tempstring.Format("5Gamma1");
    tempfilename = tempfilename.SpanExcluding(".") + tempstring + ".tfr";
    tempstring.Format("Gamma ");
    strcpy(gapd.szDescription,(const char*)tempstring);
    gapd.fDACtoWorld=(maxa[4]-mina[4])/pow(2,16);
    gaph.fScanZmax=maxa[4];
    gaph.fScanZmin=mina[4];
    gapd.iDACPDisplayZero = mina[4]/gapd.fDACtoWorld;
    gapd.fDACtoWorldZero = mina[4];
    for(int i=0;i<input.noPixels*input.noPixels;i++) outdata[i]=(t5[i]-mina[4])/ (maxa[4]-
    -mina[4])*pow(2,16);
    input.SaveTFFFile(tempfilename,gapd,gaph,outdata);

    tempstring.Empty();
    tempfilename=outputname;
    tempstring.Format("6Error");
    tempfilename = tempfilename.SpanExcluding(".") + tempstring + ".tfr";
    tempstring.Format("Error");
    strcpy(gapd.szDescription,(const char*)tempstring);
    gapd.fDACtoWorld=(maxa[5]-mina[5])/pow(2,16);
    gaph.fScanZmax=maxa[5];
    gaph.fScanZmin=mina[5];
    gapd.iDACPDisplayZero = mina[5]/gapd.fDACtoWorld;
    gapd.fDACtoWorldZero = mina[5];
    for(int i=0;i<input.noPixels*input.noPixels;i++) outdata[i]=(t6[i]-mina[5])/ (maxa[5]-
    -mina[5])*pow(2,16);
    input.SaveTFFFile(tempfilename,gapd,gaph,outdata);

    tempstring.Empty();
    tempfilename=outputname;
    tempstring.Format("7startcon");
    tempfilename = tempfilename.SpanExcluding(".") + tempstring + ".tfr";
    tempstring.Format("Start Conditions");
    strcpy(gapd.szDescription,(const char*)tempstring);
    gapd.fDACtoWorld=(17)/pow(2,16);
    gaph.fScanZmax=17;
    gaph.fScanZmin=0;
    gapd.iDACPDisplayZero = 0;
    gapd.fDACtoWorldZero = 0;
    for(int i=0;i<input.noPixels*input.noPixels;i++) outdata[i]=t7[i]/(17)*pow(2,16);
    input.SaveTFFFile(tempfilename,gapd,gaph,outdata);

    tempstring.Empty();
    tempfilename=outputname;
    tempstring.Format("fit");
    tempfilename = tempfilename.SpanExcluding(".") + tempstring + ".lfl";
    tempstring.Format("fit");
    strcpy(gapd.szDescription,(const char*)tempstring);
    inpd.fDACtoWorld=(maxa[6]-mina[6])/pow(2,16);
    inpush.fScanZmax=maxa[6];
    inpush.fScanZmin=mina[6];
    inpd.iDACPDisplayZero = mina[6]/inpd.fDACtoWorld;
    inpd.fDACtoWorldZero = mina[6];
    for(int i=0;i<input.noPixels*input.noPixels*input.nosts;i++) outdata2[i]=(tc[i]-mina[6])/
    [6])/ (maxa[6]-mina[6])*pow(2,16);
    input.SaveLFLFileNew(tempfilename,inpd,inpush,input.noPixels,input.noPixels,
    outdata2);

```

```
    return 0;  
}
```

REFERENCES

ⁱ Lourakis, M.I.A. <http://www.ics.forth.gr/~lourakis/levmar/> (2004)

APPENDIX B

a(k,w) Fitting Code

In this appendix I present my $a(k,w)$ fitting code. This requires both the C code for the Levenberg-Marquardt algorithm¹ as well as Jinho Lee's files for reading in toppometrix style files. This is basically a variation of the code presented in appendix 1, and merely replaces the line style integration there with a full summation over a quarter of the brillion zone, while getting rid of any fancy numerical integration (which doesn't help that much in reality).

```

#include <stdio.h>
#include <algorithm>
#include "lm.h"
#include "malloc.h"
#include <stdlib.h>
#include "fermi.h"
using namespace std;
float const pi = 3.14159265359;

//variable to pass back and forth
struct globalthis din;
//somethign simular
struct pass2 cheese;

// this does the band structure
float __fastcall kenergy(float kx, float ky, float p) {
    float kyl, kx1, out;
    float t1, t2, t3, t4, t5, mu, a;
    kyl=ky*pi;
    kx1=kx*pi;
    t1=-0.5908;
    t2=0.0962;
    t3=-0.1306;
    t4=-0.0507;
    t5=0.0939;
    //2201
    //t1=-0.130*2.0;
    //t2=0.040;
    //t3=-0.068;
    //t4=0.0;
    //t5=0.0;
    //mu=0.062;
    mu=p; //this changes doping orignal .1305 .16 is optimal
    // .100 for 408 data, underdoped 64k
    // .185 for run 147 guessed based off published paper slightly od
    a=1.0;
    out=t1*(cos(kx1*a)+cos(kyl*a))/2+t2*(cos(kx1*a)*cos(kyl*a))+mu+
        t3*(cos(2*kx1*a) + cos(2*kyl*a))/2+t4*(cos(2*kx1*a)*cos(kyl*a)
        + cos(kx1*a)*cos(2*kyl*a))/2+ t5*cos(2*kx1*a)*cos(2*kyl*a);
    return out;
}

//ACTUAL A(k,w)!
float __fastcall integrate(float en, float r, struct globalthis & gvar, float gammal,      ↵
    float gamma2, float D00, float B) {
    double gamma, gapm,tempgap, selfer, selfei,temp, xsize, ysize;
    xsize=(double) gvar.xsize;
    ysize=(double) gvar.ysize;
    gamma=gammal+gamma2*fabs(en);
    long double sum=0;
    r=1.0/(xsize*ysize);
    //en=(-1.0)*en;
    //this does the actuall loop, calcualting both the real and imaginary self
    energies in order to      ↵
    for(int ab=0;ab<xsize*ysize-1;ab++) {
        tempgap=(*gvar.gapm)[ab]*gvar.gaps;
        //figures out if the gap is bellow D00 so you can apply the asymetry
        if(fabs(tempgap) <= D00) {gapm=(*gvar.gapm)[ab]*gvar.gaps*B+(*gvar.gapm2)[ab]*      ↵
        gvar.gaps*(1.0-B);
        } else {
            gapm=gvar.gaps*(*gvar.gapm)[ab];
        }
        temp=(*gvar.emk)[ab];
        selfei=-gamma-gapm*gapm*gamma/((en+temp)*(en+temp)+gamma*gamma);
        selfer=gapm*gapm*(en+temp)/((en+temp)*(en+temp)+gamma*gamma);
        sum=sum-selfei*r/((en-temp-selfer)*(en-temp-selfer)+(selfei*selfei));
    }
}

```

```

E:\akw\fermi.cpp
}
    //memmory mangament
    _heapmin;
    return fabs(sum); //does the actual intergration, all stuff needed in cheese.
}

//small program to search arrays
int __fastcall searchme(valarray <float> &x, int b) {
    int end=x.size();
    float w;

    if(b==1) w=x.min();
    if(b==2) w=x.max();
    for (int y=0; y<=end; y++) {
        if (w== x[y]) {
            return y;
        }
    }

    for (int y=0; y<=end; y++) {
        if (floor(w)*100== floor(100*x[y])) {
            return y;
        }
    }

    for (int y=0; y<=end; y++) {
        if (abs(w)==abs(x[y])) {
            return y;
        }
    }
    return -1;
}
//reverses arrays
valarray <float> __fastcall reverseval(valarray <float> x) {
    valarray <float> b(x.size());
    int q=x.size();
    for( int i=0; i<q; i++) {
        b[i]=x[q-1-i];
    }
    return b;
}

//generates spectra
float * __fastcall ldos(valarray<float> &x, float gam, float gaps ,float r, struct
globalthis & gvar, float gam2, float D00, float percent) {

    float pooo=0.0, *half;
    int length;
    int i,p,q,s,si, a;
    //these are for double sided spectra which no longer work with this code
    p=gvar.p ; //simple search for the min and mx, used for extracting half a x axis ↵
    from a full
    q=gvar.q;
    if(p>500) {
        p=x.size()/2.0-1;
        q=0;
    }
    if(p<0) {
        p=0;
        q=x.size()-1;;
    }

    (gvar).gaps=gaps; //throws the gap into the structure
    if(p<q+1) (*gvar.xa)=x[slice(p,q+1,1)]; //these pull out half the x axis
}

```

```

E:\akw\fermi.cpp
else ((*gvar.xa)=x[slice(q,p+1,1)];
if(fabs((*gvar.xa)[0]) > fabs((*gvar.xa)[abs(p-q)])) {
    (*gvar.xa)=reverseval((*gvar.xa));
} //reverses the x axis if its backwards, so that the direction is
i=0;
//does the integration for each individual points
r=1.0/((float) gvar.xsize*gvarysize);
for(i=0;i < (*gvar.xa).size();i++) {
    gvar.half[i]=integrate((*gvar.xa)[i],r, gvar, gam, gam2, D00, percent); //does the
    work
}

return gvar.half;
}

//called by the fitting routine generates curves by taking all passing variables and
passing them
void dosfit(float *p, float *x, int m, int n, void *data) {
    float q=0, *tempout;
    int i=0;
    din=(globalthis *) data;
    valarray<float> in((*din.pass).x,(*din.pass).l);
    // q=1/( (float) (*(*din.pass).gapf).size());
    tempout=ldos(in,p[2],p[1],q, din, p[4],p[5],p[6]);
    for(int i=0; i<(*din.pass).l;i++) {
        x[i]=tempout[i]*p[0]+(*din.pass).x[i]*p[3];
    }
}

//fitting routine, calls correct fitting code and passes back the output
float * fitme(struct globalthis & gvar, float *input, int loops, float *p, float *low, float *high, float *opts, float * data) {
    void *adata;
    int po,i,n,q,l,zl;
    float info[9];
    //cout << LM_INFO_SZ << endl;
    adata=&gvar; //throws the passing structure into a void array to pass through the
    fitting program
    /*opts[0]=1E-03; //default 1E-03 LM_INIT_MU
    opts[1]=1E-17; //default 1E-17 LM_STOP_THRESH
    opts[2]=1E-17; //default 1E-17 LM_STOP_THRESH
    opts[3]=1E-17; //default 1E-17 LM_STOP_THRESH
    opts[4]=1E-3; //default 1E-06 LM_DIFF_DELTA */
    po=slevmar_bc_dif(dosfit, p, input, 7, (*gvar.pass).l, low, high, loops, opts, info, NULL, NULL, adata);
    for(i=0;i<7;i++) data[i]=p[i];
    for(i=0;i<7;i++) data[7+i]=info[i]; //puts the data into the idl ptr, and ends
    //cout << "# of eval " << info[7] << endl;
    return data;
}

```

```

C:\Documents and Settings\aaardvark....C-code\Visual Studio 2005\dos-full\main.cpp 1

#include <cmath>
#include <stdio.h>
#include <algorithm>
#include "lm.h"
#include "malloc.h"
#include "nr.h"
#include "numericalrecipes.h"
#include "stdafx.h"
#include <stdlib.h>
#include "fermi.h"
#include <stddef.h>
#include "TopoMetrix.h"
#include <string>
#include <time.h>
#include <sys/types.h>
#include <sys/timeb.h>

using namespace std;

float const pi = 3.14159265359;

int main(int argc, char *argv[]) {

//read in text file with prefs, input file name, output file name, loops, high, low limits
//EPS, opts, gapmap file
    string filename;
    filename=argv[1];
    char *inputname, *outputname, *gapmapname, *temp, *p;
    float EPS, high[5], low[5], opts[5], opts2[5];
    int loops, i=0,o;
    BOOL t;
    ifstream file (filename.c_str());
    if (! file) {
        // NO, abort program
        cerr << "can't open input file \\" " << filename << "\\"
            << endl;
        exit (EXIT_FAILURE);
    }

//reads in the preferane file, where it gets limits, chemical potential, and path
//information
    inputname=(char *) malloc(sizeof(char)*100);
    file.getline(inputname,100);
    inputname=(char *) realloc(inputname,file.gcount()*sizeof(char));
    outputname=(char *) malloc(sizeof(char)*100);
    file.getline(outputname,100);
    outputname=(char *) realloc(outputname,file.gcount()*sizeof(char));
    gapmapname=(char *) malloc(sizeof(char)*100);
    file.getline(gapmapname,100);
    gapmapname=(char *) realloc(gapmapname,file.gcount()*sizeof(char));

    temp=(char *) malloc(10*sizeof(char));
    for(i=0;i<5;i++) {
        temp=(char *) realloc(temp,10*sizeof(char));
        file.get(temp, 10, ',');
        temp=(char *) realloc(temp,file.gcount()*sizeof(char));
        file.ignore();
        high[i]=atof(temp);
    }
    for(int i=0;i<5;i++) {
        temp=(char *) realloc(temp,10*sizeof(char));
        file.get(temp, 10, ',');
        temp=(char *) realloc(temp,file.gcount()*sizeof(char));
        file.ignore();
        low[i]=atof(temp);
    }
}

```

```

C:\Documents and Settings\aaardvark....C-code\Visual Studio 2005\dos-full\main.cpp 2
    for(int i=0;i<5;i++) {
        temp=(char *) realloc(temp,10*sizeof(char));
        file.get(temp, 10, ',');
        temp=(char *) realloc(temp,file.gcount()*sizeof(char));
        file.ignore();
        opts[i]=atof(temp);
        opts2[i]=opts[i]*0.1;
    }
    temp=(char *) realloc(temp,100*sizeof(char));
    file.getline(temp, 100);
    file.getline(temp, 100);
    temp=(char *) realloc(temp,file.gcount()*sizeof(char));
    EPS=atof(temp);
    temp=(char *) realloc(temp,100*sizeof(char));
    file.getline(temp,100);
    temp=(char *) realloc(temp,file.gcount()*sizeof(char));
    loops=atof(temp);
    file.close();
}

//read in gap + lfl file sets up output files, all from jinho
SCANPARAMSSIMPLE inpath;
SCANPARAMSSIMPLE gaph;

bool test;
CFile inp;
CFile gapp;

DOCUMENTINFO inpd;
DOCUMENTINFO gapd;
CTFRFile input;
CTFRFile gapmap;
test=inp.Open((const char *) inputname,CFile::modeRead);
input.ReadDocumentInfo(inpd,inp); //THIS MUST BE IN THIS ORDER!?
input.ReadScanParamsSimple(inpath,inp);
inp.Close();
test=gapp.Open((const char *) gapmapname,CFile::modeRead);
gapmap.ReadDocumentInfo(gapd,gapp);
gapmap.ReadScanParamsSimple(gaph,gapp);
gapp.Close();
test=input.OpenFile(inputname);
test=gapmap.OpenFile(gapmapname);

//sets up for the fits, generates energies
float *data, *tout, *output, *outputt, start[5], startb[5], *t1,*t2,*t3,*t4,*t5,*t6,* tc, *t7, *xa, maxa[7], mina[7],tf1;
//sets up output files as needed
output=new float[14];
outputt=new float[14];
data=new float[input.nosts];
tout=new float[input.nosts];
xa=new float[input.nosts];
t1=new float[input.noypixels*input.noypixels];
for(int i=0;i<7;i++) {
    //initializes the max and min arrays, important for writing files.
    maxa[i]=-100.0;
    mina[i]=100.0;
}
t2=new float[input.noypixels*input.noypixels];
t3=new float[input.noypixels*input.noypixels];
t4=new float[input.noypixels*input.noypixels];
t5=new float[input.noypixels*input.noypixels];
t6=new float[input.noypixels*input.noypixels];
t7=new float[input.noypixels*input.noypixels];
tc=new float[input.noypixels*input.noypixels*input.nosts];

//sets up the files to store the fermi surface, sets up two,

```

```

C:\Documents and Settings\aaardvark....C-code\Visual Studio 2005\dos-full\main.cpp 3

valarray<float> zerokx1;
valarray<float> zeroky1;
valarray<float> zerokx2;
valarray<float> zeroky2;
valarray<float> gapf1,gapf2;
valarray<float> x(input.nosts);
xa=new float[input.nosts];
for(int i=0;i<input.nosts;i++) {
    //makes the energy axis file
    x[i]=(input.stsend-input.stsstart)/(input.nosts-1)*i+input.stsstart;
    xa[i]=x[i];
}
//sets up some structures to pass data, these get referenced inside the global gvar
variable passgen structure.
struct pass2 fitdata1, fitdata2;
int zerounum=input.nosts/2+1;
//generates the zero axis...
o=gen_energy(0.001,0.0,&zerokx1,&zeroky1);
o=gen_energy(0.0005,0.0,&zerokx2,&zeroky2);
zerokx1=zerokx1*pi; //they all need pi
zeroky1=zeroky1*pi;
zerokx2=zerokx2*pi;
zeroky2=zeroky2*pi;
//resizes the gap storage array
gapf1.resize(zerokx1.size());
//then stores the gap and transfers it into fitdatas
gapf1=zerokx1.apply(cos)-zeroky1.apply(cos); //evaluate the gap so it only has to be done once
fitdata1.gapf=&gapf1;
fitdata1.x=&xa;
fitdata1.l=input.nosts;
fitdata2.x=fitdata1.x;
fitdata2.l=fitdata1.l;
for(int i=0;i<input.nosts;i++) x[i]=fitdata1.x[i];
gapf2.resize(zerokx2.size());
gapf2=zerokx2.apply(cos)-zeroky2.apply(cos);
fitdata2.gap=&gapf2;
//following makes and initializes global structure
struct globalthis gvara;
//more initialization of variables arrays used latter, as well as the temp half and full
store files, dumps them into the global
valarray<float> xab1;
valarray<float> xal(51);
valarray<complex<float> >xao1(51);
complex<float> out;
float *half, *full;
half=(float *) malloc(51*sizeof(float));
full=(float *) malloc(100*sizeof(float));
gvara.half=half;
gvara.full=full;
gvara.EPS=EPS;
gvara.xab=&xab1;
gvara.xa=&xal;
gvara.xao=&xao1;

//this sets up a status file to write crap too
char tmpbuf[9];
char dbuffer [9];

string tempfilename;
tempfilename=outputname;
tempfilename = tempfilename + "status.txt";
ofstream filea (tempfilename.c_str());
if (! file) {
    // NO, abort program
}

```

```

C:\Documents and Settings\aaardvark....C-code\Visual Studio 2005\dos-full\main.cpp 4
        cerr << "can't open status file \" " << filename << "\" "
        << endl;
        exit (EXIT_FAILURE);
    }

    filea.write("Start ",6);
    _strtime( tmpbuf );
    _strdate( dbuffer );
    filea.write(tmpbuf,9);
    filea.write(" ",1);
    filea.write(dbuffer,9);
    filea.put(10);
    filea.flush();
    char *pas;
    pas=new char[3];
    float zerotemp;

//does actuall fits, goes through all points, pulls data, fits, then fits, generates
//curves, and ends
    for(int xx=0;xx<input.noxpixels;xx++) {
        for(int yy=0;yy<input.noxpixels;yy++) {
            for(int i=0;i<input.nosts;i++) {
                //grabs the data
                data[i]=input.GetConductanceFromRawData(input.GetData(xx,yy,i));
            }
            gvara.pass=&fitdata1;
            gvara.EPS=EPS;
            //does a number of loops with different starting conditions
            for(int ioo=0;ioo<11;ioo++) {
                if(ioo==0) {
                    start[0]=fabs(input.GetConductanceFromRawData(input.GetData(xx,yy,0)));
                ; //prefactor
                    start[1]=fabs(gapmap.GetConductanceFromRawData((unsigned short) xx+gapmap.noxpixels*yy)); //gap
                    start[2]=0.005*start[1]+0.0001; //alpha
                    start[3]=0.0; /slope
                    //gammal starts related to the zero bias conductance
                    start[4]=fabs(input.GetConductanceFromRawData(input.GetData(xx,yy,zeronum))); //gammal
                    for(int u=0;u<5;u++) startb[u]=start[u];
                }
                //if(ioo==1) {
                //    for(int u=0;u<5;u++) start[u]=startb[u];
                //    start[1]=(float) startb[1]*1.5;
                //}
                if(ioo==1) {
                    for(int u=0;u<5;u++) start[u]=startb[u];
                    start[1]=(float) startb[1]*2.0;
                }
                if(ioo==2) {
                    for(int u=0;u<5;u++) start[u]=startb[u];
                    start[1]=(float) startb[1]*0.5;
                }
                //if(ioo==4) {
                //    for(int u=0;u<5;u++) start[u]=startb[u];
                //    start[1]=(float) startb[1]*0.666;
                //}
                if(ioo==3) {
                    for(int u=0;u<5;u++) start[u]=startb[u];
                    start[4]=0.0;
                }
                if(ioo==4) {
                    for(int u=0;u<5;u++) start[u]=startb[u];
                    start[2]=0.0001;
                }
                if(ioo==5) {
                    for(int u=0;u<5;u++) start[u]=startb[u];
                }
            }
        }
    }
}

```

```

C:\Documents and Settings\aaardvark....C-code\Visual Studio 2005\dos-full\main.cpp      5
        start[2]=0.2;
    }
    //if(ioo==6) {
    //  for(int u=0;u<5;u++) start[u]=startb[u];
    //  start[1]=(float) start[1]*0.5;
    //  start[4]=0.0;
    //  start[2]=0.2;
    //}
    if(ioo==6) {
        for(int u=0;u<5;u++) start[u]=startb[u];
        start[1]=start[1]*0.5;
        start[2]=0.0001;
    }
    if(ioo==7) {
        for(int u=0;u<5;u++) start[u]=startb[u];
        start[1]=start[1]*0.5;
        start[4]=0.0;
    }
    if(ioo==8) {
        for(int u=0;u<5;u++) start[u]=startb[u];
        start[1]=start[1]*0.5;
        start[2]=0.0001;
    }
    if(ioo==9) {
        for(int u=0;u<5;u++) start[u]=startb[u];
        start[1]=start[1]*2.0;
        start[4]=0.0;
    }
    if(ioo==10) {
        for(int u=0;u<5;u++) start[u]=startb[u];
        start[1]=start[1]*2.0;
        start[2]=0.0001;
    }
    //if(ioo==12) {
    //  for(int u=0;u<5;u++) start[u]=startb[u];
    //  start[1]=start[1]*2.0;
    //  start[4]=0.0;
    //  start[2]=0.2;
    //}
    if(ioo==11) {
        for(int u=0;u<5;u++) start[u]=startb[u];
        start[1]=start[1]*2.0;
        start[2]=0.2;
    }
    //if(ioo==16) {
    //  for(int u=0;u<5;u++) start[u]=startb[u];
    //  start[4]=0.0;
    //  start[2]=0.2;
    //}
    //the fit
    for(int u=0;u<5;u++) {
        //makes sure the starting values aren't outside out limits casues code to crash if not done
        if(start[u]>high[u]) start[u]=high[u];
        if(start[u]<low[u]) start[u]=low[u];
    }
    //calls fitting function
    outputt=fitme(gvara,data,loops,start,low,high,opts);
    //stores it in our temp output if iteration zero, if nto zero, sees if the chi-square is smaller and if so stores it
    if(ioo==0) for(int xae=0;xae<14;xae++) outputt[xae]=outputt[xae];
    if(outputt[6]<outputt[6]) {
        for(int xae=0;xae<14;xae++) outputt[xae]=outputt[xae];
        //stores the iteration that was selected to be the best for optimizartion purposes
        t7[xx+input.noxpixels*yy]=ioo;
    }
}

```

```

C:\Documents and Settings\Aardvark....C-code\Visual Studio 2005\dos-full\main.cpp 6
//uses the lowest error from above to run a longer interation fit.

}

for(int a=0;a<5;a++) start[a]=output[a];
//starts a final fit that requires a higher convergance
output=fptime(gvara,data,loops,start,low,high,opts2);
cout <<xx << " " << yy << endl;
//dumps the data
//generates curves based off above fit
t1[xx+input.noypixels*yy]=output[0];
if(maxa[0]<output[0]) maxa[0]=output[0];
if(mina[0]>output[0]) mina[0]=output[0];
t2[xx+input.noypixels*yy]=output[1];
if(maxa[1]<output[1]) maxa[1]=output[1];
if(mina[1]>output[1]) mina[1]=output[1];
t3[xx+input.noypixels*yy]=output[2];
if(maxa[2]<output[2]) maxa[2]=output[2];
if(mina[2]>output[2]) mina[2]=output[2];
t4[xx+input.noypixels*yy]=output[3];
if(maxa[3]<output[3]) maxa[3]=output[3];
if(mina[3]>output[3]) mina[3]=output[3];
t5[xx+input.noypixels*yy]=output[4];
if(maxa[4]<output[4]) maxa[4]=output[4];
if(mina[4]>output[4]) mina[4]=output[4];
t6[xx+input.noypixels*yy]=output[6];
if(maxa[5]<output[5]) maxa[5]=output[6];
if(mina[5]>output[5]) mina[5]=output[6];
float r=1/( float ) (*fitdata2.gapf).size();
gvara.pass=&fitdata2;
gvara.EPS=1E-6;
//generates the fit return at a high precision level
tout=ldos(x, output[2], output[1] ,r , gvara, output[4]);
for(int i=0; i<input.nosts;i++) {
    tfl=tout[i]*output[0]+x[i]*output[3];
    tc[xx+input.noypixels*yy+input.noypixels*input.noypixels*i]=tfl;
    if(tfl>maxa[6]) maxa[6]=tfl;
    if(tfl<mina[6]) mina[6]=tfl;
}
//deletes the output, reformed each time to make sure we don't get mixed up ↵
with old variables
delete[] output;
}
//writes status file
filea.write("Line ",6);
ltoa(xx,pas,10);
if(xx<10) filea.write(pas,1);
if(xx>=10) if(xx<100) filea.write(pas,2); else filea.write(pas,3);
filea.write(" end ",5);
_strftime( tmpbuf );
_strdate( dbuffer );
filea.write(tmpbuf,9);
filea.write(" ",1);
filea.write(dbuffer,9);
filea.put(10);
filea.flush();
}
filea.close();
//saves actual files
unsigned short *outdata, *outdata2;
outdata=new unsigned short[input.noypixels*input.noypixels];
outdata2=new unsigned short[input.noypixels*input.noypixels*input.nosts];
CString tempstring, tempfilename;
tempfilename=outputname;

tempstring.Format("1factor");
tempfilename = tempfilename.SpanExcluding(".") + tempstring + ".tfr";

```

```

C:\Documents and Settings\aaardvark....C-code\Visual Studio 2005\dos-full\main.cpp 7
tempstring.Format("prefactor");
strcpy(gapd.szDescription,(const char*)tempstring);
gapd.fDACtoWorld=(maxa[0]-mina[0])/pow(2,16);
gaph.fScanZmax=maxa[0];
gaph.fScanZmin=mina[0];
gapd.iDACDisplayZero = mina[0]/gapd.fDACtoWorld;
gapd.fDACtoWorldZero = mina[0];
gapd.iDACDisplayRange = pow(2,16);
gapd.iDACmax = pow(2,16);
gapd.iDACmin = 0;
gapd.iDACDisplayZero=0; // [333..334] z adjust zero point in DAC units
gapd.iDACDisplayRange=pow(2,16);
gapd.iCols=gapmap.noypixels;
gapd.iRows=gapmap.noypixels;
gapd.iWorldUnitType = 1;
gapd.iLayers = 1;
gapd.bHasBkStrip = 0;
gapd.iTilt = 1;
for(int n=0;n<8;n++) gapd.dTiltC[n] = 0; // {0,0,0,0,0,0,0,0};
gaph.iDataType = 5; // ?
gaph.iDataMode = 6; // ?
gaph.iADC = 0;
gaph.iLayers = 1;

for(int i=0;i<input.noypixels*input.noypixels;i++) outdata[i]=(t1[i]-mina[0])/(maxa[0]-
-mina[0])*pow(2,16);
input.SaveTFFFile(tempfilename,gapd,gaph, outdata);

tempstring.Empty();
tempfilename=outputname;
tempstring.Format("2CapValue");
tempfilename = tempfilename.SpanExcluding(".") + tempstring + ".tfr";
tempstring.Format("Gap Value");
strcpy(gapd.szDescription,(const char*)tempstring);
gapd.fDACtoWorld=(maxa[1]-mina[1])/pow(2,16);
gaph.fScanZmax=maxa[1];
gaph.fScanZmin=mina[1];
gapd.iDACDisplayZero = mina[1]/gapd.fDACtoWorld;
gapd.fDACtoWorldZero = mina[1];
for(int i=0;i<input.noypixels*input.noypixels;i++) outdata[i]=(t2[i]-mina[1])/(maxa[1]-
-mina[1])*pow(2,16);
input.SaveTFFFile(tempfilename,gapd,gaph,outdata);

tempstring.Empty();
tempfilename=outputname;
tempstring.Format("3Gamma2");
tempfilename = tempfilename.SpanExcluding(".") + tempstring + ".tfr";
tempstring.Format("Gamma 2");
strcpy(gapd.szDescription,(const char*)tempstring);
gapd.fDACtoWorld=(maxa[2]-mina[2])/pow(2,16);
gaph.fScanZmax=maxa[2];
gaph.fScanZmin=mina[2];
gapd.iDACDisplayZero = mina[2]/gapd.fDACtoWorld;
gapd.fDACtoWorldZero = mina[2];
for(int i=0;i<input.noypixels*input.noypixels;i++) outdata[i]=(t3[i]-mina[2])/(maxa[2]-
-mina[2])*pow(2,16);
input.SaveTFFFile(tempfilename,gapd,gaph,outdata);

tempstring.Empty();
tempfilename=outputname;
tempstring.Format("4Slope");
tempfilename = tempfilename.SpanExcluding(".") + tempstring + ".tfr";
tempstring.Format("Slope");
strcpy(gapd.szDescription,(const char*)tempstring);
gapd.fDACtoWorld=(maxa[3]-mina[3])/pow(2,16);
gaph.fScanZmax=maxa[3];
gaph.fScanZmin=mina[3];

```

```

C:\Documents and Settings\aaardvark....C-code\Visual Studio 2005\dos-full\main.cpp 8
    gapd.iDADisplayZero = mina[3]/gapd.fDADtoWorld;
    gapd.fDADtoWorldZero = mina[3];
    for(int i=0;i<input.noxpixels*input.noypixels;i++) outdata[i]=(t4[i]-mina[3])/(maxa[3]-
    -mina[3])*pow(2,16);
    input.SaveTFFFile(tempfilename,gapd,gaph,outdata);

    tempstring.Empty();
    tempfilename=outputname;
    tempstring.Format("5Gamma1");
    tempfilename = tempfilename.SpanExcluding(".") + tempstring + ".tfr";
    tempstring.Format("Gamma ");
    strcpy(gapd.szDescription,(const char*)tempstring);
    gapd.fDADtoWorld=(maxa[4]-mina[4])/pow(2,16);
    gaph.fScanZmax=maxa[4];
    gaph.fScanZmin=mina[4];
    gapd.iDADisplayZero = mina[4]/gapd.fDADtoWorld;
    gapd.fDADtoWorldZero = mina[4];
    for(int i=0;i<input.noxpixels*input.noypixels;i++) outdata[i]=(t5[i]-mina[4])/(maxa[4]-
    -mina[4])*pow(2,16);
    input.SaveTFFFile(tempfilename,gapd,gaph,outdata);

    tempstring.Empty();
    tempfilename=outputname;
    tempstring.Format("6Error");
    tempfilename = tempfilename.SpanExcluding(".") + tempstring + ".tfr";
    tempstring.Format("Error");
    strcpy(gapd.szDescription,(const char*)tempstring);
    gapd.fDADtoWorld=(maxa[5]-mina[5])/pow(2,16);
    gaph.fScanZmax=maxa[5];
    gaph.fScanZmin=mina[5];
    gapd.iDADisplayZero = mina[5]/gapd.fDADtoWorld;
    gapd.fDADtoWorldZero = mina[5];
    for(int i=0;i<input.noxpixels*input.noypixels;i++) outdata[i]=(t6[i]-mina[5])/(maxa[5]-
    -mina[5])*pow(2,16);
    input.SaveTFFFile(tempfilename,gapd,gaph,outdata);

    tempstring.Empty();
    tempfilename=outputname;
    tempstring.Format("7startcon");
    tempfilename = tempfilename.SpanExcluding(".") + tempstring + ".tfr";
    tempstring.Format("Start Conditions");
    strcpy(gapd.szDescription,(const char*)tempstring);
    gapd.fDADtoWorld=(17)/pow(2,16);
    gaph.fScanZmax=17;
    gaph.fScanZmin=0;
    gapd.iDADisplayZero = 0;
    gapd.fDADtoWorldZero = 0;
    for(int i=0;i<input.noxpixels*input.noypixels;i++) outdata[i]=t7[i]/(17)*pow(2,16);
    input.SaveTFFFile(tempfilename,gapd,gaph,outdata);

    tempstring.Empty();
    tempfilename=outputname;
    tempstring.Format("fit");
    tempfilename = tempfilename.SpanExcluding(".") + tempstring + ".lfl";
    tempstring.Format("fit");
    strcpy(gapd.szDescription,(const char*)tempstring);
    inpd.fDADtoWorld=(maxa[6]-mina[6])/pow(2,16);
    inpush.fScanZmax=maxa[6];
    inpush.fScanZmin=mina[6];
    inpd.iDADisplayZero = mina[6]/inpd.fDADtoWorld;
    inpd.fDADtoWorldZero = mina[6];
    for(int i=0;i<input.noxpixels*input.noypixels*input.nosts;i++) outdata2[i]=(tc[i]-mina[6])/
    /(maxa[6]-mina[6])*pow(2,16);
    input.SaveLFLFileNew(tempfilename,inpd,inpush,input.noxpixels,input.noypixels,
    outdata2);

```

```
return 0;  
}
```

REFERENCES

¹ Lourakis, M.I.A. <http://www.ics.forth.gr/~lourakis/levmar/> (2004)

APPENDEX C

Initial Area Fitting Results

Introduction

Now that we have a successful model that allows us a complete parameterization of the electronic structure, we can attempt to map out these parameters as they vary in real space across our sample. This of course is a non-trivial task given the increased complexity of our model, as well as its poor numerical fitting characteristics; however I have made some initial progress towards a solution. The ability to get local information about the variables will allow us not only an increased data set to map out the relationship of parameters, but also the ability to see which ones vary continuously and which vary uniquely with doping, if any. This should help us map out the ranges in which phenomena exist and how they coexist in real space, especially the checkerboard and the ECG.

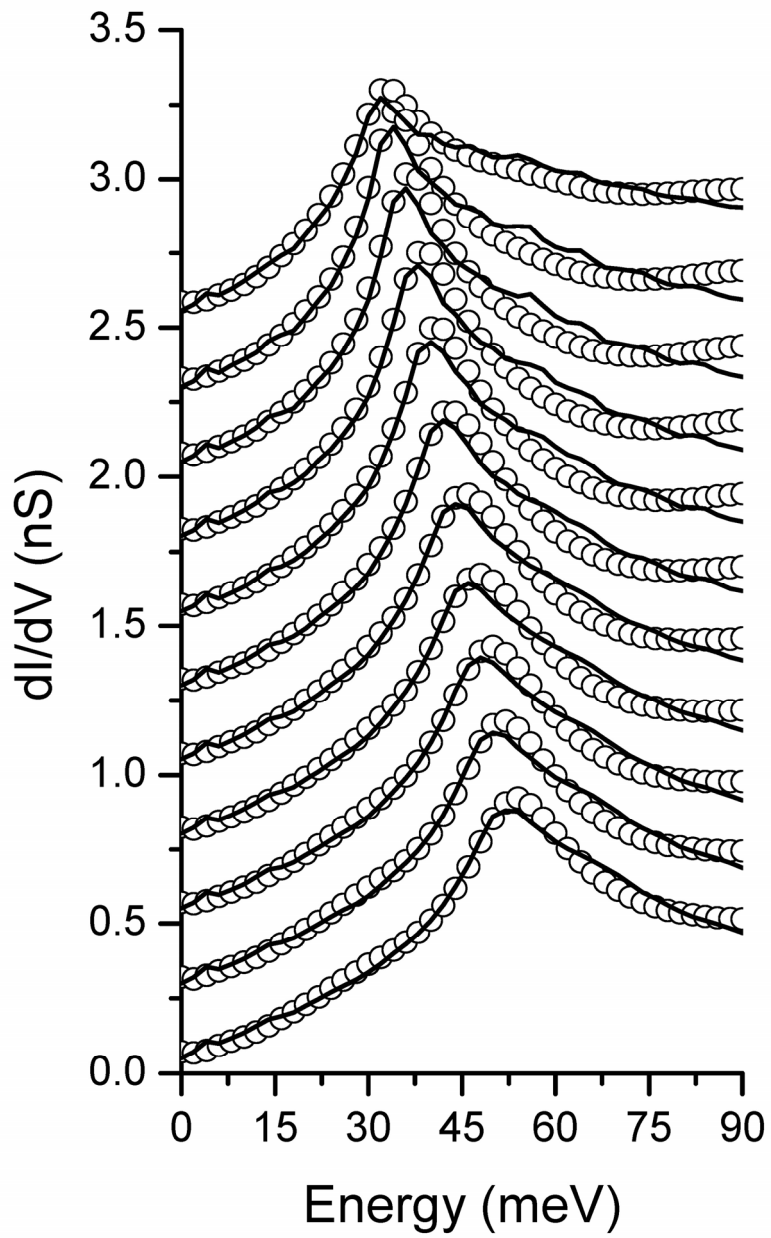
Our initial results show some interesting phenomena, although at this stage of the game it is hard to sort out what is real and what is an artifact of an immature fitting process. The fits however, do reproduce the data extremely well, and in fact subtracting the fits from the actual data removes the checkerboard and ECG signatures almost completely leaving just a QPI pattern in q-space. However in marching individual curves, the current code needs to be expanded, in order to ensure an appropriate fit. This will drive up the computation time needed, and unfortunately at the moment we are running at the largest practical time given the cluster size and load (~1-3 weeks per fit including waiting in queue).

Bi-2212

However we have some nice preliminary results, some of which meet our expectations from our individual curve fits, and some of which that don't. As of the moment it is a bit hard get the correct fit, however there is room for improvement within our computation limits, and while doubling the time to fit may be painful, it is quite doable if it is required. The main problem is the fact that the features are very small especially compared to other parts of the spectrum that may be superfluous to what we are trying to measure. This can be seen in figures AC-1 and AC-2, where the area difference between the fits and the data outside the gap for example, are much larger than any errors caused by a too small Δ_{00} .

The return for our fits gives us our usual assortment of parameters which are shown in figure AC-3 and AC-5 for UD65K and UD74K respectively. These compare very favorably to our previous model which can be seen in chapter 2. The Δ_1 values overall tend to underestimate the peak position by a couple meV, and this can be seen in figures AC-1 and AC-2 also. This is mainly at low Δ_1 values, where the fit runs into problems with the background outside the gap as well as poor resolution ink-sapce. This can probably be solved if we can apply a better model for our background, however this will no doubt add additional parameters which detract from the overall validness of our fits.

The Γ_1 channel picks up the zero bias density of states quite nicely and provides the locations of the zinc impurities and Cu vacancies in a similar way to the old fits. The alpha channel also reproduces the pattern of the old fits, although as we will see our new model allows a much better fit to the peaks at Δ_1 and no longer saturates at zero as our previous model did, in part due to a better model along with a problem with resolution in k-space at low lifetimes. Most unexpectedly the slope now displays a unique pattern. This resembles strongly clusters placed on a topographic



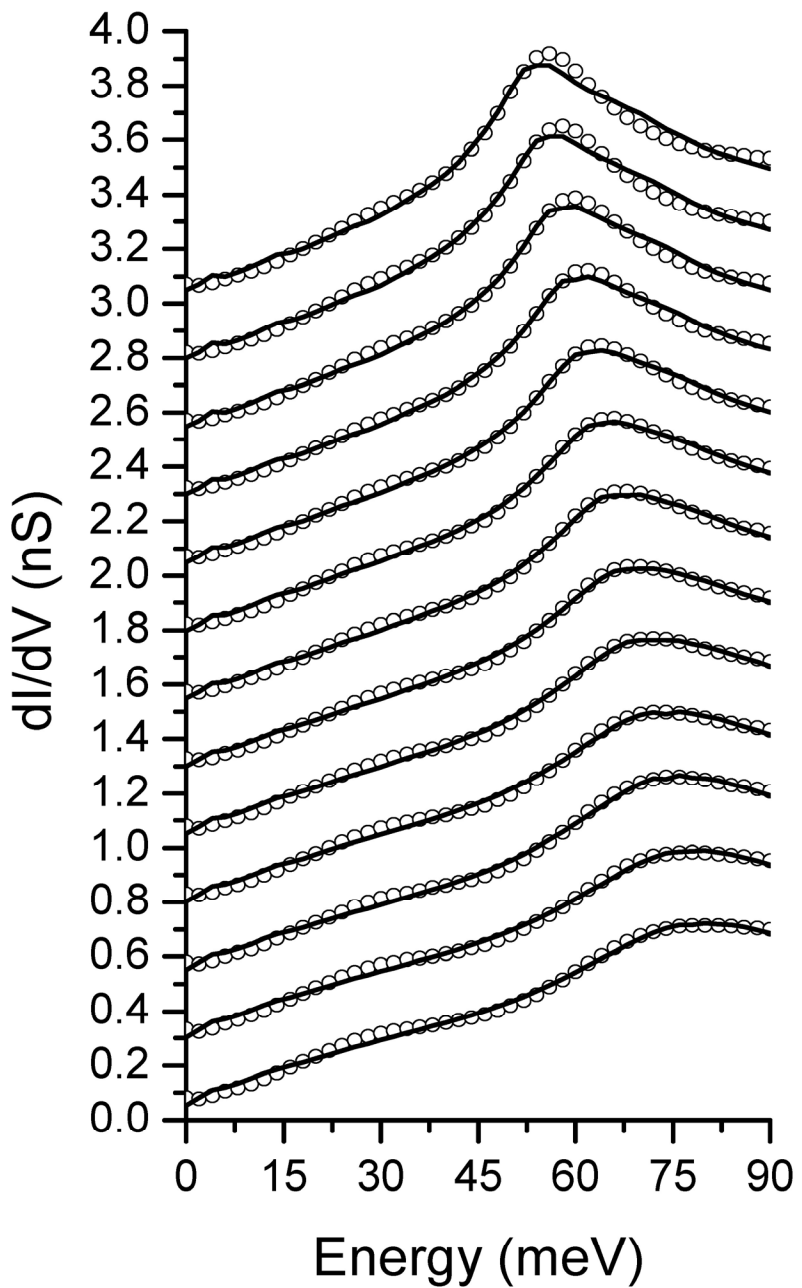


Figure AC-2: A continuation of figure AC-1 for higher Δ_1 values. Here there appears that B is underestimated for large Δ_1 values, this is probably due the limit of 0.7 enforced on B and hopefully will be corrected in the next version of the code.

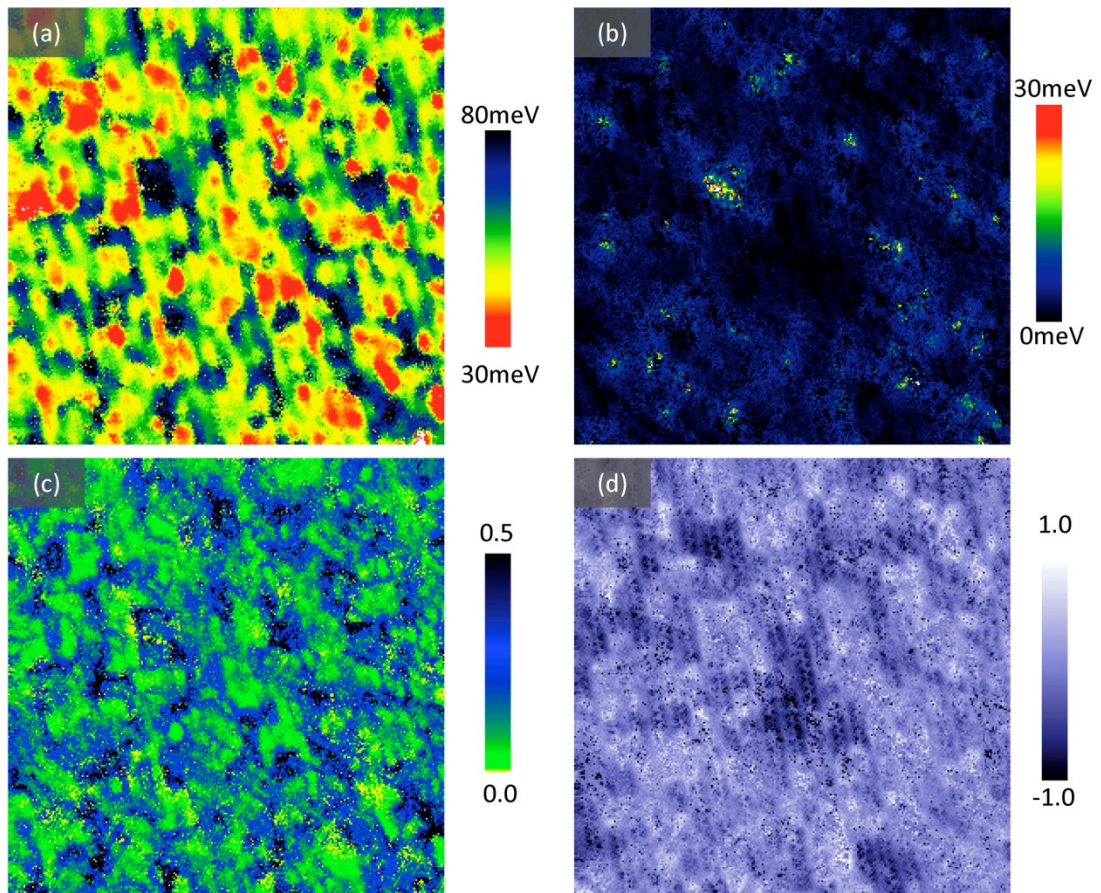


Figure AC-3: These are the initial fitting attempts for UD65K sample with zinc impurities. This can be favorably compared with the fitting results from our simplified model in chapter 2. (a) Δ_1 , which averages in a 52meV smaller than our peak to peak fitting as well as our previous fits. (b) Γ_1 , (c) α , (d) is the one sided slope, which looks rather like large clusters placed down on a background of super modulation.

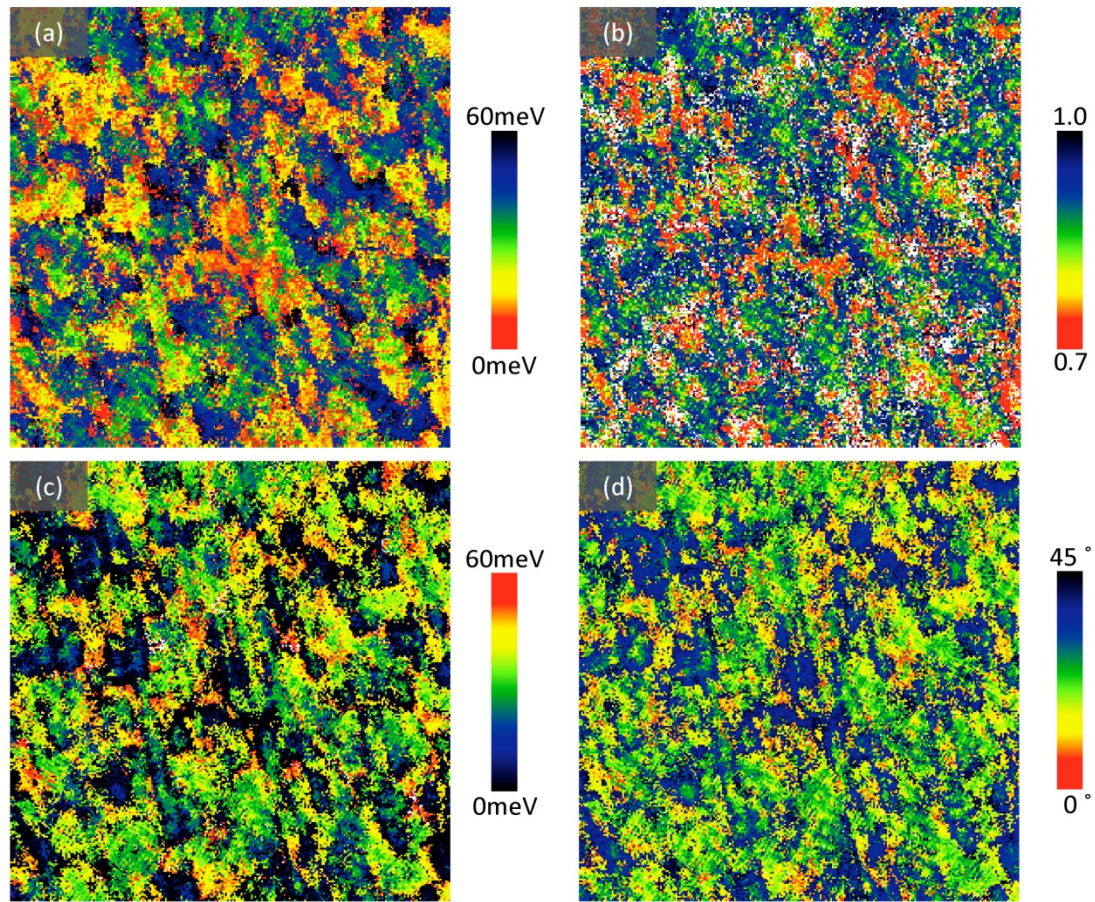


Figure AC-4: Our new fit parameters and derivatives. (a) Δ_{00} , (b) B , (c) Δ_0 , (d) Θ_{term} , which is the angle where given a constant μ the coherent quasiparticles would terminate. Δ_1 correlated with Δ_{00} is 0.345, Δ_1 with Δ_0 is 0.240, Δ_{00} with Δ_0 is 0.933.

background. You can make out the \$ signs, as well as bumps associated with supermodulation, but you have these large blobs. It would be very interesting if these are related to the oxygen atoms in any way. Since the pattern doesn't appear to correlate strongly with any other measurement. These can be seen in figure AC-3(d) and AC-5(d).

In figure AC- 4 and AC-6 we show the returns of our new parameters, these are overall very noisy right now, due mainly to the problems we have outlined above. We show the Δ_{00} pattern in (a) and the higher harmonic variation in B, both of these show some structure similar to the Δ_1 map, however they both contain vectors associated with Q_1 /the checkerboard. This modulation in these two parameters causes the fits to pick this and the ECG up, an obvious result when you consider previous work¹. It has been shown that the ECG pattern does indeed modulate the low energy peaks, therefore with enough spatial resolution we expect to see this also. However the patterns here bring to mind the patterns associated with the omega bosonic maps, and it will be interesting to see if there is any correlation. In (c) we show the Δ_0 or the smaller energy scale that since the B here seems to scale with Δ_{00} , we expect to see approach Δ_{00} in structure. In (d) we present the termination angle or Θ_{term} . This is the angle measured from the edge of the brillion zone, where Δ_0/Δ_{00} sits, and represents where the coherent low energy states are destroyed locally.

Figure AC-7 shows our initial fits for UD45K. Once again the Δ_1 fits look very much if not exactly like the ones in chapter 2. The gamma1 map is also unremarkable. However we can see a sort of patterning in the alpha channel in AC-7(c). This is probably due to it picking up modulations in Δ_1 associated with the ECG pattern. It is also worthy to note that in AC-7(d) our slope no longer appears to show oxygen clusters. This could be due to the fact that this data set had a setup condition on the

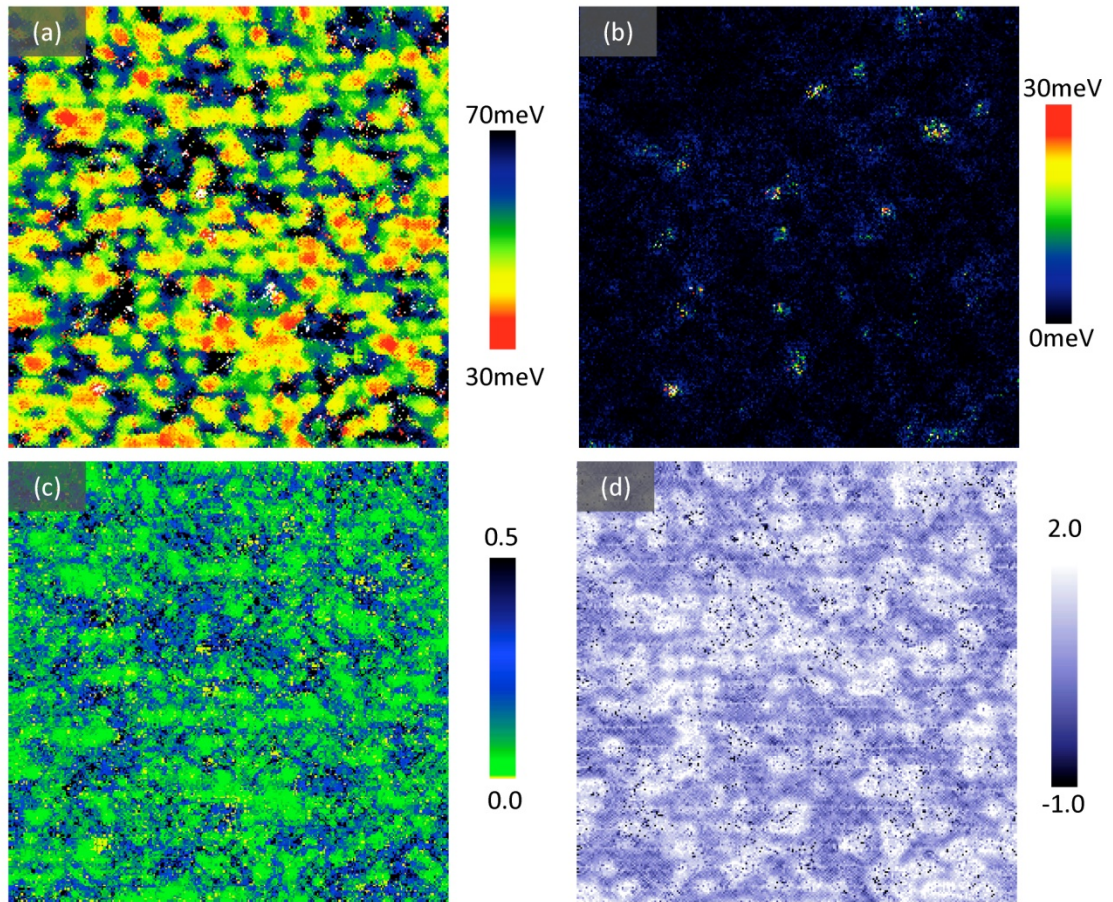


Figure AC-5: These are the initial fitting attempts for UD74K. This can be favorably compared with the fitting results from our simplified model in chapter 2. (a) Δ_1 , which averages in a 49meV smaller then our peak to peak fitting as well as our previous fits. (b) Γ_1 , (c) α , (d) is the one sided slope, which looks rather like large clusters placed down on a background of super modulation once again.

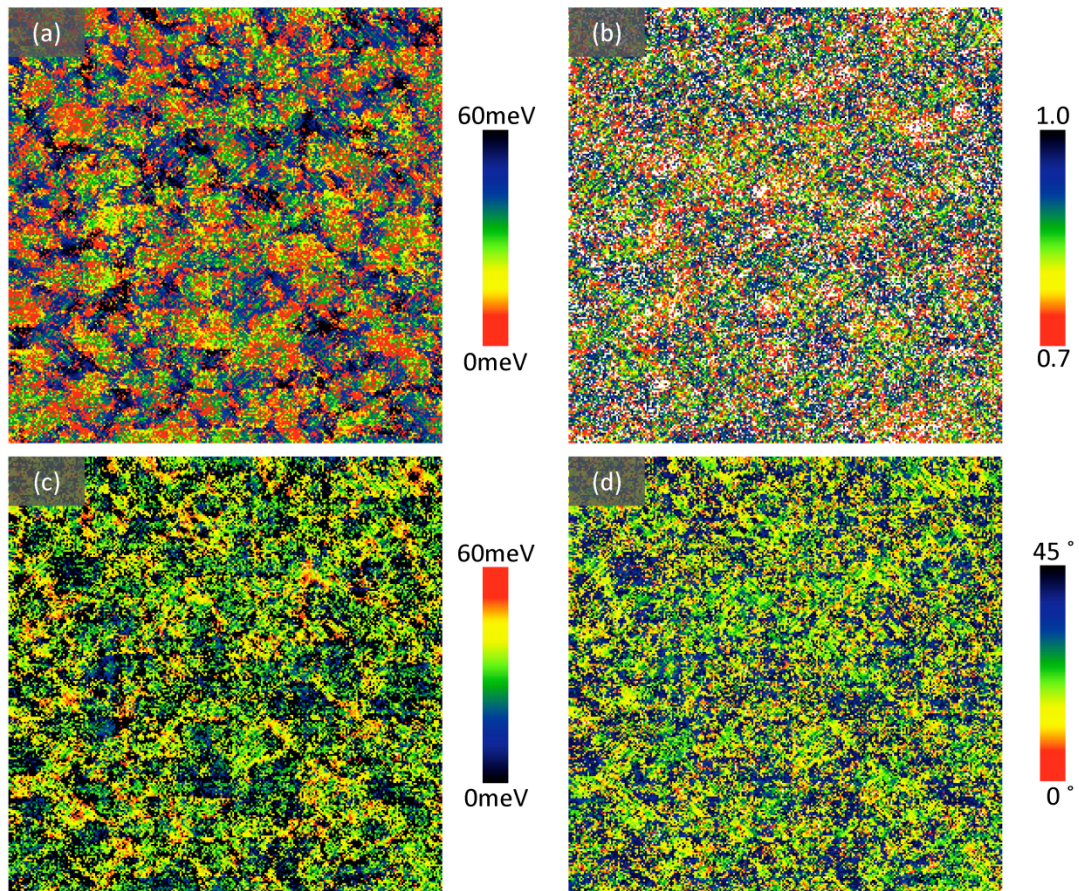


Figure AC-6: Our new fit parameters and derivatives. (a) Δ_{00} , (b) B , (c) Δ_0 , (d) Θ_{term} , which is the angle where given a constant μ the coherent quasiparticles would terminate. Δ_1 correlated with Δ_{00} is 0.432, Δ_1 with Δ_0 is 0.301, Δ_{00} with Δ_0 is 0.926.

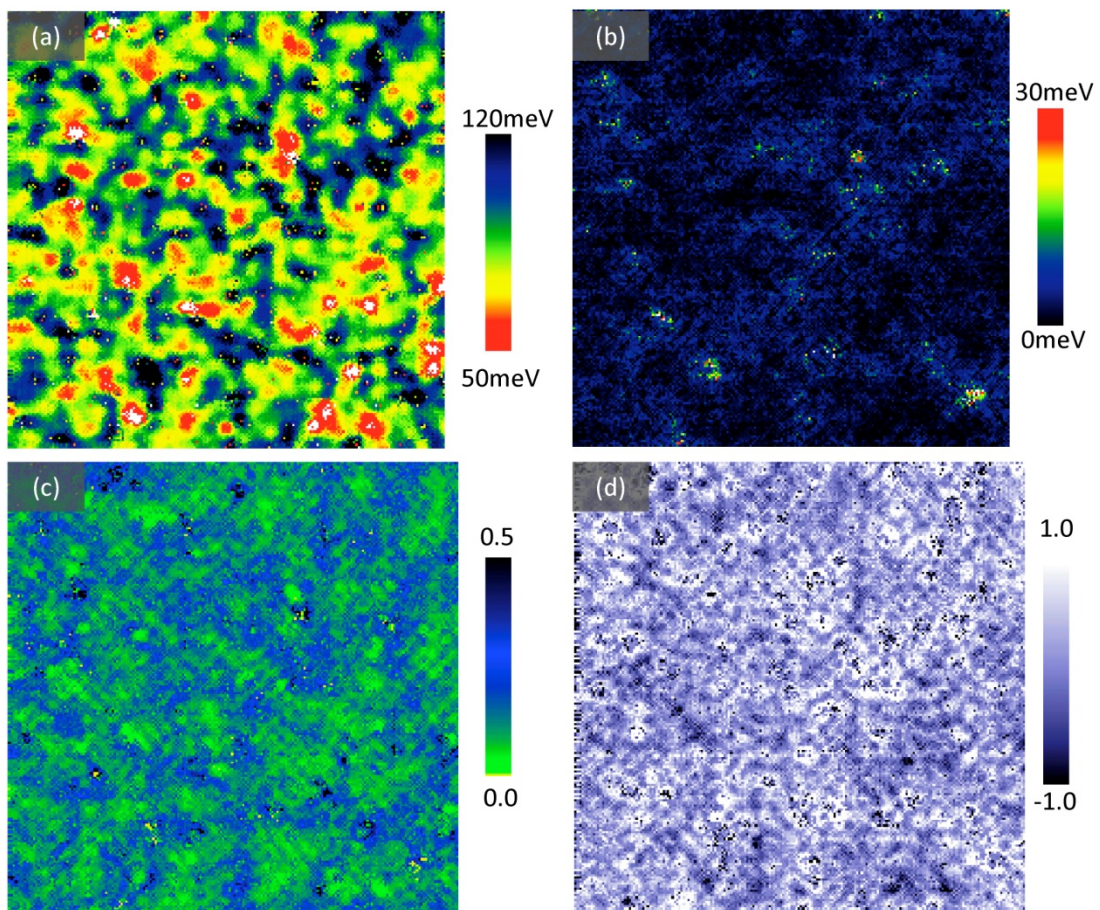


Figure AC-7: These are the initial fitting attempts for UD45K. This can be favorably compared with the fitting results from our simplified model in chapter 2. (a) Δ_1 (b) Γ_1 , (c), (d) is the one sided slope, which is a marked departure from the previous two, either due to lower doping effects, or because the data had a setup voltage on the positive side, instead of the negative side like the previous two.

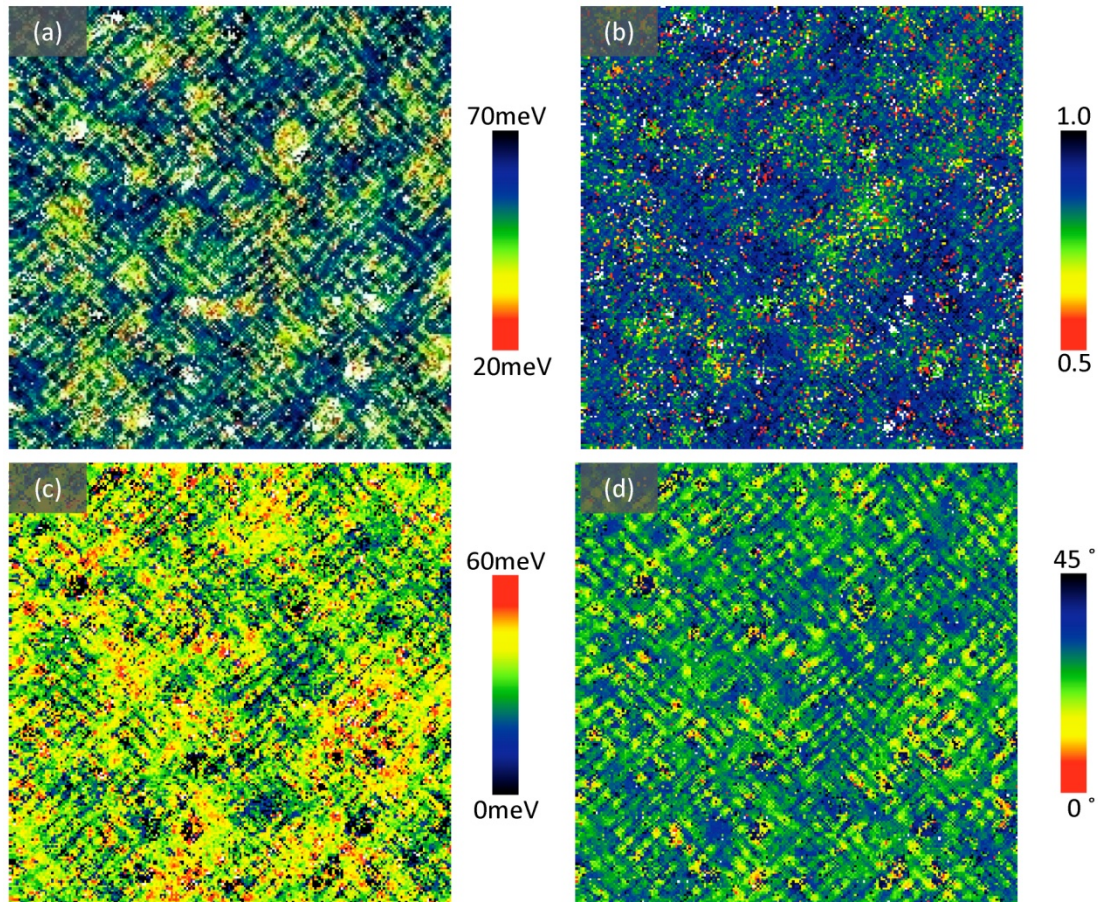


Figure AC-8: Our new fit parameters and derivatives for UD45K. (a) Δ_{00} , (b) B , (c) Δ_0 , (d) Θ_{term} , which is the angle where given a constant μ the coherent quasiparticles would terminate. Δ_1 correlated with Δ_{00} is 0.367, Δ_1 with Δ_0 is -0.05, Δ_{00} with Δ_0 is 0.717. Here we have set the limit of B as 0.5, instead of the previous 0.7.

positive side which might obscure the effect. Or it could be due to the onset of the ECG pattern which is dominating the higher energy states. In fact in this sample we see large effects due to the checkerboard pattern and/or the ECG. In AC-8(a) we see Δ_{00} shows a large scale background modulation, while also display a checkerboard modulation. It is unclear if this is an actual variation in this parameter or if it is the result of the checkerboard excitation. That is whether it is a real change in this parameter or weather the checkerboard pattern is causing an error in the fits due to its modulation in the region. In AC-8(b) we show the B term of our fits, which also has some checkerboard striping. This of course results in the termination angle and Δ_0 also having similar patterns. AC-8(c),(d).

We can start comparing our fits by looking at histograms and plots of various parameters vs others (notably Δ_1). In figure AC-9 we show the histogram of Δ_{00} and Δ_0 as a function of doping. We can see in AC-9(a) that Δ_{00} seems to grow larger with doping, while in AC- 9(b) we can see a small shift downwards in the Δ_0 distribution for UD45K. In figure AC-10 we show the B and the Θ_{term} histograms. The B for UD65K and UD74K shows some strange trends with UD64K being bigger then UD74K which is unexpected. However the UD45K sits at a lower value that is constant with the median gap averaged fit shown in chapter 4. In AC-10(b) we show the termination angle for all three dopings, which progress as one would expect with Θ_{term} increasing with decreasing doping. However there is a much larger jump then one would expect for the UD45K and the overall angle tends to be below what one would expect for intersection with the AF-zone boundary (dotted lines).

In figure AC-11, we investigate the relationship between Δ_1 and the two lower energy scales. In 11(a) we see that across all three dopings, there is a universal trend in Δ_{00} . However we would expect Δ_{00} to converge to Δ_1 at higher dopings. We suspect that this is caused by errors in fits at small gaps due to a limited resolution inside the

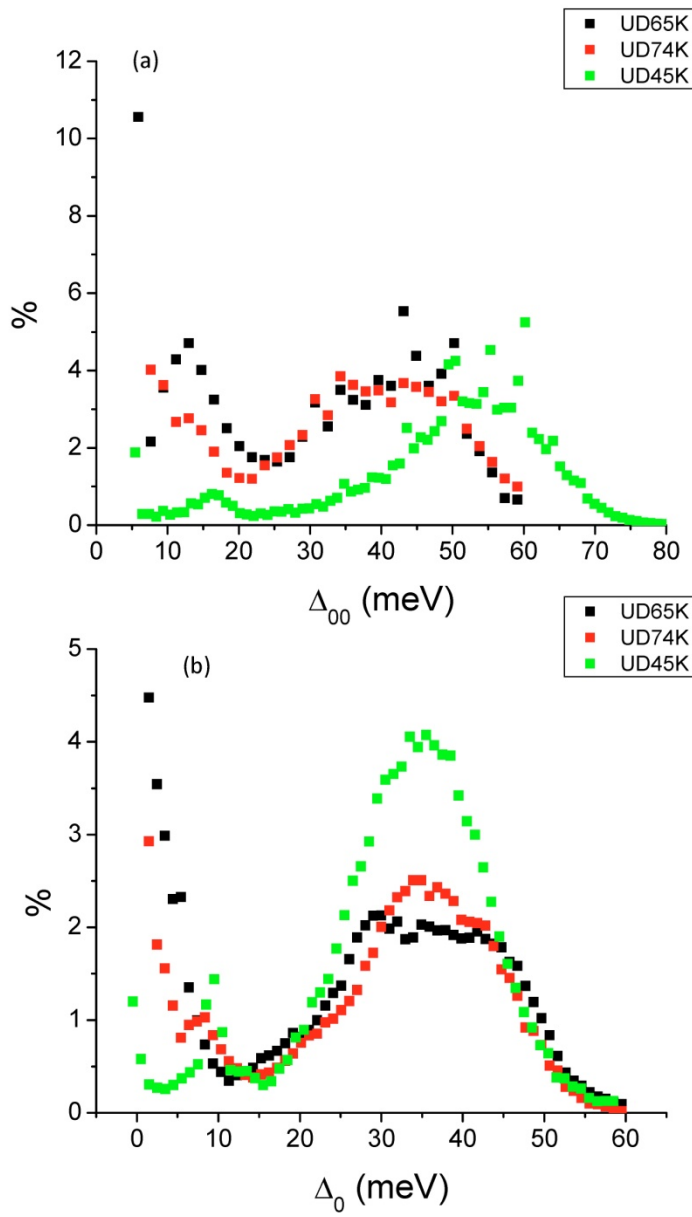


Figure AC-9: (a) histograms of our Δ_{00} parameter, showing the two distributions that are apparent in the maps. It is unclear if this is a fitting problem or not due to a high cap on the lower limit of B. This may be fixed in the UD45K sample which shows a marked decrease in the smaller distribution, of course this could just be due to a higher overall Δ_{00} value. (b) The Δ_0 parameter for the fits, the UD65K does show a shift downwards as expected as does UD45K.

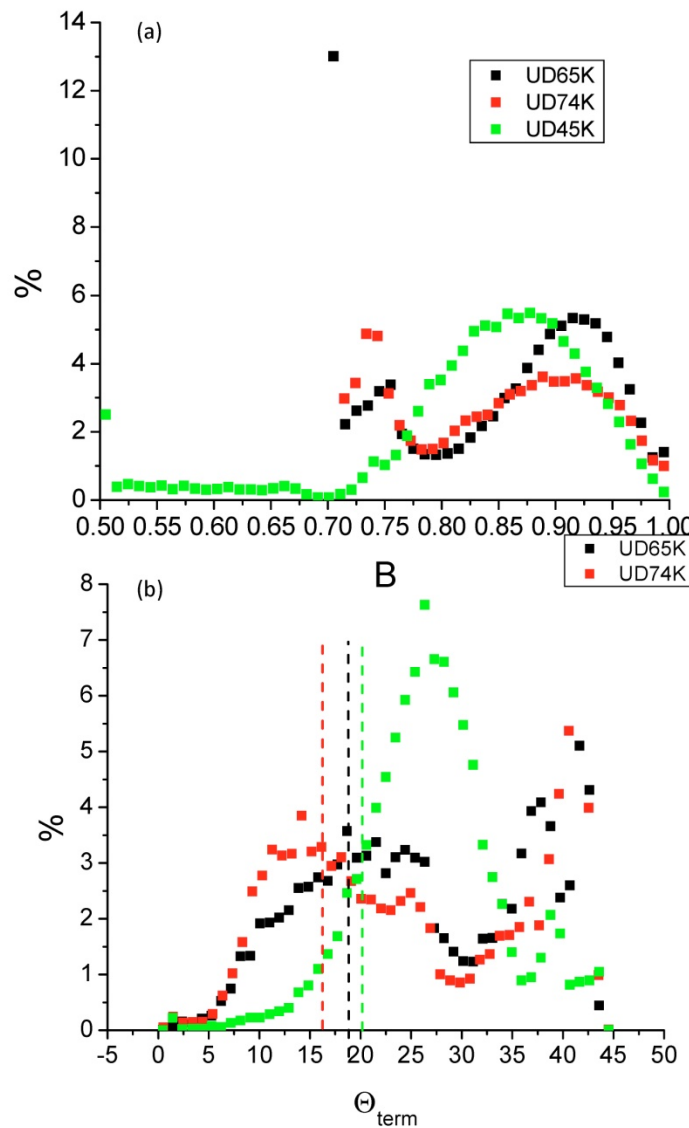


Figure AC-10: (a) B term histograms, showing somewhat unexpected behavior with a seemingly lower B for UD74K as opposed to UD65K. Could be related to the 10% or so of points sitting at 0.7. However the histogram for UD45K looks right, although surprisingly it shows two different behaviors divided at 0.7 (b) Termination angle for samples. The main lower valued bump scales as expected, with the calculated value for UD64K being 18.9° , and 16.1° for UD74K (marked by the dash lines). The higher values are either an artifact or something interesting. UD45K is a marked departure with an overall larger value than what we would expect.

gap, coupled with a very small kink signature. From observation the kink signature is hard if not impossible to detect at small gap values. We suspect that it will require higher resolution lower noise data to detect this feature at these dopings. Another problem is since the lifetime decreases with decreasing Δ_1 value, we run into a resolution problem in k-space. That is we have been using 128X128 uniform grids to generate the LDOS, and at low alphas these become unviable, and just return noise. We believe we have solved these problems through the introduction of an adaptive gridding system that boosts the resolution as we approach the Fermi level for each particular energy. In AC-11(b) we show Δ_0 as a function of Δ_1 . We see a similar universal trend at high energies where at low energies we once again seem to underestimate Δ_0 , while it seems to be corrected somewhat in the UD74K data. One would expect that Δ_0 converges to Δ_1 at these low energies. This suffers from the same problems described for Δ_{00} above.

In figure AC-12 we have out B as a function of Δ_1 , which seems to show no clear trend, possibly due to variations associated with the checkerboard state. However it does seem to drop off at low Δ_1 values, which is the opposite of what we would expect from chapter 4. However the low gap values in these samples can be associated with impurity atoms or Copper site vacancies. Therefore they may relate more to impurity effects rather than any universal scaling. In figure AC-12(b) we see a very interesting trend. UD74K and UD65K show a universal lifetime behavior, however UD45K shows a marked divergence. This is probably due to the onset of the ECG state which stabilizes the lifetime on the positive side of the spectrum. We expect (and have preliminary evidence from previous fits) that the negative side of the spectrum the lifetime continues along the line marked by UD74K and UD65K. This divergence may divide the actual data into two sections, one with the ECG and one without. It will be of interest to pursue this with better fits, and negative side fits.

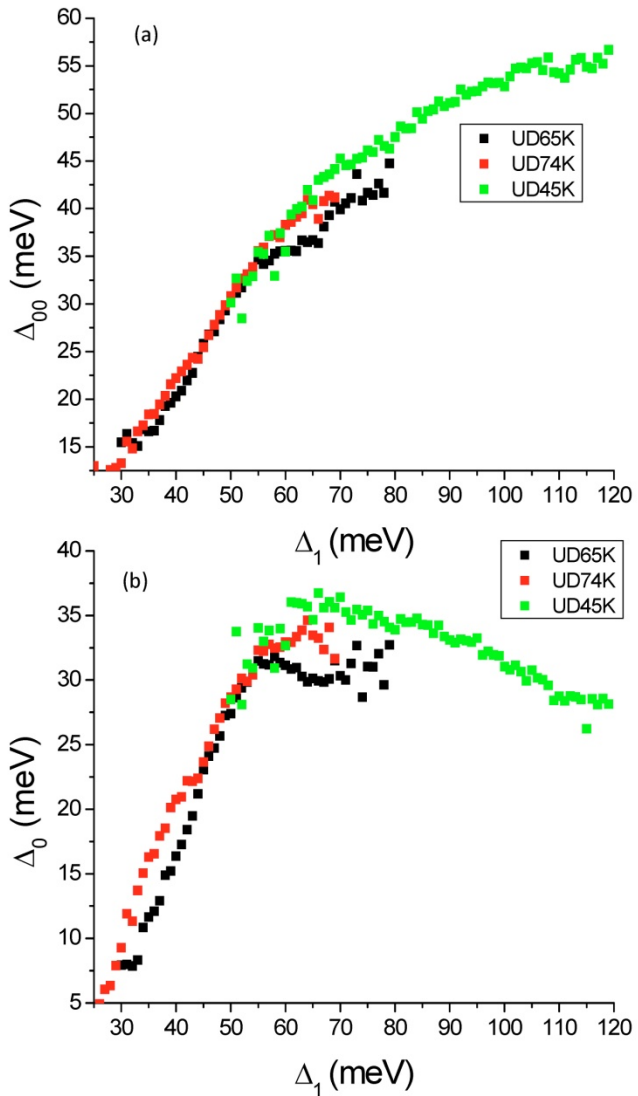


Figure AC-11: (a) shows the trend for Δ_{00} as a function of Δ_1 showing a pretty universal trend. With an interesting higher energy turnover viable in UD65K and UD45K. This is where I would peg the ECG state to set in. However one would expect it to depart from the linear background at low values of Δ_1 , this is something which needs to be investigated. (b) Δ_0 as a function of Δ_1 , showing an expected departure for UD74k from the UD65k data, since Δ_0 is expected to scale with Tc trend should continue and does with UD45K which starts to turn over.

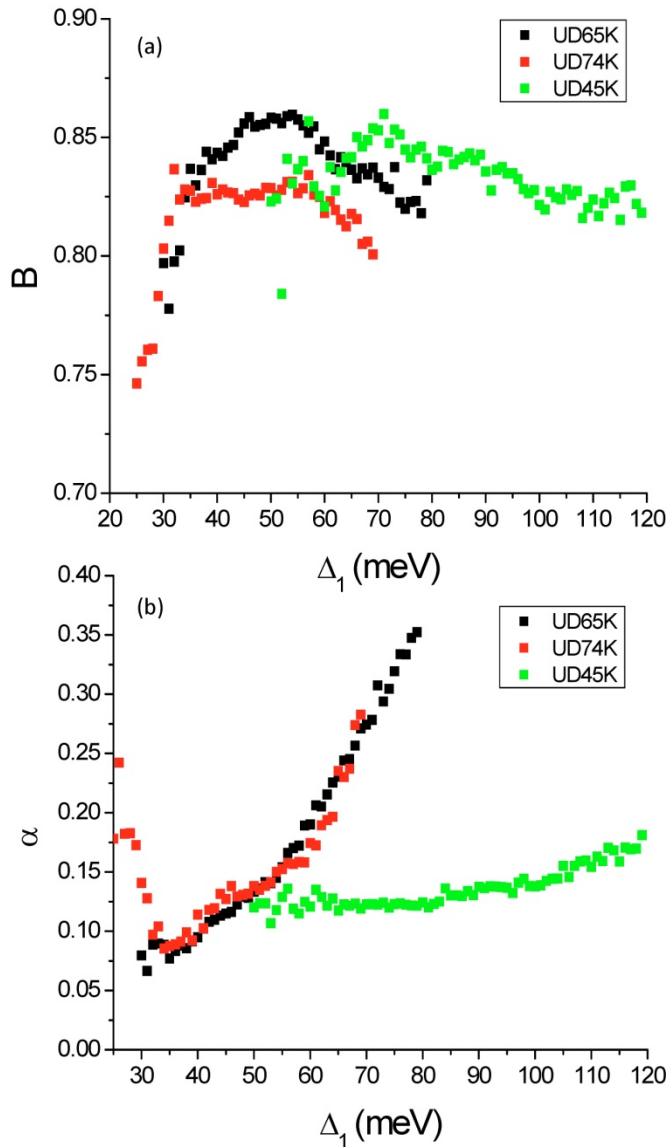


Figure AC-12: (a) B as a function of Δ_1 , it is curious that UD74K is lower overall than UD65K, this could be a fitting problem, or an averaging problem. The drop off at low dopings is interesting, and probably has something to do with Cu vacancies/zinc impurities. (b) α as a function of Δ_1 , this is expected and consistent with our previous results. Of interest however is the upturn at low gaps. This follows out latest fits, and it will be of interest if this trend follows at higher dopings. However UD45K departs from this background at the energy where Δ_0 turns over, suggesting, that we really do have two different regions of interest.

Bi-2201

We switch gears slightly in figure AC-13,14. Here we present the first successful fits of a La doped Bi-2201 data. The 2201 data has always had a large kink that has up to this point managed to frustrate previous fitting attempts. However here as shown in figure AC-13,14 we manage to do quite a good job of capturing the spectra. We use a tight binding 2201 band structure, taken from ARPES². In figure AC-15 we show our standard fitting parameters, we note that while there are some problem areas, the gap map does look very nice. Even nicer still is the alpha map in AC-15(c). This seems to show a modulation of the peak heights and is once again probably associated with the ECG pattern. The slope also shows a strong ECG type pattern. We note that this is a single sided slope, and therefore the only reference it has to the negative side is a possible overall modulation caused by the normalization setup condition. In figure AC-16 we show the rest of the fitting parameters. We get clusters of extremely small Δ_{00} , which could be real, but more likely since they are correlated with small Δ_1 ; they are the same problem we were running to in 2212. The rest of the parameters are highly disordered. And also occur at small energy scales, especially Δ_0 . If we plot a histogram of B we see that it is a bimodal distribution. We are as of yet unsure if this is real or not. But in examining AC-16(b) we see an interdispersed pattern of yellow and green, which could represent these two different regions. It is also possible that this has something to do with the checkerboard modulation and that is bleeding through to these parameters. In AC-17(b) we show the Δ_{00} which has a large spike at 5meV which is the minimum we allowed in this particular fit. In 18(a) we see a very nice histogram of Δ_0 showing a distributed small energy scale, which scales as we

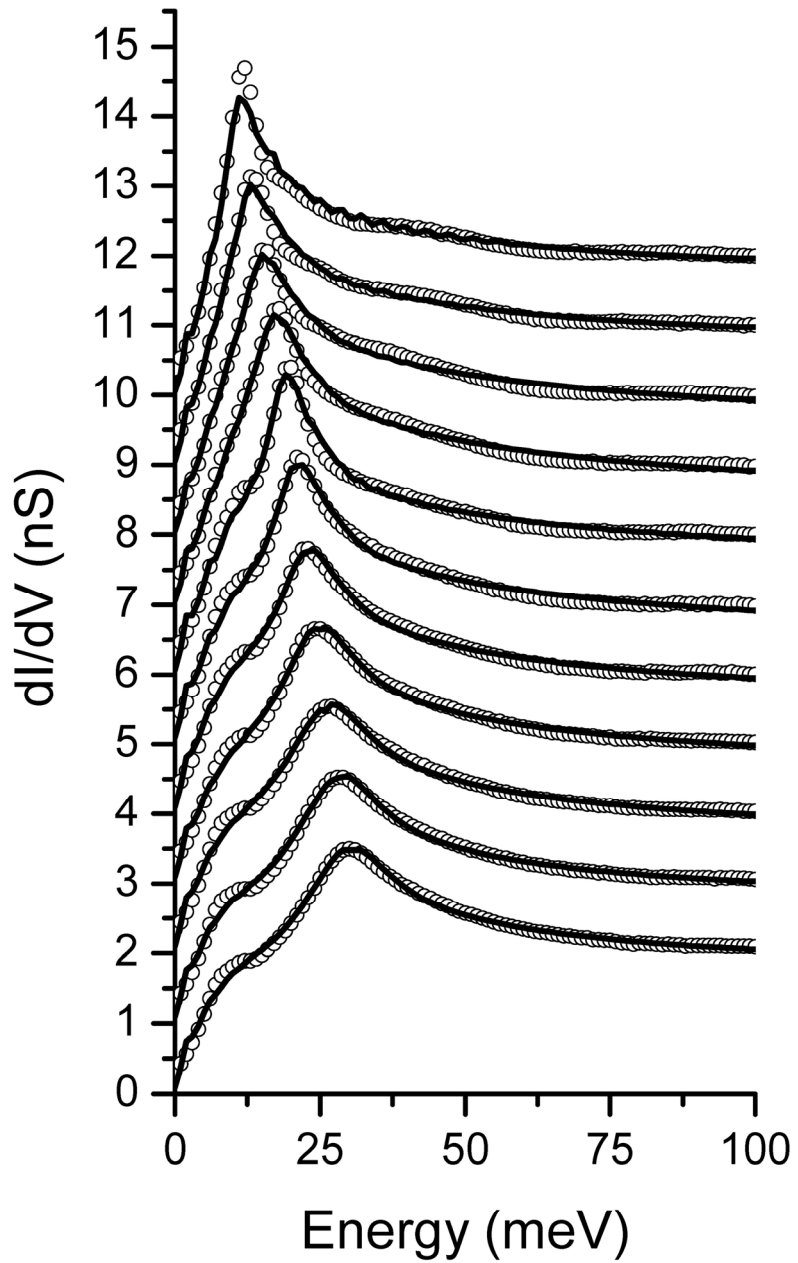
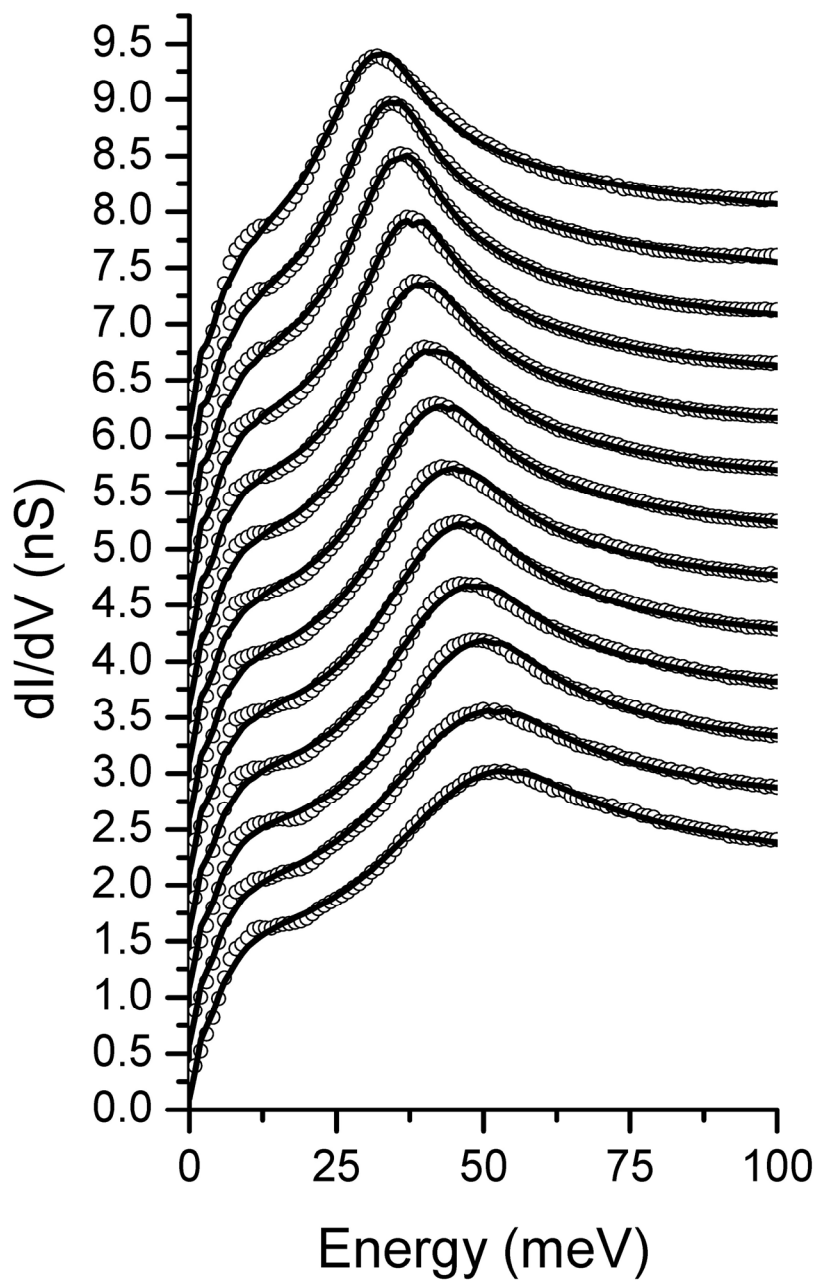


Figure AC-13: Δ_1 averaged spectra from La-2201 35K sample, starting at 10meV and progressing upward in 2meV increments. The open circles are the data, while the heavy black line is the fits.



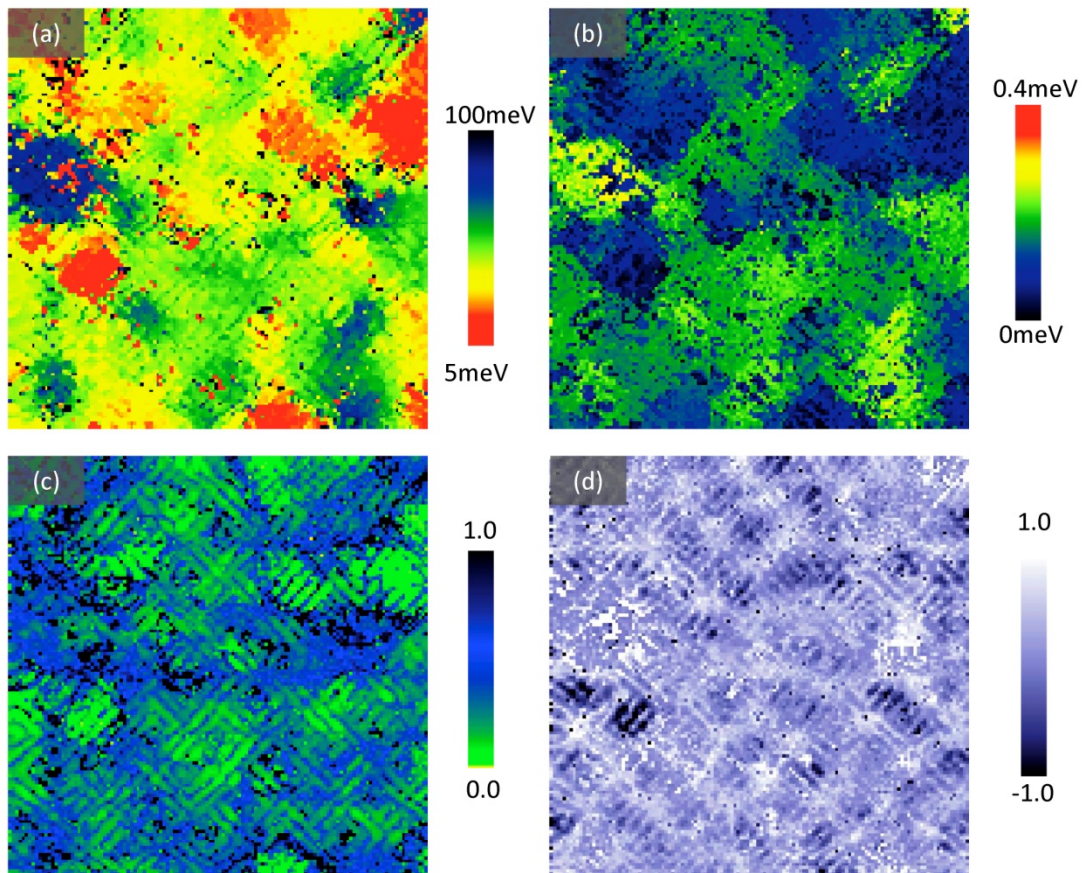


Figure AC-15: These are the initial fitting attempts for 35K La-2201. The idea here is to look at small scale structure of 2201 and compare to 2212. In 2201 we have pronounced secondary peak or kink, as seen in figure (a) Δ_1 (b) Γ_1 , (c) α , (d) is the one sided slope.

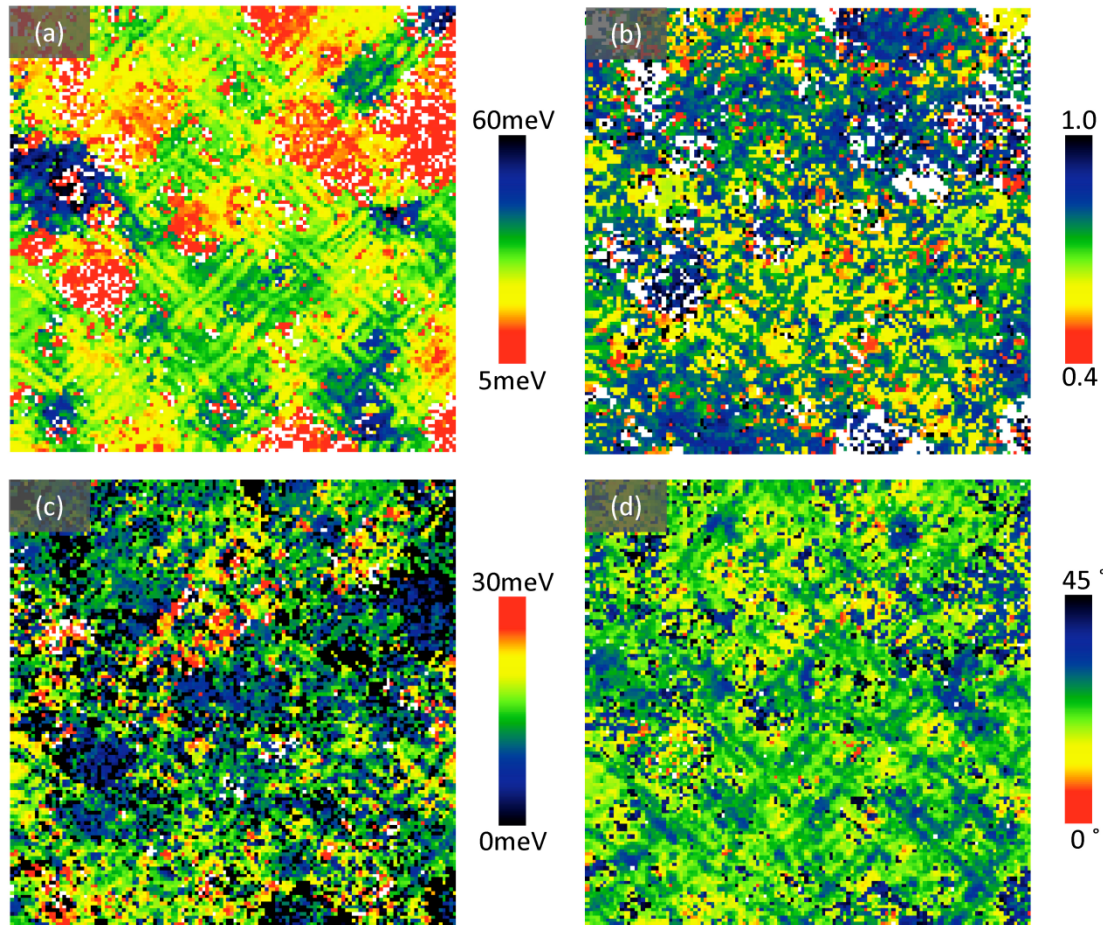


Figure AC-16: More 2201 fitting parameters. (a) Δ_{00} , (b) B , (c) Δ_0 , (d) Θ_{term} , which is the angle where given a constant μ the coherent quasiparticles would terminate. Δ_1 correlated with Δ_{00} is 0.326, Δ_1 with Δ_0 is 0.076, Δ_{00} with Δ_0 is 0.6

would expect. That is Δ_0 is smaller in 2201 than 2212 since this scales with Tc. We also show the Θ_{term} in AC-18(b).

We look at the dependence of B on Δ_1 in figure AC-19. Here we can see the two distributions, with their differing behavior at low Δ_1 . We follow this up with the dependence of Δ_{00} and Δ_0 on Δ_1 in figure AC-20. Here we see the Δ_0 seems to max out at a much lower value of Δ_1 than 2212. Since scales with Tc this is also expected. Δ_{00} also departs from Δ_0 around 35-40meV in 2201 while a similar transition happens around 75meV in 2212. A most intriguing experiment would be to map this across all three biscoco compound that is extend this to tri-layer-2223.

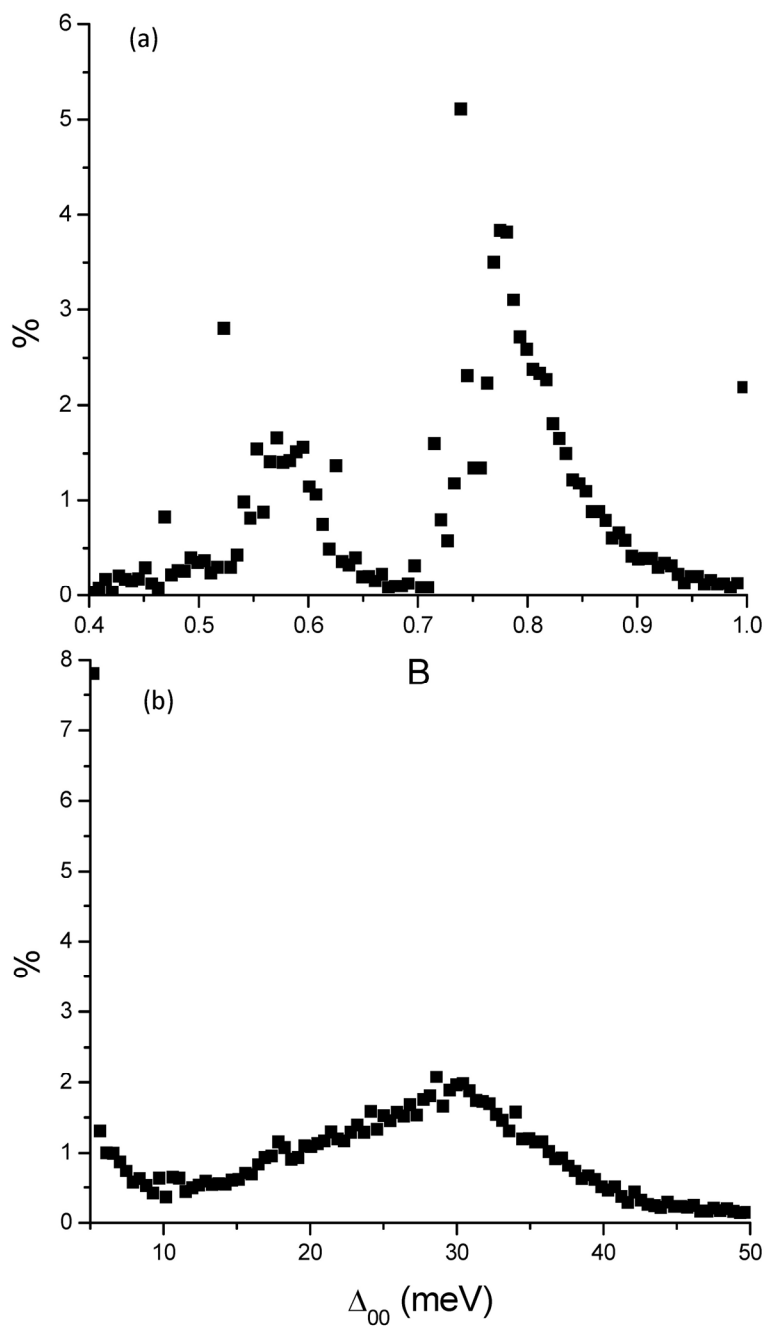


Figure AC-17: (a) B histogram, showing the clear division into the two different regions, similar to UD45K 2212. (b) D00 histogram, showing a large peak around 5meV the minimum. Need to investigate if this is an artifact or not.

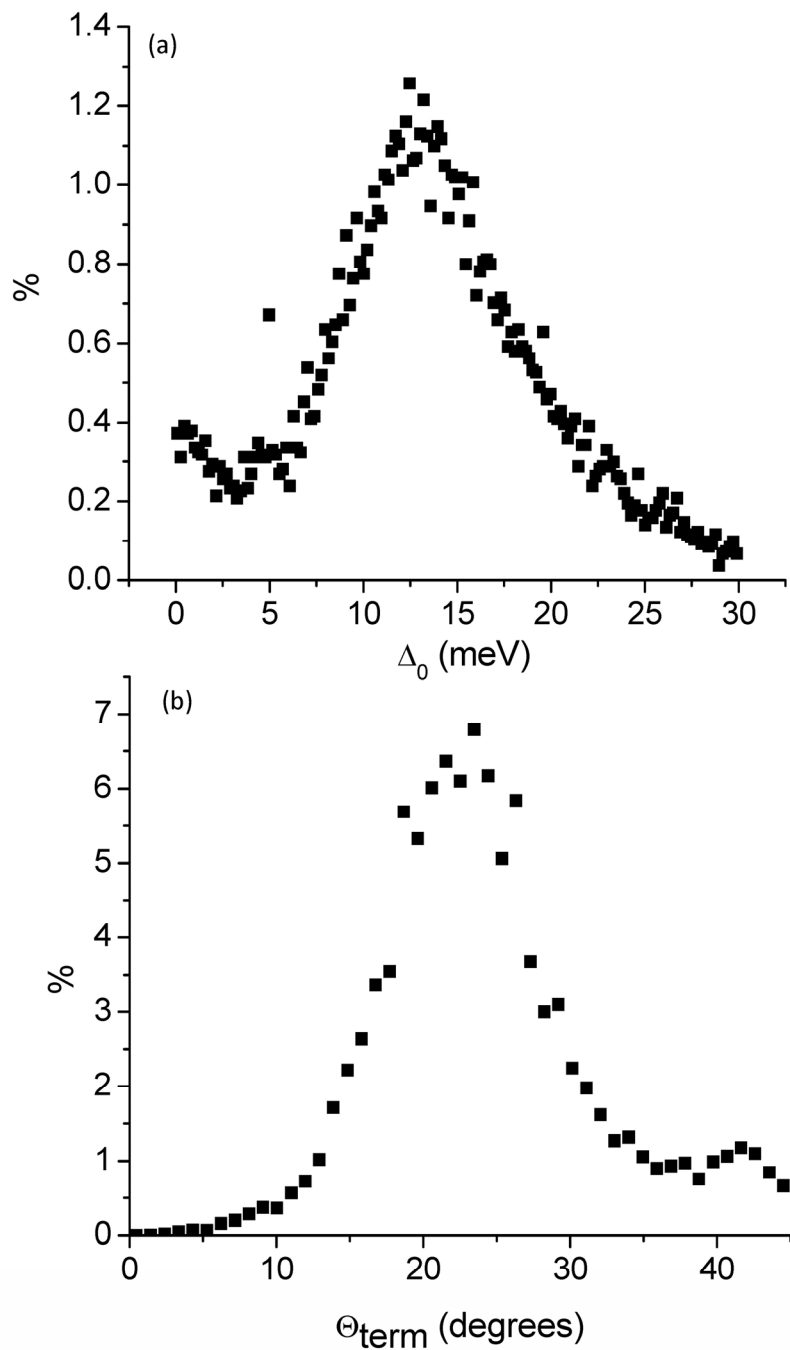


Figure AC-18: (a) Δ_0 plot, showing a small energy scale, as well as the distribution size. (b) The termination angle

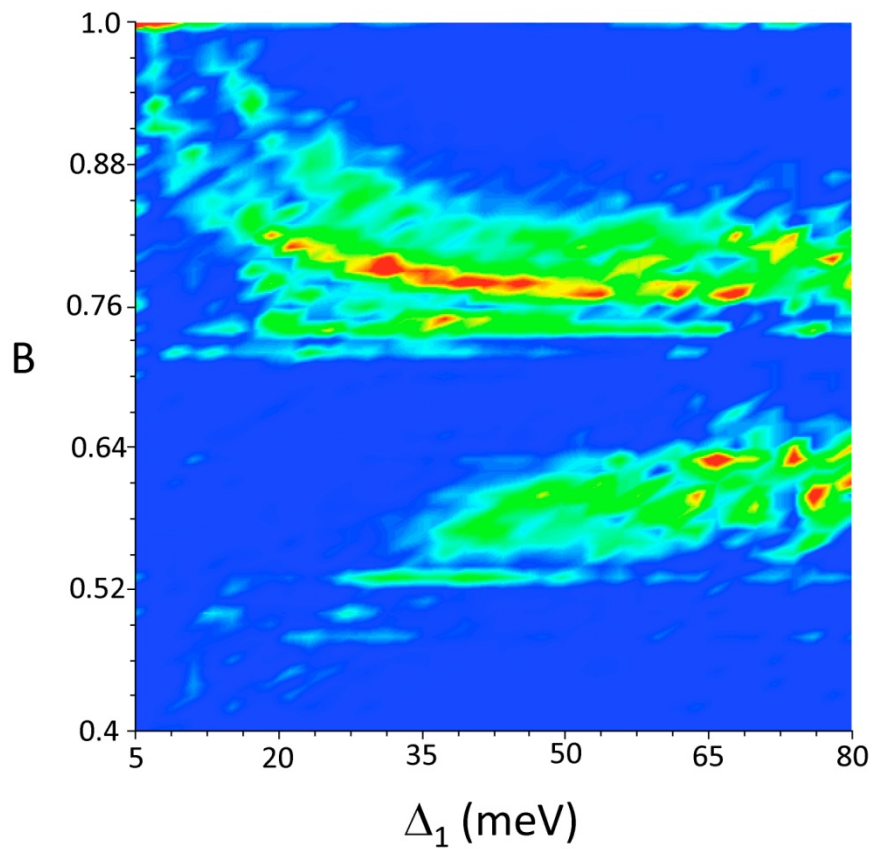


Figure 19: Contour plot showing the two distributions of B and their dependence on Δ_1 .

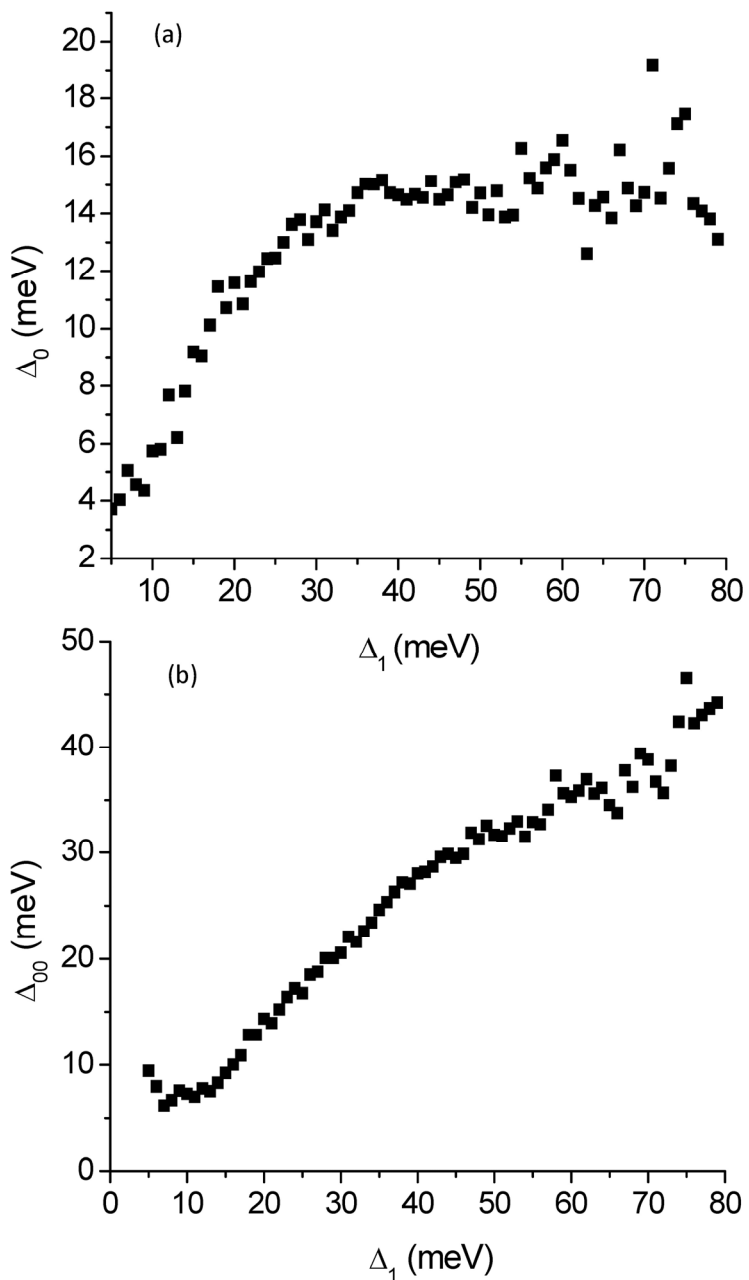


Figure 20: (a) Δ_0 vs Δ_1 showing a similar turnover as seen in 2212. (B) Δ_{00} scaling with Δ_1 , once again similar to 2212. In order to map out these behaviors we would need more data across doings.

Conclusion

Overall this analysis has the prospect of revealing some interesting behavior and expanding our knowledge of the variation in the local electronic structure. Hopefully the code can be flushed out, as well as higher quality data sets being obtained. We can then apply this as a function of doping, as a function of layer, and as a function of temperature. It is quite probable we can watch the lower energy states close and map out the area and the temperature dependence of these phenomena. However this work will have to be continued.

REFERNCES

¹

²

APPENDIX D

Science as Art

Here I present a collection of various images that never made it into any other published work. They are alternative figures, proposed cover images, and results of analysis that didn't quite make the grade, however all of them have one thing in common, they are pretty. Not only have that, but they all for the most part provided a unique perspective on a particular physical phenomena, whether it be through a clever way to encode a measured physical quantity, or a generated display of our underlying model., or simply a byproduct of a simple coding or design project. In any case these pictures exist regardless of what they are trying to represent, although in many cases that simply adds to the beauty.

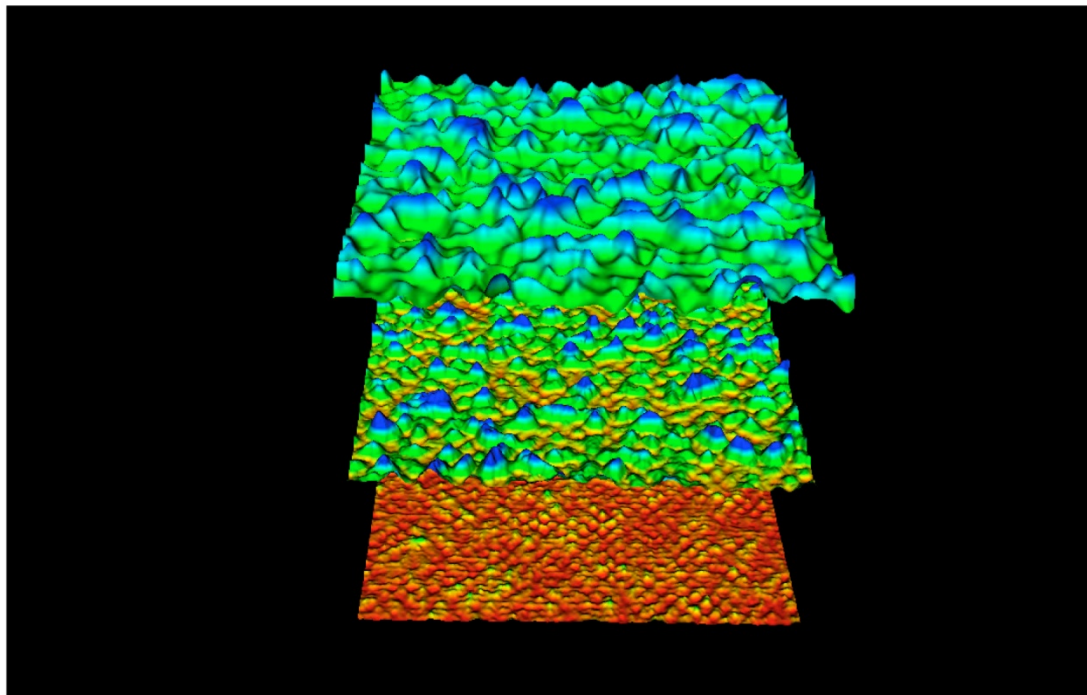


Figure AD-1: 3D view of UD74K data, showing the three separate sections. The bottom layer shows QPI pattern, the middle layer shows the destruction of the QPI by the onset of the higher energy gap disorder, and the top layer shows the Higher order gap disorder.
 50nm^2

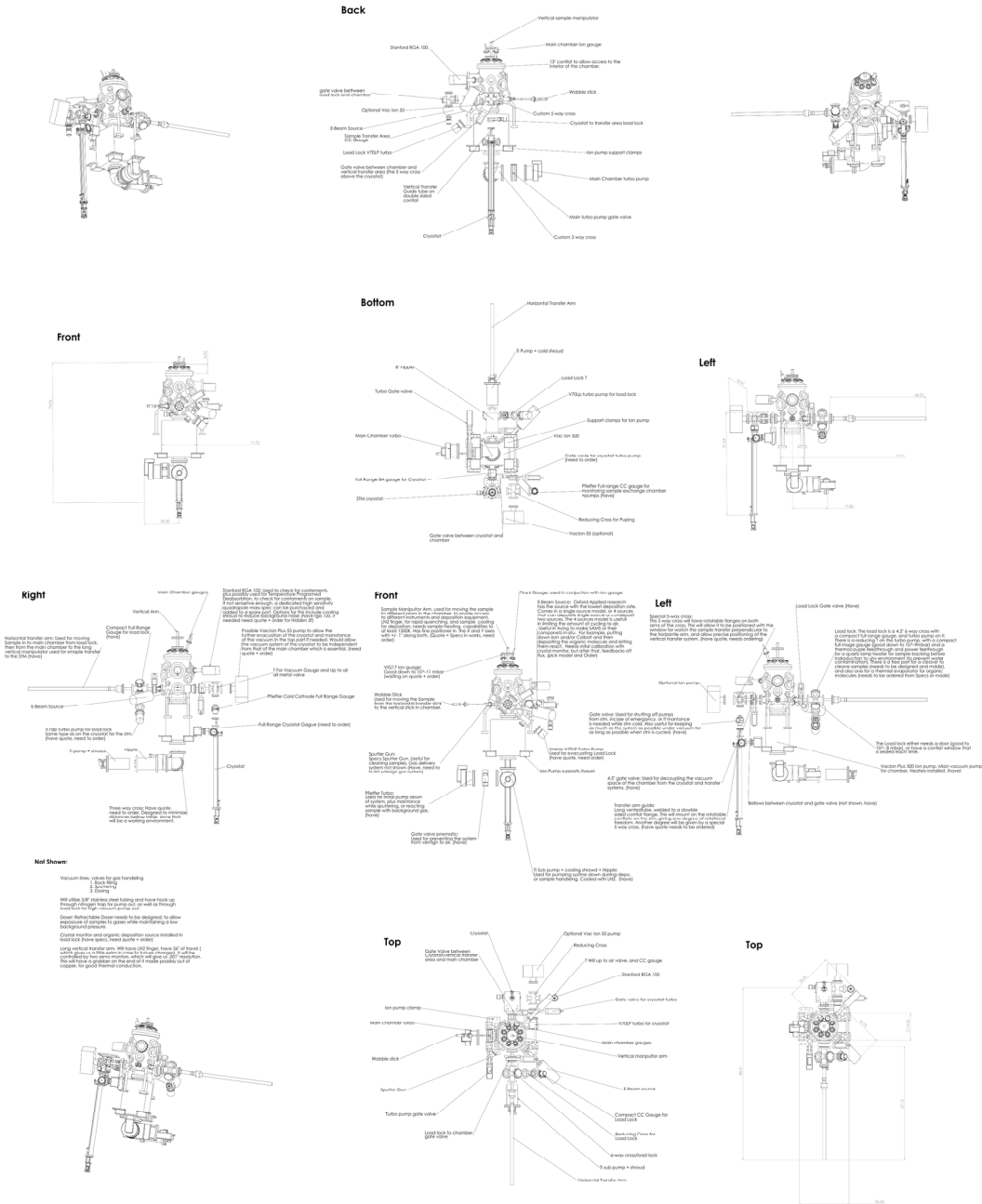


Figure AD-2: Titled “The vacuum system that never was...” This represents the plans for a UHV component to STM3, never came to pass due to issues with getting STM3 working, as well as the pointlessness of adding a UHV system to a vacuum system that had been contaminated with thermally evaporated Apizon grease and small narrow tubes incapable of being pumped upon.

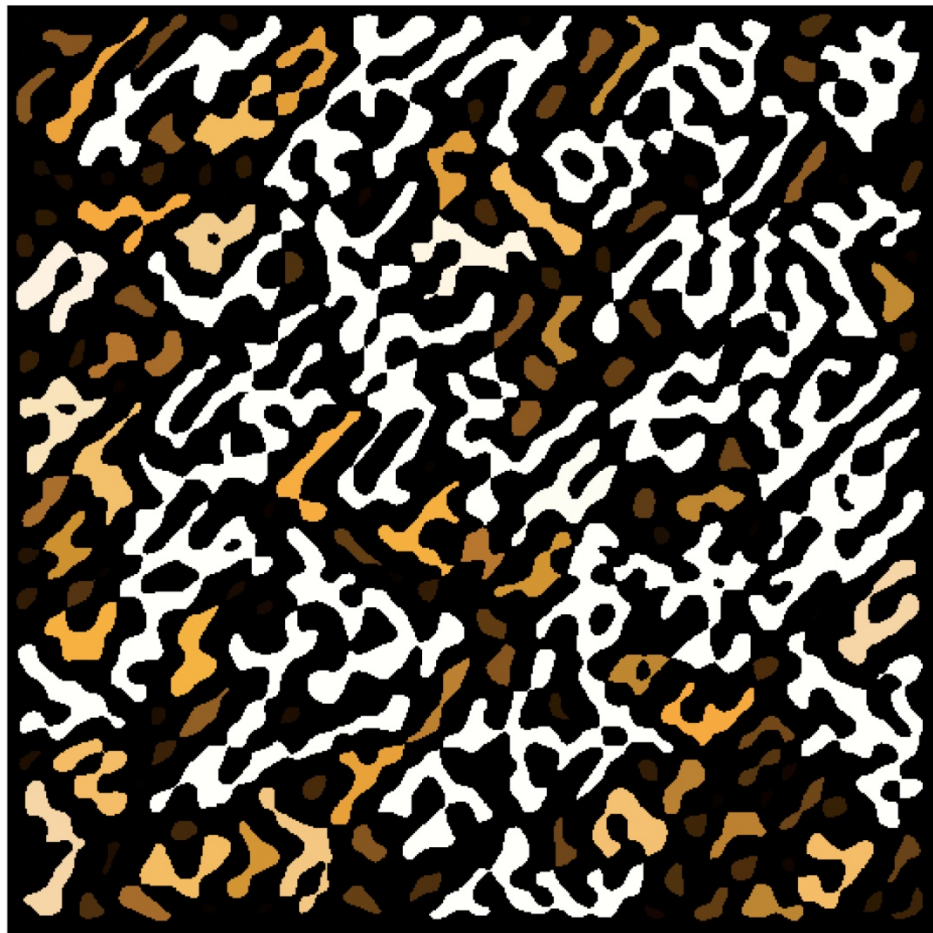


Figure AD-3: Mapping the ECG state of high Tc's by measuring the cluster size distribution in the ratio maps. Color corresponds to cluster size. Never came to pass due to lack of data. This from Gd² doped Bi-2201 12nm

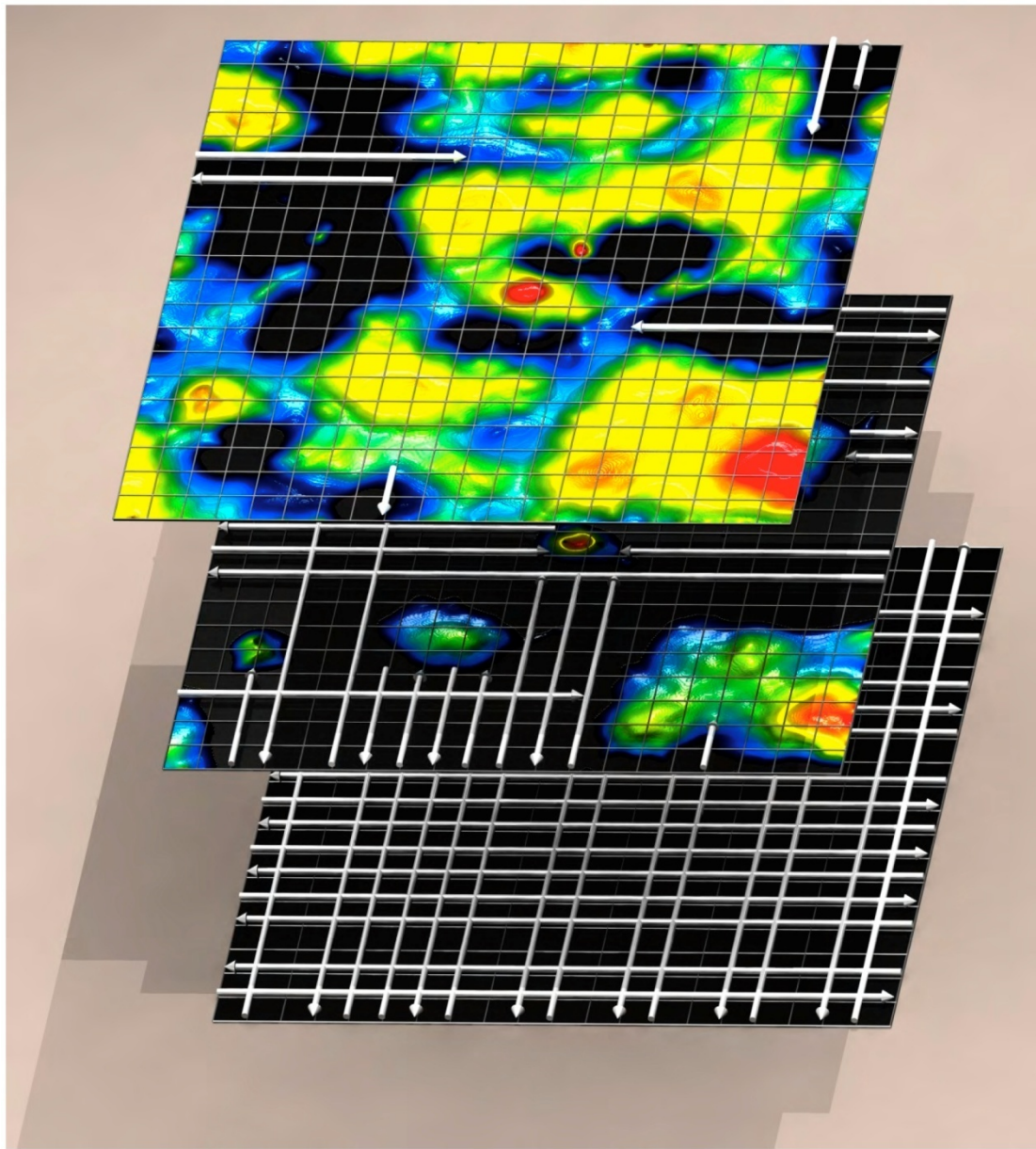
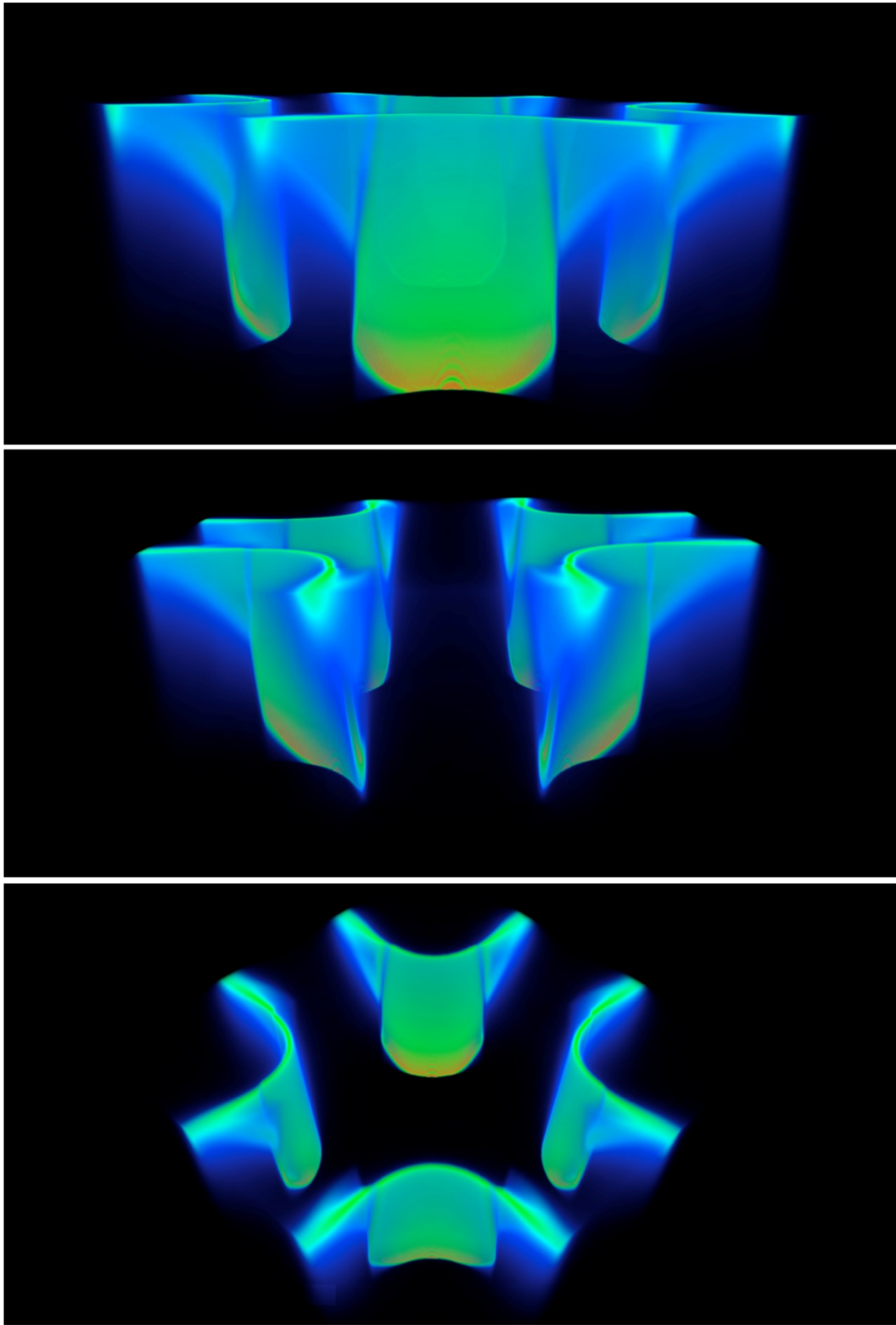


Figure AD-4: Illustration showing the decreasing area of coherence with increasing energy in High-Tc's. The arrows represent the coherent cooper pairs which are disrupted by increasing disorder.

Figure AD-5: ‘The eerie specter of $a(k,\omega)$ ’ These are the complete first billion zone for positive energies, of the $a(k,\omega)$ proposed in chapter 4. The color and transparency represent the intensity of the spectral density of states, with red being highest. For UD45K data.



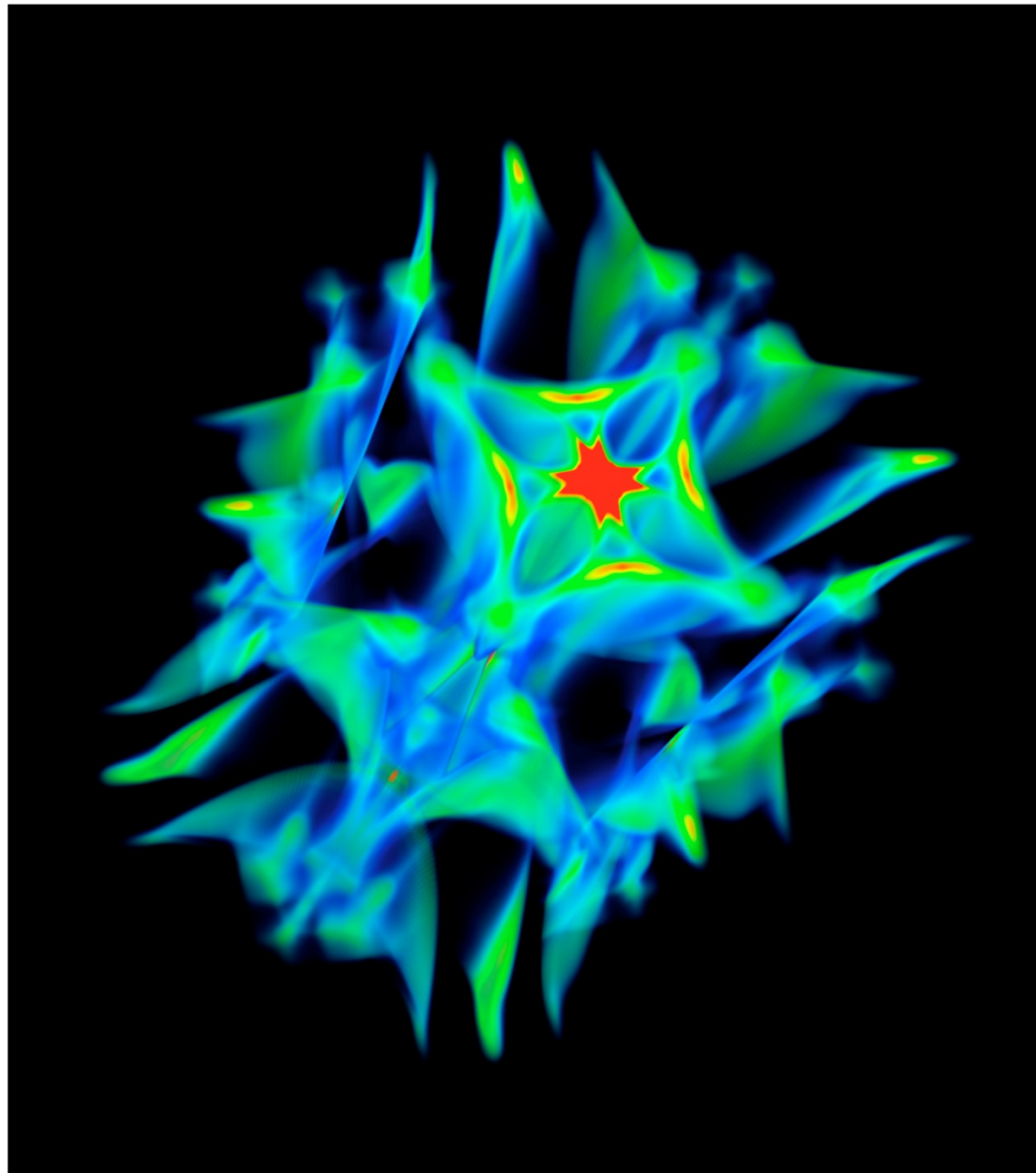


Figure AD-6: JDOS-1: A representation of the Joint Density of States, ranging from -50meV-50meV. The perspective here is out on the positive end, looking backwards towards -50meV.0 Color and transparency are linked to intensity with red and solid being high.

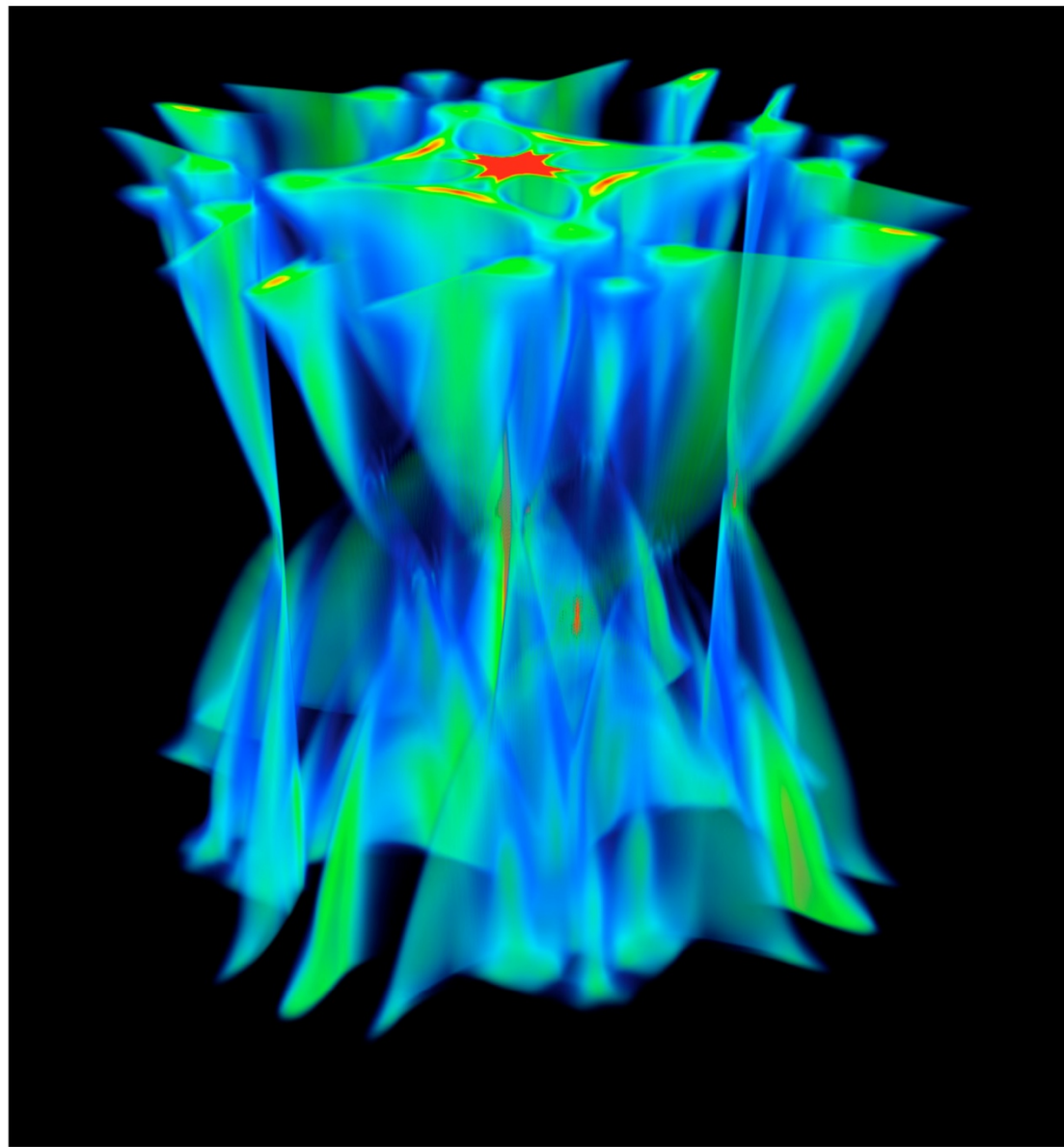


Figure AD-7: JDOS-2: A representation of the Joint Density of States, ranging from -50meV-50meV. The perspective here is from the side with 0meV being in the middle. Color and transparency are linked to intensity with red and solid being high.

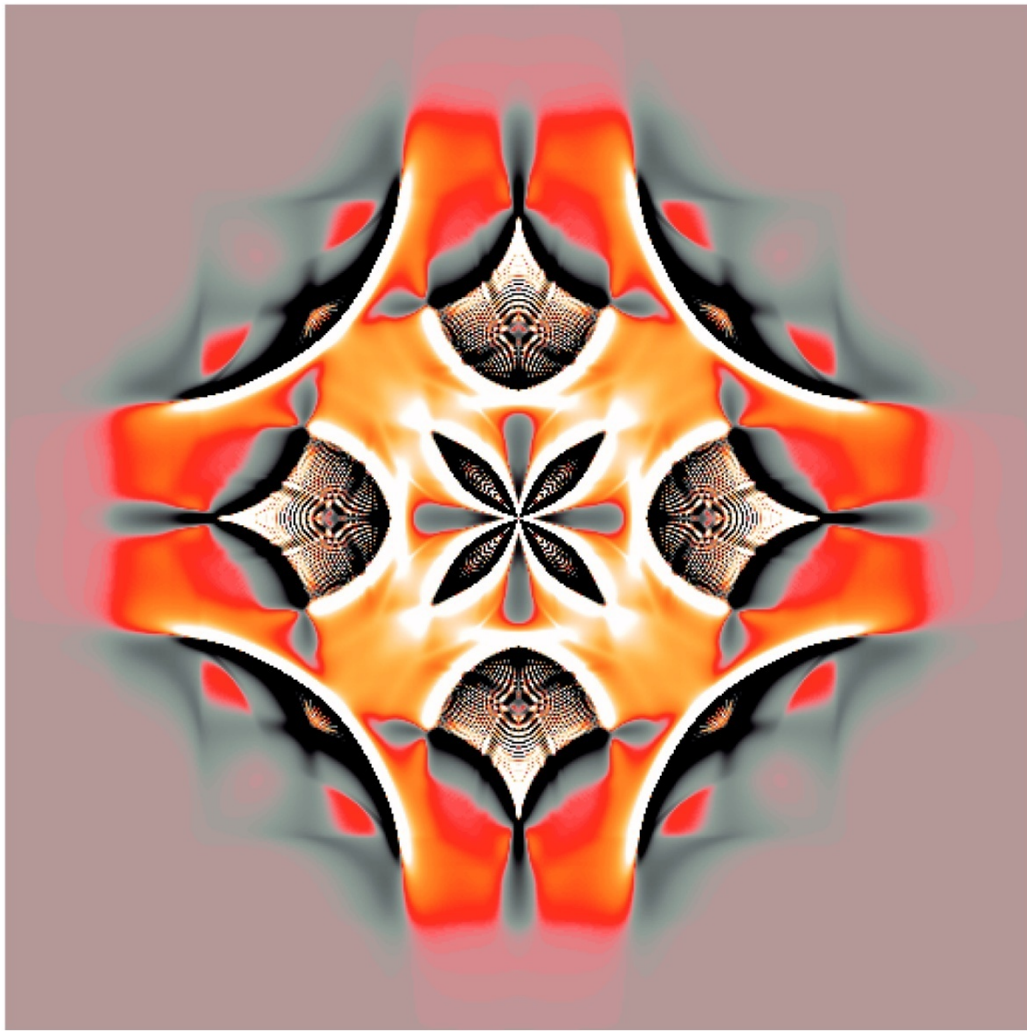


Figure AD-8: Seen before in chapter 3, this represents the difference between positive and negative JDOS. For 14meV UD74K.

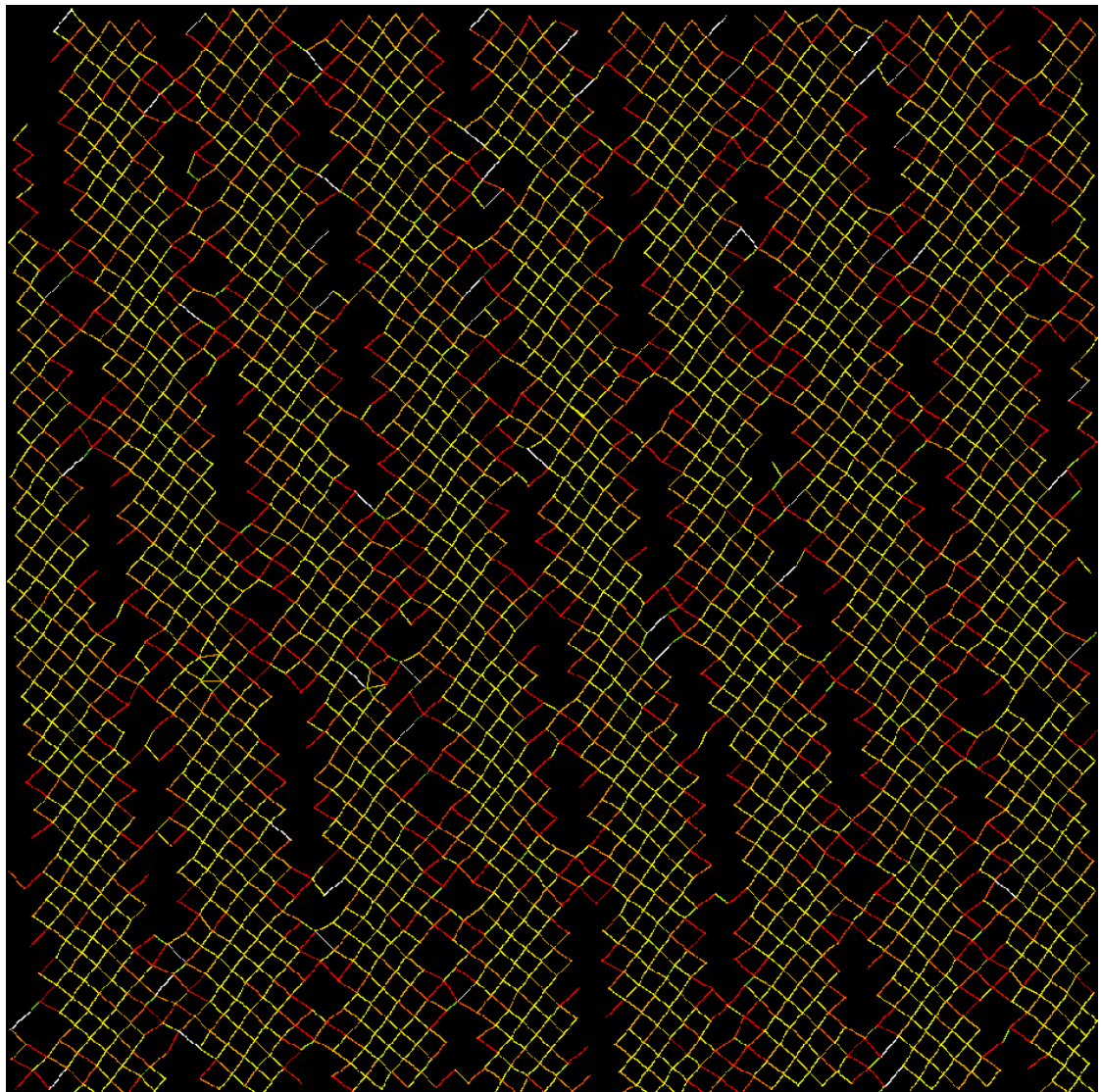


Figure AD-8: Mapping out the inter atomic distances on the BIO plane. The color represents the distance between BI atoms, with red being the longest, and yellow being the shortest. This was done in an attempt to compare Bi distortions to computer models. Approx. 20nm²

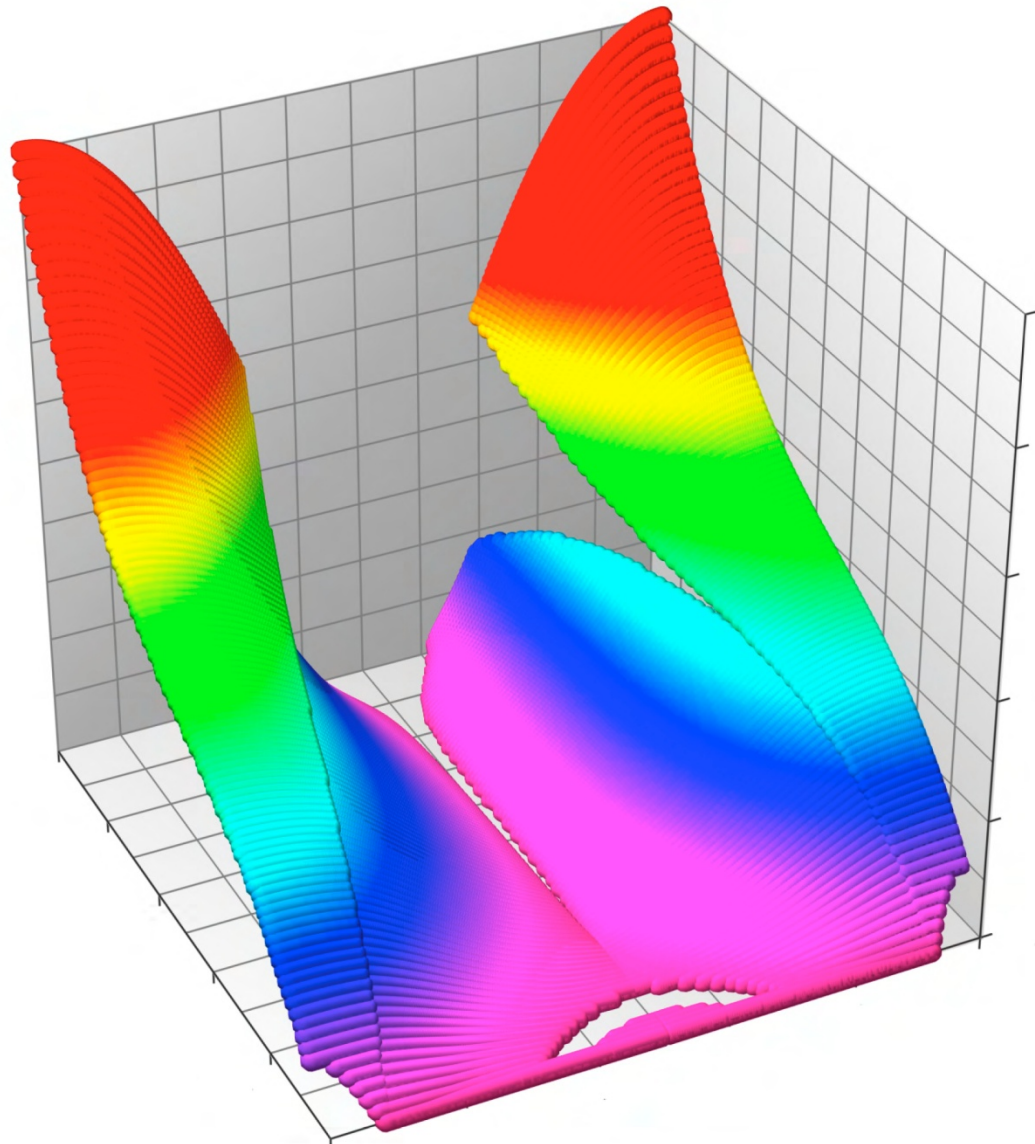


Figure AD-9: k-space gap as a function of angle and doping. Highest doping close to viewer, with 45 degrees being in the middle. Color coded with Gap value. This shows the peeling away of the low energy gap structure with decreasing doping, as well as the convergence of the two scales at higher doping.

Figure AD-10: ‘Seamus as Data’. My first project in coding was automating the extraction and leveling of all of our data sets to create this. Each pixel is replaced by an appropriate intensity data set, with images ranging from FFT’s to vortex cores, to nanotubes, to topographs.

